Effect of CEC, Salinity, Mineralogy, Sand Content, and Particle Size Distribution on Mud Rock Properties

A Thesis

Presented to

The Department of Petroleum Engineering

University of Houston

In Partial Fulfillment

Of the Requirements for the Degree

Master of Science

By

Mohab Dessouki

December 2015

Effect of CEC, Salinity, Mineralogy, Sand Content, and Particle Size Distribution on Mud Rock Properties

Mohab Dessouki

Approved:

Dr. Michael Myers, Associate Professor, Chair of the Committee, Cullen College of Engineering

Committee Members:

Dr. Lori Hathon, Assistant Professor, Petroleum Engineering Department

Dr. John T. Germaine, Research Professor, Tufts School of Engineering

Dr. Suresh K. Khator, Associate Dean, Cullen College of Engineering

Dr. Tom Holley, Professor and Director, Petroleum Engineering Department

Acknowledgements

I would like to express my gratitude to my committee chair, Professor Michael Myers. My experience working with him was extremely positive. I really appreciate his intellectual skills and experience which have added considerably to my graduate experience. I would like to thank him for his extreme patience, and believing in my abilities while providing me with all kinds of assistance throughout my experimental and research work. Professor Myers gave the freedom of working on my own, at the same time continuing to contribute with valuable advice, and guidance. Without his encouragement and effort this thesis would not have been completed or written.

Very special thanks go to my advisor, Professor Lori Hathon, who has provided me with guidance, assistance, and expertise that I needed to complete this thesis. I would like to thank her for always being supportive and encouraging. I feel very privileged to have been her student.

I am very thankful to my advisor, Professor John Germaine, who has vast expertise and knowledge in soil mechanics, which is the heart of this thesis. I really appreciate his guidance and support. It has been a great honor to have him as my thesis advisor. I would like to thank Jana Marjanovic for helping me with data interpretation.

I would like to thank my lab mates for their support. To Abdulla Bilal, who helped me with setting up the mechanical tests. To Malek Al-Salman, who helped with experiment setup training. To Dan Coleff, who helped in installing lab equipments. To Jong Moon Lee, who helped in performing CEC measurements.

Effect of CEC, Salinity, Mineralogy, Sand Content, and Particle Size Distribution on Mud Rock Properties

An Abstract

Of a

Thesis

Presented to

The Department of Petroleum Engineering

University of Houston

In Partial Fulfillment

Of the Requirements for the Degree

Master of Science in Petroleum Engineering

By

Mohab Dessouki

December 2015

Abstract

Mudrocks are fine grained, extremely low porosity and permeability sedimentary rocks that contain significant amounts of clay minerals. These rocks are difficult to characterize their physical properties or test their mechanical behavior. Clay's cation exchange capacity (CEC) make these rocks water sensitive due to double layer expansion or collapse. Conductometric titration and methylene blue colorimetry were used to measure CEC and compared to cobalt hexamine technique values provided by a vendor.
In this work, we studied petrophysical and geomechanical properties of resedimented mudrock core samples. Three major properties were varied; they are clay's percentage, cation Exchange capacity and brine salinity.

The use of the reconsolidation technique allows us to create mud rocks in the laboratory while controlling mineralogy, sorting, brine salinity, and axial stress, this is similar to sand pack experiments performed by (Hathon & Myers, 2011) which showed that mineralogy, grain size, sorting, stress history and incipient overgrowth cements all affect the porosity as a function of depletion stress.

Triaxial testing is commonly used to determine the failure envelope for mudrocks. The most common application of this technique requires multiple identical samples. In heterogeneous formation identical samples are often difficult to obtain. The twinning problem is overcome by performing 'multistage' tri-axial tests. These tests were performed on reconsolidated mud rocks to determine their strength properties (Salman, Myers, & Sharf Aldin, 2015). Strength data are compared based on the sample's variations such as CEC, brine salinity, and clay content.

Table of Contents

List of Figures

List of Tables

Chapter 1 : Introduction

1.1 Overview

Mudrocks comprise as much as 90 percent of the penetrated section of sedimentary basins. They provide the sealing lithology for most conventional hydrocarbon accumulations. In this setting mudrocks are usually cored only by accident making the availability of mudrock samples for measurement rare. The presence of clay minerals causes deviations from the normal ‘physiochemical relations found to exist for non-shale reservoirs’ (Hill, Shirley, & Klein, 1979). A portion of the water present in shale’s pore spaces is closely associated to clay’s surface as bound water. The amount of bound water is related to the Cation exchange capacity and the concentration of the equilibrating electrolyte solution. The goal of this thesis is to further the understanding of the impact of some of the major factors involved in mudrock petrophysical and geomechanical properties.

In chapter one starts with a general description of the predominant clays studied in terms of their chemical structure. This discussion is included to give the reader an elementary understanding of the high variabilities of these materials physical properties.

In chapter two we discussed the detailed experimental procedures for the CEC measurements, reconsolidation, and multistage triaxial tests. This section is included to document the specific procedures we used which are sometimes significantly different from what found in the literature. This section may be skipped without significantly loss of understanding of the results section.

Chapter three presents the experimental results of CEC measurements, reconsolidation, and multistage triaxial tests.

1.1.1 Clays Description

Clays are hydrous aluminum silicates with a sheet like layer structure and very small particle size. Clay minerals are composed of essentially of silica, alumina or magnesia or both, and water, but iron substitutes for aluminum and magnesium in varying degrees, and appreciable quantities of potassium, sodium, and calcium are frequently present as well. Clays consist of two fundamental crystal sheets, the tetrahedral or silica, and the octahedral or alumina sheets. The particular way, in which these sheets are stacked together with different bonding and different metallic ions in the crystal lattice, constitute the different clay minerals (Holtz & Kovacs, 1981).The tetrahedral sheet is a combination of silica tetrahedral units which consist of four oxygen atoms at the corner, surrounding a single silicon atom. The oxygen atoms at the base of each tetrahedron are combined to form a sheet structure, the oxygen at the bases of each tetrahedron are in one plane, and all the oxygen atoms at the individual corners point at the same direction as shown in **Figure 1 Silica tetrahedron lattice structure** (Holtz & Kovacs, 1981).

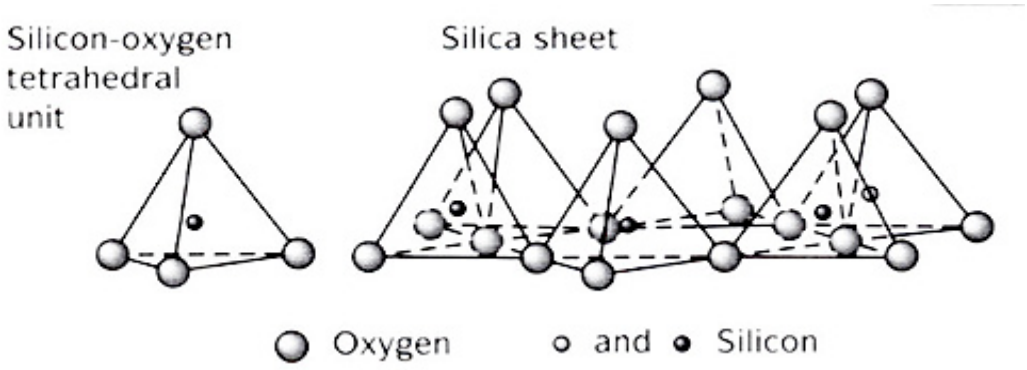

Figure 1 Silica tetrahedron lattice structure.

The octahedral sheet is basically a combination of octahedral units consisting of six oxygen or hydroxyls enclosing aluminum, magnesium, iron, or other atom as shown in **Figure 2 Alumina octahedral structure** (Holtz & Kovacs, 1981).

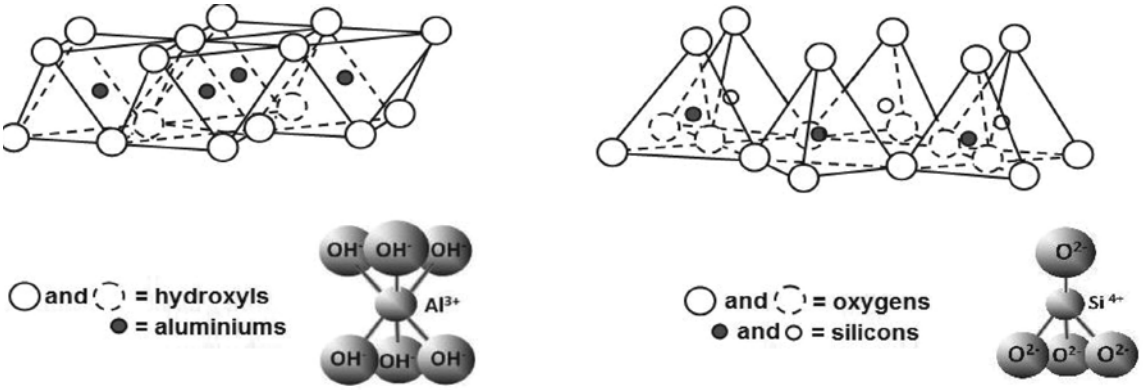

Figure 2 Alumina octahedral structure.

Substitution of cations in the octahedral sheet is common and leads to a different clay mineral. Since the ions substituted are of the same size, such substitution is called isomorphous. Some octahedrons do not contain a cation, which results in a different crystalline structure. (Holtz & Kovacs, 1981).

The octahedral and tetrahedral sheets are stacked together in various stacking patterns giving rise to the different clay minerals that have been used for our study.

1.1.2 Clays Types and composition

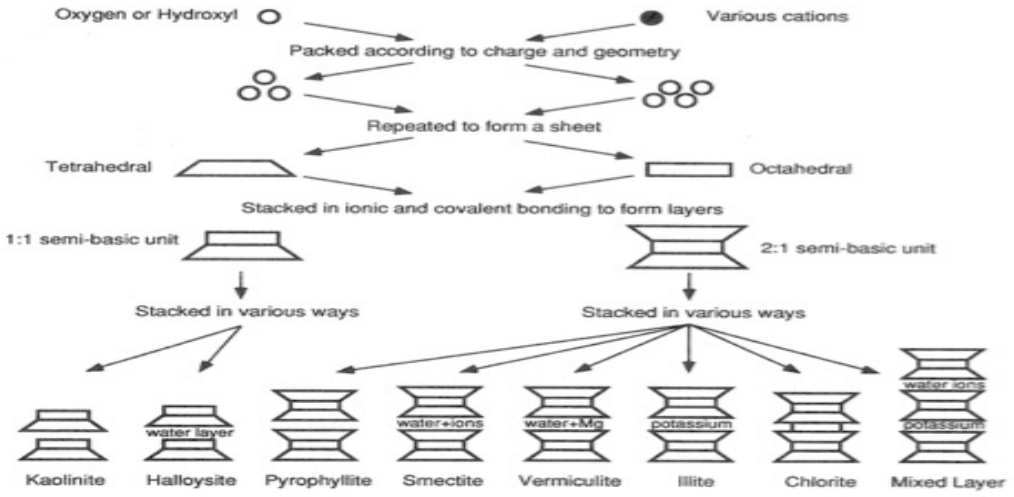

Figure 3 Composition of clay minerals **(Mitchell, 1993)**.

1.2.2.1 Smectite Group

Smectite group includes the di-octahedral minerals montmorillonite, beidellite, nontronite, and the tri-octahedral minerals hectorite (Li-rich), saponite (Mg-rich), and sauconite (Zn-rich). The basic structural unit is a layer consisting of two inward pointing tetrahedral sheets with a central alumina octahedral sheet. The bonds between layers are week and have excellent cleavage, allowing water to enter between layers causing swelling (U.S Gelogical Survey, n.d.).

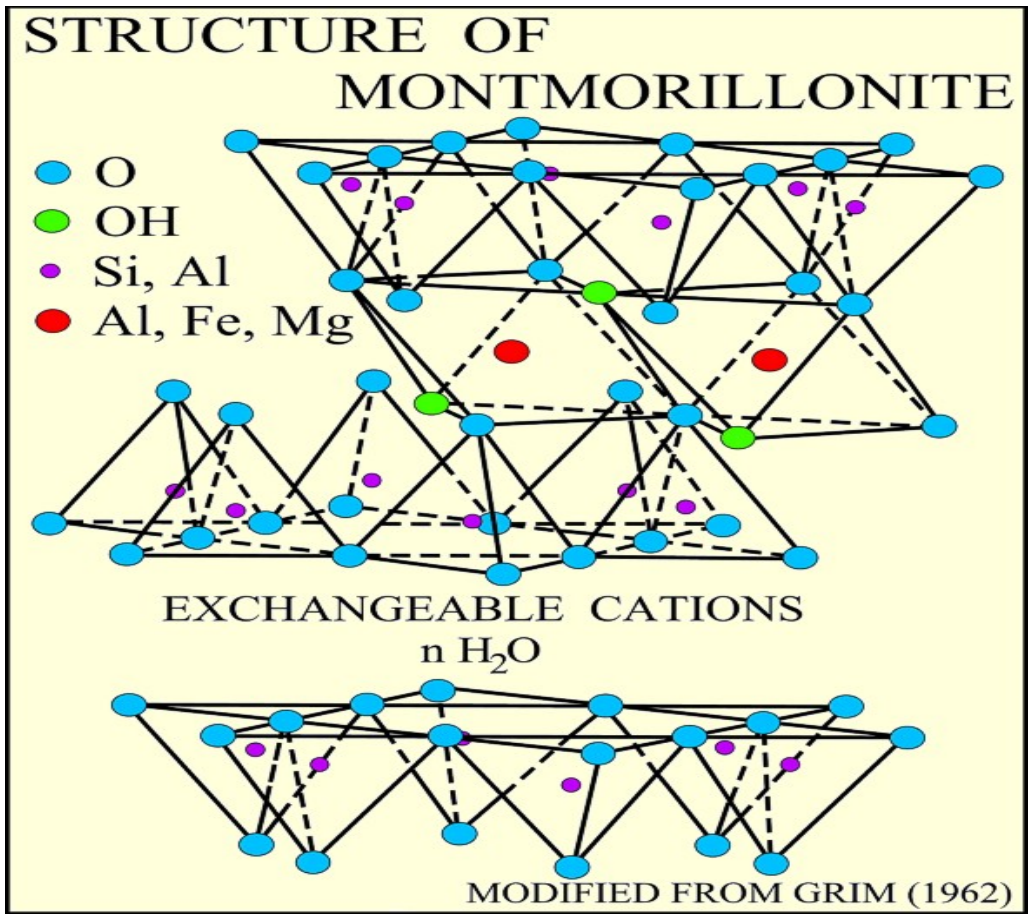

Figure 4 Structure of Montmorillonite mineral.

1.2.2.2 Illite Group

Illite is essentially a group name for clay, di-octahedral, micaceous minerals. Its basic unit is a layer of two inward-pointing silica tetragonal sheets with a central octahedral sheet, they form by the weathering of silicates. Formation of Illite is favored by alkaline conditions and by high concentrations of Aluminum and potassium (U.S Gelogical Survey, n.d.).

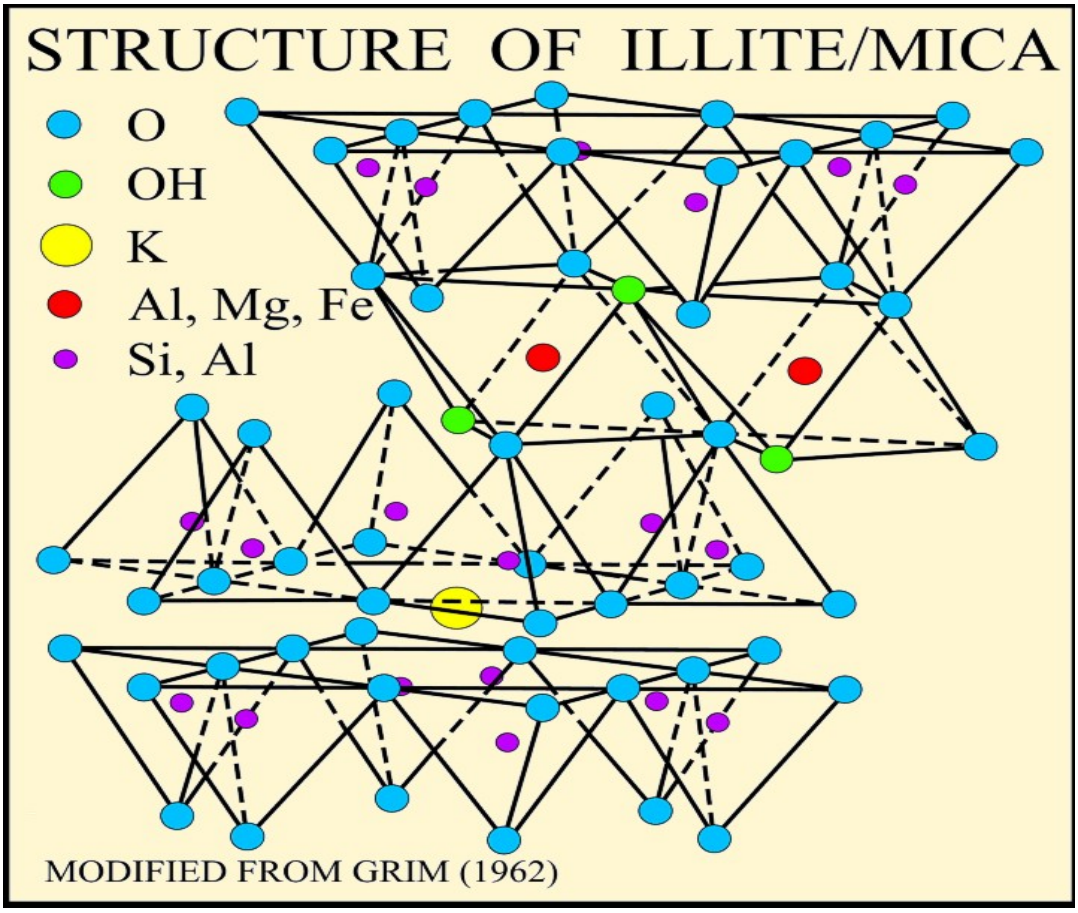

Figure 5 Structure of Illite mineral.

1.2.2.3 Chlorite Group

The basic structure of chlorite consists of negatively charged mica-like layers regularly alternating with positively charged brucite-like octahedral sheets. The members are differentiated by the kind and amount of substitutions within the brucite layer and the tetrahedral and octahedral positions of the mica layer (U.S Gelogical Survey, n.d.).

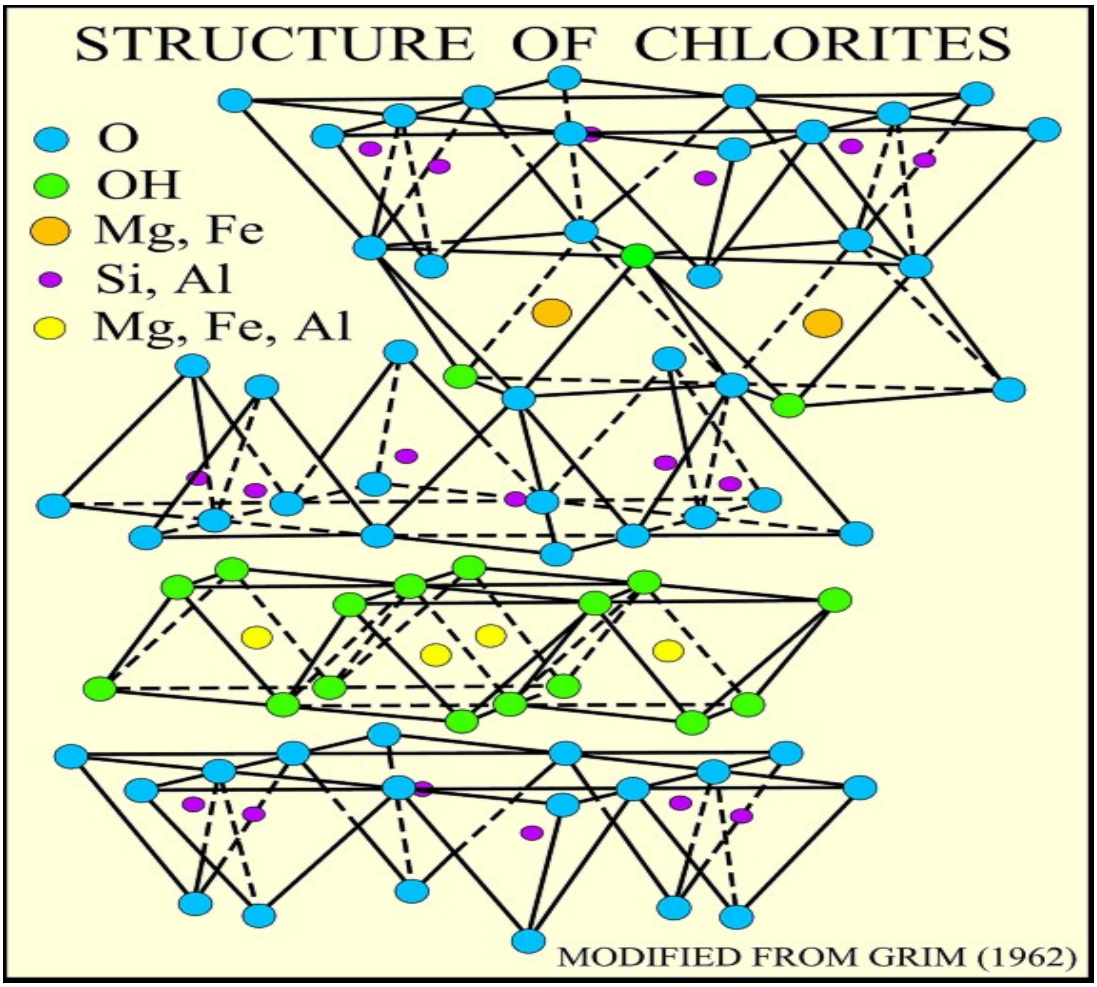

Figure 6 Structure of Chlorite mineral.

1.2.2.4 Kaolinite Group

The main structural unit of this group is a layer composed of one octahedral sheet condensed with one tetrahedral sheet. In the di octahedral minerals the octahedral sites are occupied by aluminum; in the tri octahedral minerals these sites are occupied by magnesium and iron. Kaolinite, dickite, and nacrite occur as plates; halloysite can have a single layer of water between its sheets, occurs in a tubular form (U.S Gelogical Survey, n.d.).

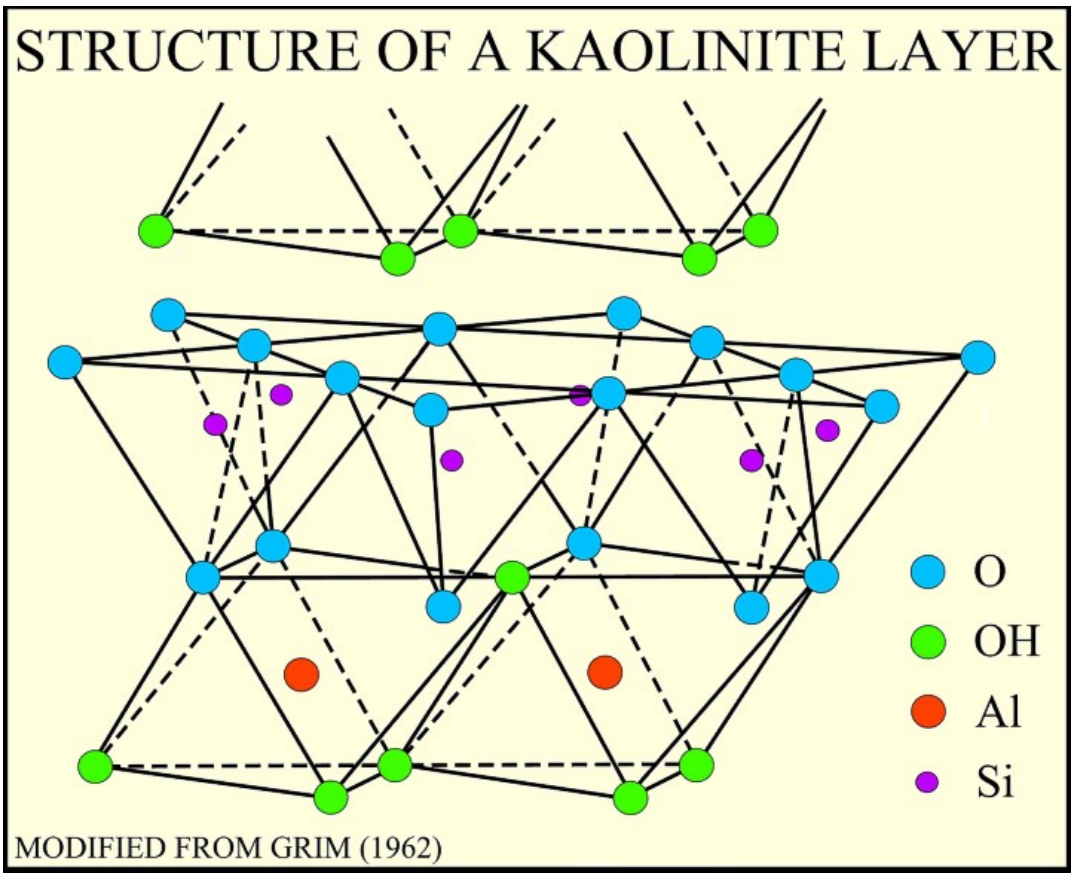

Figure 7 Structure of Kaolinite mineral.

1.2 Electrical Double Layer

The plane of oxygen ions bounding each side of 2:1 clay mineral layer is called siloxane surface. A reactive site within this surface is the hexagonal cavity formed by the bases of six corner sharing Si tetrahedral. It has a diameter of 0.26 nm and is bordered by six oxygen atoms. The absence of nearby isomorphic cation substitutions creates negative charge. If isomorphic substitution of Si by Aluminum occurs in the tetrahedral sheet, this creates stronger adsorption with cations and stronger hydrogen bonds to vicinal water molecules Figure **8** Interlayer and External complexes (Sposito, et al., 1998).

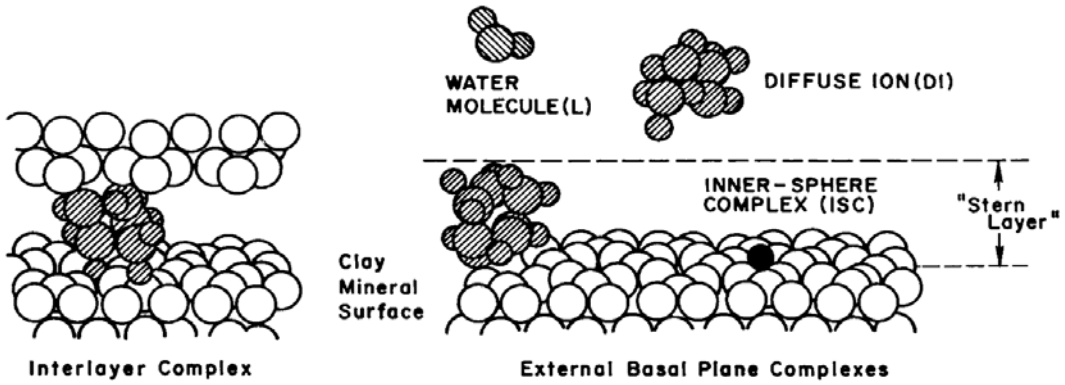

Figure 8 Interlayer and External complexes **(Sposito, et al., 1998)**.

Charged sites also exist on the edges of clay mineral crystallites (Sposito, et al., 1998). Cations that neutralize the negative charges on the surface of clay particles in water are exchangeable with other cations. Clays negative charges tend to attract the cations, but the cations diffuse toward the lower cation concentration away from clay particles. The clay particle is surrounded by a domain known as electric double layer.

The cation exchange reaction depends on the relative concentrations of cations in the water and also on the electrovalence of the cations. The highly polar water molecule forms strong bonds with the surface of clay particles, as well as with the exchangeable cations that surround it.

The inner layer of the double layer is the clay negative charges. The outer layer is the excess of cations and deficiency of anions compared to the concentration in the free water not influenced by the force of the clay. The cation concentration near the clay surface decreases exponentially with distance to the concentration of the cations in the free water as shown in Figure **9** Distribution of Ions adjacent to clay surface.

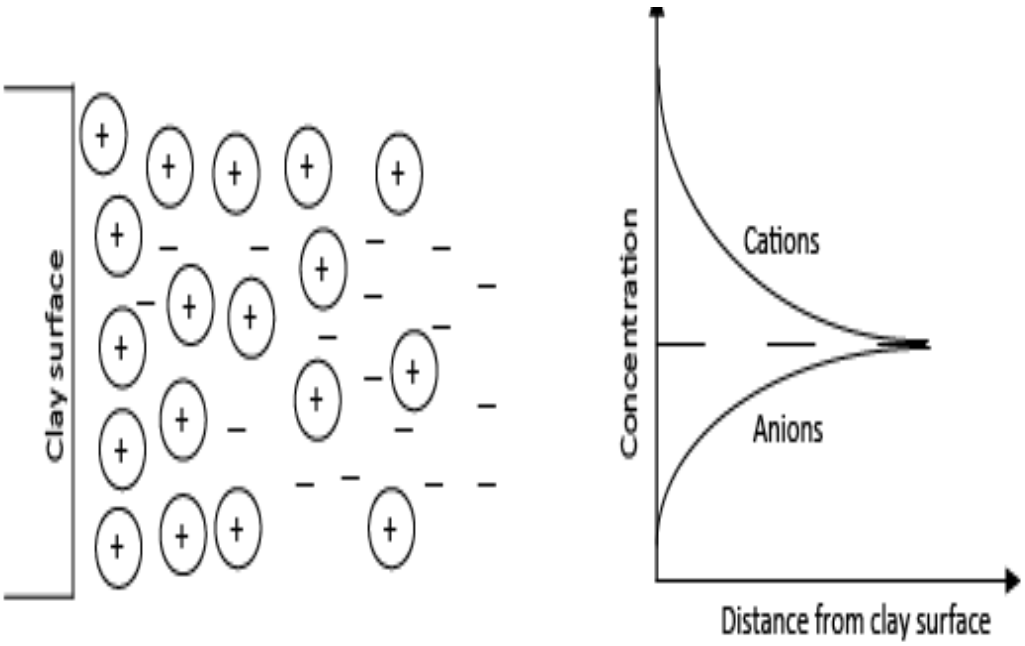

Figure 9 Distribution of Ions adjacent to clay surface **(Mitchell, 1993)**.

Thick double layer develops with low electrovalence exchangeable ions, and in low electrolyte brine concentration, this double layer expansion is responsible for clay swelling **(Terzaghi, Peck, & Mesri)**.

1.2.1 Bound Water

When clay particles approach each other during deposition or consolidation, their geometrical arrangements are influenced by a number of long-range and short-range inter particle forces. Repulsion forces develop between particles when their double layers come in contact. The particles remain dispersed unless an external force is applied. An increase in brine concentration depresses double layer thickness which allows closer approach of the particles. Extremely high pressures are required to expel bound water out of the clay surface. A pressure of 18129 Psi is required to bring two parallel plates of monmorillonite to within 0.5 nm of each other, and a pressure of 58015 Psi is required to expel the last bound water layer (Terzaghi, Peck, & Mesri, 1963). 0.5 nm corresponds to a mono layer on each surface.

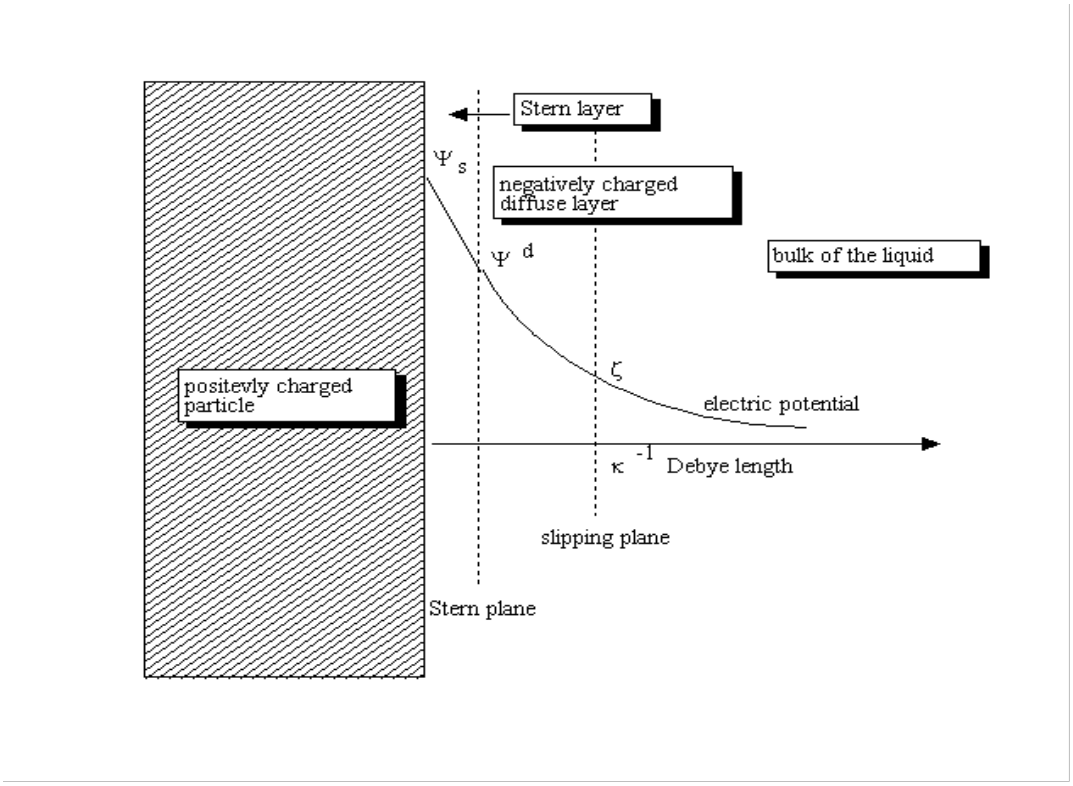

Figure 10 Cations concentration distribution at the electrical double layer.

1.3 Sample Characterization

XRD analysis is used to characterize the mineralogy of the samples used in this study. The table shows the XRD data for all the samples used in the measurements. We use the XRD data to determine the initial quartz content which ranges of quartz content from 15 to 45 percent, Brazos sand is listed because we added it to the other samples to increase the mudrock quartz content. We also used this data as a check for the measured grain densities in the reconsolidation experiments, these properties are listed below in section 1.3.1.

Table 1 XRD data for all samples used in this study

Sample	Quartz	Plagioclase	K-Feldspar	Calcite	Dolomite	Siderite	Pyrite	Anatase	Clinoptilolite	Barite	Halite	Muscovite	Mixed Layer	Chlorite(Tri)	Kaolinite
Pierre Shale	22.5	5.8	3.4	1.3	0.6	0	0.6	0	0	0	0	2.6	58.8	1.6	2.8
Illite	15.6	0	2.9	10.1	0	0	0	0	0	0	0	3.3	57.7	0.6	9.7
Sample-A	37.8	7.6	4.5	1	1.5	1.2	0.4	0	0	6.5	1.1	4.1	32	0.5	1.6
Sample-B	37.5	8.4	3.9	3.7	3.5	0.5	0.4	0	0	0.3	0.6	5.5	33.7	2.1	0
Sample-C	45.3	10.9	4.8	2.2	3.2	0.4	0.3	0	1	0	0.7	3.3	26.7	1.2	0
Sample-D	45.2	5.7	2.4	11.1	10.7	0.4	0.4	0	0	0	0.3	6.4	13.3	4.1	0
Sample-E	39.4	7.7	1.9	0.2	0	4.3	0.6	0.2	0	0	0.4	6	29.2	5.7	4.4
Brazos Sand	91.1	2.4	2.7	3.8	0	0	0	0	0	0	0	0	0	0	0

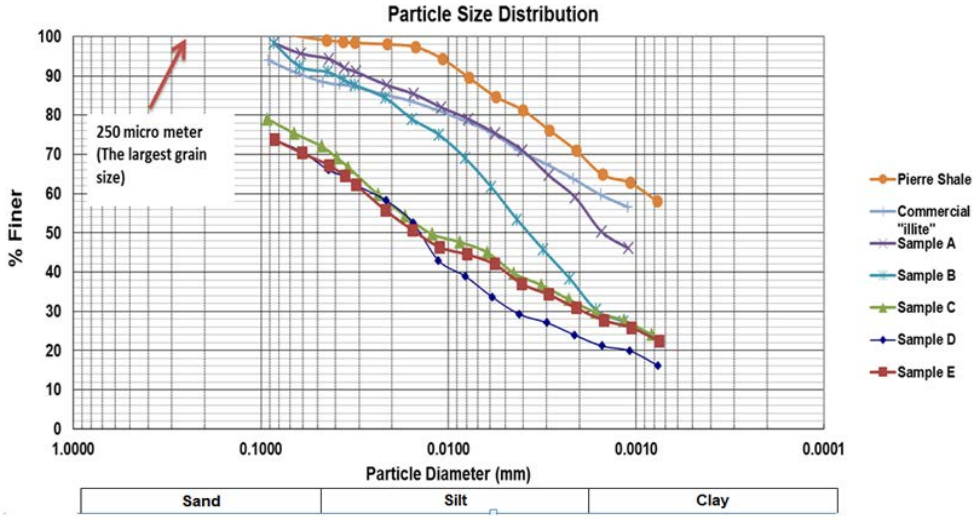

Figure 11 Particle size distribution for measured samples.

1.3.1 Mineralogy Composition

Quartz

Is a continuous framework of silicon-oxygen tetrahedral crystal structure. Chemical composition - SiO2 , Specific gravity -2.6 to 2.65

(https://www.esci.umn.edu/courses/1001/minerals/quartz.shtml, n.d.)

Plagioclase

Is a member of the feldspar group and is a framework silicate. Plagioclase consists of a solid solution between the albite and anorthite end-members. Chemical composition - $CaAl_2Si_2O_8$ (anorthite), $NaAlSi_3O_8$ (albite), Specific gravity - 2.6-2.8

K-Feldspar

Potassium Feldspar has a chemical composition - $KAlSi_3O_8$, specific gravity- 2.6

(https://www.esci.umn.edu/courses/1001/minerals/potassium_feldspar.shtml, n.d.)

Calcite

Is the only common non-silicate rock forming mineral, being instead calcium carbonate.

Chemical composition - $CaCO_3$, specific gravity-2.7

(http://flexiblelearning.auckland.ac.nz/rocks_minerals/minerals/plagioclase.html, n.d.)

Dolomite

It is a calcium magnesium carbonate. Chemical composition - $(CaMg)(CO_3)_2$

Specific gravity – 2.8 to 2.9 (http://geology.com/minerals/dolomite.shtml, n.d.)

Siderite

Is a mineral composed of iron carbonate. Chemical composition - $FeCO_3$

Specific gravity – 3.7 to 3.9 (http://www.minerals.net/mineral/siderite.aspx, n.d.)

Pyrite

It is composed of iron sulfide. Chemical composition - FeS_2

Specific gravity- 4.9 to 5.2 (http://www.minerals.net/mineral/pyrite.aspx, n.d.)

Anatase

Anatase is composed titanium dioxide. Chemical composition - TiO_2

Specific gravity- 3.8-3.9 (http://www.minerals.net/mineral/anatase.aspx, n.d.)

Clinoptilolite

Chemical composition – $(Na,K,Ca)_2$-$3Al_3(Al,Si)_2Si1_3O_{36}\cdot 12H_2O$, specific gravity- 2.1-2.2

(http://webmineral.com/data/Clinoptilolite-Ca.shtml#.Vf9k-WeFOUk, n.d.)

Barite

Is a mineral composed of barium sulfate. Chemical composition – $BaSO_4$, specific gravity- 2.5-3.5 (http://geology.com/minerals/barite.shtml, n.d.)

Halite

Halite is composed of sodium chloride. Chemical composition – NaCl

Specific gravity- 2.17 (http://webmineral.com/data/Halite.shtml#.Vf9nPGeFOUk, n.d.)

Muscovite

Is phyllosilicate mineral of aluminum and potassium. Chemical composition – $KAl_2(Si_3AlO_{10})(OH)_2$, Specific gravity- 2.8-2.9 (http://geology.com/minerals/muscovite.shtml, n.d.)

Illite

Is composed of layered alumino-silicate, the interlayer space is mainly occupied by poorly hydrated potassium cations responsible for the absence of swelling. Chemical composition – $(K,H_3O)(Al,Mg,Fe)_2(Si,Al)_4O_{10}[(OH)_2,(H_2O)]$ but there is considerable ion substitution Specific gravity- 2.6-2.9 (http://webmineral.com/data/Illite.shtml#.Vf9rXWeFOUk, n.d.)

Smectite group

Includes dioctahedral smectites such as montmorillonite, nontronite, and trioctahedral

Chemical composition – $(Na,Ca),3(Al,Mg)_2Si_4O_{10}(OH)_2 \bullet n(H_2O)$, specific gravity- 2-2.7

(http://webmineral.com/data/Montmorillonite.shtml#.Vf9u3WeFOUk, n.d.)

Chlorite group

Is a group of phyllosilicate minerals. Chemical composition – $(Mg,Fe,Li)6AlSi_3O_{10}(OH)_8$ Specific gravity- 2.6-3.3 (http://www.minerals.net/mineral/chlorite.aspx, n.d.)

Kaolinite

Is a layered silicate mineral. Chemical composition – $Al_2Si_2O_5(OH)_4$

Specific gravity- 2.6 (http://webmineral.com/data/Kaolinite.shtml#.Vf9ygGeFOUk, n.d.)

1.4 Consolidation

In this section we will derive the equation necessary to estimate the permeability from reconsolidation data. We will start by assuming effective stress concepts hold during the time we are estimating permeability, and incompressible fluids and matrix, all volume changes come out due to pore volume changes.

1.4.1 Consolidation Process

Mudrocks are visco-elastic materials that exhibit significant time dependent strain behavior, which is the result of two processes, hydraulic flow, and creep. Initially primary consolidation takes place when hydraulic flow dominates and then the secondary consolidation stage occurs where the compaction is creep dominated. The Terzaghi effective stress principle is assumed to hold only during primary consolidation. The increment in pore pressure is therefore equal to the increment in the applied load. The pore pressure then dissipates with time as brine flows out of the sample. The excess pore pressure at a given time, where P is the total pore pressure and P_s is the static pressure at a specific point is given by Terzaghi effective stress principle (Terzaghi, Peck, & Mesri, 1963)

$$P' = P - P_s. \tag{1}$$

1.4.2 Primary Consolidation; Fluid Flow Dominated Compaction

During primary consolidation the flow of fluid is due to a pore volume change. In our experimental geometry brine is expelled only through vertical drainage which we assume to be in z-direction. The conservation of mass for one dimensional flow assuming incompressible grains and fluids is then given by

$$\frac{\partial v}{\partial z} = -\partial \emptyset \backslash \partial\, t, \tag{2}$$

where v is the fluid velocity, and ∅ is porosity and t is time. Ignoring frictional forces and body forces and assuming Darcy flow, gives the following relationship between the pore pressures at any position z with fluid velocity.

$$v = -\frac{K \partial P'}{\partial z}, \tag{3}$$

where $\gamma_w(\frac{KN}{m^3})$ is unit weight of water, K (m/s) is coefficient of vertical permeability, Expressing 'Ø' in terms of void ratio 'e', we get

$$\frac{K}{\gamma_w}\frac{\partial^2 P\prime}{\partial z^2} = \frac{\partial}{\partial t}\left(\frac{e}{1+e}\right). \tag{4}$$

Assuming that the change in void ratio is small, (1+e) can be approximated to$(1 + e_0)$, where e_0 is the initial reconsolidation void ratio, so$\frac{1}{(1+e_0)}$, which is the volume of solid in the sample, is time independent, we get

$$\frac{K}{\gamma_w}\frac{\partial^2 P'}{\partial z^2} = \frac{1}{1+e}\frac{\partial e}{\partial t}. \tag{5}$$

Starting with the definition of vertical compressibility

$$\frac{de}{dt} = \left(\frac{\partial e}{\partial \sigma_v'}\right)\frac{d\sigma_v'}{dt} + \left(\frac{\partial e}{\partial t}\right)_{\sigma_v} = a_{vs}\frac{d\sigma_v'}{dt} + a_{vt}. \quad (6)$$

$$a_v\left(\frac{1}{KPa}\right) = coefficient\ of\ compressibility$$

$$a_{vs} = a_v = \frac{\partial e}{\partial \sigma_v'} = compressibility\ with\ respect\ to\ effective\ stress$$

$$a_{vt}\left(\frac{1}{s}\right) = \frac{\partial e}{\partial t} = compressibility\ with\ respect\ to\ time$$

Assuming that the time lag of the compression is caused due to the finite permeability of mudrock, then $a_{vt} = 0$, and if we assume that $a_{vs} = -a_v$, which is constant for each layer and in each stage of consolidation, we get (we used the chain rule to rewrite the definition of vertical compressibility),

$$\frac{de}{dt} = a_v\frac{d\sigma_v'}{dt}. \quad (7)$$

Assuming that vertical load σ_v and P_s are constant during consolidation, then the effective stress is equal to the change in the effective pore pressure $\frac{d\sigma_v'}{dt} = -\frac{dP'}{dt}$ and substituting:

$$\frac{K}{\gamma_w}\frac{\partial^2 P'}{\partial z^2} = \frac{a_v}{1+e}\frac{\partial P'}{\partial t}. \quad (8)$$

Defining the coefficient of vertical compression m_v

$$m_v = \frac{a_v}{1+e} \text{ and} \quad (9)$$

$$m_v = \frac{\Delta\varepsilon_v}{\Delta\sigma_v'}\ where\ \Delta\varepsilon_v\ is\ vertical\ strain. \quad (10)$$

$$m_v\left(\frac{1}{KPa}\right)\ is\ coefficient\ of\ vertical\ compression$$

$$\frac{1}{\gamma_w}\frac{K}{m_v}\frac{\partial^2 P'}{\partial z^2} = \frac{\partial P'}{\partial t}, \tag{11}$$

the coefficient of consolidation $\mathbf{c_v}$ is defined as

$$c_v = \frac{1}{\gamma_w}\frac{K}{m_v}, \tag{12}$$

where $C_v(\frac{m^2}{year})$: coefficient of consolidation

and

$$c_v \frac{\partial^2 u'}{\partial z^2} = \frac{\partial u'}{\partial t}. \tag{13}$$

The variable u' is a function of the independent variables z and t, two boundary conditions are required to solve for the excess pore pressure. At time t not equal zero at the drainage surface z=H, the excess pore pressure is zero; u'(H,t)=0, at the time t not equal zero at the impermeable surface z=0, assuming that we have single drainage from the top; $\frac{\partial u'(0,t)}{\partial z} = \mathbf{0}$

Using Fourier expansion method, solving eqn. 13 we get

$$u'(z,t) = \Delta\sigma_v \sum_{m=0} \frac{2}{M} \sin\left(M\frac{z}{H}\right) \exp(-M^2 T_v), \tag{14}$$

$$M = \frac{\pi(2m+1)}{2}, \text{ and} \tag{15}$$

$$T_v = \frac{c_v t}{H^2}, \tag{16}$$

where H is the maximum drainage distance and T is a time factor, the drainage path for double drainage is equal to half the height H.

The degree of consolidation is

$$U(z,t) = \frac{e_0 - e}{e_0 - e_p} \text{ and} \tag{17}$$

$$e_p \text{ is the void ratio at excess pore pressure} = 0.$$

The solution of u in terms of the consolidation ratio is given by (Holtz & Kovacs, 1981)

$$U_z = \frac{\sigma' - \sigma_1'}{\sigma_2' - \sigma_1'} = \frac{u_i - u}{u_i} = 1 - \frac{u}{u_i} \text{ and} \tag{18}$$

$$U_z = 1 - \sum_{n=0}^{\infty} f_1(Z) f_2(T). \tag{19}$$

Uz is the percent of consolidation, it is possible to find the degree of consolidation graphically from **Figure 12 Consolidation ratio at any location and time factor for double drainage consolidation** (Germaine & Germaine, 2009), all we need are Cv, height, and boundary conditions to solve for T.

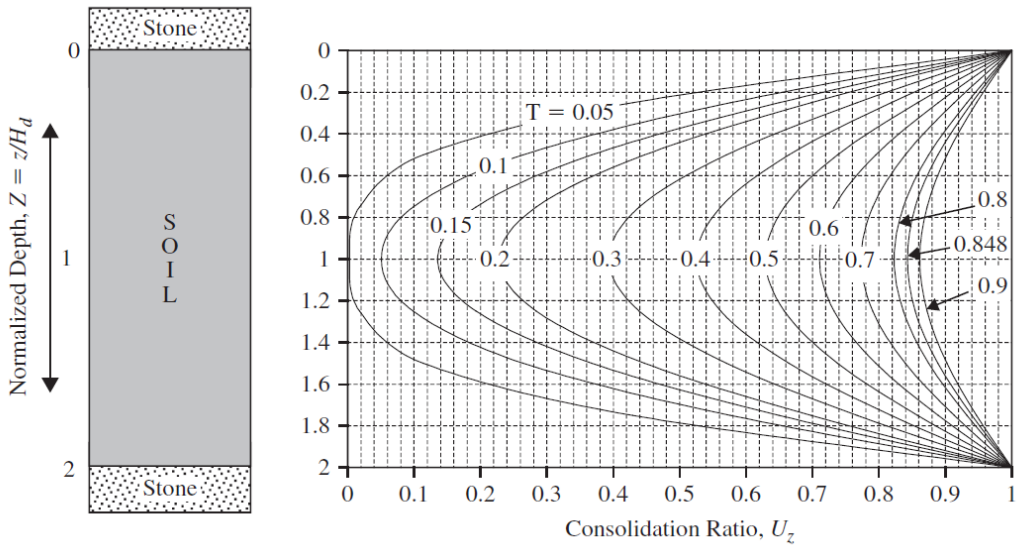

Figure 12 Consolidation ratio at any location and time factor for double drainage consolidation **(Germaine & Germaine, 2009)**.

The degree of consolidation is a function of the time factor T, and the early time data (up to 60% consolidation) can be represented by the equation (Murthy, 2002)

$$T = \frac{\pi}{4}\frac{U\%^2}{100}. \tag{20}$$

Substituting for T in terms of the real time, t, we arrive at:

$$\frac{U\%}{100} = \sqrt{\frac{4C_v}{\pi H^2}}\sqrt{t}. \tag{21}$$

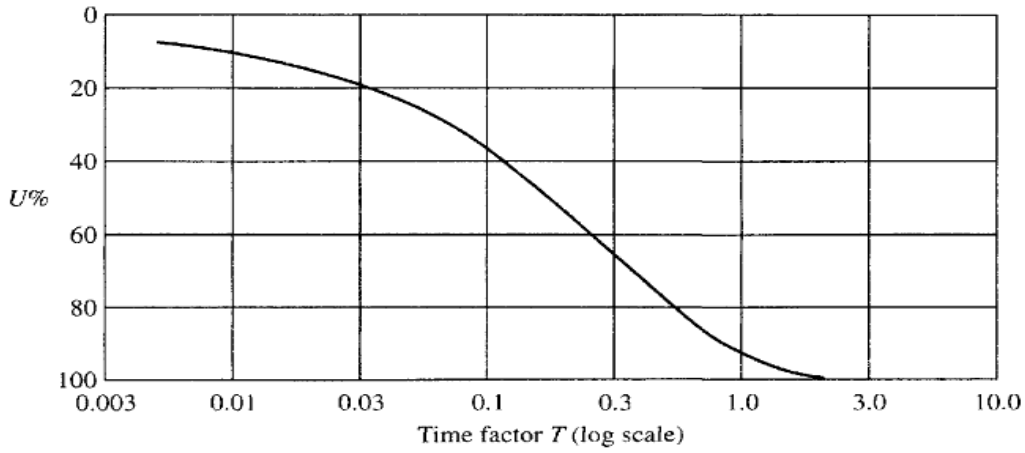

Figure 13 Degree of consolidation as a function of the time factor.

U%	T	U%	T	U%	T
0	0	40	0.126	75	0.477
10	0.008	45	0.159	80	0.565
15	0.018	50	0.197	85	0.684
20	0.031	55	0.238	90	0.848
25	0.049	60	0.287	95	1.127
30	0.071	65	0.342	100	∞
35	0.096	70	0.405		

Figure 14 The relationship of percent consolidation U with time factor T, We used the value for dimensionless time (T) to estimate the consolidation coefficient, and ultimately the permeability **(Murthy, 2002)**.

1.4.3 Logarithm of Time Fitting Method

This method was proposed by (Casagrande & Fadum, 1940) to show the relationship between strain and the logarithm of time. The logarithm of time method is plotting strain versus the time on a log scale. This method is based on the similarity of the curve shape to the theoretical consolidation curve as shown in Figure **14** The relationship of percent consolidation U with time factor T, We used the value for dimensionless time (T) to estimate the consolidation coefficient, and ultimately the permeability (Murthy, 2002).

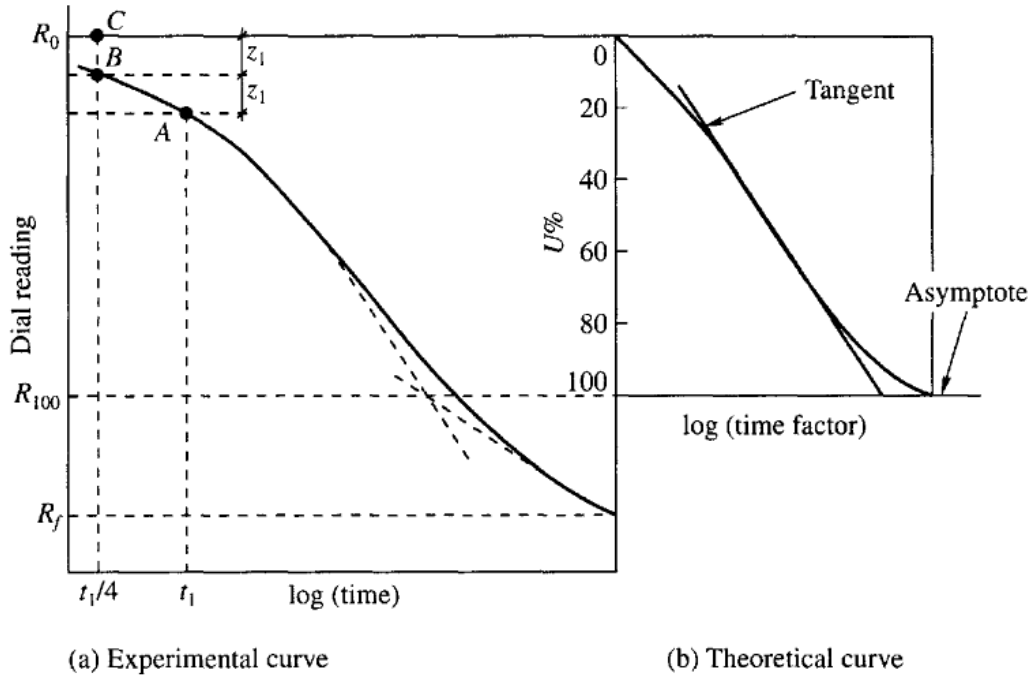

Figure 15 The curve on the left is an experimental curve showing the relation between strain and the logarithm of time, The curve on the right shows the theoretical relationship between the percent consolidation to the time factor.

The relationship is parabolic in the early stages as the theoretical curve because it is flow dominated and obeys the diffusional equation. On the experimental curve, the intersection of the tangent line to the final slope with the tangent line to the linear part of the curve is accepted as the 100 percent consolidation point. We empirically estimate the 50% value using this geometric construction. The interval between zero to 100% consolidation can be divided into equal intervals of percent consolidation. , the value of the coefficient of consolidation C_v can be obtained by taking the time t and time factor T at 50 percent consolidation.

The equation to be used is

$$C_{v=\frac{T_{50}}{t_{50}}H_{dr}^2}. \quad (22)$$

From Figure **14** The relationship of percent consolidation U with time factor T, We used the value for dimensionless time (T) to estimate the consolidation coefficient, and ultimately the permeability (Murthy, 2002), we have at 50% percent consolidation, T=0.197

Now the equation for C_v may be written as

$$C_{v=\frac{0.197}{t_{50}}H_{dr}^2}. \quad (23)$$

1.4.4 Hydraulic Conductivity

Hydraulic conductivity describes the rate of flow through shale; it can be calculated from the compressibility and the coefficient of consolidation at each load increment (Germaine & Germaine, 2009). The calculation of the hydraulic conductivity using approximations to the theoretical solution, the hydraulic conductivity equation is

$$k_v = c_v m_v \rho g \text{ and} \tag{24}$$

$$Permeability(m^2) = \frac{k_v * Viscosity}{\rho_w * g}, \tag{25}$$

where,

$$K_v = vertical\ hydraulic\ conductivity \left(\frac{m}{s}\right),$$

$$\rho_w = density\ of\ Brine\ \left(\frac{g}{m^3}\right),$$

$$g = gravitational\ constant \left(\frac{m}{s^2}\right),$$

$$C_v = \frac{T_v H_d^2}{t},$$

$$C_v = coefficient\ of\ consolidation \left(\frac{m^2}{s}\right), \text{ and}$$

$$T_v = dimensionless\ time\ factor$$

$$H_d = drainage\ height\ at\ 50\%\ consolidation(m).$$

The hydraulic conductivity of clay minerals is less than about 1 X 10^{-7} m/s, and may be less than 1 X 10^{-12}m/s for some monovalent ionic smectite minerals at low porosity. For clay minerals compared at the same water saturation, the hydraulic conductivities are in the order smectite< attapulgite < illite < kaolinite (Mitchell, 1993).

1.5 Rock Mechanics

Once the samples were consolidated we performed rock strength measurements to assess the impact of salinity, CEC, grain size distribution, and silt content. We now introduce the fundamental concepts of the triaxial test needed to understand this work.

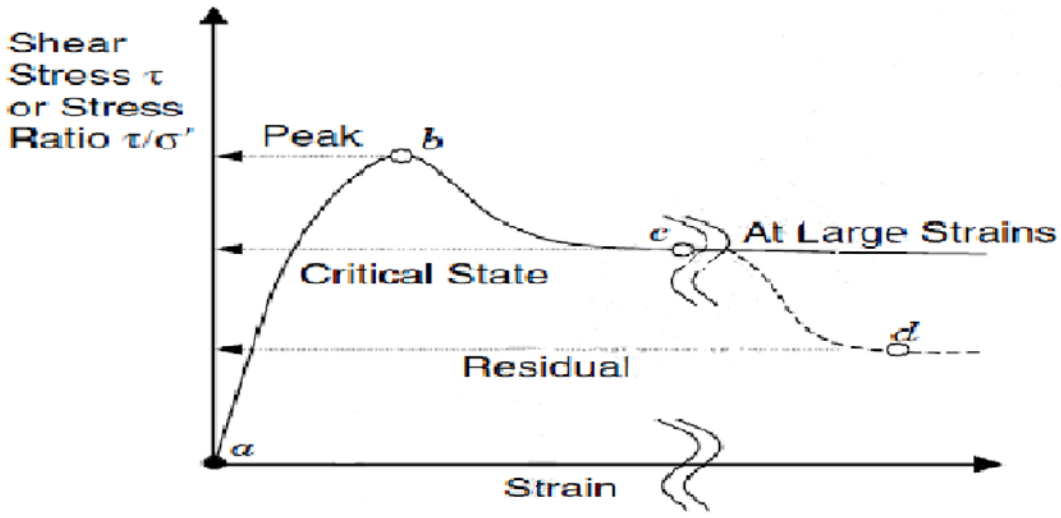

Figure 16 Stress-strain curve **(Mitchell, 1993).**

The maximum strength is at the peak point (b), then the strength decreases to a critical state point (c). The grain particles align along a failure plane at high shear strain and the strength decreases to the residual strength state at point (d). Peak failure envelopes are usually curved, caused by dilatancy and grain crushing.

1.5.1 Mohr-Coulomb

Friction is a measure of how rock strength increases with increasing confining stress. Cohesion is defined as shear strength at zero confining stress on the plane of failure. The Mohr-Coulomb equation is the most common assumption for the relationship of rock strength to increasing confining stress. It assumes that the cohesion and friction angle are independent of the stress, and therefore it is given as

$$\tau = c + \sigma tan\emptyset, \tag{26}$$

where τ is the shear stress at failure, c is the cohesion, σ is the effective stress on the normal plane, and $\emptyset$ is the friction angle. In theory, the rock strength depends on many factors, the shear strength equation may be given as shear strength= F (e, c', Ø', σ, C, H, T, strain), where e is void ratio, C is the composition, H is stress history, and T is temperature. (Mitchell, 1993) We will be studying the effects of salinity, stress, grain size distribution, and mineralogy.

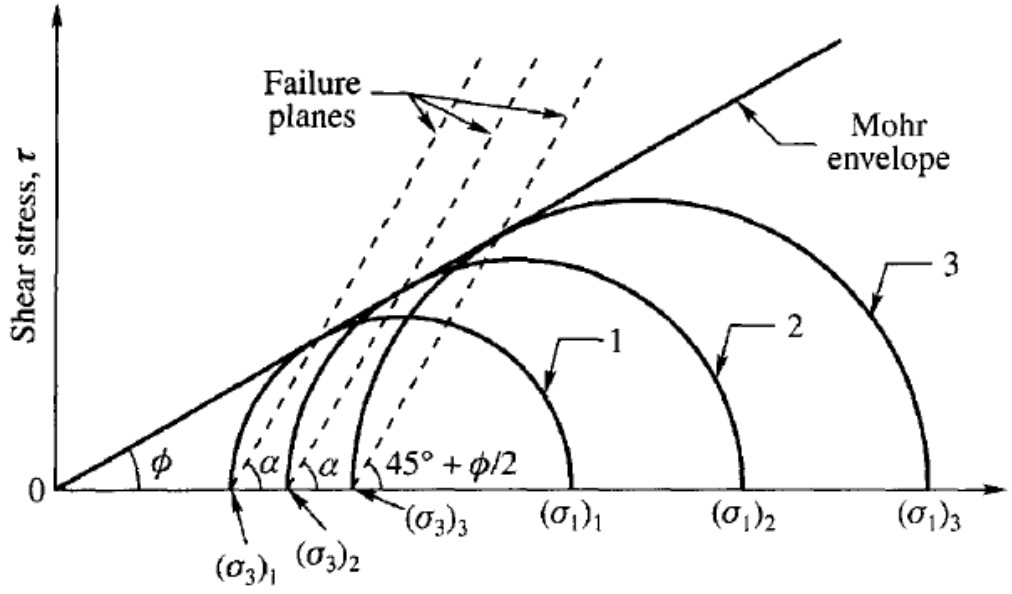

Figure 17 Mohr circle at three confining pressures **(Murthy, 2002)**.

1.5.2 Friction Angle (Literature Survey)

Earlier work has shown a relationship between clay content and friction angle at low stress (100 Psi). The finer grained rock and the greater the amount of clay, the smaller the friction angle (Mitchell, 1993) Friction angles as low as 8^0 have been observed for clay rich materials. We have extended this work to much higher stress 4000 Psi (29 MPa).These stresses are more relevant to the oil industry. As expected these low stresses the cohesion is zero.

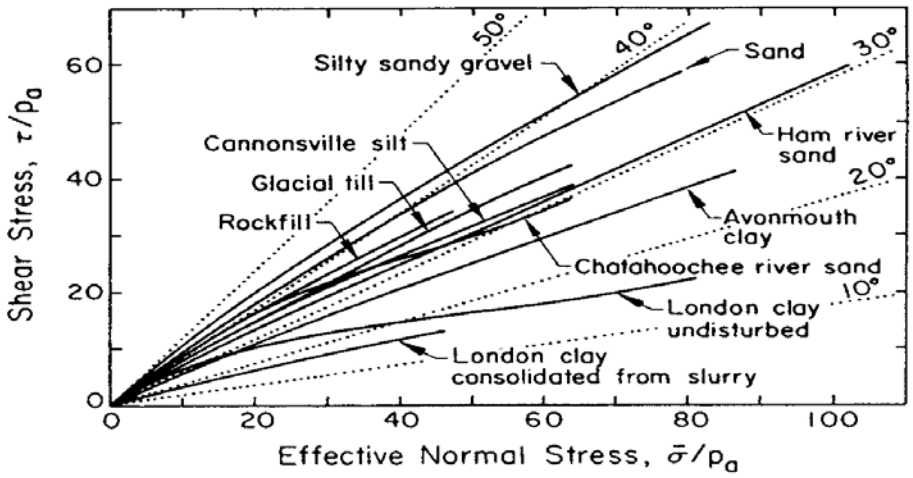

Figure 18 Failure envelopes for a range of rock types **(Bishop, 1966)**.

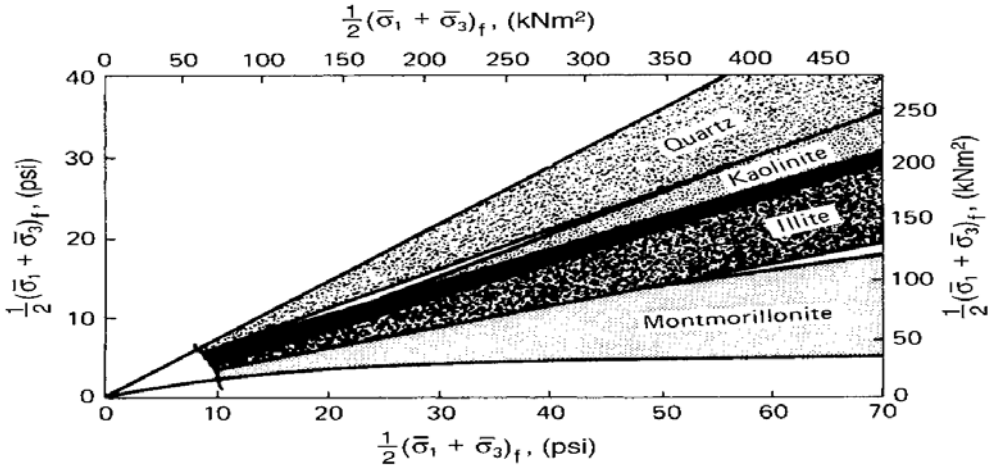

Figure 19 Failure envelopes for a range of clay types and quartz **(Olsen, 1974)**.

Chapter 2: Methodology and Experiments

We believe a key variable is a measure of cation exchange capacity for determining rock strength and permeability. It is measured using several techniques. In order to understand the impact of different measurements we undertook a series of experiments to compare and contrast the various techniques commonly used, conductometric titration, methylene blue absorbance, and cobalt hexamine technique. The cobalt hexamine measurements were performed by a third party.

2.1 Conductometric Titration Technique for CEC

The reaction of Barium saturated soil with the Magnesium Sulfate of a standardized titrating solution to form insoluble Barium Sulfate is utilized for determining soil cation-exchange capacity. The endpoint of the reaction is determined by Conductometric Titration. Specific conductance remains comparatively constant while the barium on the exchange complex is being replaced by Magnesium. Once the exchange sites are saturated with Magnesium the conductance increases as increments of the titrating solution are added. The endpoint of the exchange reaction is obtained from the intersection of the two linear portions of the curve. The exchange capacity in milli-equivalents is calculated by multiplying the normality of the standard Magnesium Sulfate solution by the number of ml corresponding to the end point.

Experiment preparation:

1- Weight 20 grams of crushed shale.

2- Mix the crushed shale with 400 ml of De-Ionized water, Stir the mixture for 20 minutes at 2000 RPM using a magnetic stirrer. Reflux the solution for 20 minutes if the sample is saturated with oil.

3- Centrifuge the solution for 10 minutes using large centrifuge bottles, noting that this will avoid having clay stuck at the bottom of regular centrifuge tubes. Increase time or speed if fine grains are still in the supernatant.

4- Test the supernatant liquid for Anhydrite (CaSO4)

5- On a black spot plate or vial.

6- Add three drops of 1N BaCl2 to the supernatant liquid.

7- The presence of Anhydrite (CaSO4) or Na2CO3 with produce a cloud and precipitate BaSO4 or BaSO3.

8- If onlyNa2CO3 is present, adding HCl to the cloudy precipitate will clear out.

9- If Anhydrite (CaSO4) is not present, go to step five. If Anhydrite (CaSO4) is present, Mix the shale with 200 ml of Sodium Thiosulfate (Na2S2O3) and stir for an hour at 2000 RPM.

10- Centrifuge the mixture for 10 minutes, then decant the supernatant.

11- Wash sample with De-Ionized water, the solution must be checked for Sodium Thiosulfate and CaSO4 by adding BaCl2 and showing no precipitation.

12- Wash the sample with 1N Barium Chloride (BaCl2) using magnetic stirrer for 10 minutes, then centrifuge the solution to separate the solids from liquid. Repeat this step twice.

13- Wash the sample twice with 1 part Isopropyl Alcohol (C3H8O) and 2 parts of De-Ionized water using stirring and centrifuging. Test the supernatant using 0.05N Silver Nitrate Solution until no Cl- ions are present.

14- Prepare Magnesium Sulfate solution with concentrations of 1 N for high clay content, or 0.5 N for medium clay content. Concentrations may be adjusted based on the sample's expected CEC range.

Measurement:

15- Transfer the sample to a 400 ml beaker with 300 ml 1:1 Isopropyl Alcohol/De-Ionized water.

16- Stir the mixture for 4 minutes.

17- From a 10 ml burette, add 0.25, 0.5 ml of Magnesium Sulfate solution to the mixture as it is stirred.

18- measure the conductance using a conductance meter by submerging the conductance probe in to the solution, but enough time must be allowed for the system to approach equilibrium (about four minutes)

19- Add another increment of the Magnesium Sulfate solution and measure the conductance again when equilibrium conditions are approached.

- As Magnesium ions replace the Barium ions on the exchanged sites of the clay, no appreciable change in conductance is noted until all Barium ions are replaced.
- The first few Magnesium Sulfate solution concentration should not be higher than the milli-equivalents in the sample. In this case all Barium ions would be replaced in the first increments and the measured conductance will be due to adding Magnesium not from replacing Barium.

20- After the end point has been reached (replacing all Barium sites with Magnesium and having a steeper conductance change), Take at least 3 measurements to establish the straight line relationship.

Calculations:

1- Plot the titration curve as Conductance versus Magnesium Sulfate increments (ml)

2- The titration end point is determined from the intersection of two straight lines resulting from the plot, where the conductance change due to Barium replacement will have low

slope, while the conductance from adding magnesium after replacing all Barium sites will yield to a steeper slope.

3- The Exchange capacity in milli-equivalents is calculated by multiplying the Normality of the standard solution by the number of ml corresponding to the endpoint. as

$$\mathrm{CEC}\left(\frac{\mathrm{meq}}{100\mathrm{grams}}\right) = \frac{\text{Solution Normality} * \text{Millilitres at endpoint} * 100}{\text{Clay's Weight}}. \qquad (27)$$

2.2 Methylene blue technique for CEC determination:

The Methylene blue method provides a rapid technique to determine the clays cation exchange capacity by measuring the amount of methylene blue cations that are absorbed by clays.

A sample of clays is combined with a methylene blue solution at a specific concentration and mixed for a period of time. The resulting mixture of clays and methylene blue solution is filtered by centrifugation and diluted. A colorimeter is used to determine the absorbance of the final solution, which is correlated with the concentration of methylene blue prior to dilution. The change in the methylene blue solution concentration is the clays cation exchange capacity, where the results are reported in meq/100grams.

Colorimeter Calibration:

1. Fill two burettes, one with 5 x 10−5 mol /liter methylene blue solution and an equal volume with deionized water.
2. Label 6 test tubes 1 to 6 and use the burettes to add the volumes of solutions shown in the table:

Table 2 Colorimeter calibration data

Test tube	Volume 5*10-5 mol/Litre methylene blue solution(ml)	Volume of deionized water(ml)	Concentration of methylene blue(mol/Litre)
1	10	0	5*10-5
2	8	2	4*10-5
3	6	4	3*10-5
4	4	6	2*10-5
5	2	8	1*10-5
6	0	10	0

3. Measure the absorbance of solutions in tubes 1 to 6 using a colorimeter.
4. Adjust the colorimeter wavelength to 635 nm.

5 Allow the colorimeter to warm up for 5 minutes.

6 Insert a cuvette, filled with the measured solution into the colorimeter.

7 Collect absorbance data for selected samples.

8 Plot a graph of absorbance (y-axis) versus concentration of methylene blue (mol/Litre) (x-axis) for solutions in tubes 1 to 6. This is the calibration curve obtained by Beer's law.

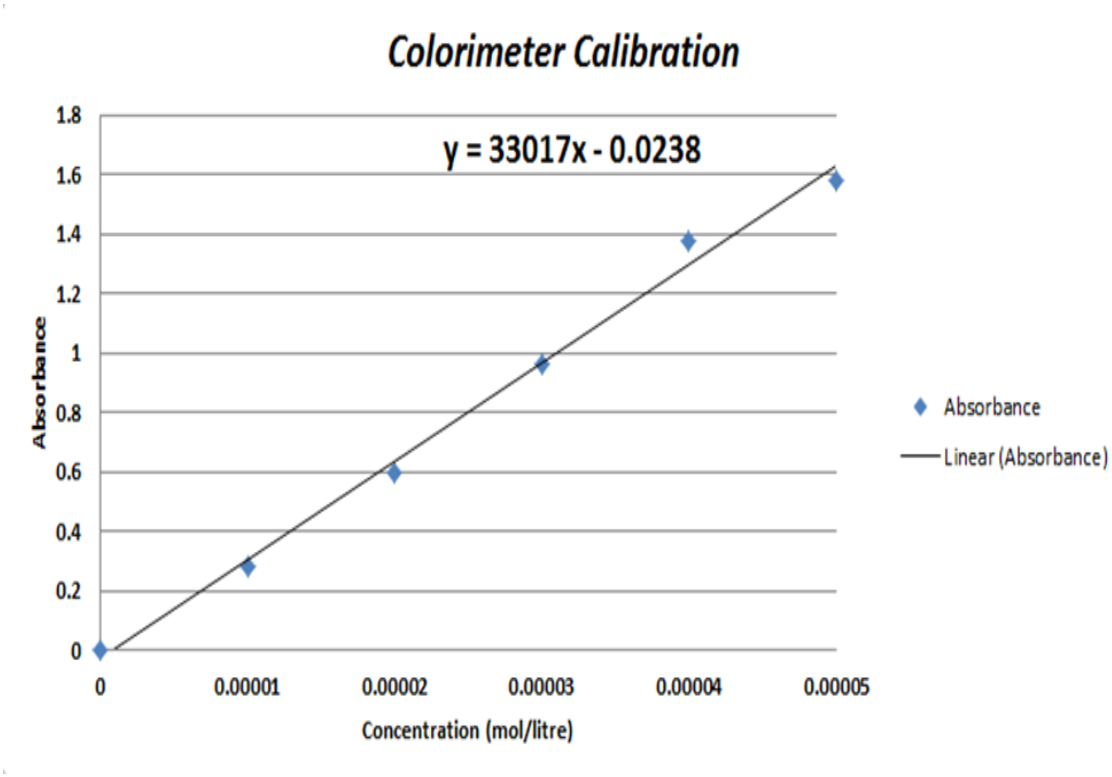

Figure 20 The linear relationship of methylene blue concentration to incident light absorbance.

Determining cation exchange capacity:

1- Weigh out 1 g of shale sample and place it in a 100 ml beaker.

2. Add 30-50 ml of 0.01 (mol/litre) methylene blue solutions, Stir the mixture for 30 minutes using a magnetic stirrer.

3. Use a burette to add 15 cm3 of De-Ionized water to the flask and mix thoroughly.

4. Filter the mixture from clays using centrifusion.

5. Pipette 1 ml of supernatant solution into a 100 ml volumetric flask. Make the volume up to 100 ml with De-Ionized water, the dilution is required to have absorbance values less than 1.

6. Measure the absorbance of this solution using a colorimeter

7. Use the calibration curve to find the concentration of this solution after mixing with the shale and diluting it.

CEC Calculations:

1. Calculate the concentration of the methylene blue solution after mixing with the soil and before it was diluted.

2. Calculate the number of moles of methylene blue in the solution added to 1 g of soil.

3. Calculate the number of moles of methylene blue in the solution after mixing with the shale.

4. Calculate the number of moles of methylene blue exchanged by the shale sample. Calculate the methylene blue cation exchange capacity, CEC, as meq/100grams.

2.3 Reconsolidation Technique

This technique was developed for testing soils up to one hundred Psi. This technique was originally developed to minimize the influence of sample heterogeneity and damage. For similar reasons we have assembled equipment (Coleff & Myers, 2011) to allow consolidation measurements up to 4000 Psi.

2.3.1 Reconsolidation Assembly

The reconsolidation experimental apparatus is composed of the following parts:

1- Oedometer cell: In our experiments the Oedometer used is a cylindrical steel structure with a 7 inches length, 4 inches outer diameter, and with an inner diameter of 1.3 inches which can be reduced by a peak rod to any other inner diameter; in our samples we used a peak rod with 1 inch inner diameter.

2- The Oedometer cell is supported by a top and bottom disks, each of 7 inches outer diameter, fixed by 4 iron rods, each of them has a welded screw head and the other side is fixed by a washer and nut.

3- A piston is installed to be pushed through the inner Odeometer diameter, used to apply pressure on the slurry, the movement of the piston is supported by a step motor, this piston has an inner drainage path to allow bottom drainage.

4- Drainage lines; they are outlet lines installed for expelling the excess brines present in the slurry, double drainage lines were installed in our experiments, top drainage was allowed using a top drainage head which has a fitting connected to peak tube line, bottom drainage line passes through the bottom piston to a tap connecting to a peak tube line.

5- Vertical displacement is measured using LVDT (linear variable displacement transformer), it converts displacement to a voltage, then this voltage is converted to length using calibration, this LVDT is fixed to the bottom stand shown in **Figure 21 Reconsolidation**

6- Pressures are measured using a load cell; it is a transducer that converts a mechanical force into an electrical output in voltages.

7- Stepper motor; they support the mechanical force to system, which moves the piston responsible to apply force on the sample; they are controlled using a PID (proportional integral derivative) controller shown in **Figure 22 PID parameters & Ramp control**.

8- Experimental data is monitored using a GUI (graphical user interface), data is plotted in the real time, or the monitoring software can save and plot the data every specific time interval.

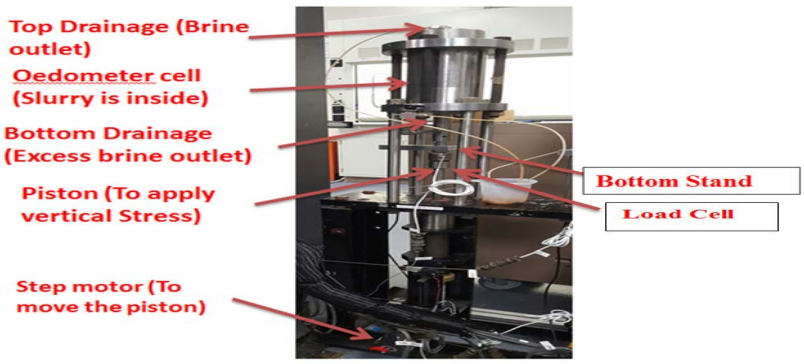

Figure 21 Reconsolidation Equipment.

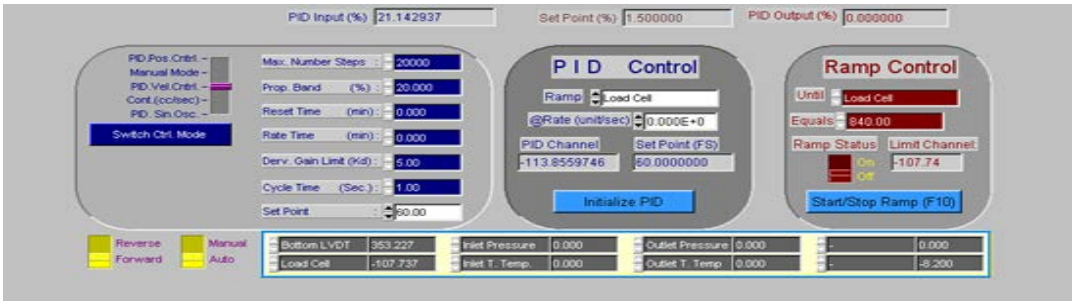

Figure 22 PID parameters & Ramp control.

2.3.2 Sample Preparation

1- Grind and sieve your sample to the desired grain size distribution, mixing mineralogy can be mixed to prepare a desired rock mixture that represents our study objective.

2- Prepare the saturation fluid, typically brine which is composed of De-Ionized water mixed with a desired NaCl (Sodium Chloride) concentration, prepared at a specific KPPM (Kilo Particles Per Million), in our study three Salinity concentrations were used (35 KPPM, 100 KKPM, and 200 KKPM), X KPPM solution is prepared by adding x-grams of NaCl to a volumetric flask, then adding De-Ionized water to a 1 Liter volume, Solutions can be prepared at smaller volumes by keeping the same preparation ratios.

3- Use a mixer to prepare slurry consists of the sample mixed with brine; different weights of either the sample or brine can be mixed until you reach the desired consistency, Keep note of the added weights of your sample or the added brine, Mix the slurry for 30 minutes, cover with a saran wrap, the used percentages for this paper ranges from 33% to 50 % of brine weight, let the slurry sit for 24 hours.

4- Place the slurry in an Erlenmeyer flask with a vacuum outlet, plug the top of the Erlenmeyer flask with a stopper, place a vacuum line and start degassing the slurry for 30 minutes, to make sure that no gasses are present in the slurry.

2.3.3 Experiment Setup

1- Adjust the moving piston to a desired position.

2- Measure the height of the inner cylinder of odeometer cell using a caliper.

3- Place a permeable frit at the bottom of the odeometer inner cylinder, put a filter paper on the top of the frit, this is to drain brine while to prevent the transport of fine particles.

3- Transfer the slurry into the odeometer cylinder using a large pipette.

4- Place a permeable frit with a filter paper on the top of the slurry.

5- Install the top drainage head.

6- Adjust the LVDT to a fully extended position while touching the bottom of the lower disk.

7- Apply a vertical load of 60 Psi; hold this pressure until the strain becomes constant; this step may take three to four days.

8- Once the strain stabilizes, start the segment list, the segment list is set of stress and hold steps designed at a desired configuration. **Figure 23 Segment list, it is a set of commands for desired stress & hold configurations**

9- Monitor the stress/strain behavior.

10- Data is plotted and saved then exported to a spreadsheet for further analysis.

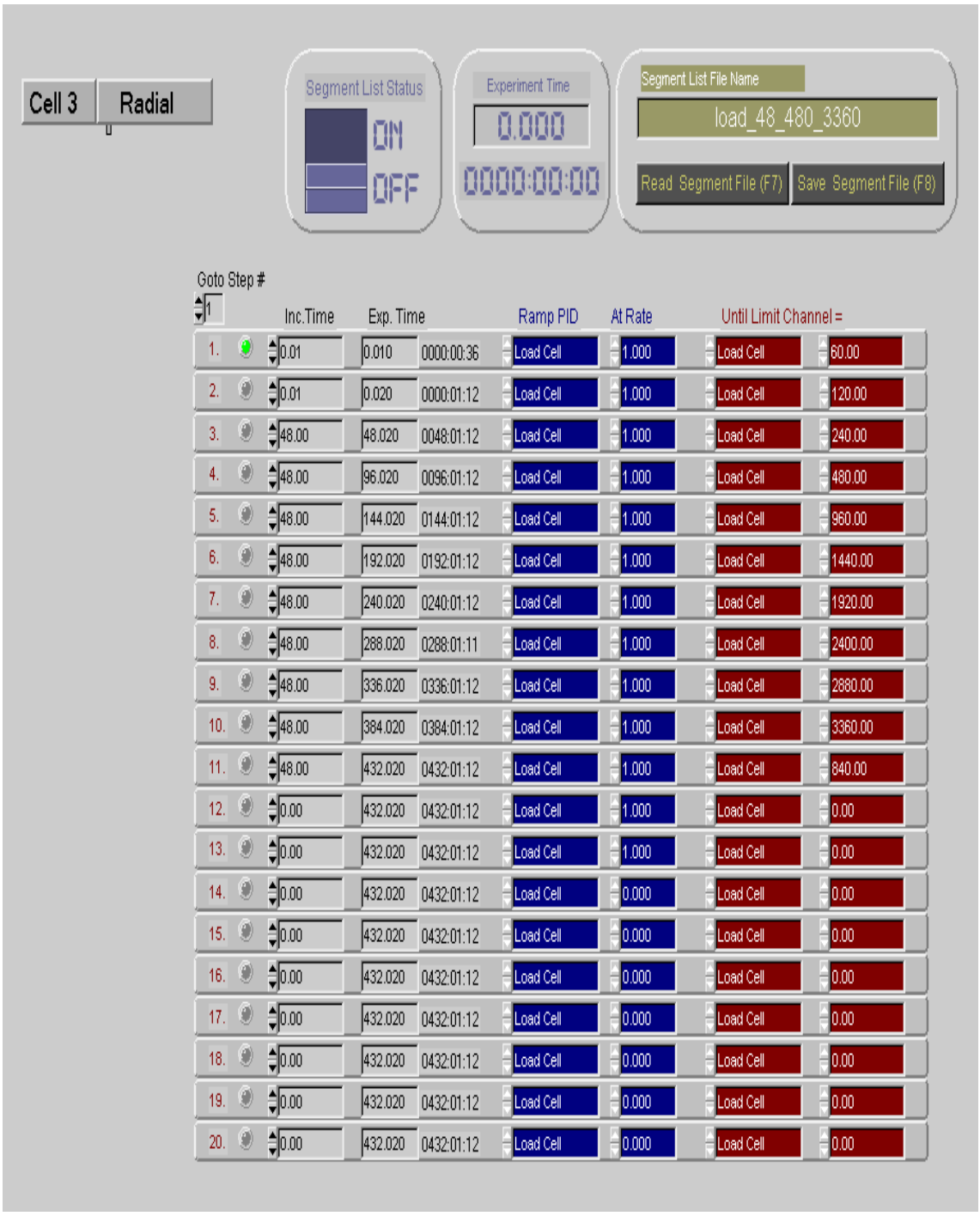

Figure 23 Segment list, it is a set of commands for desired stress & hold configurations.

2.4 Multistage Triaxial Test

A complete failure envelope may be interpreted from a multistage tri-axial test using only one core sample. As a starting step, the axial and the confining pressures are increased until both of them reach the value of the confining pressure of the first stage, bringing the core sample into isostatic stress condition. The axial stress is then increased while the confining pressure is kept constant. These tests were performed at constant pore pressure. Failure is defined as the point of positive dilatancy at Poisson ratio equals half.

2.4.1 Tri-axial Equipment

All of the multistage tests in this study were done in the tri-axial equipment shown in **Figure 24 Tri-axial test equipment**, A one inch diameter by two inch long cylindrical plug of reconsolidated rocks are used for this study, the sample is mounted in the tri-axial cell as shown in **Figure 25 A sleeved sample is mounted between a top and bottom acoustic endcaps, two pore lines are connected to the sidewalls of the sample, Cantilever bridge is mounted on the sample side walls to measure the radial strain** The assembly is then place into the tri-axial pressure vessel.

To measure the axial and radial strains, two LVDTs are mounted to measure the vertical displacement, and one cantilever bridge with four transducer arms to measure the radial strain. The load cell is mounted above the top endcap to measure the axial load.

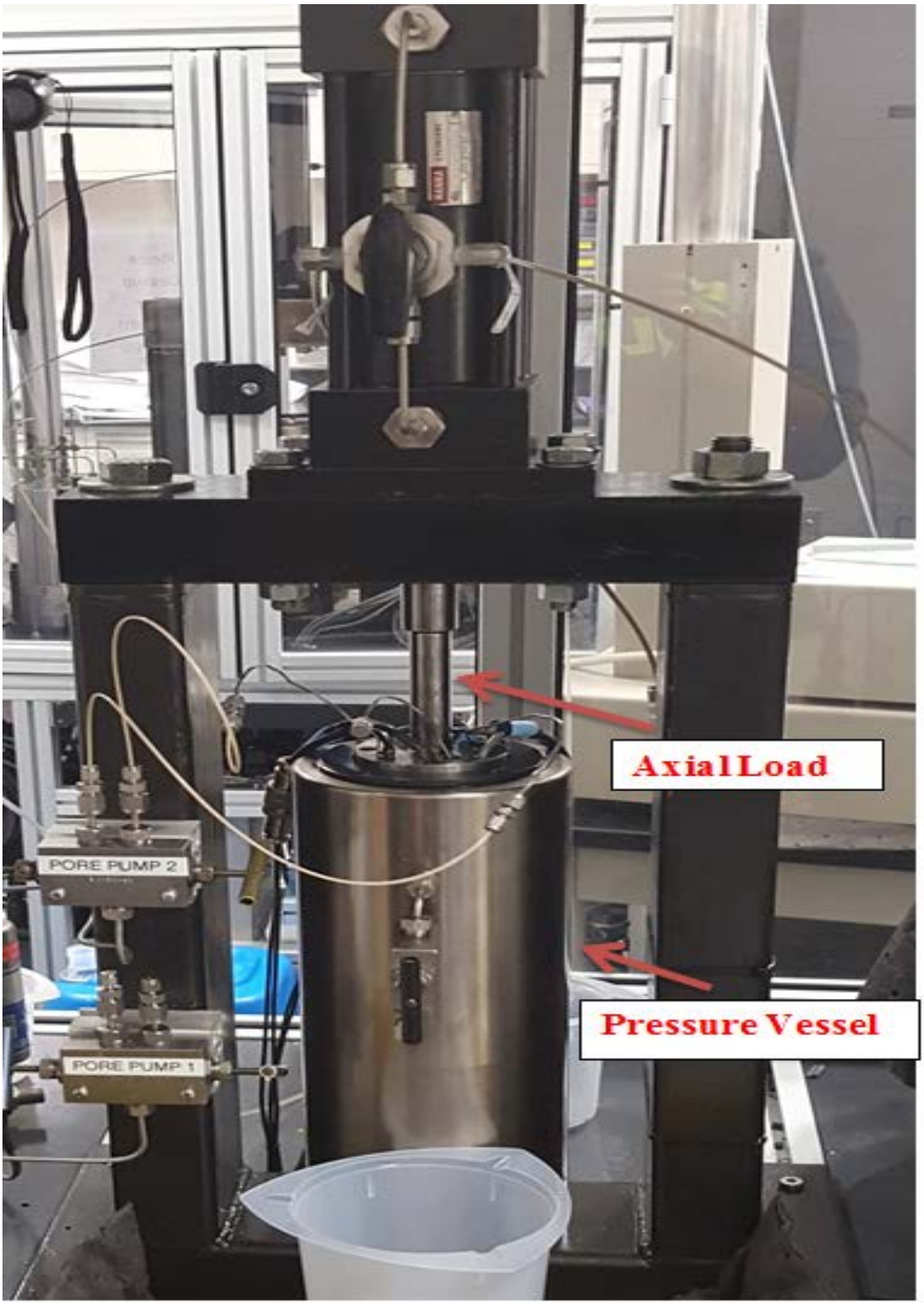

Figure 24 Tri-axial test equipment, showing a presure vessel where the tri-axial assembly is placed inside it.

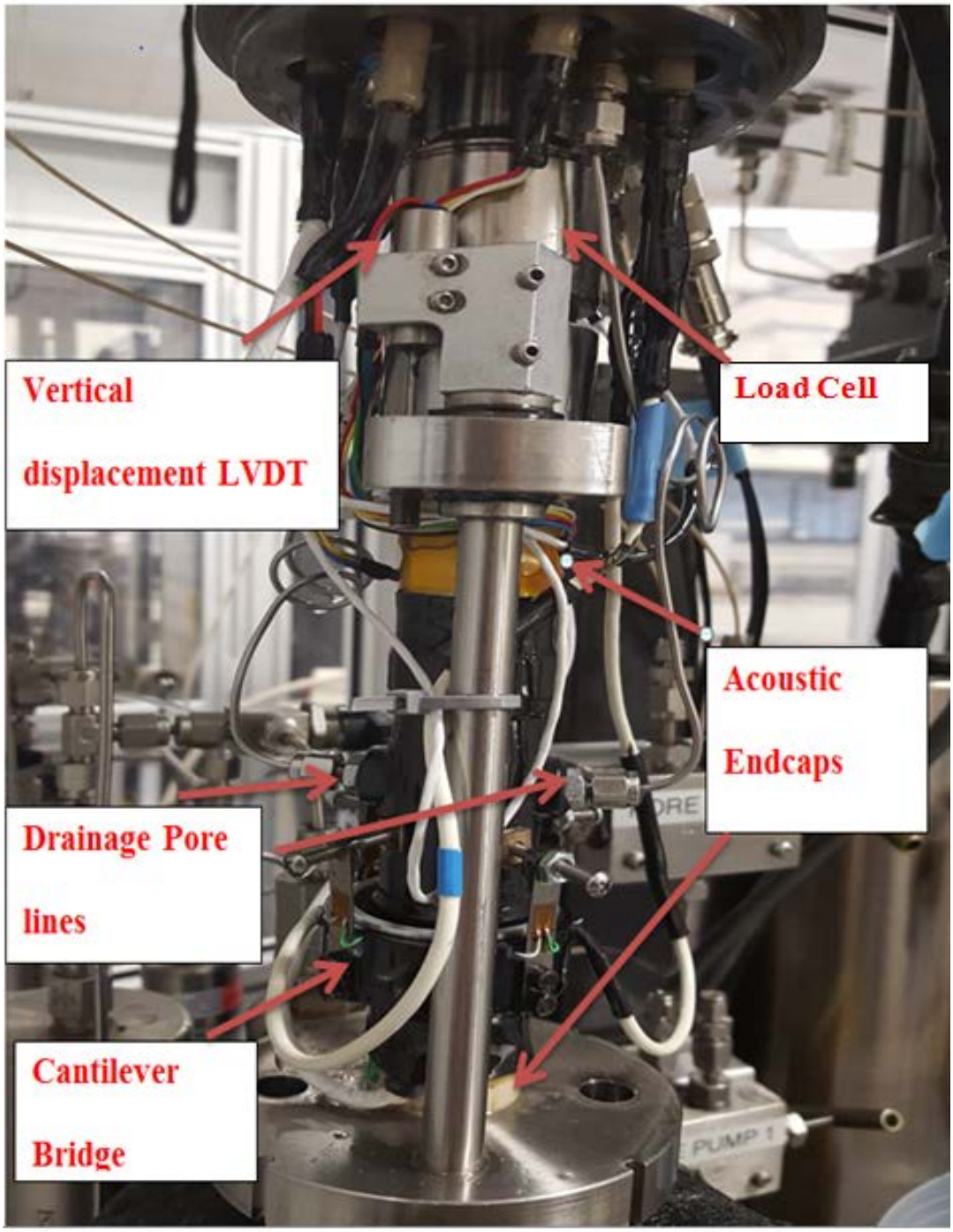

Figure 25 A sleeved sample is mounted between a top and bottom acoustic endcaps, two pore lines are connected to the sidewalls of the sample, Cantilever bridge is mounted on the sample side walls to measure the radial strain.

A graphical user interface (GUI) is used to setup and monitor the experiment. It can make plots in the real time where the user can monitor the rock behavior under stress. One of the features of the (GUI) is the Master Segment List which is used to setup a list of steps that implement the desired the test routine. An example of a Master Segment list setup is shown in Figure **26** Segment list setup for a 48 hour stress and hold steps, it shows as well the stress ramp increase rate for each incremental stress step.

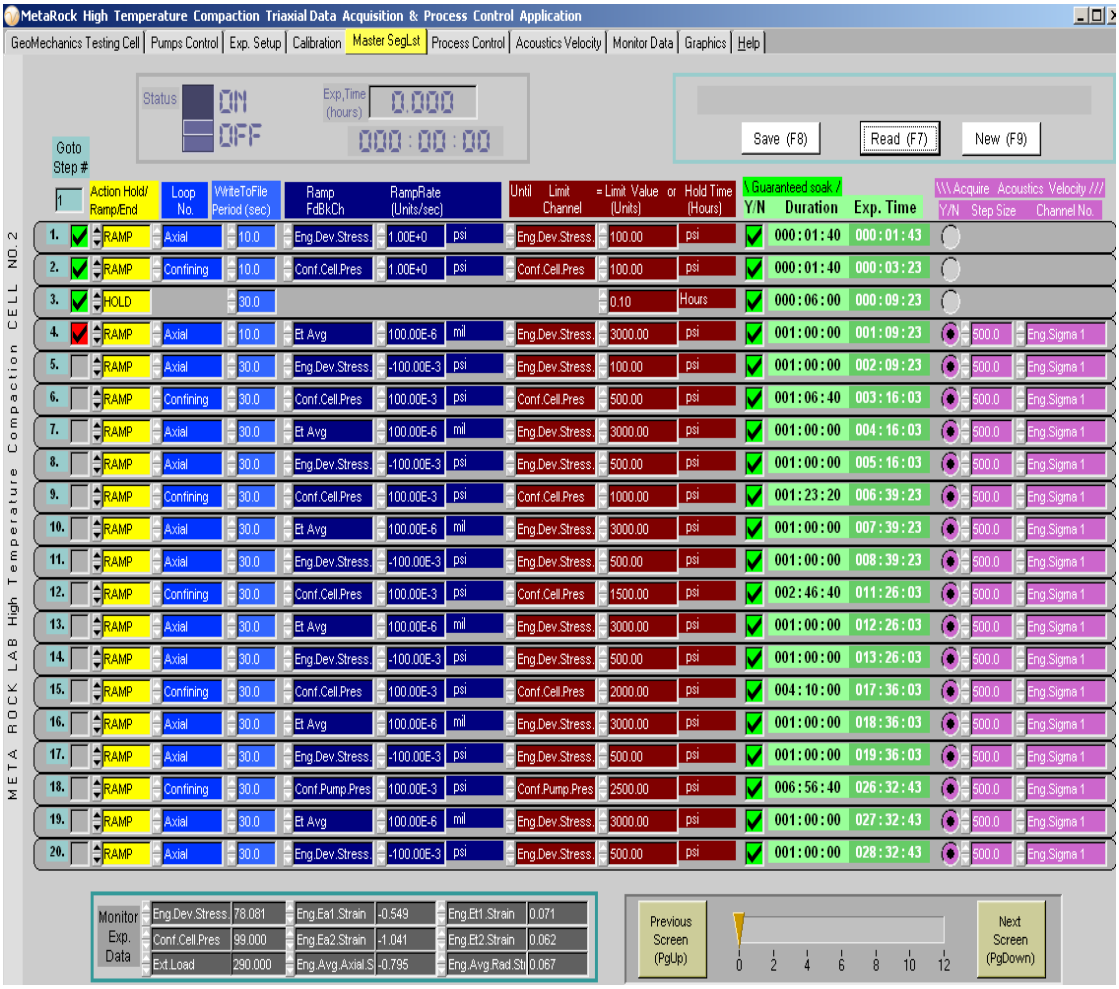

Figure 26 Segment list setup for a 48 hour stress and hold steps, it shows as well the stress ramp increase rate for each incremental stress step.

2.4.2 Experiment Setup

1- Cut Teflon approximately four inches, along with two 1 inch as double sleeves.

2- Trim the sample to two inches.

3- Expand the Teflon using mandrels, and heat gun.

4- Punch a hole through the Teflon sleeve, approximately 1.5 inches from one side.

5- Cut a Teflon screen half inch by two inches, for side drainage.

6- Put the screen around the sample.

7- Put the nut with the pore line through the hole on sleeve; make sure that shorter length side from hole is to the top. Orient the nut on the side that matches the sample curvature.

8- Put the sample inside the sleeve.

9- Put the top and bottom endcaps.

10- Shrink the sleeve using the heat gun.

11- Place the assembly into the pressure vessel, and then tighten the head into the vessel.

12- Use hand pump to move the vertical piston to touch the sample.

13- Increase the confining pressure to a desired pressure, in our study the first stage pressure is 100 Psi.

14- Use the Process control to ramp the axial pressure to iso-static equilibrium (100 Psi), and let it sit until reaching constant volumetric strain.

15- Turn ON the Master segment list, to implement the multistage test.

Chapter 3: Results

In the following section, the experimental results of the CEC measurements, reconsolidation, and multistage triaxial tests are presented.

3.1 CEC Measurement Validation

Results from conductometric titration and methylene blue methods were validated against the cobalt hexamine method.

Conductometric Titration Data Sample:

The endpoint of the exchange reaction is obtained from the intersection of the two linear portions of the curve. The exchange capacity in milli-equivalents is calculated by multiplying the normality of the standard Magnesium Sulfate solution by the number of ml corresponding to the end point.

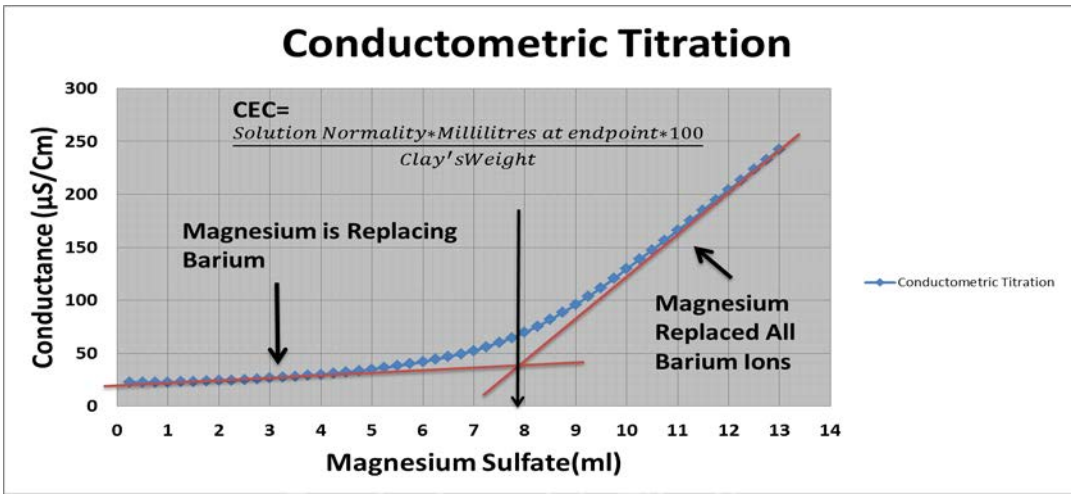

Figure 27 Typical experimental data for conductometric titration, the CEC is determined by the intersection of the two asymptotes.

CEC Calculation:
Solution Normality= 1 Normal Intersection at 7.9 millilitres
Clay's Weight = 20 grams
$\text{CEC} = \frac{1\text{Normal}*7.9(\text{millilitre})*100}{20\ \text{Grams}}$=39.5 (meq/100grams)

Methylene Blue Technique Data Sample:

Sample: Pierre Shale

-Sample Weight = 1 gram

-Methylene Blue Concentration = 0.01 Molarity

-Volume of Methylene Blue = 60 milli-liter, contains 0.6 meq before mixing it with clays

-Volume of Supernatant sample = 1 milli-liter, then diluted to 200 ml.

-Absorbance after dilution = 0.189

-**From the calibration curve:**

- Absorbance = 33017 (Concentration) – 0.189

- Concentration of diluted solution of 200 ml = $\frac{0.189+0.0238}{33017} = 6.44324 * 10^{-6}$ mol/liter ,

- Number of moles in the diluted solution of 200 ml = $6.44324 * 10^{-6} * 0.2 = 1.28865 * 10^{-6}$ moles

- Meq in the diluted solution = Meq in the Supernatant sample = $1.28865 * 10^{-6} * 1000 =$ 0.00128865 meq

-Meq in Methylene blue solution (60ml) after mixing with clays = 0.00128865*60 = 0.077319 meq

-$\boldsymbol{CEC = (0.6 - 0.077319) * 100 = 52.2\ meq/100 grams}$

Table 3 Comparison of the CEC measurement using three different techniques for the same sample type, CEC units is in meq/100 grams.

CEC Data			
Sample Name	Conductometric Titration	Cobalt Hexamine	Methylene Blue
Pierre Shale	39.5	39.5	52.2
Illite	35	37.7	48.3
A	18.7	17.1	25.1
B	19.5	20	19.5
C	15.5	16.4	18.1
D	6.75	7	6.1
E	11.2	11	12.9

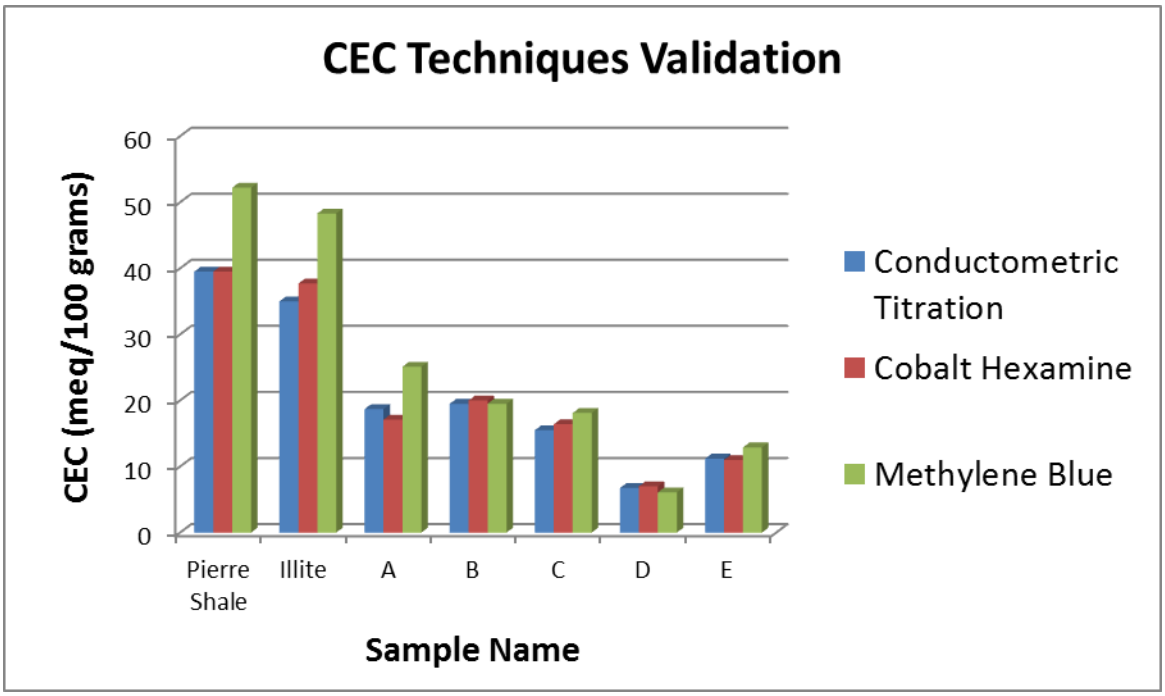

Figure 28 CEC measured using three different techniques for data validation.

CEC values obtained by using conductometric titration and cobalt hexamine are very similar for most of the measured samples.

3.2 Reconsolidation

Petrophysical properties were measured using the reconsolidation technique. Cross-plots of porosity-permeability-stress were developed for samples varying in salinity, mineralogy, CEC, and grain size distribution.

Permeability interpretation:

Permeability may be calculated from reconsolidation stress/strain data. Plotting strain versus logarithm of time helps in showing the details of compaction with time, up to 60 % consolidation, compaction can be considered hydraulic flow dominated. The hundred percent consolidation is obtained at the intersection point of two tangents. First, a tangent to the linear part of the curve, second, a tangent to the secondary consolidation. The 50% consolidation is at half the 100% consolidation strain. From calculating the coefficient of consolidation at 50% consolidation using,

$$C_{v=}\frac{0.197}{t_{50}}H_{dr}^{2}. \tag{28}$$

Permeability can be given as $K=C_vM_v\mu$

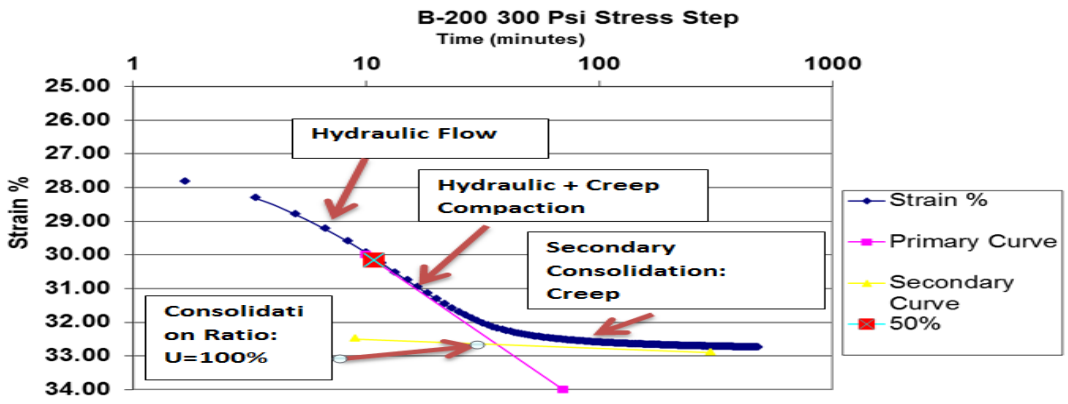

Figure 29 Strain versus the logarithm of time at 300 Psi step & hold.

Porosity Calculations:

Porosity may be calculated as a function of stress using reconsolidation stress/strain data.

1-First method, porosity is calculated from final sample weight, sample volume, grain density, and brine density. Porosity is back calculated as a function of stress by accounting expelled brine volume; expelled brine volume may be calculated from vertical displacement per stress stage which may be measured by Linear Variable Displacement Transducer (LVDT)

2-Second method, initial porosity may be calculated from initial grain weight, grain density, initial brine weight, and brine density. Change in porosity as a function of stress may be calculated from expelled brine volume which is calculated from vertical displacement.

3-Third method, apply thermo-gravimetric analysis to the reconsolidated sample. The reduction in weight is due to the evaporation of brine which fills 100% of pore space, from weight reduction, brine density, and sample volume the porosity may be calculated.

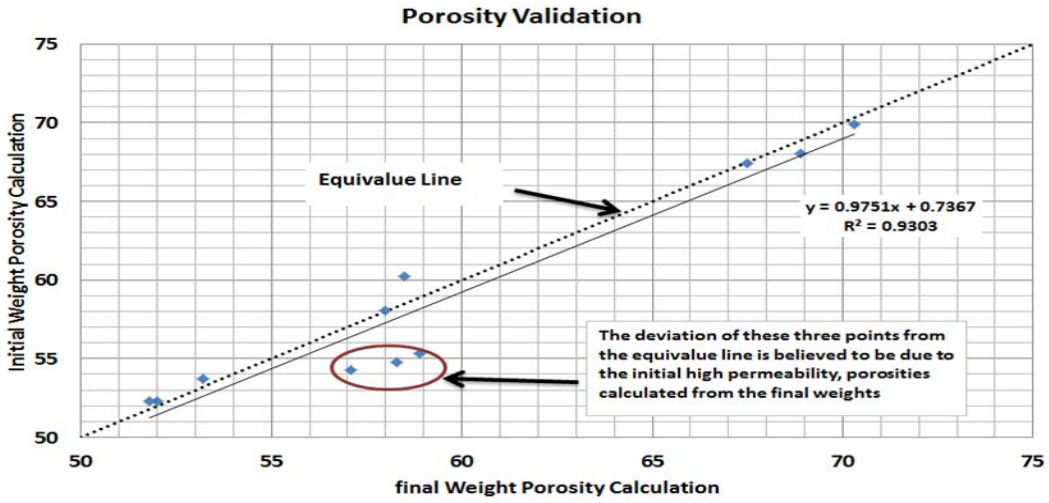

Figure 30 Porosity measurement comparison using the post test weights, and Initial weight for reconsolidated samples.

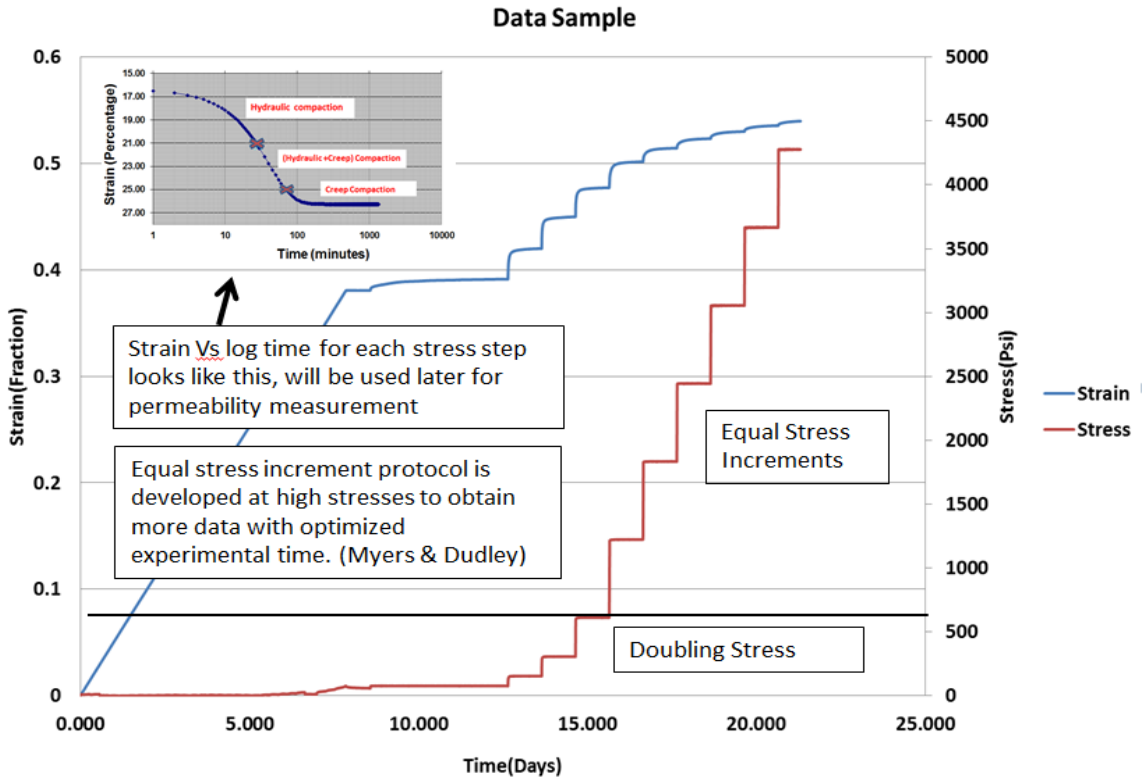

Figure 31 Stress/Strain relationship.

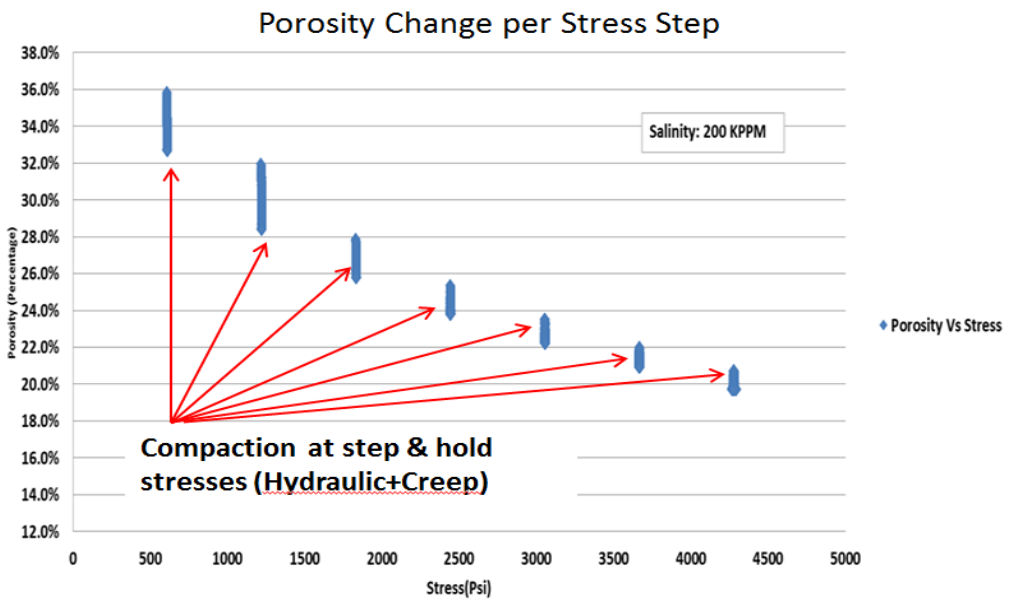

Figure 32 Porosity change as a function of stress caused by hydraulic & creep compaction.

3.2.1 Salinity Dependence for Sample-B

Sample-B is a rock sample cored from a reservoir in Gulf of Mexico, in this section; the data shown is for samples resedimented at three different salinities 35 KPPM, 100 KPPM, and 200 KPPM and will be named Sample B-35, Sample B-100, and Sample B-200 respectively.

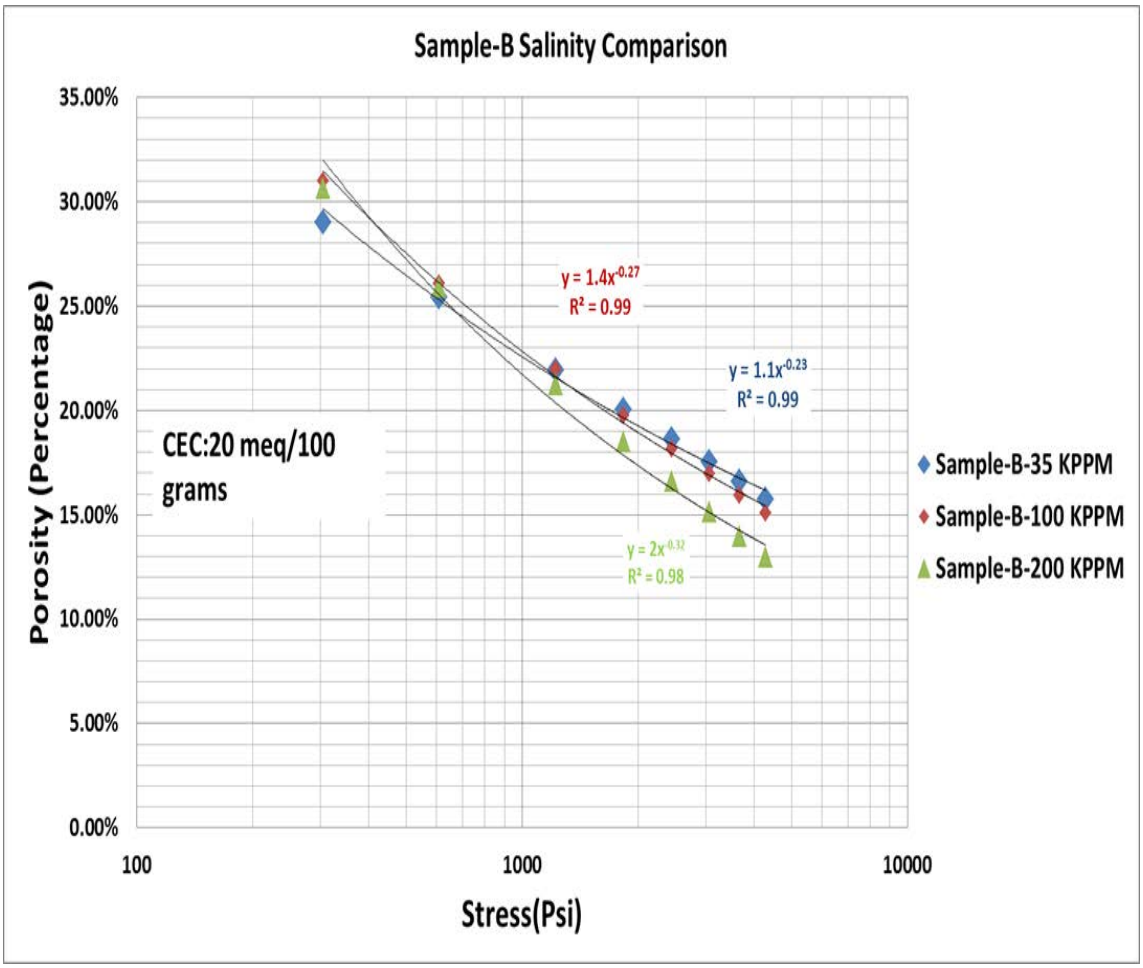

Figure 33 Increasing salinity decreased porosity, that was expected due to the double layer shrinkage, the relationship of porosity with stress is power law.

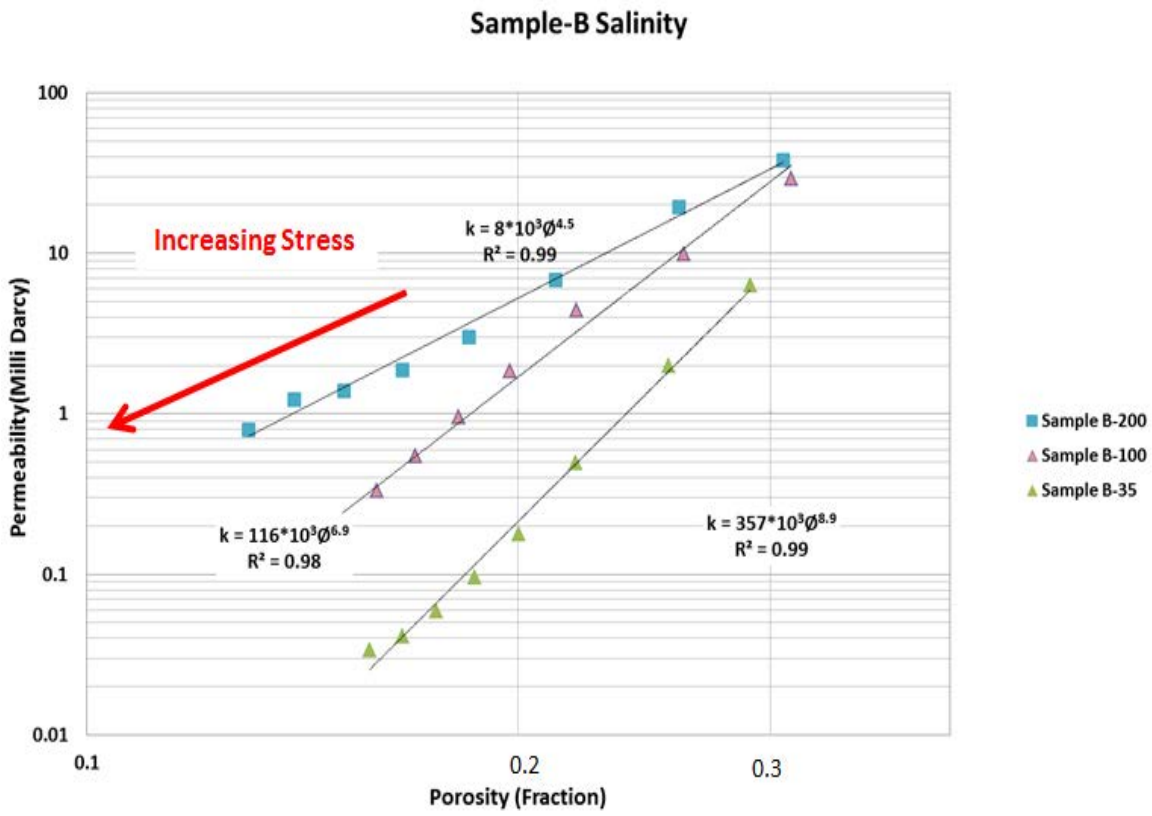

Figure 34 Increasing salinity increases permeability, high salinity samples have larger permeability even though lower porosity (Double Layer Effect), Porosity-Permeability relationship as a function of stress is power law.

Summary Data Table:

Table 4 Porosity and permeability as a function of stress and salinity for Sample-B. Increasing salinity decreases porosity while increases permeability.

Stress (Psi)	Sample-B-35		Sample-B-100		Sample-B-200	
	Porosity	Permeability (milli Darcy)	Porosity	Permeability (milli Darcy)	Porosity	Permeability (milli Darcy)
305	29.03	6.29	31.00	29.36	30.62	38.09
610	25.45	1.99	26.10	9.93	25.90	19.48
1220	21.94	0.50	21.97	4.42	21.22	6.86
1830	20.02	0.18	19.74	1.84	18.49	3.01
2440	18.65	0.10	18.17	0.96	16.60	1.87
3050	17.52	0.06	16.95	0.55	15.11	1.39
3660	16.60	0.04	15.94	0.33	13.96	1.23
4280	15.75	0.03	15.08	0.19	12.97	0.80

3.2.2 Salinity Dependence for Sample-A

Sample-A is a rock sample cored from a reservoir in Gulf of Mexico, in this section; the data shown is for samples reconsolidated at two different salinities 35 KPPM, and 200 KPPM and will be named Sample A-35 and Sample A-200 respectively.

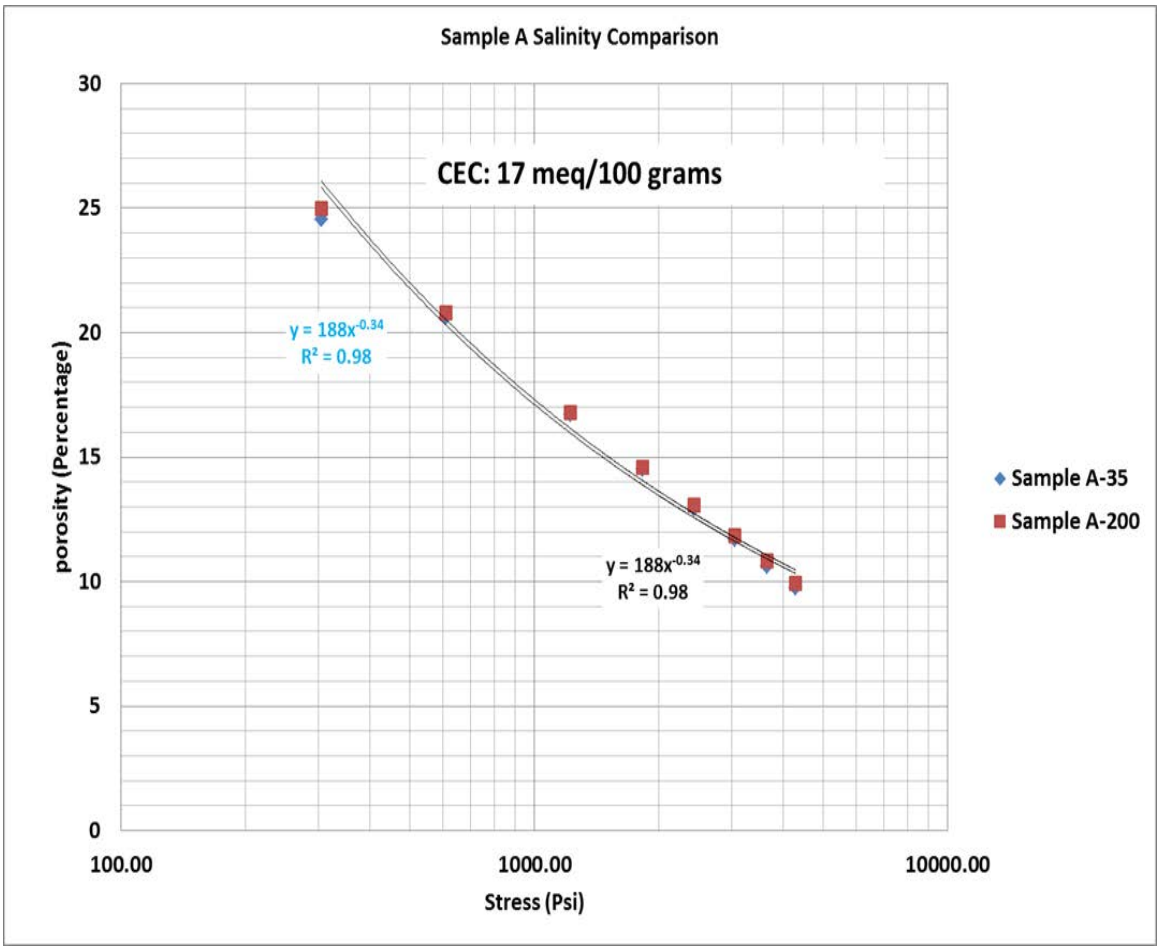

Figure 35 Unlike the expected trend from Sample-B, porosities matched perfectly for the two salinities. The relationship of porosity with stress is power law.

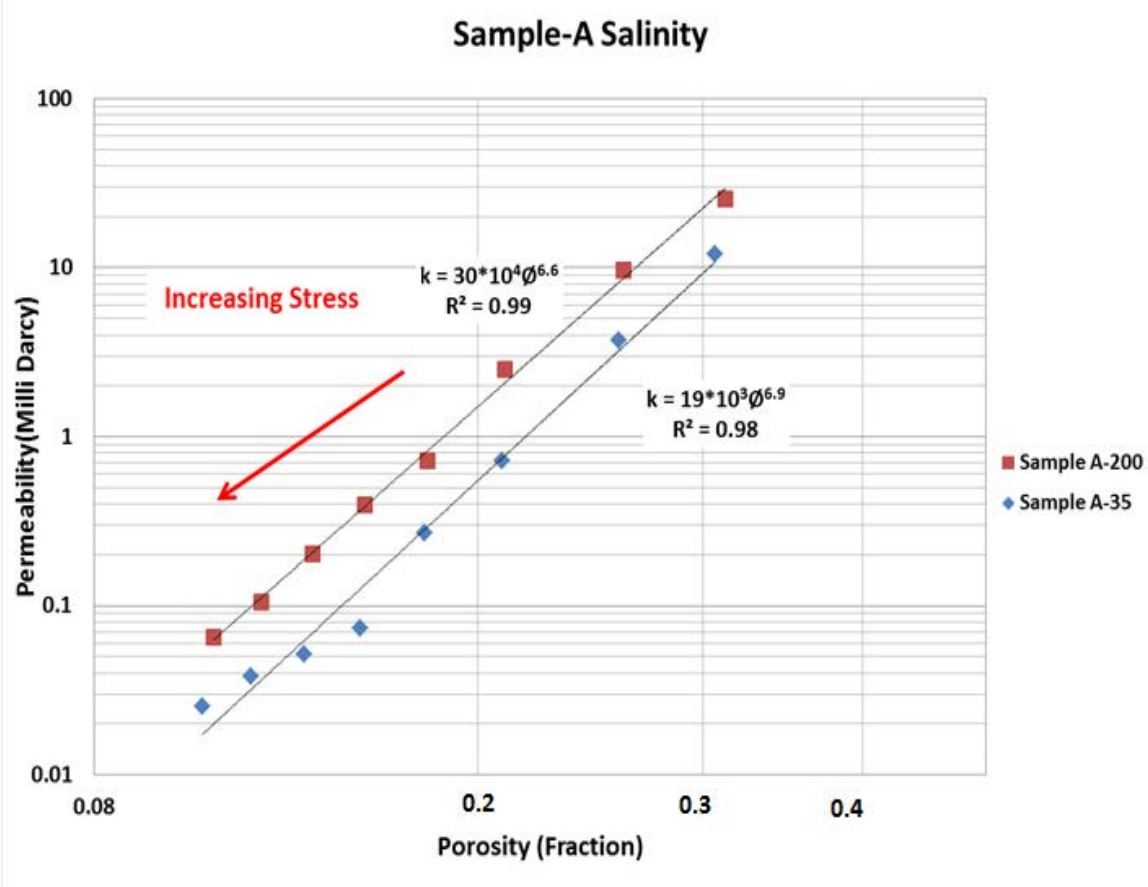

Figure 36 Increasing Salinity increases permeability. Porosity-Permeability relationship as a function of stress is power law. The slopes are almost identical.

Summary Data Table:

Table 5 Sample-A salinity effect on porosity & permeability as a function of stress

Stress (Psi)	Sample A-35		Sample A-200	
	Porosity	Perm (milli Darcy)	Porosity	Perm (milli Darcy)
305	24.55	12.05	24.98	25.46
610	20.61	3.70	20.78	9.68
1220	16.72	0.72	16.79	2.48
1830	14.52	0.27	14.59	0.72
2440	12.92	0.07	13.05	0.40
3050	11.69	0.05	11.86	0.20
3660	10.63	0.04	10.82	0.10
4280	9.73	0.03	9.93	0.07

3.2.3 Salinity Dependence for Pierre Shale

Pierre shale is an outcrop mudrock collected from South Dakota, in this section; the data shown is for samples resedimented at three different salinities 35 KPPM, 100 KPPM, and 200 KPPM and will be named Pierre shale-35, Pierre shale-100, and Pierre shale-200 respectively.

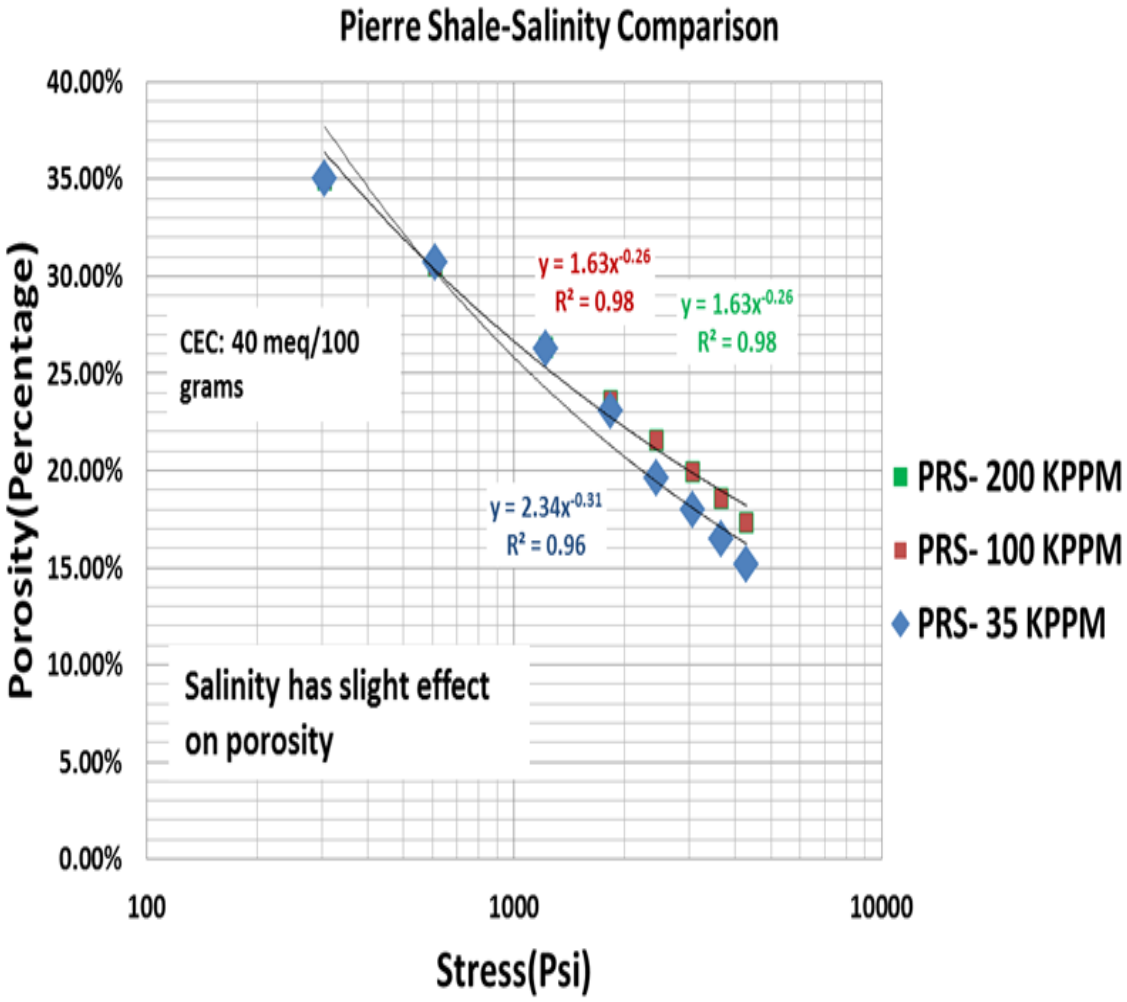

Figure 37 Lower salinity has lower porosity, that was not expected. Expelled brine salinity should be measured to understand the effect of the change in brine salinity with compaction. The relationship of porosity with stress is power law.

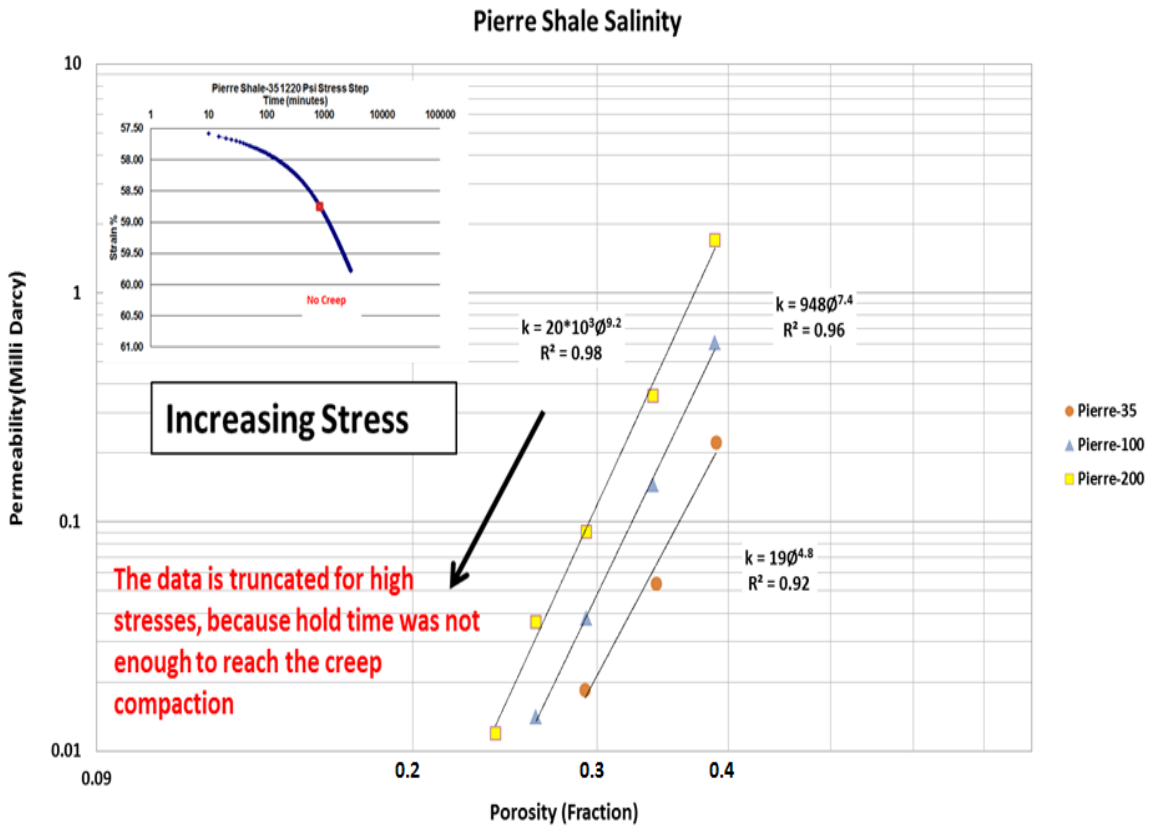

Figure 38 Increasing Salinity increases permeability. Porosity-Permeability relationship as a function of stress is power law. For high CEC samples, the hold time should be longer than 48 hours per step.

Summary Data Table:

Table 6 Porosity and permeability as a function of stress and salinity for Pierre shale, salinity has no effect on porosity, while it changes the permeability at low stresses

Stress (Psi)	Pierre shale-35		Pierre shale-100		Pierre shale-200	
	Porosity	Permeability(milli Darcy)	Porosity	Permeability(milli Darcy)	Porosity	Permeability(milli Darcy)
300	35.025	0.221	34.960	0.602	34.960	1.695
600	30.714	0.054	30.523	0.144	30.523	0.355
1220	26.284	0.019	26.343	0.038	26.343	0.091
1830	23.050	0.008	23.601	0.014	23.601	0.037
2440	19.598	0.007	21.588	0.007	21.588	0.012
3050	17.943	0.005	19.967	0.006	19.967	0.005
3660	16.452	0.004	18.537	0.004	18.537	0.005
4280	15.194	0.002	17.330	0.003	17.330	0.003

3.2.3 Clay Percentage Effect on Properties

In this section, we measured the porosity and permeability as a function of changing the clay percentage; we mixed a mudrock (Sample-B) with Brazos river sand at different percentages by weight 25%, and 50% of sand added to the mudrock. The original clay percent in Sample-B is determined from XRD data as 35% of mixed layer. All samples are prepared at a salinity of 100KPPM, so data of mixed samples can be compared with Sample B-100.

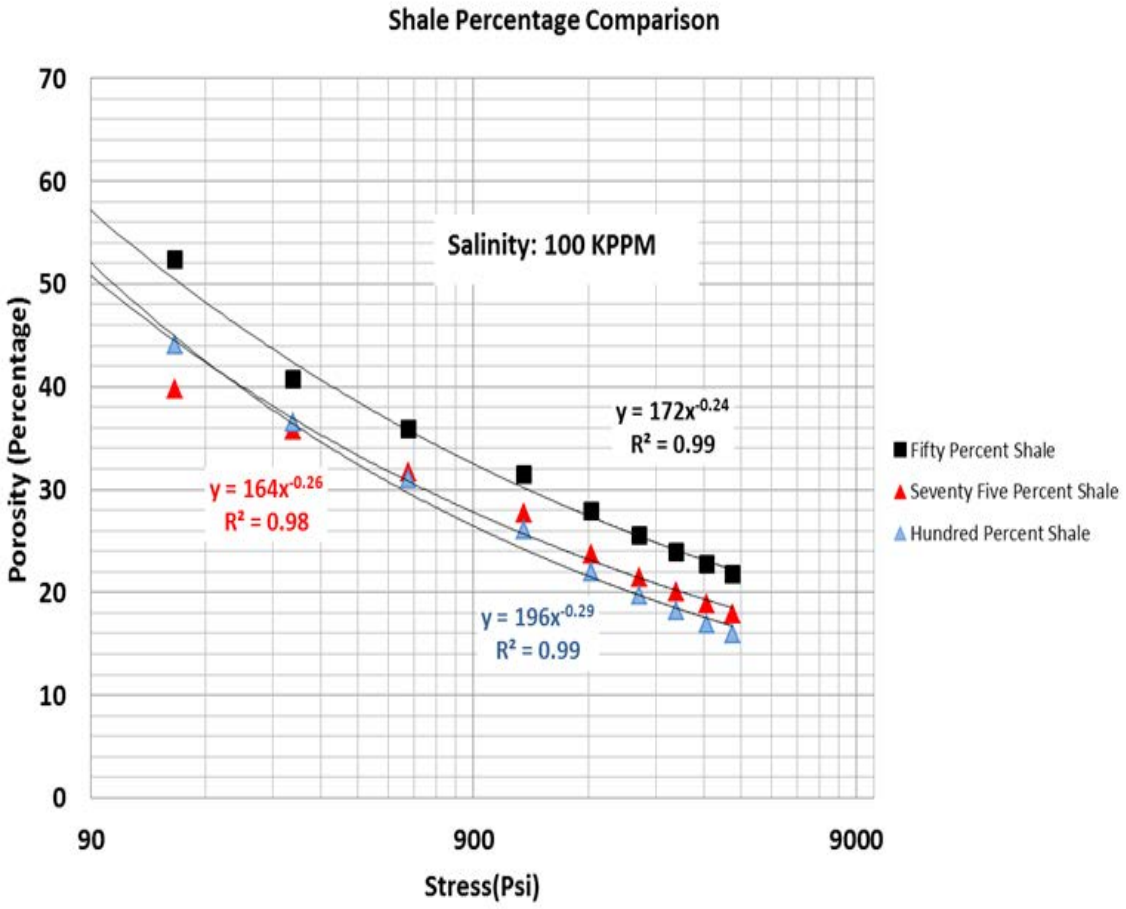

Figure 39 Increasing sand increases porosity. The relationship of porosity with stress is power law.

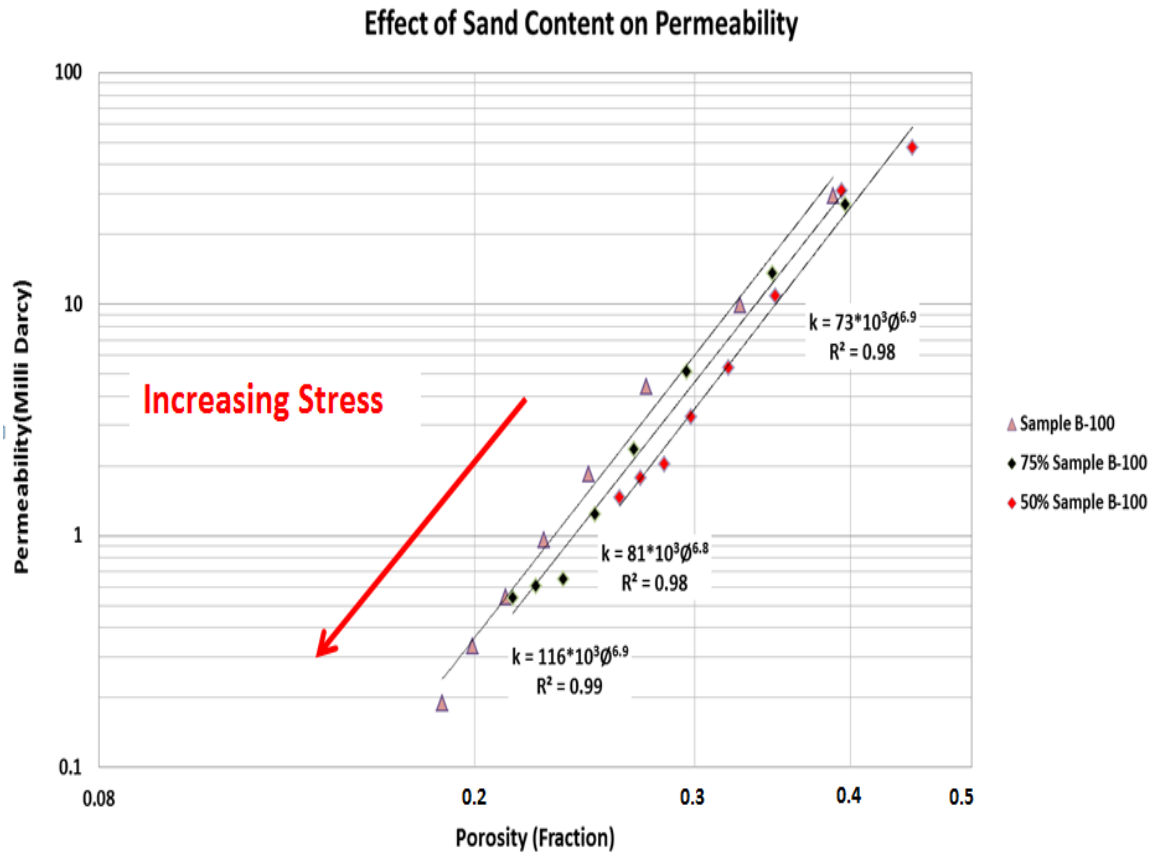

Figure 40 Increasing sand content increases porosity & permeability. Porosity-Permeability relationship as a function of stress is power law. The slopes are almost identical.

Summary Data Table:

Table 7 Porosity and permeability as function of stress for 100%, 75%, and 50% shale. The data shows that adding sand increases porosity as well as permeability

Stress (Psi)	100% Shale (Sample B-100)		75% Shale		50% Shale	
	Porosity	Permeability (milli Darcy)	Porosity	Permeability (milli Darcy)	Porosity	Permeability (milli Darcy)
305	30.997	29.359	31.697	26.801	35.905	47.519
610	26.104	9.934	27.732	13.562	31.508	30.827
1220	21.968	4.417	23.667	5.101	27.869	10.783
1830	19.735	1.838	21.483	2.352	25.559	5.319
2440	18.171	0.956	19.985	1.233	23.864	3.267
3050	16.952	0.545	18.833	0.651	22.694	2.032
3660	15.942	0.334	17.927	0.603	21.743	1.775
4280	15.078	0.188	17.162	0.540	20.902	1.456

3.2.4 Reconsolidation Summary

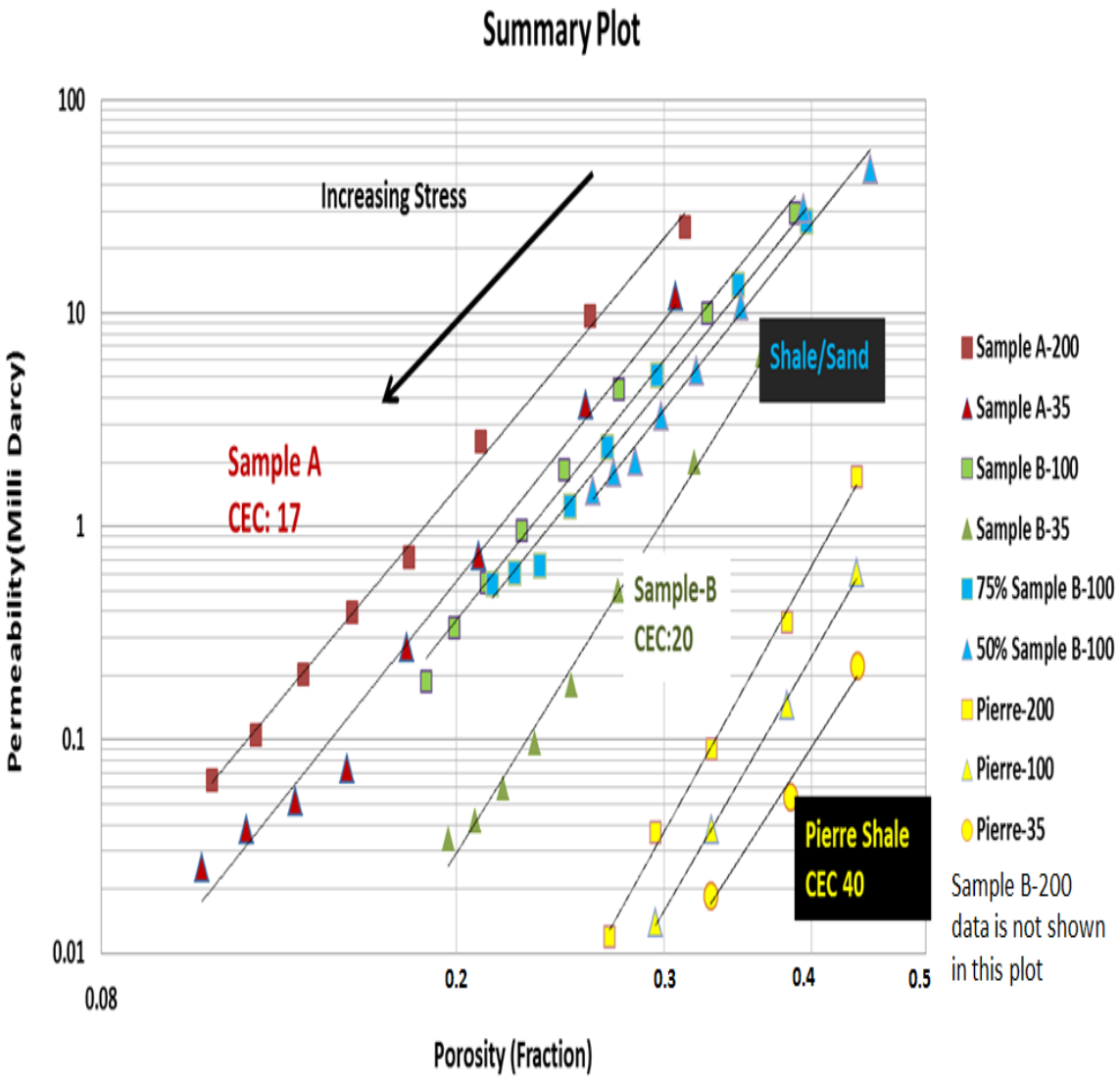

Figure 41 Porosity-Permeability relationship as a function of stress is power law for all samples. Salinity has strong effect on permeability. Sand content has an effect on porosity & permeability. CEC has an effect on permeability.

3.3 Multistage Test

Multistage test is used to determine rock failure envelope, we use resedimented plugs. Core plugs used in this study vary in their mineralogy, salinity, CEC, and grain size distribution.

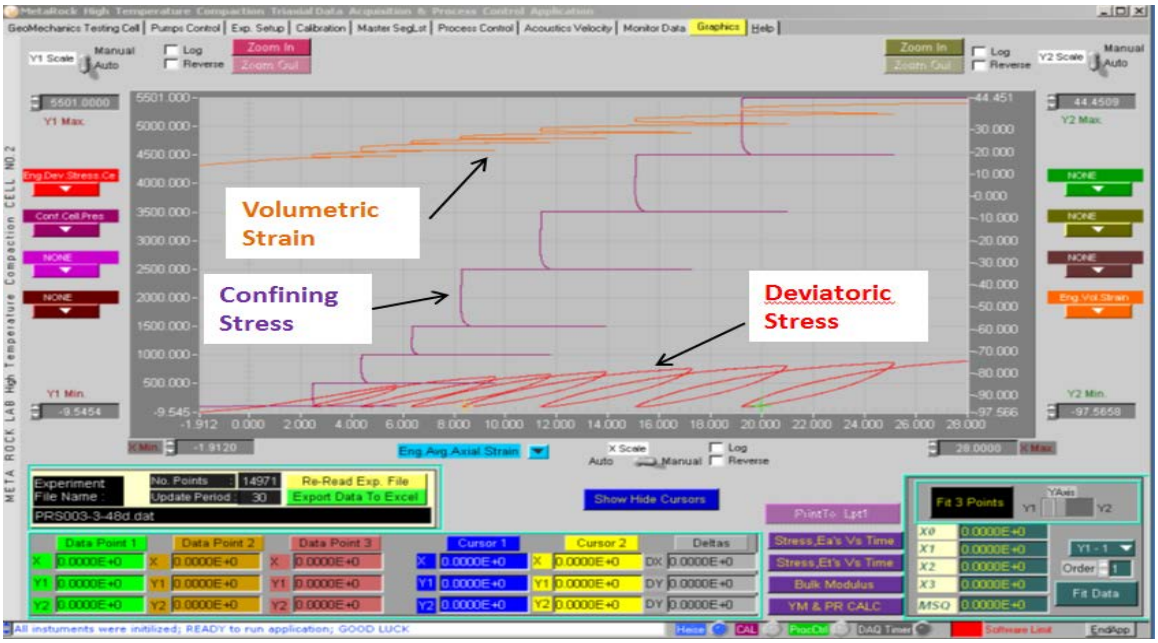

Figure 42 from multistage triaxial data, a whole strength envelope is obtained using only one sample. The slope of strength change is low for this sample ‘’Low Friction Angle’’ (will be discussed later).

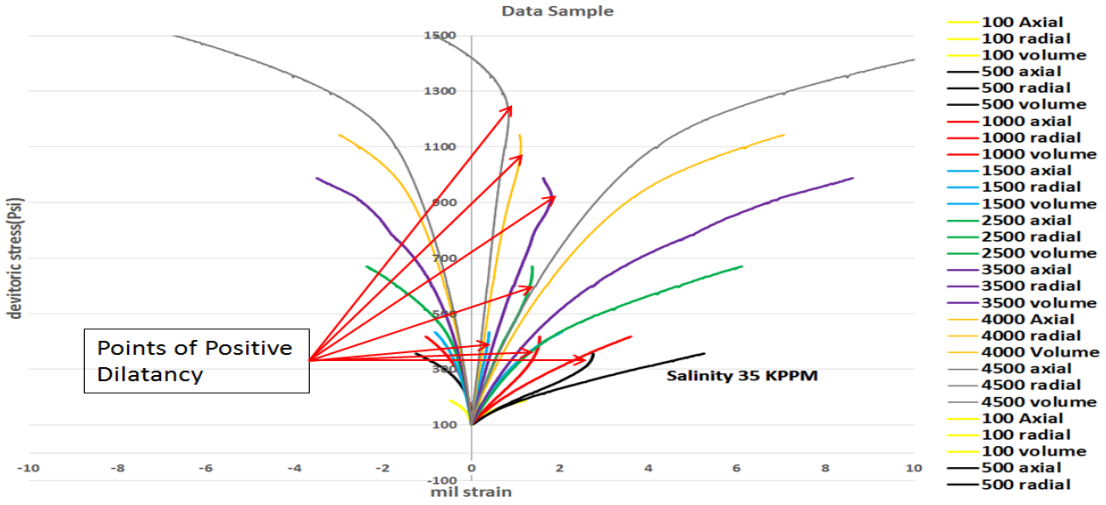

Figure 43 Points of positive dilatancy at Poisson ratio equals half, when volumetric strain becomes constant.

3.3.1 Salinity Effect on Sample-A Strength

Strength is determined for core plugs resedimented at 35 KPPM, and 100 KPPM.

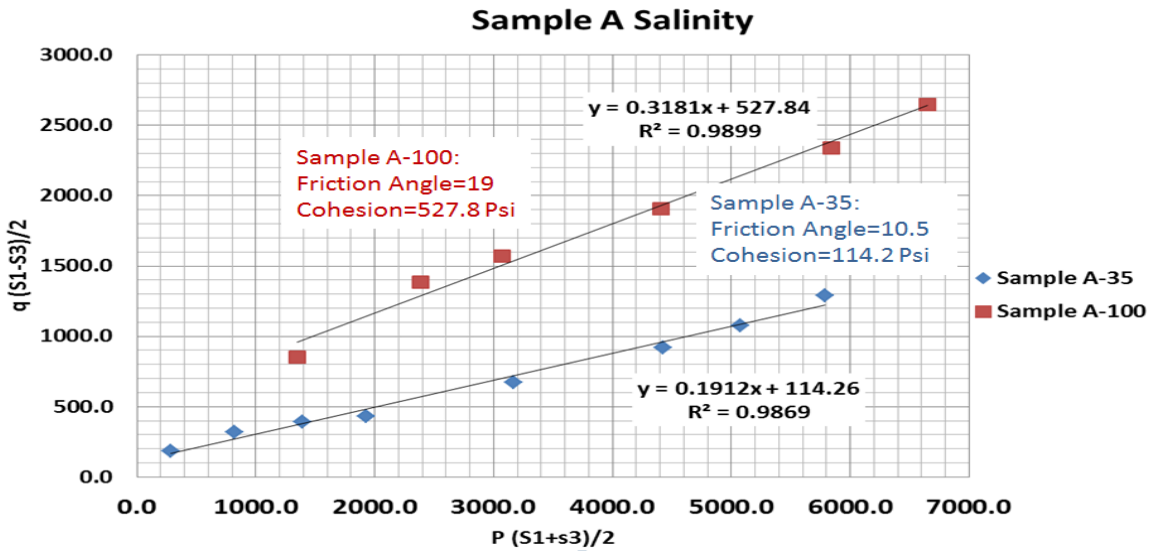

Figure 44 Increasing salinity has increased friction angle. Increasing salinity has increased the interpreted cohesion. Cohesion values in this study is not fully trusted, because it is based on a correction factor of two.

3.3.2 Salinity Effect on Sample-B Strength

Strength is determined for core plugs resedimented at 35 KPPM, and 100 KPPM.

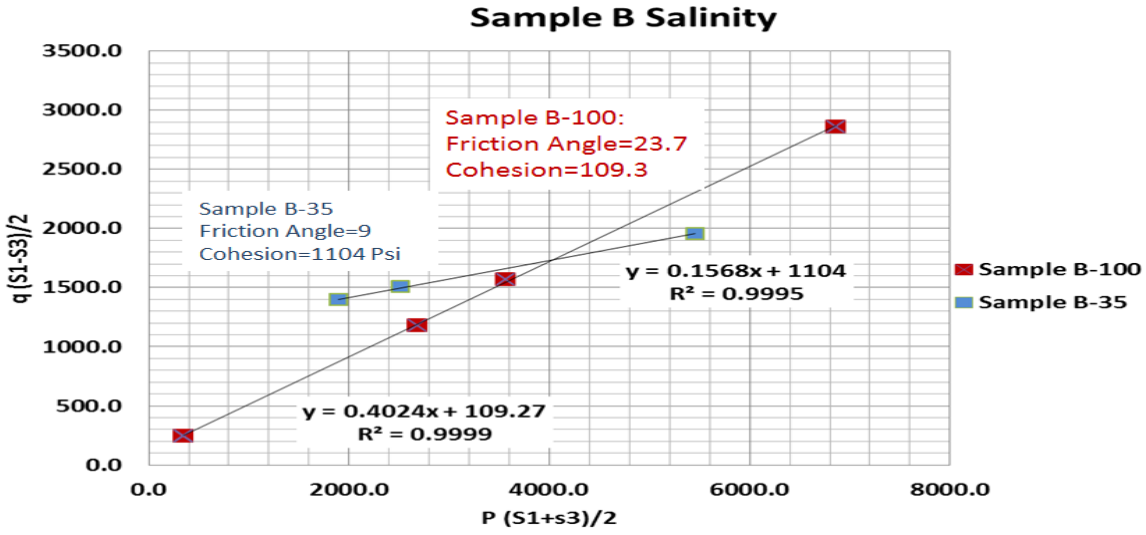

Figure 45 increasing salinity has increased friction angle. Increasing salinity has decreased cohesion. Sample B-35 has too large cohesion.

3.3.3 Effect of Salinity on Pierre Shale

Strength is determined for core plugs resedimented at 35 KPPM, 100 KPPM and 200 KPPM.

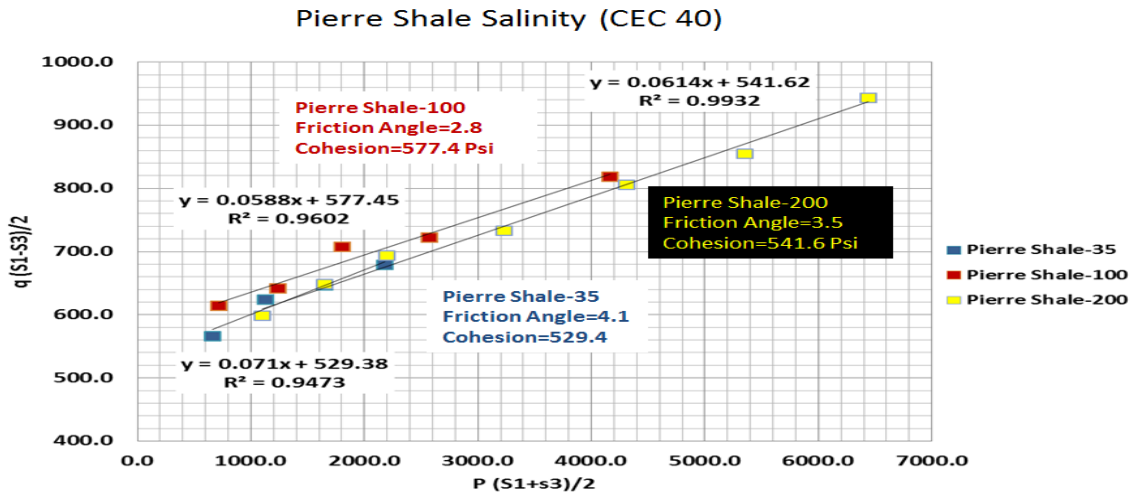

Figure 46 Pierre shale has very low friction angle, this is believed to be due to the high CEC. No salinity effect on friction angle or cohesion.

3.3.4 Effect of Increasing Sand to Mud Rock Mechanics

Sand is added to Sample-B at percentages of 25%, 50%, and 75% to check the transition from mud rock behavior to sand behavior.

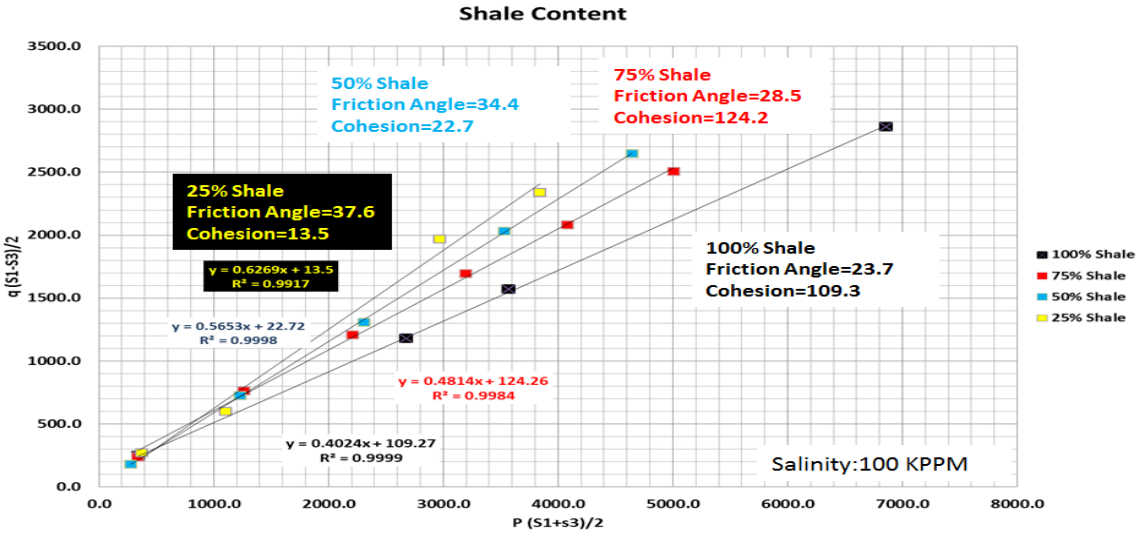

Figure 47 Increasing sand increases friction angle & decreases cohesion.

3.3.5 Effect of CEC on Friction Angle

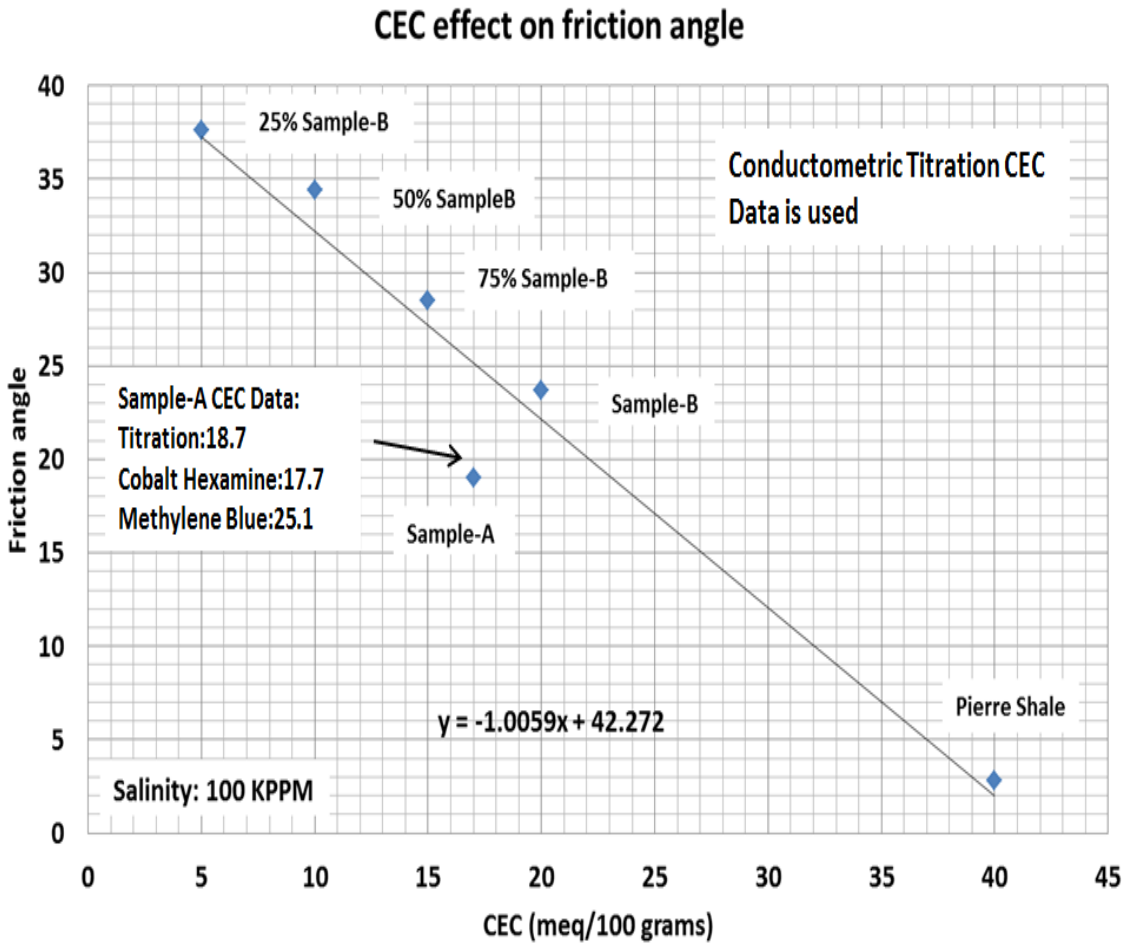

Figure 48 Friction angle decreases with increasing CEC. The deviation in Sample-A data may be due to many factors like salinity sensitivity, and grain size distribution or might be the methylene blue is the best way to measure the CEC.

Chapter 4: Conclusion

CEC values obtained by using conductometric titration and cobalt hexamine are very similar for most of the measured samples; however methylene blue technique CEC measurement has slightly higher CEC values for high smectitic samples such as Pierre shale, and Illite.

Porosity is affected by two factors; primary compaction which is hydraulic flow dominated, and secondary compaction which is creep dominated. Permeability increases with increasing salinity, but the duration of the hydraulic flow is shorter in high salinity samples, this could be the reason of not seeing large differences in porosity with salinity. Salinity has very small effect on porosity on low smectitic samples, and has no effect on porosity for high smectitic samples. Increasing sand percentage in mudrocks increases porosity and permeability.

CEC has a strong effect on permeability, Pierre shale has much lower permeabilies as Sample-A, and Sample-B, although Pierre shale has larger porosities, this low permeabilies can be due to the double layer effect in Pierre shale.

Friction angle decreases with high CEC, Previous work was done at low stresses, data trends were validated at much higher stresses, and strong data match was observed.

No salinity effect on friction angle on high smectitic samples, however increasing salinity has increased friction angle of low smectitic samples to double its value. Increasing sand percentage in mudrocks increased friction angle and decreased cohesion.

5 Appendix

5.1 Conductometric Titration

In this section, conductometric titration results used for CEC measurements are shown for Pierre shale, Illite, and five other samples. Specific conductance remains comparatively constant while the barium on the exchange complex is being replaced by Magnesium. Once the exchange sites are saturated with Magnesium the conductance increases as increments of the titrating solution are added. The endpoint of the exchange reaction is obtained from the intersection of the two linear portions of the curve. The exchange capacity in milli-equivalents is calculated by multiplying the normality of the standard Magnesium Sulfate solution by the number of ml corresponding to the end point.

Sample: Pierre Shale

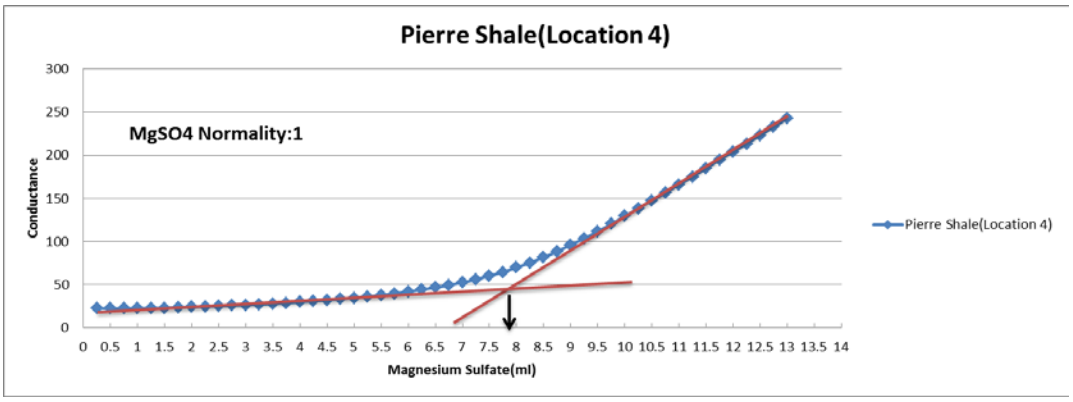

Figure 49 The magnesium sulfate titrating solution concentration is 1 Normal. The endpoint is at 7.9 ml. Clay weight is 20 grams.

CEC Calculation:
Solution Normality= 1 Normal Intersection at 7.9 millilitres
Clay's Weight = 20 grams
$\mathrm{CEC} = \frac{1\mathrm{Normal} * 7.9(\mathrm{millilitre}) * 100}{20\ \mathrm{Grams}}$=39.5 (meq/100grams)

Sample: Illite

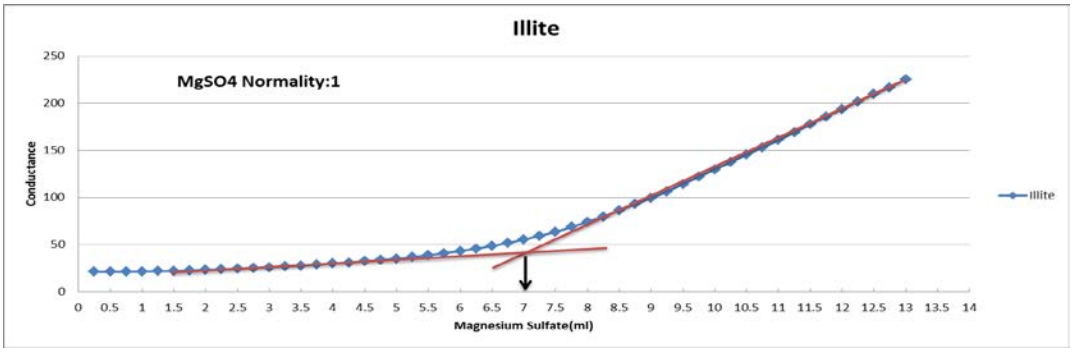

Figure 50 The magnesium sulfate titrating solution concentration is 1 Normal. The endpoint is at 7 ml. Clay weight is 20 grams.

CEC Calculation:

Solution Normality= 1 Normal Intersection at 7 millilitres

Clay's Weight = 20 grams

$$\text{CEC} = \frac{1\text{Normal} * 7(\text{millilitre}) * 100}{20\ \text{Grams}} = 35\ (\text{meq}/100\text{grams})$$

Sample: A

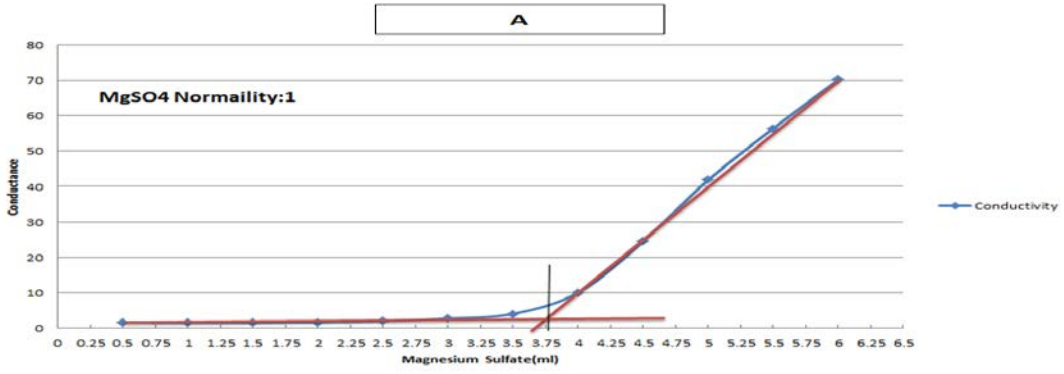

Figure 51 The magnesium sulfate titrating solution concentration is 1 Normal. The endpoint is at 3.75 ml. Clay weight is 20 grams.

Solution Normality= 1 Normal Intersection at 3.75 millilitres

Clay's Weight = 20 grams

$$\text{CEC} = \frac{1\text{Normal} * 3.75(\text{millilitre}) * 100}{20\ \text{Grams}} = 18.75\ (\text{meq}/100\text{grams})$$

Sample: B

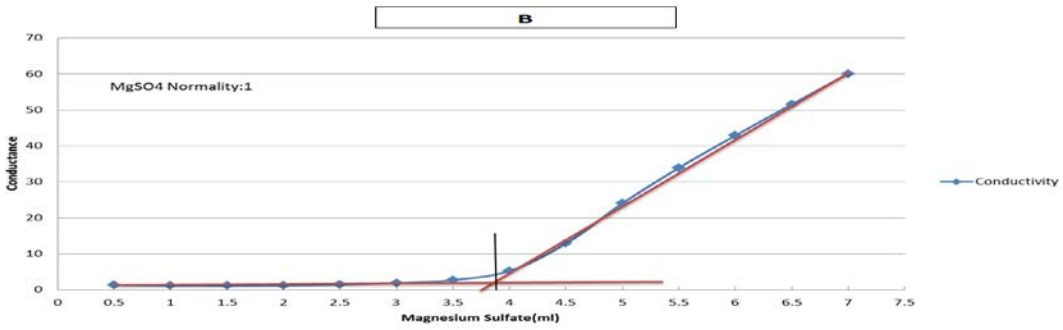

Figure 52 The magnesium sulfate titrating solution concentration is 1 Normal. The endpoint is at 3.9 ml. Clay weight is 20 grams.

CEC Calculation:

Solution Normality= 1 Normal Intersection at 3.9 millilitres

Clay's Weight = 20 grams

$\text{CEC} = \frac{1\text{Normal} * 3.9(\text{millilitre}) * 100}{20\ \text{Grams}}$=19.5 (meq/100grams)

Sample C

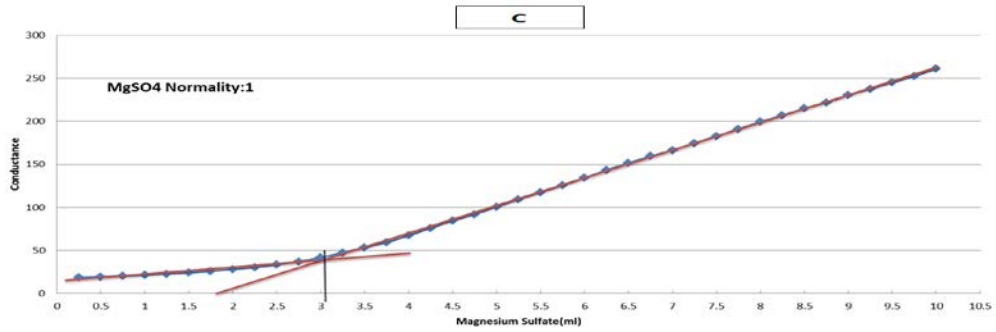

Figure 53 The magnesium sulfate titrating solution concentration is 1 Normal. The endpoint is at 3.1 ml. Clay weight is 20 grams.

CEC Calculation:

Solution Normality= 1 Normal Intersection at 3.1 millilitres

Clay's Weight = 20 grams

$\text{CEC} = \frac{1\text{Normal} * 3.1(\text{millilitre}) * 100}{20\ \text{Grams}}$=15.5 (meq/100grams)

Sample: D

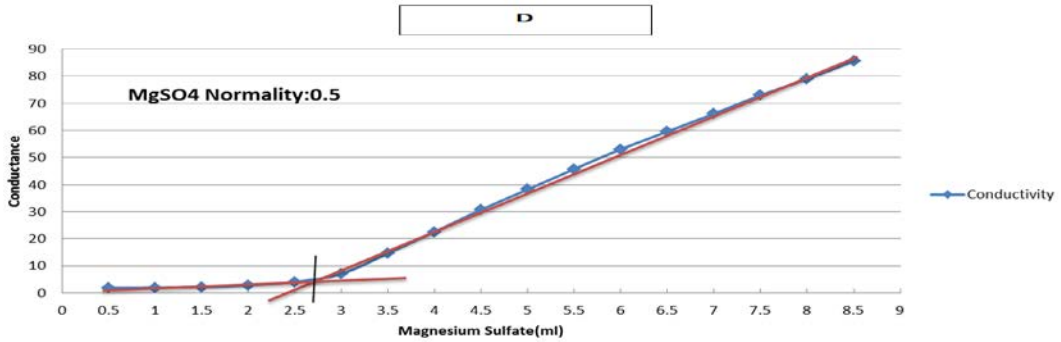

Figure 54 The magnesium sulfate titrating solution concentration is 0.5 Normal. The endpoint is at 2.7 ml. Clay weight is 20 grams.

CEC Calculation:

Solution Normality= 0.5 Normal Intersection at 2.7 millilitres

Clay's Weight = 20 grams

$$\text{CEC} = \frac{0.5\text{Normal} * 2.7(\text{millilitre}) * 100}{20\ \text{Grams}} = 6.75\ (\text{meq}/100\text{grams})$$

Sample: E

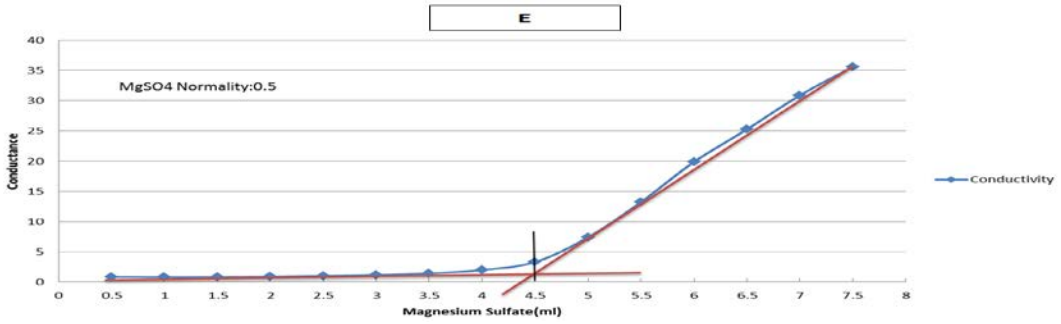

Figure 55 The magnesium sulfate titrating solution concentration is 0.5 Normal. The endpoint is at 4.5 ml. Clay weight is 20 grams.

CEC Calculation:

Solution Normality= 0.5 Normal Intersection at 4.5 millilitres

Clay's Weight = 20 grams

$$\text{CEC} = \frac{0.5\text{Normal} * 4.5(\text{millilitre}) * 100}{20\ \text{Grams}} = 11.25\ (\text{meq}/100\text{grams})$$

5.2 Methylene Blue Technique

In this section, CEC results using methylene blue technique are presented. A sample of ground rock is combined with a methylene blue solution at a specific concentration and mixed for a period of time (1 Hour). The resulting mixture of clays and methylene blue solution is filtered by centrifugation and diluted. A colorimeter is used to determine the absorbance of the final solution, which is correlated with the concentration of methylene blue prior to dilution. The change in the methylene blue solution concentration is the clays cation exchange capacity, where the results are reported in meq/100grams.

Sample: Pierre Shale

-Sample Weight $= 1$ gram

-Methylene Blue Concentration $= 0.01$ Molarity

-Volume of Methylene Blue $= 60$ milli-liter, contains 0.6 meq before mixing it with clays

-Volume of Supernatant sample $= 1$ milli-liter, then diluted to 200 ml.

-Absorbance after dilution $= 0.189$

-From the calibration curve:

- Absorbance = 33017 (Concentration) – 0.189

- Concentration of diluted solution of 200 ml $= \frac{0.189+0.0238}{33017} = 6.44324 * 10^{-6}$ mol/liter ,

- Number of moles in the diluted solution of 200 ml $= 6.44324 * 10^{-6} * 0.2 = 1.28865 * 10^{-6}$ moles

- Meq in the diluted solution $=$ Meq in the Supernatant sample $= 1.28865 * 10^{-6} * 1000 = 0.00128865$ meq

-Meq in Methylene blue solution (60ml) after mixing with clays = 0.00128865*60 = 0.077319 meq

$$\textbf{-}\boldsymbol{CEC} = (\mathbf{0.6 - 0.077319}) * \mathbf{100} = \mathbf{52.2}\ \boldsymbol{meq/100grams}$$

Sample: Illite

-Sample Weight = 1 gram

-Methylene Blue Concentration = 0.01 Molarity

-Volume of Methylene Blue = 60 milli-liter, contains 0.6 meq before mixing it with clays

-Volume of Supernatant sample = 1 milli-liter, then diluted to 200 ml.

-Absorbance after dilution = 0.298

-From the calibration curve:

- Absorbance = 33017 (Concentration) – 0.298

- Concentration of diluted solution of 200 ml = $\frac{0.298+0.0238}{33017} = 9.74397 * 10^{-6}$ mol/liter ,

- Number of moles in the diluted solution of 200 ml = $9.74397 * 10^{-6} * 0.2 = 1.94879 * 10^{-6}\ moles$

- Meq in the diluted solution = Meq in the Supernatant sample = $1.94879 * 10^{-6} * 1000 = 0.00194879\ meq$

-Meq in Methylene blue solution (60ml) after mixing with clays = 0.00194879*60 = 0.1169274 meq

-$CEC = (0.6 - 0.1169274) * 100 = 48.3\ meq/100grams$

Sample: A

-Sample Weight = 1 gram

-Methylene Blue Concentration = 0.01 Molarity

-Volume of Methylene Blue = 30 milli-liter, contains 0.3 meq before mixing it with clays

-Volume of Supernatant sample = 1 milli-liter, then diluted to 200 ml.

-Absorbance prior dilution = 0.241

-From the calibration curve:

- Absorbance = 33017 (Concentration) – 0.241

- Concentration of diluted solution of 200 ml = $\frac{0.241+0.0238}{33017} = 8.0179 * 10^{-6}$ mol/liter ,

- Number of moles in the diluted solution of 200 ml = $8.0179 * 10^{-6} * 0.2 = 1.60358 * 10^{-6}\ moles$

- Meq in the diluted solution = Meq in the Supernatant sample = $1.60358 * 10^{-6} * 1000 = 0.00160358\ meq$

-Meq in Methylene blue solution (30ml) after mixing with clays = 0.00160358 *30 = 0.0481074 meq

-$CEC = (0.3 - 0.0481074\ ) * 100 = 25.1\ meq/100grams$

Sample: B

-Sample Weight = 1 gram

-Methylene Blue Concentration = 0.01 Molarity

-Volume of Methylene Blue = 30 milli-liter, contains 0.3 meq before mixing it with clays

-Volume of Supernatant sample = 1 milli-liter, then diluted to 200 ml.

-Absorbance after dilution = 0.551

-**From the calibration curve:**

- Absorbance = 33017 (Concentration) – 0.241

- Concentration of diluted solution of 200 ml = $\frac{0.551+0.0238}{33017} = 1.74053 * 10^{-6}$ mol/liter ,

- Number of moles in the diluted solution of 200 ml = $1.74053 * 10^{-6} * 0.2 = 3.48106 * 10^{-6}\ moles$

- Meq in the diluted solution = Meq in the Supernatant sample = $3.48106 * 10^{-6} * 1000 = 0.00348106\ meq$

-Meq in Methylene blue solution (30ml) after mixing with clays =0.00348106 *30 = 0.1044318 meq

-$\boldsymbol{CEC = (0.3 - 0.1044318) * 100 = 19.5\ meq/100 grams}$

Sample: C

-Sample Weight = 1 gram

-Methylene Blue Concentration = 0.01 Molarity

-Volume of Methylene Blue = 30 milli-liter, contains 0.3 meq before mixing it with clays

-Volume of Supernatant sample = 1 milli-liter, then diluted to 200 ml.

-Absorbance after dilution = 0.629

-From the calibration curve:

- Absorbance = 33017 (Concentration) – 0.241

- Concentration of diluted solution of 200 ml = $\frac{0.629+0.0238}{33017} = 1.97673 * 10^{-5}$ mol/liter ,

- Number of moles in the diluted solution of 200 ml = $1.97673 * 10^{-5} * 0.2 = 3.395346 * 10^{-6}\ moles$

- Meq in the diluted solution = Meq in the Supernatant sample = $3.395346 * 10^{-6} * 1000 = 0.00395346\ meq$

-Meq in Methylene blue solution (30ml) after mixing with clays =0.00395346 *30 = 0.1186038 meq

-$\boldsymbol{CEC = (0.3 - 0.1186038) * 100 = 18.1\ meq/100 grams}$

Sample: D

-Higher sample weight is used due to the low CEC value

-Sample Weight = 4 grams

-Methylene Blue Concentration = 0.01 Molarity

-Volume of Methylene Blue = 30 milli-liter, contains 0.3 meq before mixing it with clays

-Volume of Supernatant sample = 1 milli-liter, then diluted to 200 ml.

-Absorbance after dilution = 0.285

-From the calibration curve:

- Absorbance = 33017 (Concentration) – 0.241

- Concentration of diluted solution of 200 ml = $\frac{0.285+0.0238}{33017} = 9.35030 * 10^{-6}$ mol/liter ,

- Number of moles in the diluted solution of 200 ml = $9.35030 * 10^{-6} * 0.2 = 1.870006 * 10^{-6}\ moles$

- Meq in the diluted solution = Meq in the Supernatant sample = $1.870006 * 10^{-6} * 1000 = 0.001870006\ meq$

-Meq in Methylene blue solution (30ml) after mixing with clays =0.001870006*30 = 0.05610018 meq

-$\boldsymbol{CEC = (0.3 - 0.05610018\ ) * \frac{100}{4} = 6.1\ meq/100 grams}$

Sample: E

-Sample Weight = 1 gram

-Methylene Blue Concentration = 0.01 Molarity

-Volume of Methylene Blue = 30 milli-liter, contains 0.3 meq before mixing it with clays

-Volume of Supernatant sample = 1 milli-liter, then diluted to 200 ml.

-Absorbance after dilution = 0.917

-**From the calibration curve:**

- Absorbance = 33017 (Concentration) – 0.241

- Concentration of diluted solution of 200 ml = $\frac{0.917+0.0238}{33017} = 2.84885 * 10^{-5}$ mol/liter ,

- Number of moles in the diluted solution of 200 ml = $2.84885 * 10^{-5} * 0.2 = 5.6977 * 10^{-6}\ moles$

- Meq in the diluted solution = Meq in the Supernatant sample = $5.6977 * 10^{-6} * 1000 = 0.0056977\ meq$

-Meq in Methylene blue solution (30ml) after mixing with clays =0.0056977 *30 = 0.170931 meq

5.3 Sample-B Reconsolidation

In this section, strain/log time plots are presented for Sample-B prepared at salinities of 35 KPPM, 100 KPPM, and 200 KPPM. Permeability is calculated from these plots as a function of vertical stress, and the relationship of permeability with the 50% consolidation point is described in section 3.2. The strain at 50% is the midpoint between the start of the stress step to 100% consolidation. The 100% consolidation is empirically obtained from the intersection of primary with secondary slopes.

5.3.1 Sample B-35

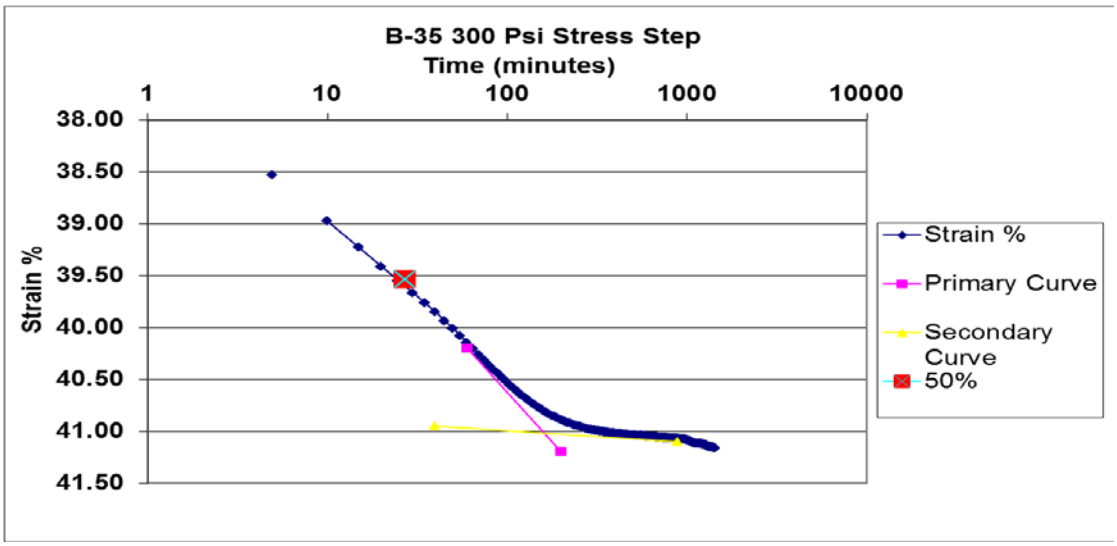

Figure 56 Strain versus the logarithm of time at a constant stress of 300 Psi.

Table 8 Time and strain at 100% and 50% consolidation at 300 Psi.

t_p=	160.44
ε_{100}=	41.017
ε_{50}=	39.534
t_{50}=	26.92

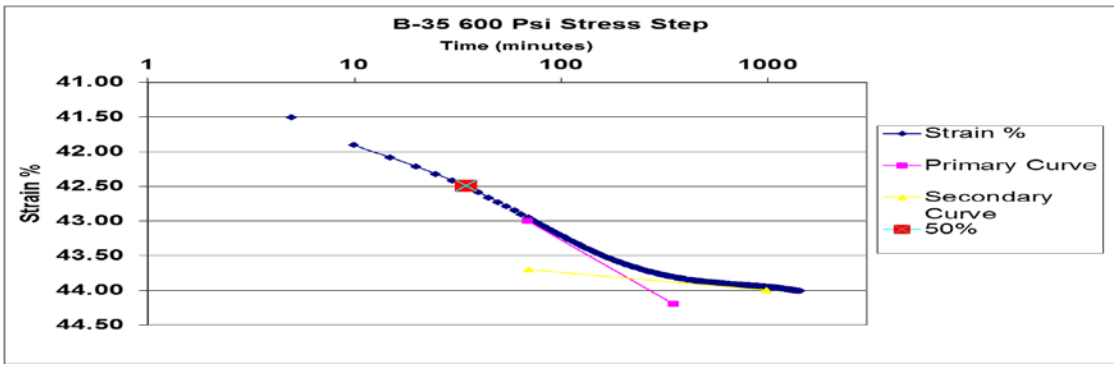

Figure 57 Strain versus the logarithm of time at a constant stress of 600 Psi.

Table 9 Time and strain at 100% and 50% consolidation at 600 Psi

$t_p =$	210.48
$\varepsilon_{100} =$	43.824
$\varepsilon_{50} =$	42.492
$t_{50} =$	34.72

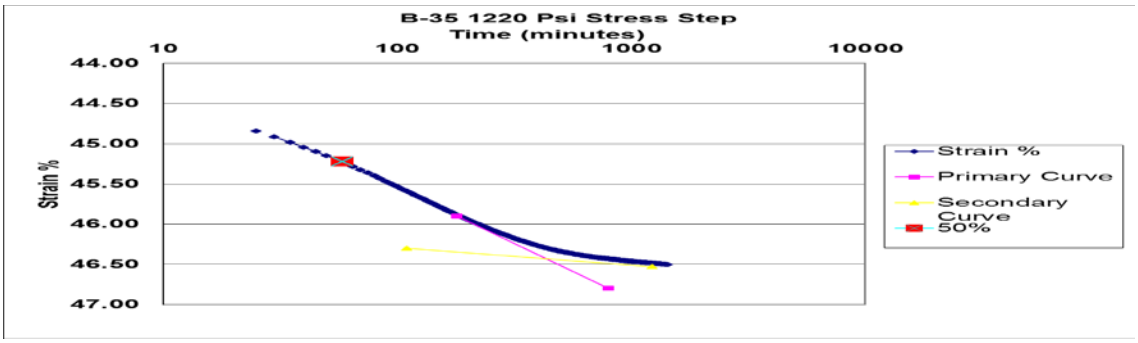

Figure 58 Strain versus the logarithm of time at a constant stress of 1220 Psi.

Table 10 Time and strain at 100% and 50% consolidation at 1220 Psi

$t_p =$	433.60
$\varepsilon_{100} =$	46.430
$\varepsilon_{50} =$	45.220
$t_{50} =$	58.30

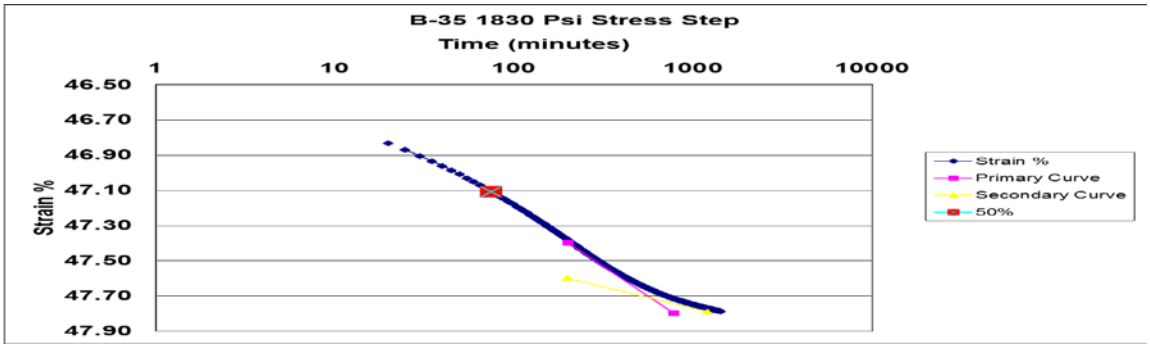

Figure 59 Strain versus the logarithm of time at a constant stress of 1830 Psi.

Table 11 Time and strain at 100% and 50% consolidation at 1830 Psi

$t_p =$	578.33
$\varepsilon_{100} =$	47.712
$\varepsilon_{50} =$	47.108
$t_{50} =$	74.13

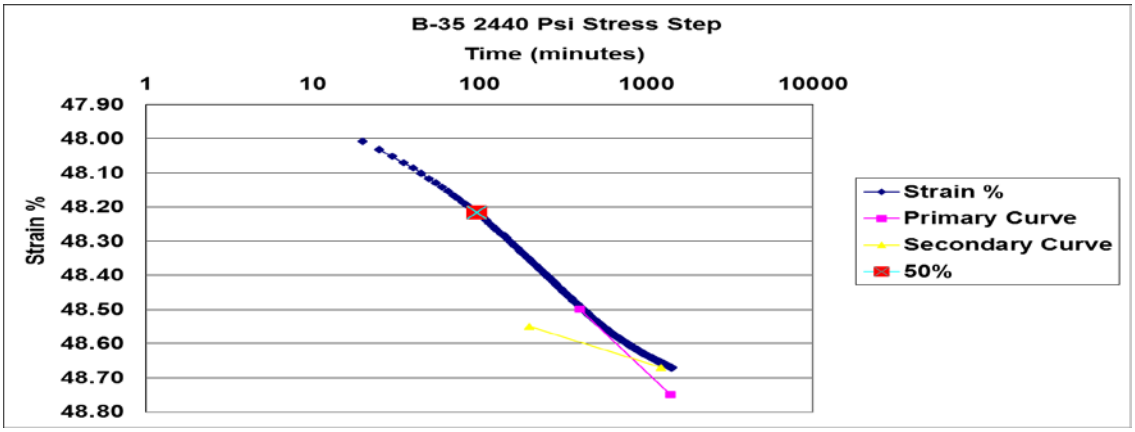

Figure 60 Strain versus the logarithm of time at a constant stress of 2440 Psi

Table 12 Time and strain at 100% and 50% consolidation at 2440 Psi

$t_p =$	818.50
$\varepsilon_{100} =$	48.643
$\varepsilon_{50} =$	48.216
$t_{50} =$	96.38

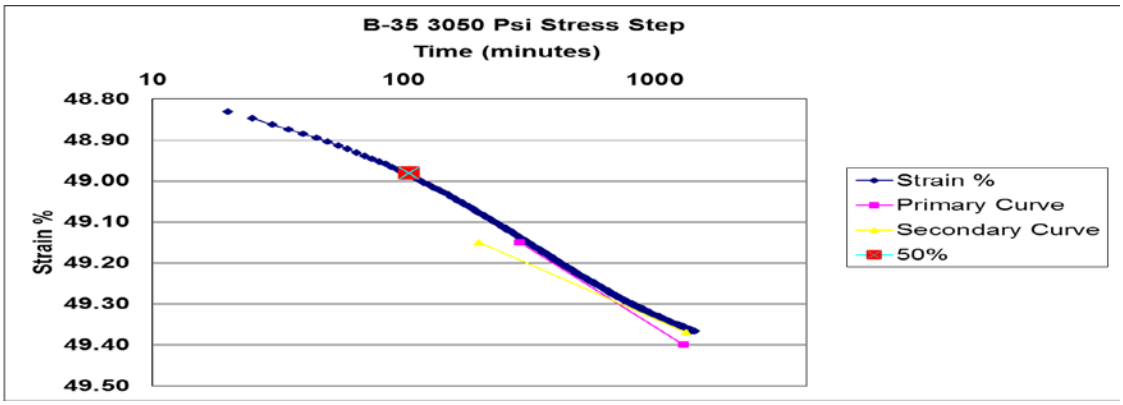

Figure 61 Strain versus the logarithm of time at a constant stress of 3050 Psi.

Table 13 Time and strain at 100% and 50% consolidation at 3050 Psi

$t_p =$	677.45
$\varepsilon_{100} =$	49.291
$\varepsilon_{50} =$	48.982
$t_{50} =$	105.52

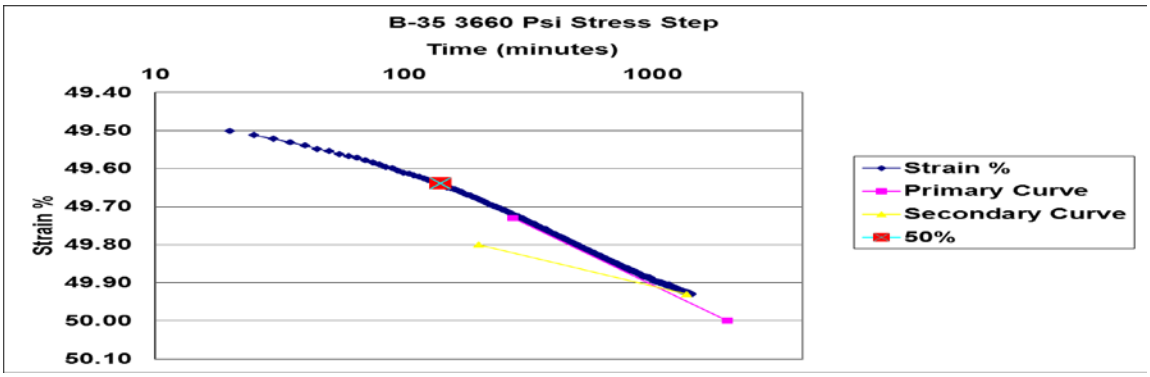

Figure 62 Strain versus the logarithm of time at a constant stress of 3660 Psi.

Table 14 Time and strain at 100% and 50% consolidation at 3660 Psi

$t_p =$	1042.38
$\varepsilon_{100} =$	49.911
$\varepsilon_{50} =$	49.639
$t_{50} =$	141.18

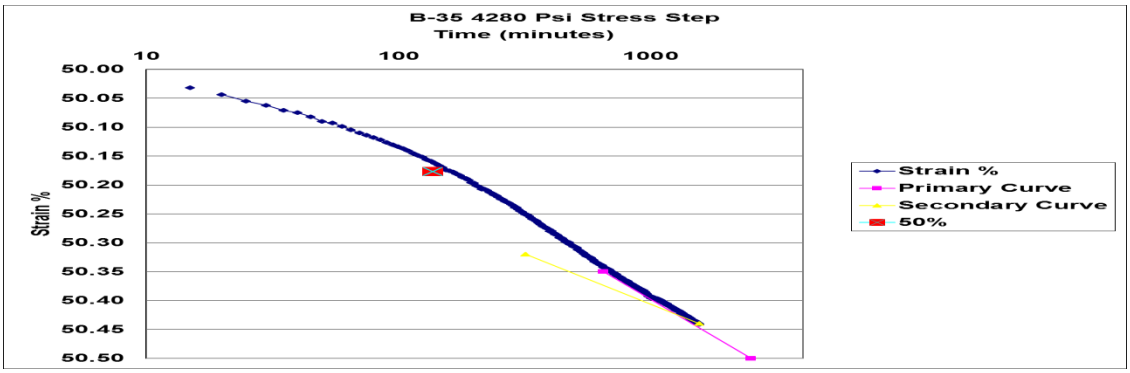

Figure 63 Strain versus the logarithm of time at a constant stress of 4280 Psi.

Table 15 Time and strain at 100% and 50% consolidation at 4280 Psi

$t_p =$	1264.17
$\varepsilon_{100} =$	50.424
$\varepsilon_{50} =$	50.177
$t_{50} =$	137.11

5.3.2 Sample B-100

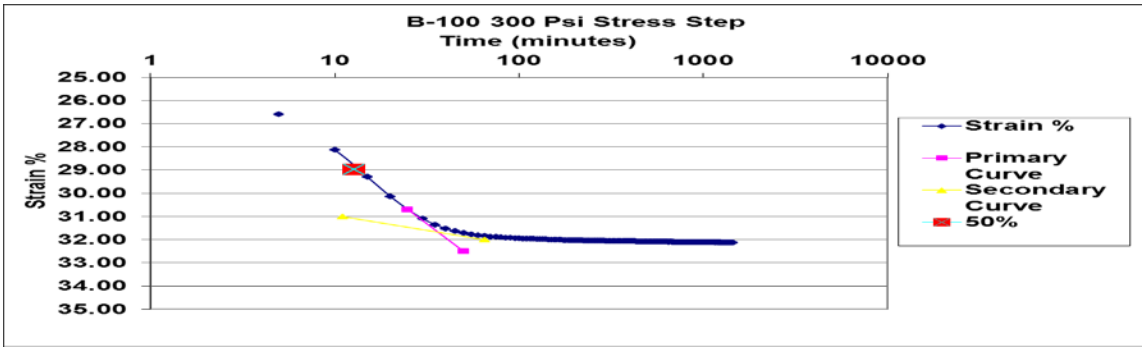

Figure 64 Strain versus the logarithm of time at a constant stress of 300 Psi.

Table 16 Time and strain at 100% and 50% consolidation at 300 Psi

$t_p =$	36.36
$\varepsilon_{100} =$	31.673
$\varepsilon_{50} =$	28.968
$t_{50} =$	12.83

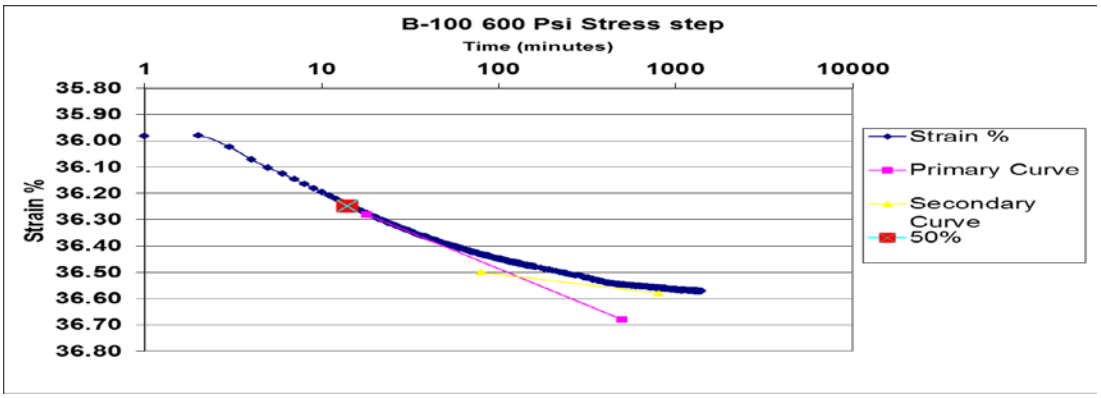

Figure 65 Strain versus the logarithm of time at a constant stress of 600 Psi.

Table 17 Time and strain at 100% and 50% consolidation at 600 Psi

$t_p =$	128.43
$\varepsilon_{100} =$	36.516
$\varepsilon_{50} =$	36.249
$t_{50} =$	13.96

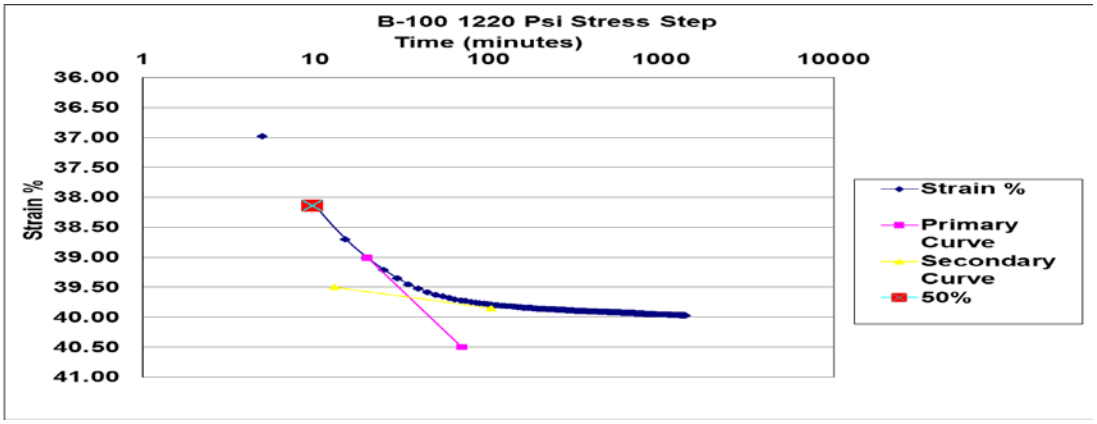

Figure 66 Strain versus the logarithm of time at a constant stress of 1220 Psi.

Table 18 Time and strain at 100% and 50% consolidation at 1220 Psi

$t_p =$	34.67
$\varepsilon_{100} =$	39.664
$\varepsilon_{50} =$	38.138
$t_{50} =$	9.61

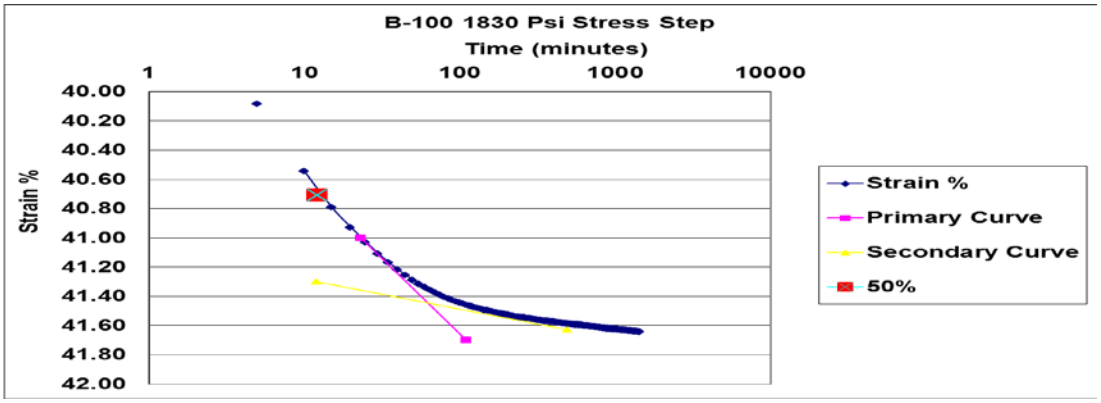

Figure 67 Strain versus the logarithm of time at a constant stress of 1830 Psi.

Table 19 Time and strain at 100% and 50% consolidation at 1830 Psi

$t_p =$	62.30
$\varepsilon_{100} =$	41.446
$\varepsilon_{50} =$	40.709
$t_{50} =$	12.00

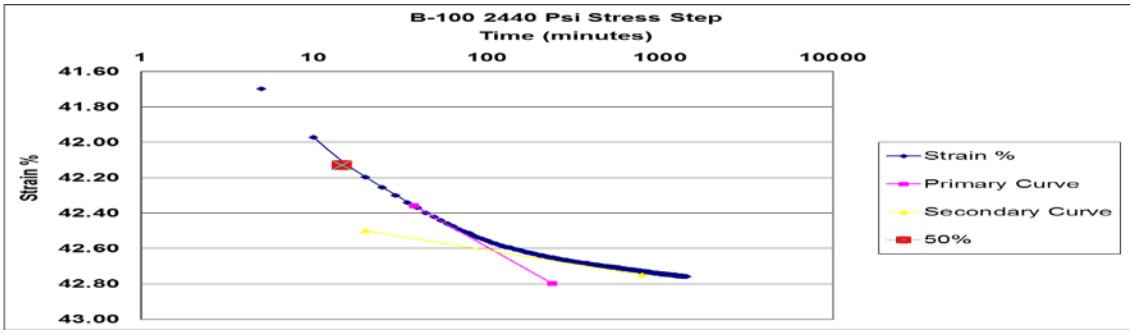

Figure 68 Strain versus the logarithm of time at a constant stress of 2440 Psi.

Table 20 Time and strain at 100% and 50% consolidation at 2440 Psi

$t_p =$	111.15
$\varepsilon_{100} =$	42.616
$\varepsilon_{50} =$	42.129
$t_{50} =$	14.45

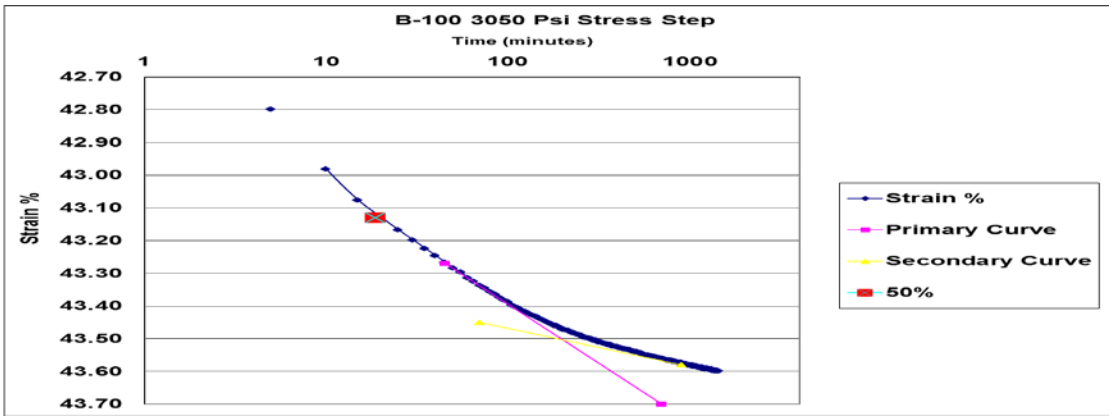

Figure 69 Strain versus the logarithm of time at a constant stress of 3050 Psi.

Table 21 Time and strain at 100% and 50% consolidation at 3050 Psi

$t_p =$	199.48
$\varepsilon_{100} =$	43.503
$\varepsilon_{50} =$	43.131
$t_{50} =$	18.53

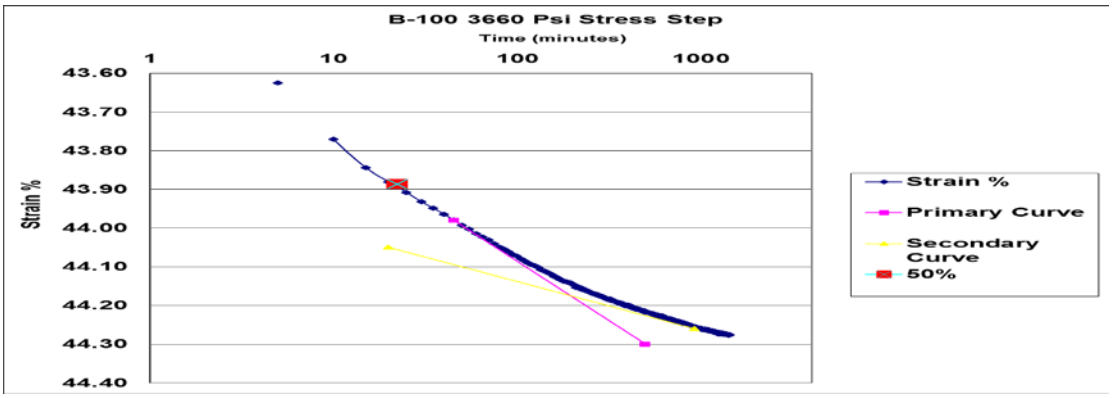

Figure 70 Strain versus the logarithm of time at a constant stress of 3660 Psi.

Table 22 Time and strain at 100% and 50% consolidation at 3660 Psi

$t_p =$	194.66
$\varepsilon_{100} =$	44.175
$\varepsilon_{50} =$	43.887
$t_{50} =$	22.30

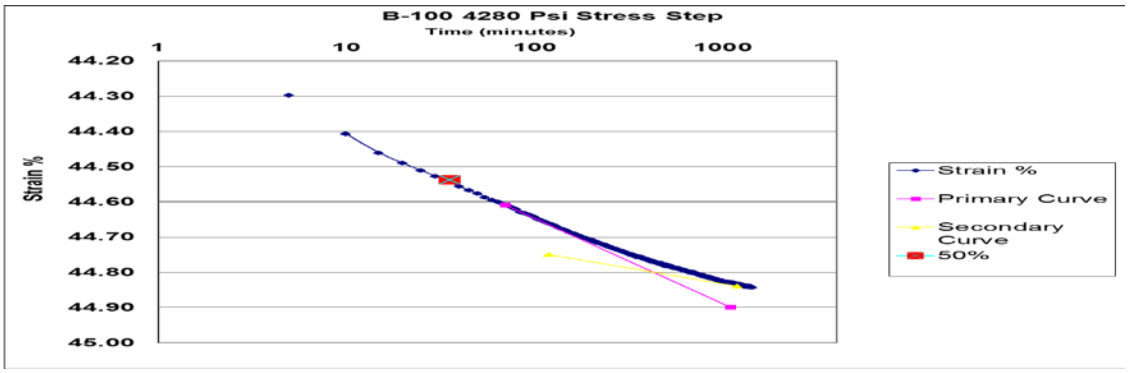

Figure 71 Strain versus the logarithm of time at a constant stress of 4280 Psi.

Table 23 Time and strain at 100% and 50% consolidation at 4280 Psi

$t_p =$	422.10
$\varepsilon_{100} =$	44.799
$\varepsilon_{50} =$	44.538
$t_{50} =$	35.34

5.3.3 Sample B-200

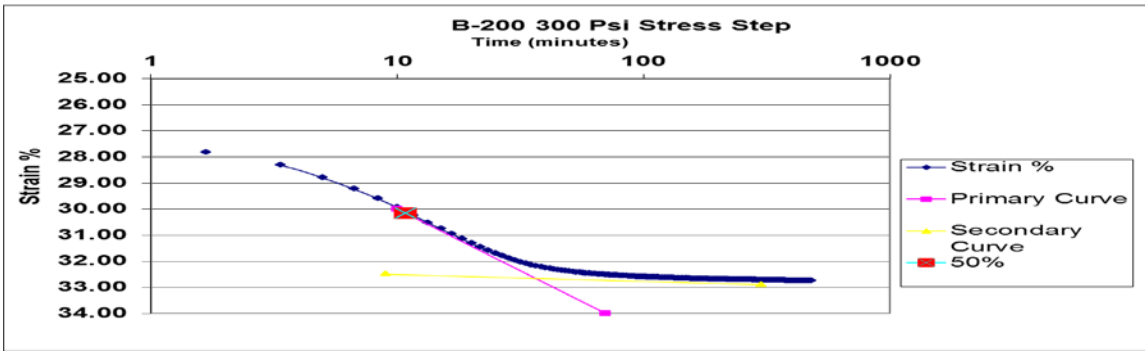

Figure 72 Strain versus the logarithm of time at a constant stress of 300 Psi.

Table 24 Time and strain at 100% and 50% consolidation at 300 Psi

$t_p =$	36.47
$\varepsilon_{100} =$	32.660
$\varepsilon_{50} =$	30.170
$t_{50} =$	10.86

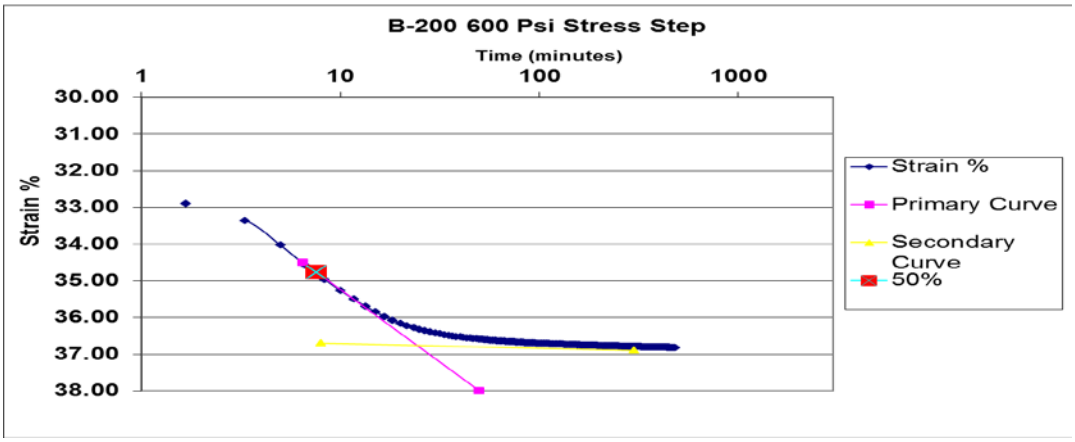

Figure 73 Strain versus the logarithm of time at a constant stress of 600 Psi.

Table 25 Time and strain at 100% and 50% consolidation at 600 Psi

$t_p =$	24.29
$\varepsilon_{100} =$	36.761
$\varepsilon_{50} =$	34.773
$t_{50} =$	7.62

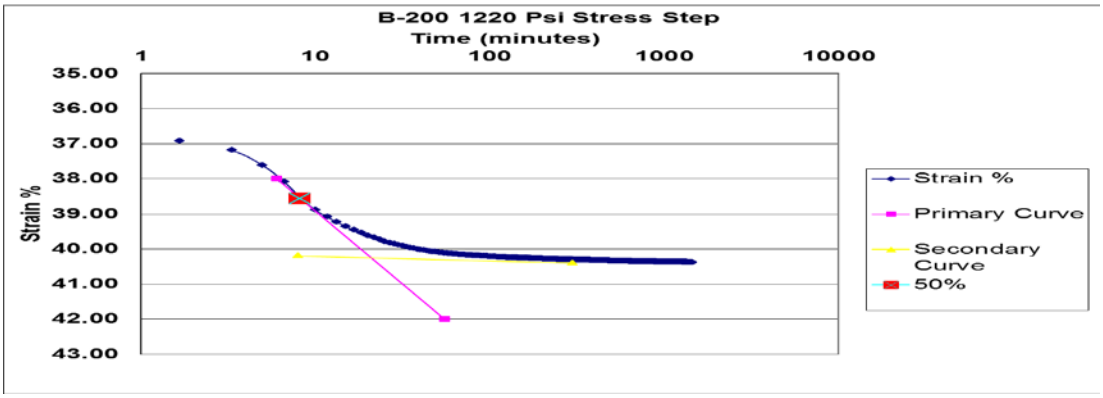

Figure 74 Strain versus the logarithm of time at a constant stress of 1220 Psi.

Table 26 Time and strain at 100% and 50% consolidation at 1220 Psi

$t_p =$	20.90
$\varepsilon_{100} =$	40.253
$\varepsilon_{50} =$	38.558
$t_{50} =$	8.17

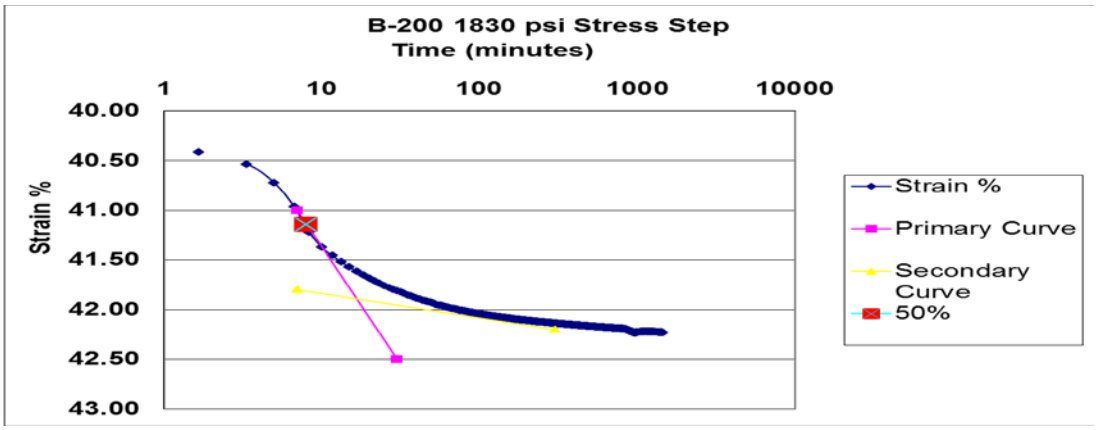

Figure 75 Strain versus the logarithm of time at a constant stress of 1830 Psi.

Table 27 Time and strain at 100% and 50% consolidation at 1830 Psi

$t_p =$	16.63
$\varepsilon_{100} =$	41.892
$\varepsilon_{50} =$	41.140
$t_{50} =$	8.02

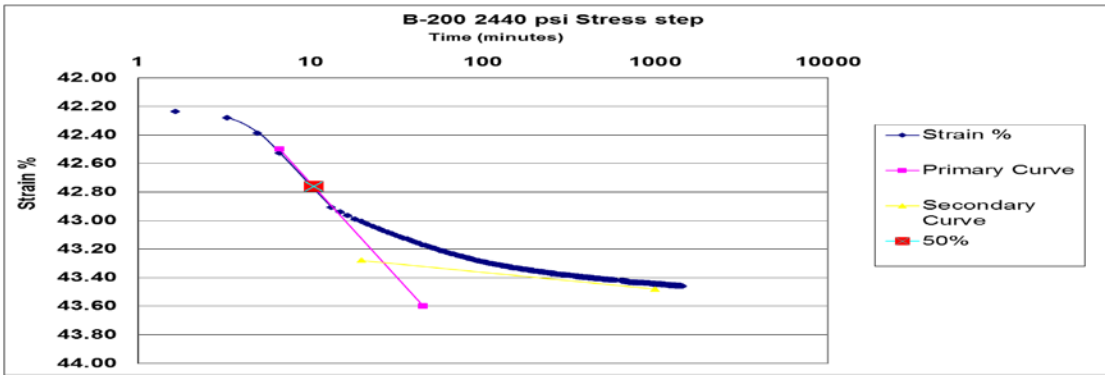

Figure 76 Strain versus the logarithm of time at a constant stress of 2440 Psi.

Table 28 Time and strain at 100% and 50% consolidation at 2440 Psi

$t_p =$	26.39
$\varepsilon_{100} =$	43.294
$\varepsilon_{50} =$	42.762
$t_{50} =$	10.43

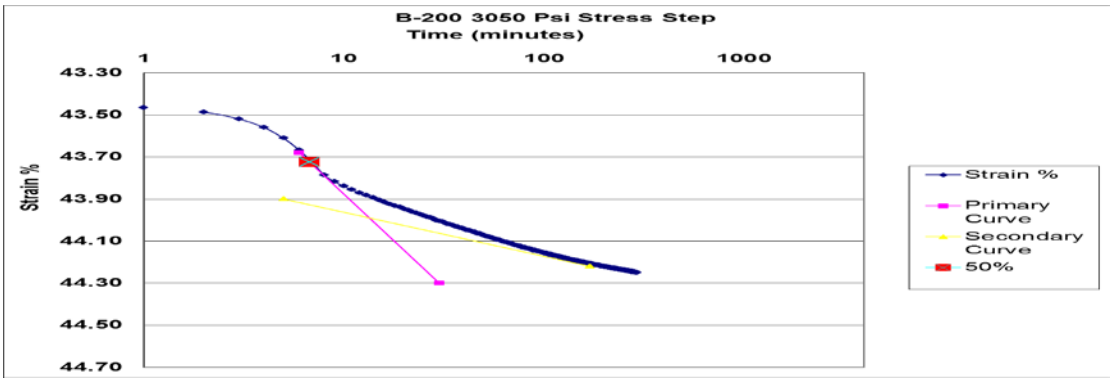

Figure 77 Strain versus the logarithm of time at a constant stress of 3050 Psi.

Table 29 Time and strain at 100% and 50% consolidation at 3050 Psi

$t_p =$	13.40
$\varepsilon_{100} =$	43.989
$\varepsilon_{50} =$	43.725
$t_{50} =$	6.74

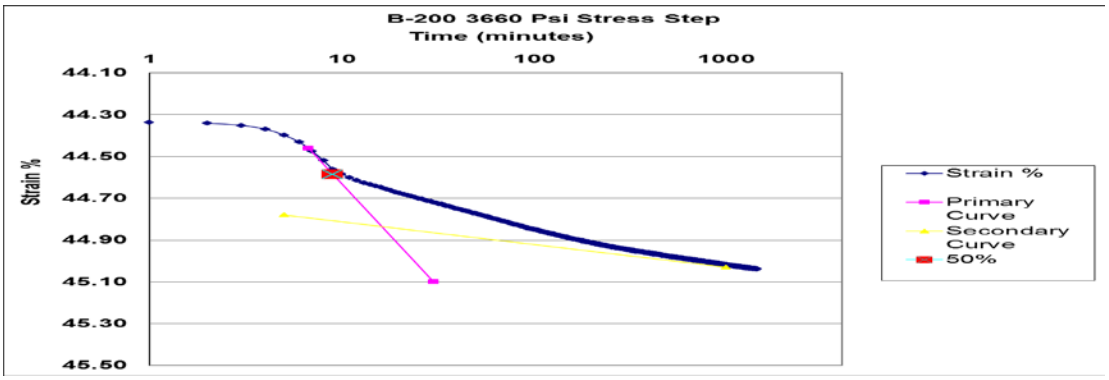

Figure 78 Strain versus the logarithm of time at a constant stress of 3660 Psi.

Table 30 Time and strain at 100% and 50% consolidation at 3660 Psi

$t_p =$	16.14
$\varepsilon_{100} =$	44.835
$\varepsilon_{50} =$	44.586
$t_{50} =$	9.00

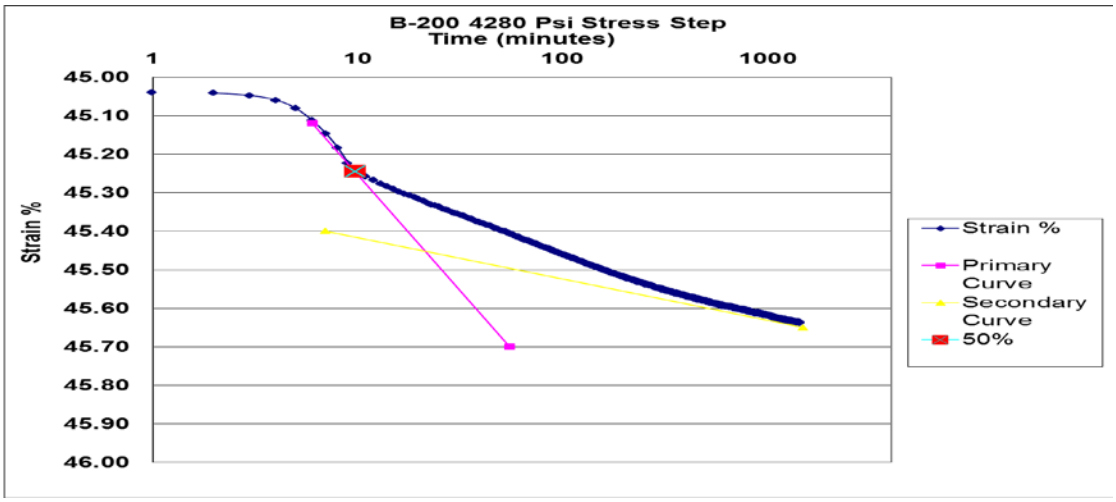

Figure 79 Strain versus the logarithm of time at a constant stress of 4280 Psi.

Table 31 Time and strain at 100% and 50% consolidation at 4280 Psi

$t_p =$	21.32
$\varepsilon_{100} =$	45.452
$\varepsilon_{50} =$	45.246
$t_{50} =$	9.69

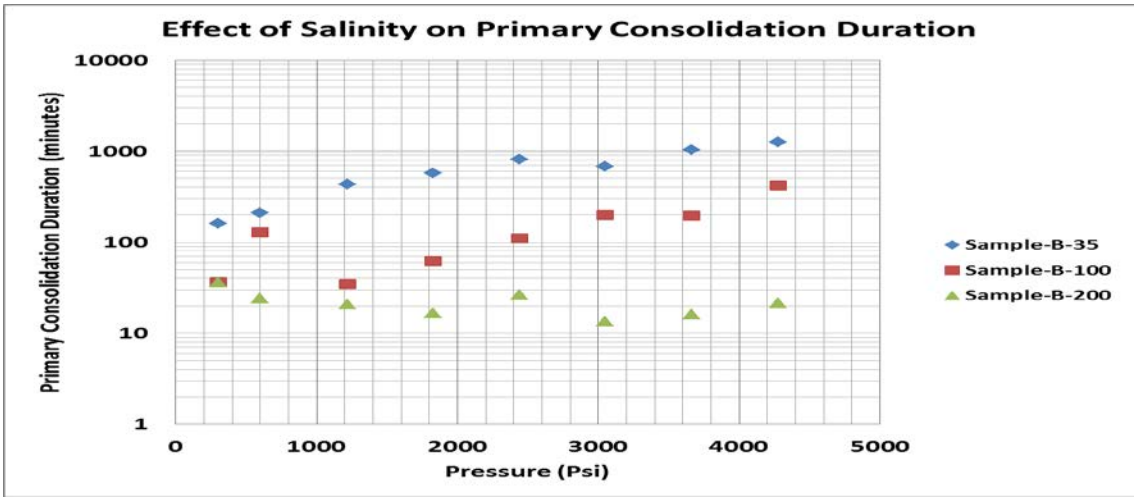

Figure 80 A relationship of salinity with the duration of the primary consolidation time, it shows that the higher the salinity the shorter the primary consolidation duration.

5.4 Pierre Shale Reconsolidation

In this section, strain/log time plots are presented for Pierre shale prepared at salinities of 35 KPPM, 100 KPPM, and 200 KPPM. Permeability is calculated from these plots as a function of vertical stress, and the relationship of permeability with the 50% consolidation point is described in section 3.2. The strain at 50% is the midpoint between the start of the stress step to 100% consolidation. The 100% consolidation is empirically obtained from the intersection of primary with secondary slopes.

5.4.1 Pierre Shale-35

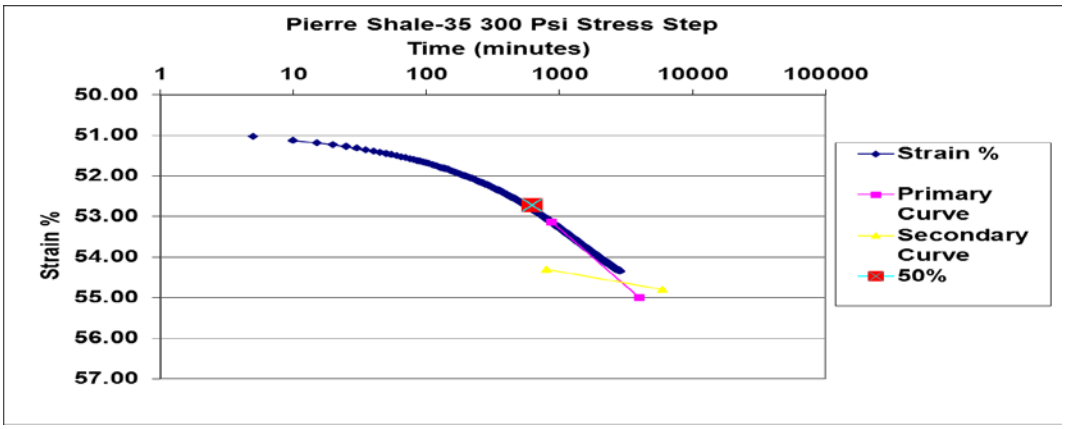

Figure 81 Strain versus the logarithm of time at a constant stress of 300 Psi, the 100% consolidation point is estimated.

Table 32 Time and strain at 100% and 50% consolidation at 300 Psi

t_p=	2941.71
ε_{100}=	54.623
ε_{50}=	52.721
t_{50}=	624.00

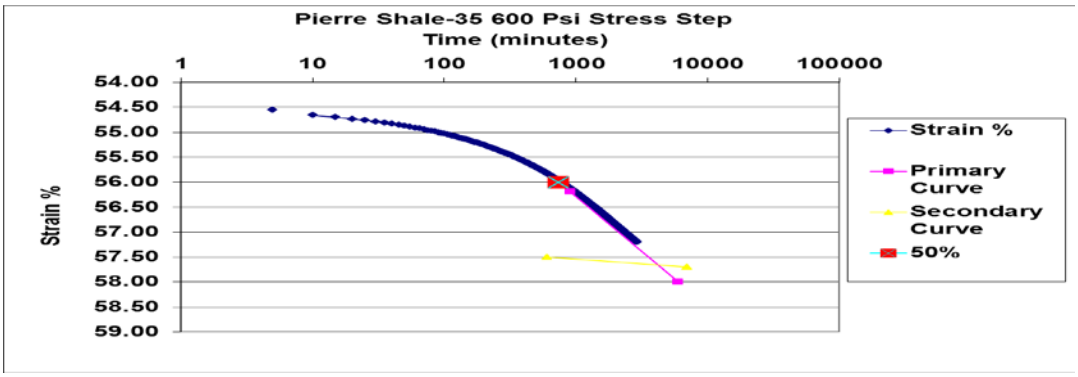

Figure 82 Strain versus the logarithm of time at a constant stress of 600 Psi, the 100% consolidation point is estimated.

Table 33 Time and strain at 100% and 50% consolidation at 600 Psi

$t_p =$	4193.80
$\varepsilon_{100} =$	57.658
$\varepsilon_{50} =$	56.007
$t_{50} =$	742.75

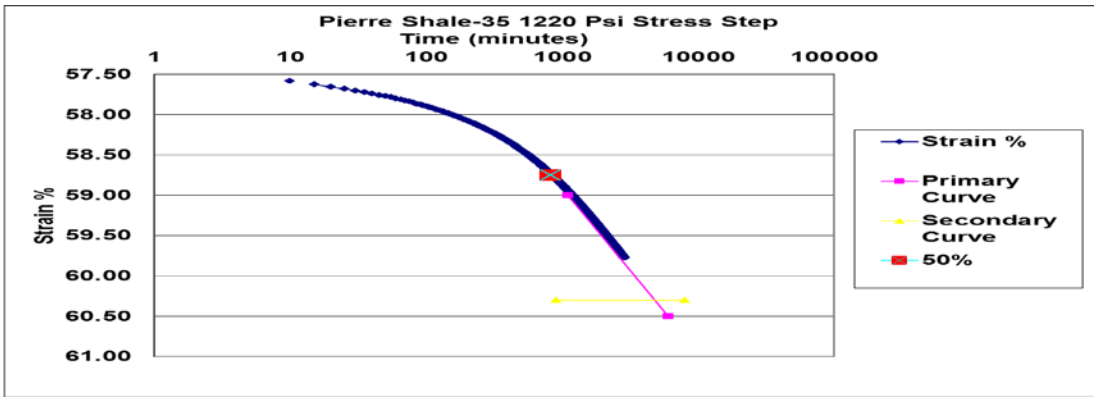

Figure 83 Strain versus the logarithm of time at a constant stress of 1220 Psi, the 100% consolidation point is estimated.

Table 34 Time and strain at 100% and 50% consolidation at 1220 Psi

$t_p =$	4785.38
$\varepsilon_{100} =$	60.300
$\varepsilon_{50} =$	58.748
$t_{50} =$	826.84

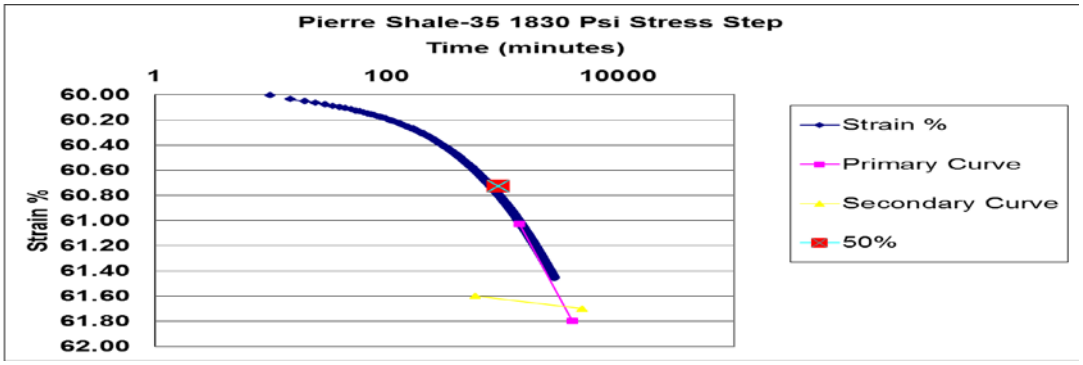

Figure 84 Strain versus the logarithm of time at a constant stress of 1830 Psi, the 100% consolidation point is estimated.

Table 35 Time and strain at 100% and 50% consolidation at 1830 Psi

$t_p =$	3405.01
$\varepsilon_{100} =$	61.682
$\varepsilon_{50} =$	60.729
$t_{50} =$	928.16

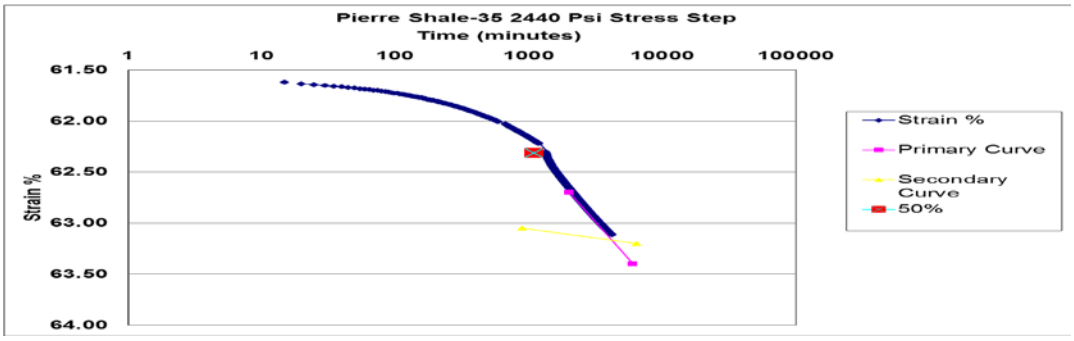

Figure 85 Strain versus the logarithm of time at a constant stress of 2440 Psi, the 100% consolidation point is estimated, the anomaly in data is because of pressure fluctation at this step.

Table 36 Time and strain at 100% and 50% consolidation at 2440 Psi

$t_p =$	4156.30
$\varepsilon_{100} =$	63.166
$\varepsilon_{50} =$	62.312
$t_{50} =$	1088.21

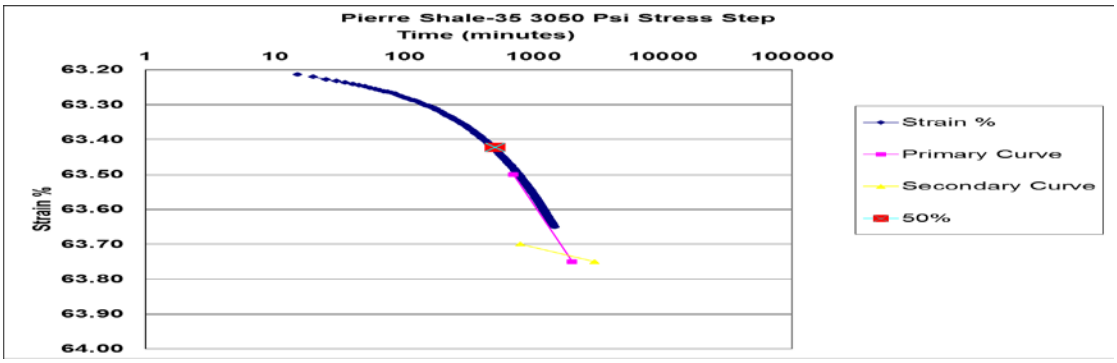

Figure 86 Strain versus the logarithm of time at a constant stress of 3050 Psi, the 100% consolidation point is estimated.

Table 37 Time and strain at 100% and 50% consolidation at 3050 Psi

$t_p =$	1852.57
$\varepsilon_{100} =$	63.732
$\varepsilon_{50} =$	63.422
$t_{50} =$	505.22

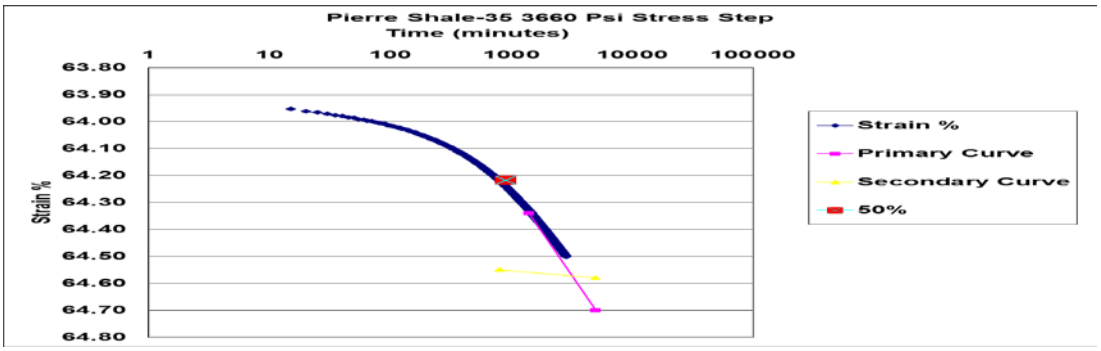

Figure 87 Strain versus the logarithm of time at a constant stress of 3660 Psi, the 100% consolidation point is estimated.

Table 38 Time and strain at 100% and 50% consolidation at 3660 Psi

$t_p =$	3186.89
$\varepsilon_{100} =$	64.573
$\varepsilon_{50} =$	64.218
$t_{50} =$	908.60

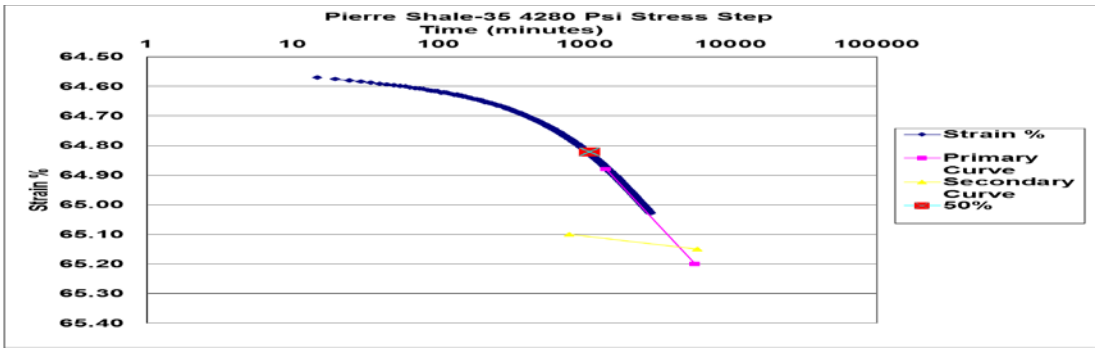

Figure 88 Strain versus the logarithm of time at a constant stress of 4280 Psi, the 100% consolidation point is estimated.

Table 39 Time and strain at 100% and 50% consolidation at 4280 Psi

$t_p =$	4428.33
$\varepsilon_{100} =$	65.142
$\varepsilon_{50} =$	64.822
$t_{50} =$	1084.67

5.4.2 Pierre Shale-100

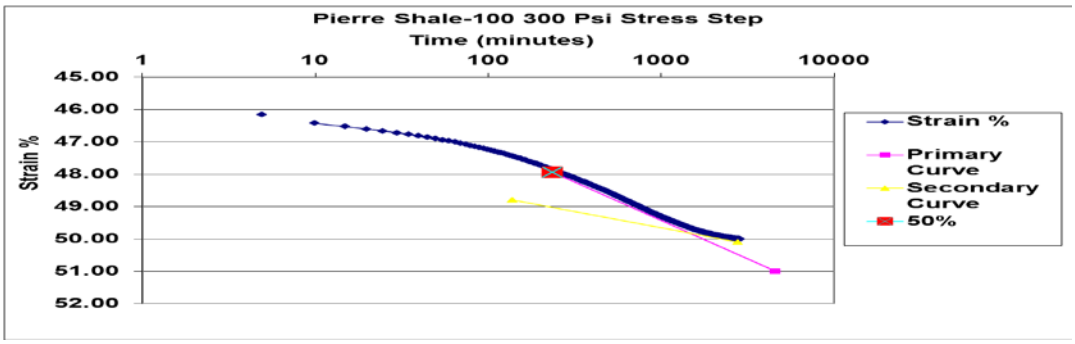

Figure 89 Strain versus the logarithm of time at a constant stress of 300 Psi

Table 40 Time and strain at 100% and 50% consolidation at 300 Psi

$t_p =$	1458.96
$\varepsilon_{100} =$	49.817
$\varepsilon_{50} =$	47.938
$t_{50} =$	235.36

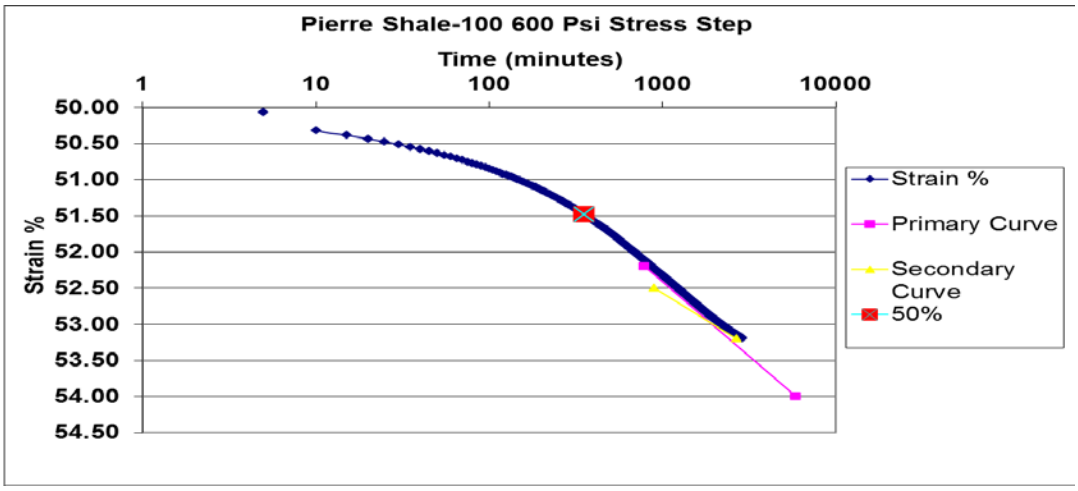

Figure 90 Strain versus the logarithm of time at a constant stress of 600 Psi.

Table 41 Time and strain at 100% and 50% consolidation at 600 Psi

$t_p =$	1865.32
$\varepsilon_{100} =$	52.969
$\varepsilon_{50} =$	51.484
$t_{50} =$	355.02

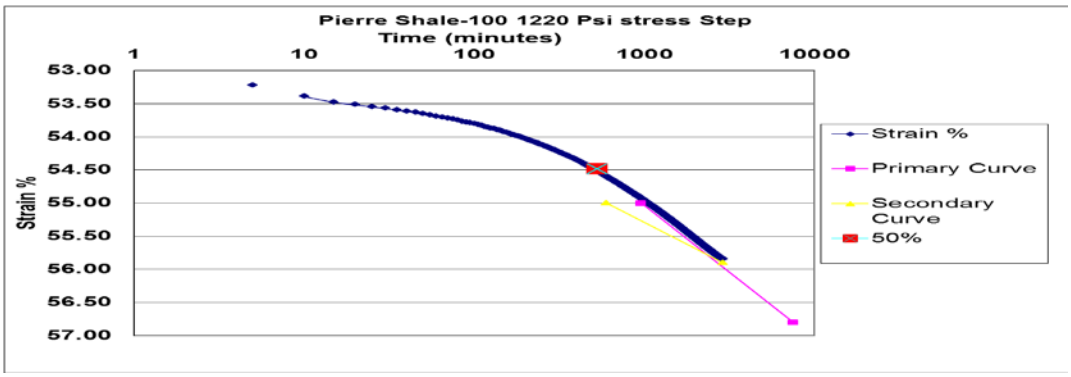

Figure 91 Strain versus the logarithm of time at a constant stress of 1220 Psi.

Table 42 Time and strain at 100% and 50% consolidation at 1220 Psi

$t_p =$	2319.31
$\varepsilon_{100} =$	55.772
$\varepsilon_{50} =$	54.482
$t_{50} =$	531.40

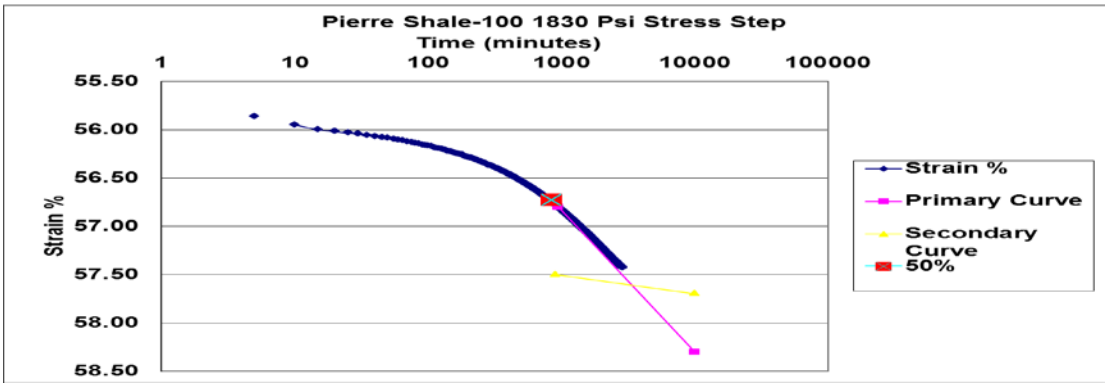

Figure 92 Strain versus the logarithm of time at a constant stress of 1830 Psi, the 100% consolidation point is estimated.

Table 43 Time and strain at 100% and 50% consolidation at 1830 Psi

$t_p =$	3386.92
$\varepsilon_{100} =$	57.610
$\varepsilon_{50} =$	56.729
$t_{50} =$	849.85

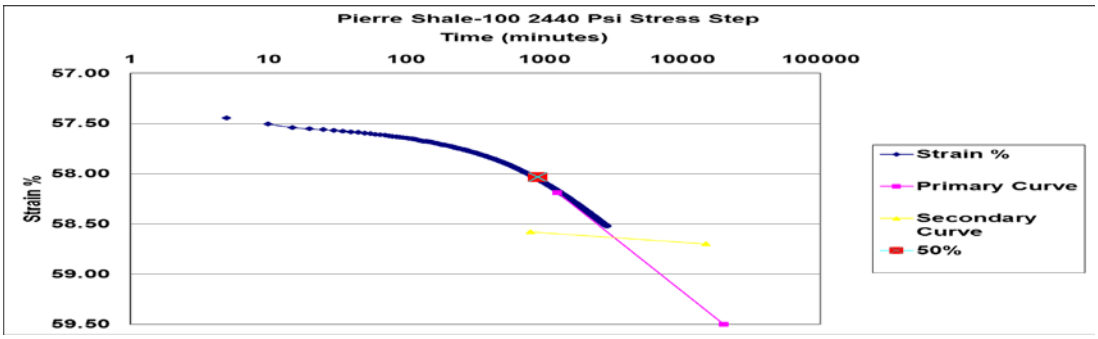

Figure 93 Strain versus the logarithm of time at a constant stress of 2440 Psi, the 100% consolidation point is estimated.

Table 44 Time and strain at 100% and 50% consolidation at 2440 Psi

$t_p =$	3219.46
$\varepsilon_{100} =$	58.637
$\varepsilon_{50} =$	58.035
$t_{50} =$	900.41

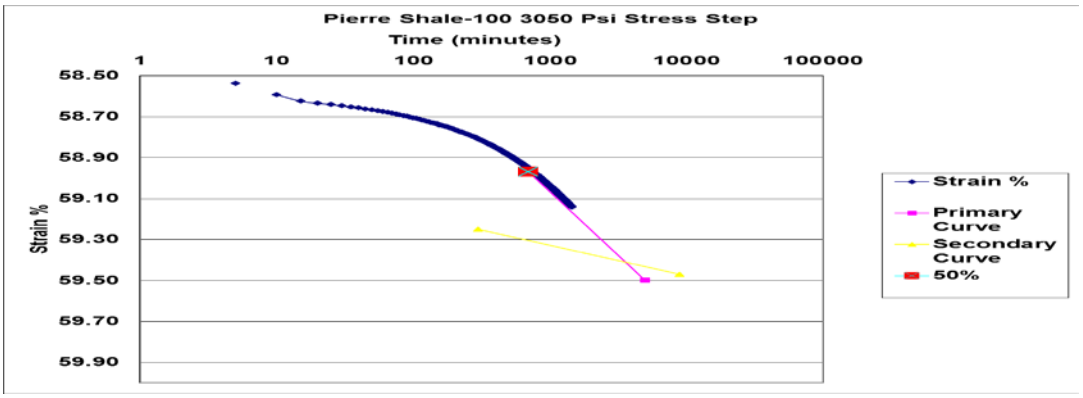

Figure 94 Strain versus the logarithm of time at a constant stress of 3050 Psi, the 100% consolidation point is estimated.

Table 45 Time and strain at 100% and 50% consolidation at 30 50 Psi

$t_p =$	3587.47
$\varepsilon_{100} =$	59.411
$\varepsilon_{50} =$	58.968
$t_{50} =$	694.82

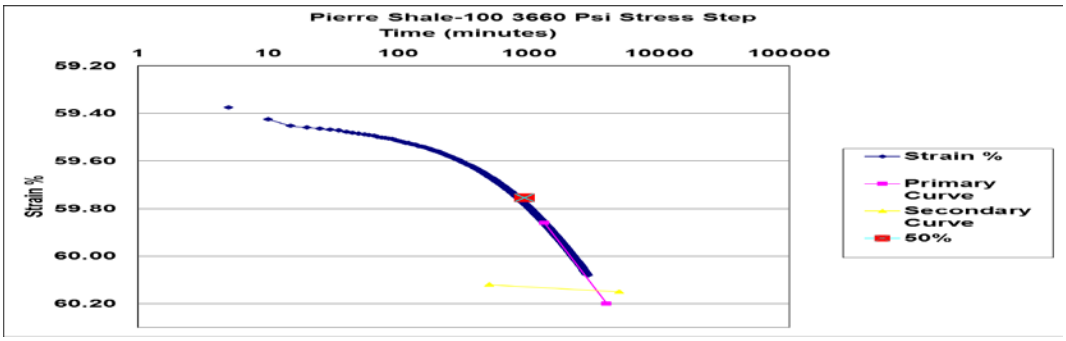

Figure 95 Strain versus the logarithm of time at a constant stress of 3660 Psi, the 100% consolidation point is estimated.

Table 46 Time and strain at 100% and 50% consolidation at 3660 Psi

$t_p =$	3342.65
$\varepsilon_{100} =$	60.145
$\varepsilon_{50} =$	59.755
$t_{50} =$	942.32

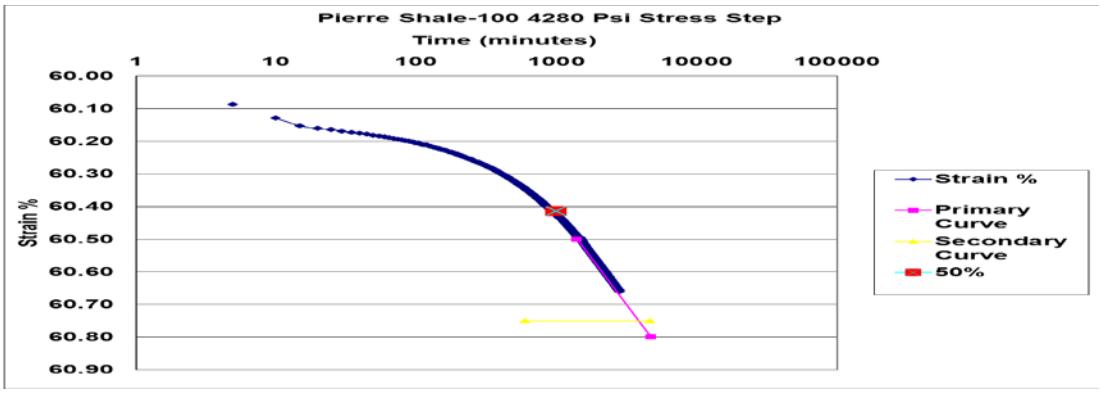

Figure 96 Strain versus the logarithm of time at a constant stress of 4280 Psi, the 100% consolidation point is estimated.

Table 47 Time and strain at 100% and 50% consolidation at 4280 Psi

$t_p =$	3840.93
$\varepsilon_{100} =$	60.750
$\varepsilon_{50} =$	60.415
$t_{50} =$	991.41

5.4.3 Pierre Shale-200

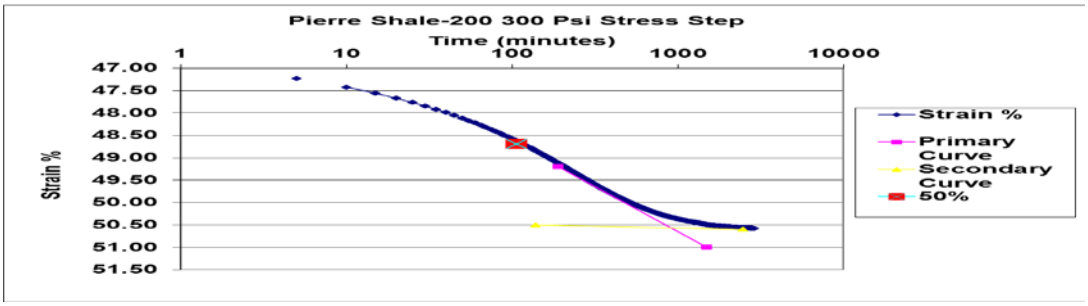

Figure 97 Strain versus the logarithm of time at a constant stress of 300 Psi.

Table 48 Time and strain at 100% and 50% consolidation at 300 Psi

$t_p =$	910.36
$\varepsilon_{100} =$	50.565
$\varepsilon_{50} =$	48.700

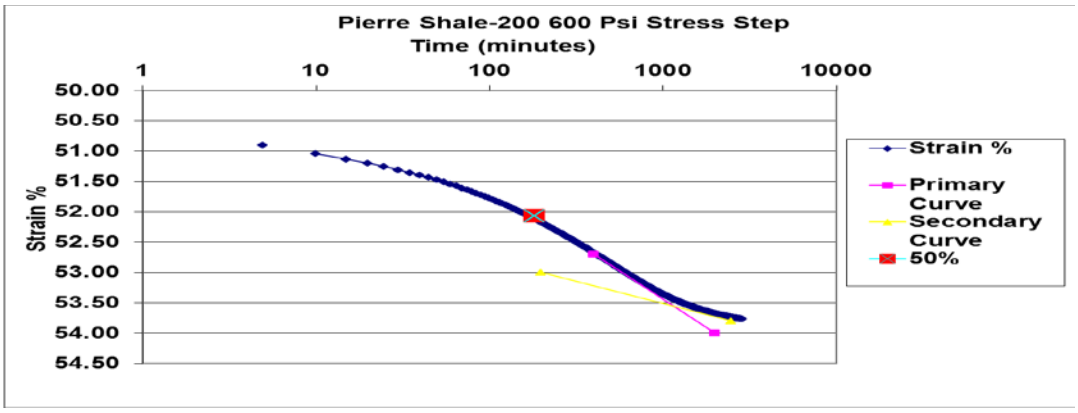

Figure 98 Strain versus the logarithm of time at a constant stress of 600 Psi.

Table 49 Time and strain at 100% and 50% consolidation at 600 Psi

$t_p =$	1152.42
$\varepsilon_{100} =$	53.555
$\varepsilon_{50} =$	52.065
$t_{50} =$	182.31

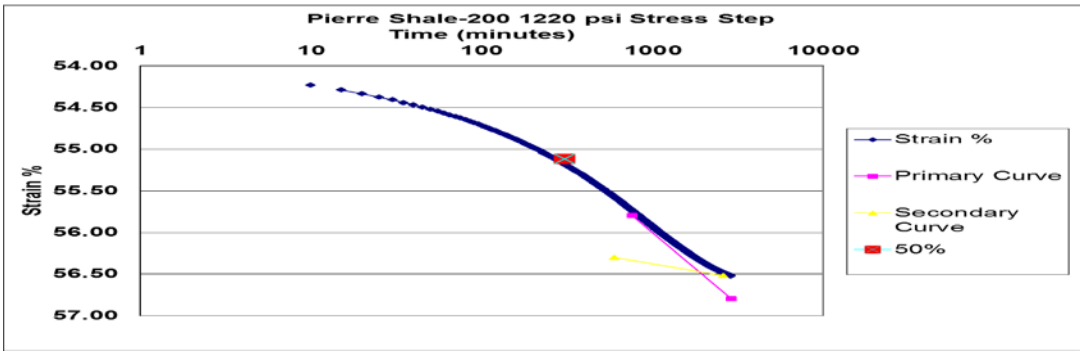

Figure 99 Strain versus the logarithm of time at a constant stress of 1220 Psi.

Table 50 Time and strain at 100% and 50% consolidation.

$t_p =$	1864.38
$\varepsilon_{100} =$	56.470
$\varepsilon_{50} =$	55.118
$t_{50} =$	304.87

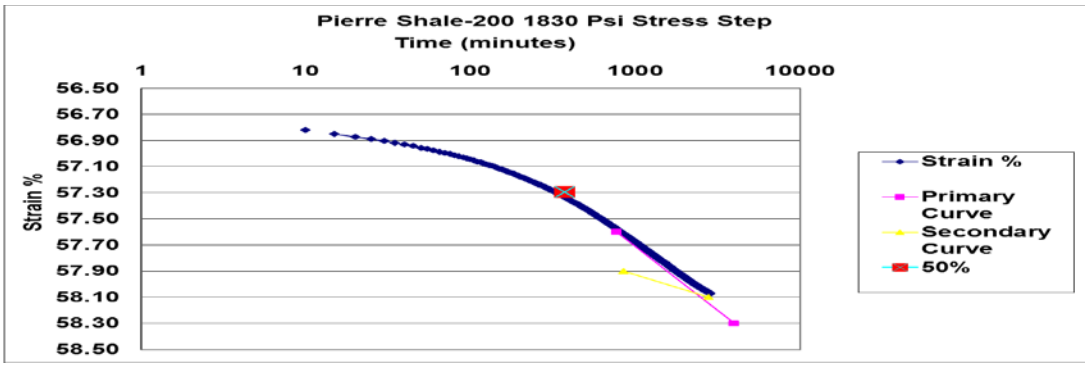

Figure 100 Strain versus the logarithm of time at a constant stress of 1830 Psi, the 100% consolidation point is estimated.

Table 51 Time and strain at 100% and 50% consolidation at 1830 Psi

$t_p =$	2318.88
$\varepsilon_{100} =$	58.068
$\varepsilon_{50} =$	57.295
$t_{50} =$	375.90

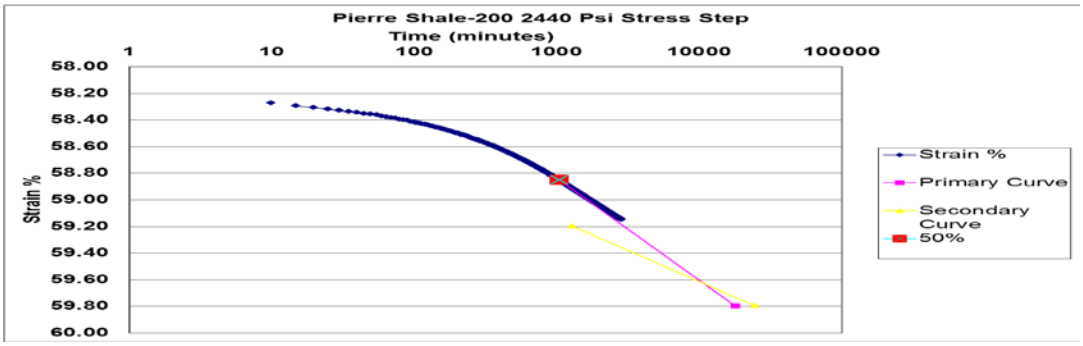

Figure 101 Strain versus the logarithm of time at a constant stress of 2440 Psi, the 100% consolidation point is estimated.

Table 52 Time and strain at 100% and 50% consolidation at 2440 Psi

$t_p =$	10769.40
$\varepsilon_{100} =$	59.629
$\varepsilon_{50} =$	58.852
$t_{50} =$	1041.59

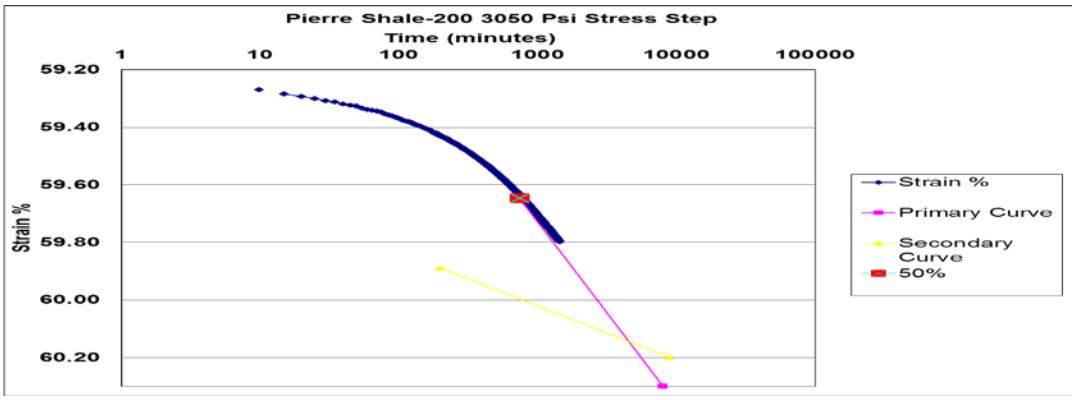

Figure 102 Strain versus the logarithm of time at a constant stress of 3050 Psi, the 100% consolidation point is estimated.

Table 53 Time and strain at 100% and 50% consolidation at 3050 Psi

$t_p =$	4529.43
$\varepsilon_{100} =$	60.144
$\varepsilon_{50} =$	59.647
$t_{50} =$	739.96

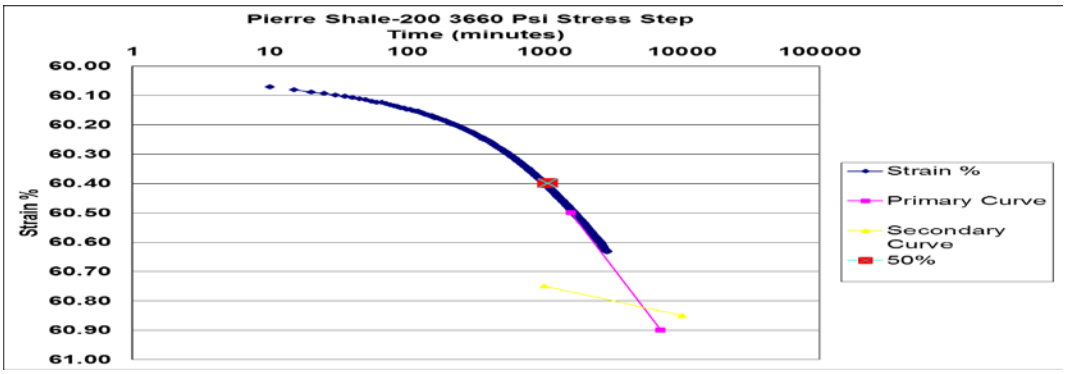

Figure 103 Strain versus the logarithm of time at a constant stress of 3660 Psi, the 100% consolidation point is estimated.

Table 54 Time and strain at 100% and 50% consolidation at 3660 Psi

$t_p =$	5210.91
$\varepsilon_{100} =$	60.822
$\varepsilon_{50} =$	60.400
$t_{50} =$	1061.96

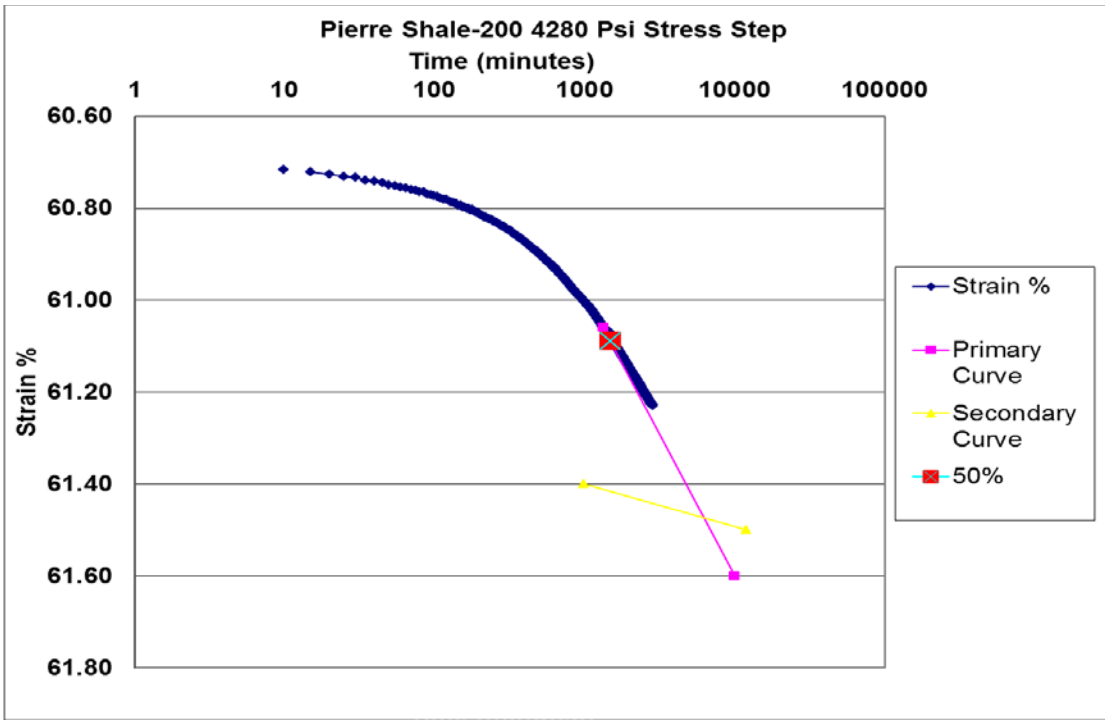

Figure 104 Strain versus the logarithm of time at a constant stress of 4280 Psi, the 100% consolidation point is estimated.

Table 55 Time and strain at 100% and 50% consolidation at 4280 Psi

$t_p =$	6224.81
$\varepsilon_{100} =$	61.474
$\varepsilon_{50} =$	61.089
$t_{50} =$	1474.19

5.5 Mixing with Sand Reconsolidation

In this section, strain/log time plots are presented for Sample-B mixed with 25%, and 50% of Brazos sand. Permeability is calculated from these plots as a function of vertical stress, and the relationship of permeability with the 50% consolidation point is described in section 3.2. The strain at 50% is the midpoint between the start of the stress step to 100% consolidation. The 100% consolidation is empirically obtained from the intersection of primary with secondary slopes.

5.5.1 Seventy Five Percent Shale

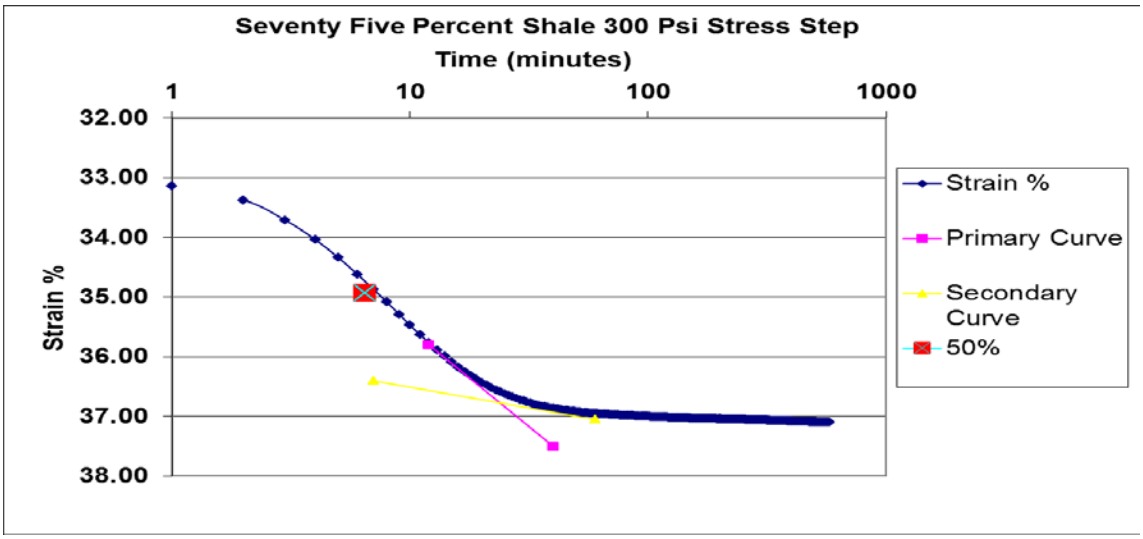

Figure 105 Strain versus the logarithm of time at a constant stress of 300 Psi.

Table 56 Time and strain at 100% and 50% consolidation at 300 Psi

t_p=	23.87
ε_{100}=	36.771
ε_{50}=	34.933
t_{50}=	6.50

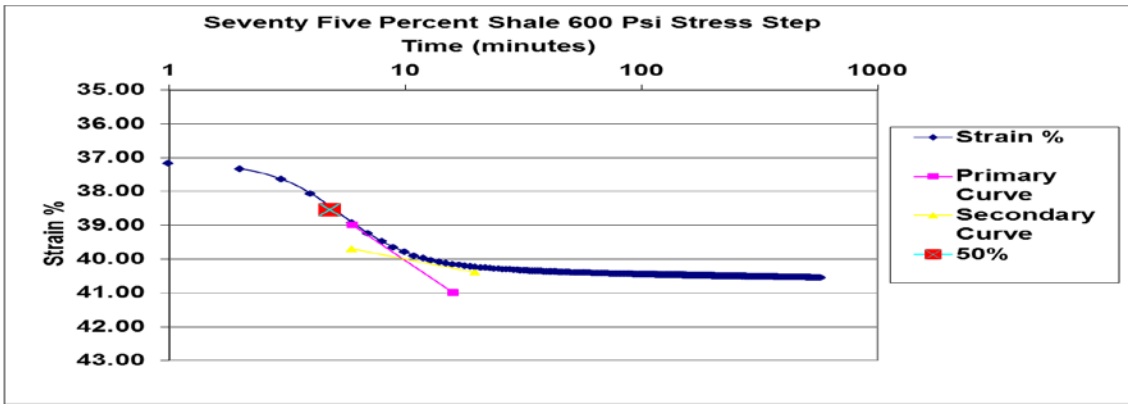

Figure 106 Strain versus the logarithm of time at a constant stress of 600 Psi.

Table 57 Time and strain at 100% and 50% consolidation at 600 Psi

$t_p =$	9.70
$\varepsilon_{100} =$	39.979
$\varepsilon_{50} =$	38.553
$t_{50} =$	4.82

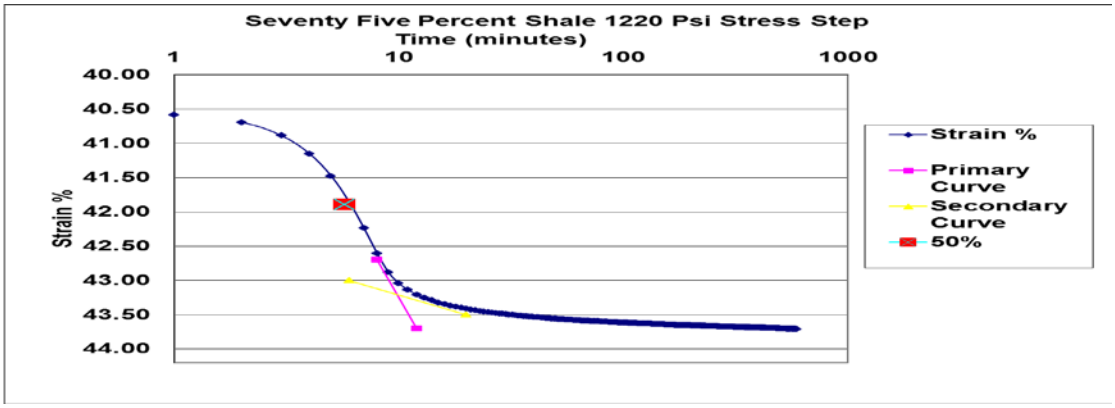

Figure 107 Strain versus the logarithm of time at a constant stress of 1220 Psi

Table 58 Time and strain at 100% and 50% consolidation at 1220 Psi

$t_p =$	9.82
$\varepsilon_{100} =$	43.204
$\varepsilon_{50} =$	41.890
$t_{50} =$	5.76

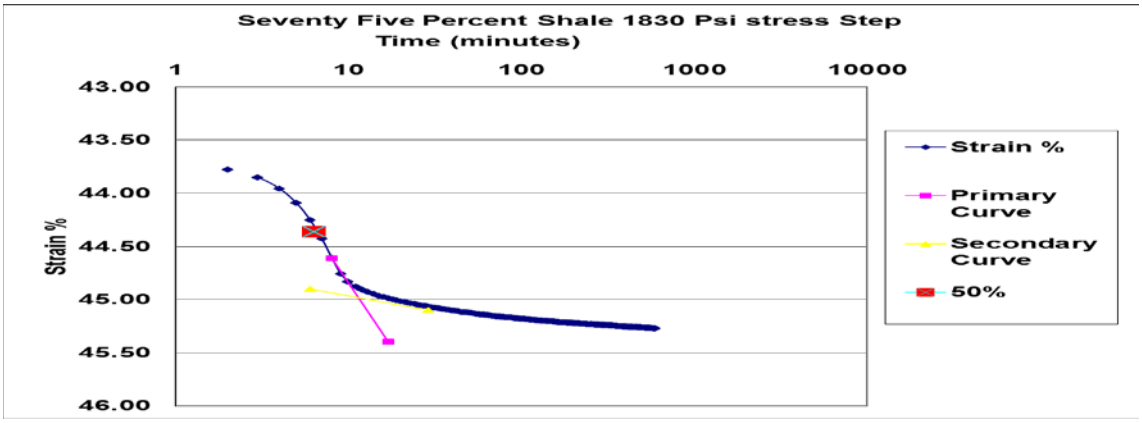

Figure 108 Strain versus the logarithm of time at a constant stress of 1830 Psi.

Table 59 Time and strain at 100% and 50% consolidation at 1830 Psi

t_p=	11.40
ε_{100}=	44.982
ε_{50}=	44.361
t_{50}=	6.31

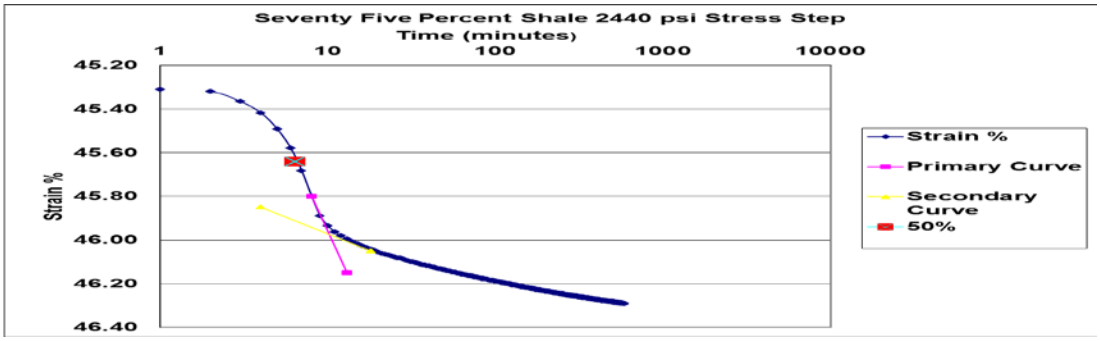

Figure 109 Strain versus the logarithm of time at a constant stress of 2440 Psi.

Table 60 Time and strain at 100% and 50% consolidation at 2440 Psi

t_p=	10.19
ε_{100}=	45.974
ε_{50}=	45.641
t_{50}=	6.42

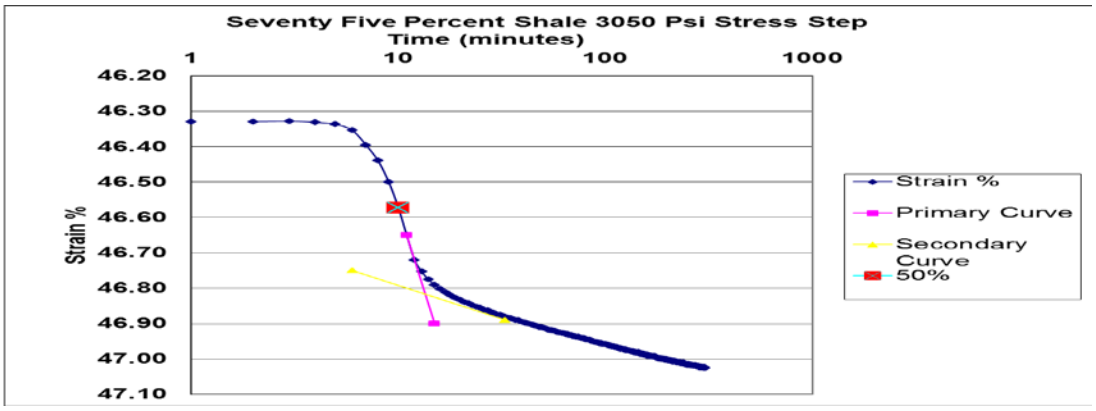

Figure 110 Strain versus the logarithm of time at a constant stress of 3050 Psi.

Table 61 Time and strain at 100% and 50% consolidation at 3050 psi

$t_p =$	13.52
$\varepsilon_{100} =$	46.817
$\varepsilon_{50} =$	46.573
$t_{50} =$	9.97

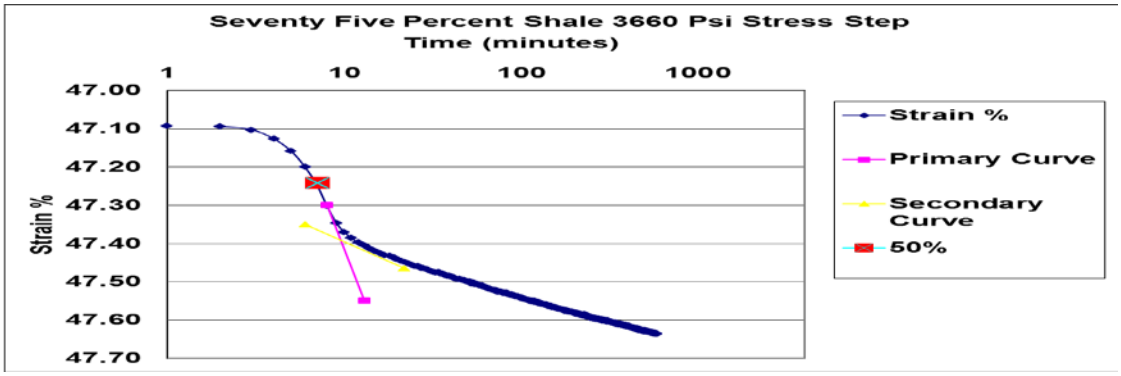

Figure 111 Strain versus the logarithm of time at a constant stress of 3660 Psi.

Table 62 Time and strain at 100% and 50% consolidation at 3660 Psi

$t_p =$	9.55
$\varepsilon_{100} =$	47.391
$\varepsilon_{50} =$	47.242
$t_{50} =$	7.15

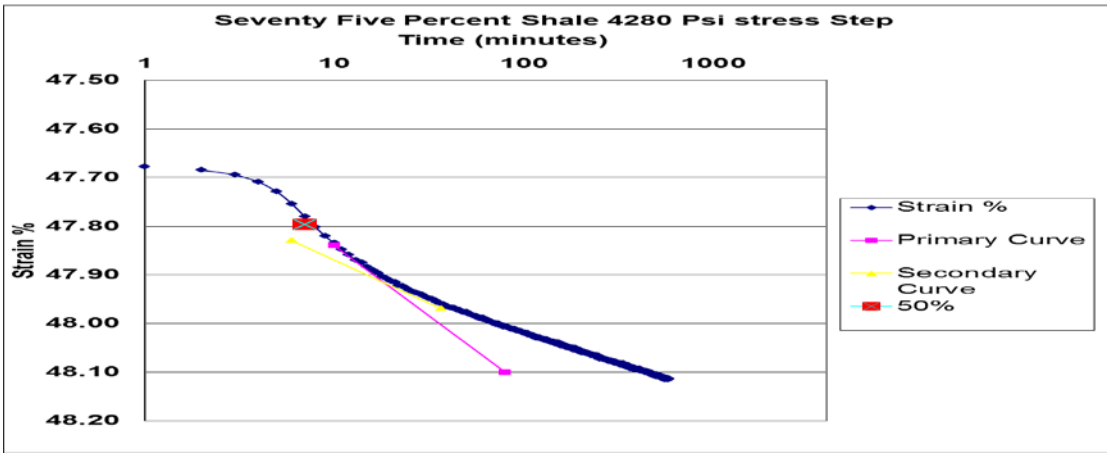

Figure 112 Strain versus the logarithm of time at a constant stress of 4280 Psi

Table 63 Time and strain at 100% and 50% consolidation at 4280 Psi

$t_p =$	18.40
$\varepsilon_{100} =$	47.916
$\varepsilon_{50} =$	47.796
$t_{50} =$	7.03

5.5.2 Fifty Percent Shale

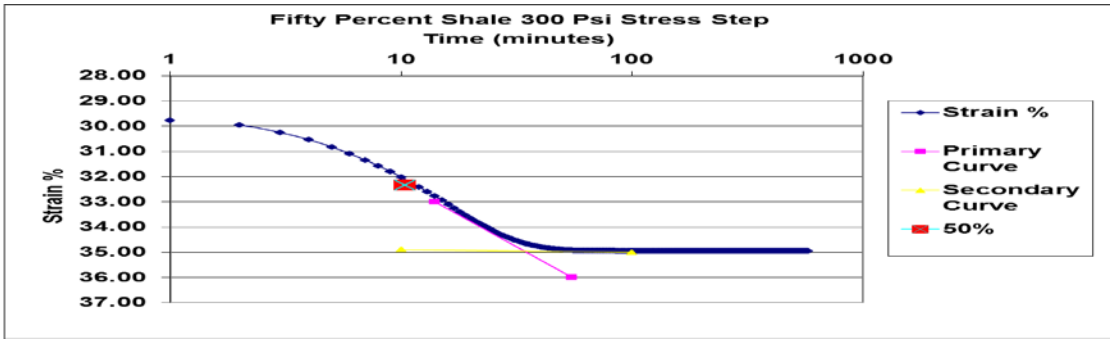

Figure 113 Strain versus the logarithm of time at a constant stress of 300 Psi.

Table 64 Time and strain at 100% and 50% consolidation at 300 Psi

$t_p =$	34.12
$\varepsilon_{100} =$	34.953
$\varepsilon_{50} =$	32.346
$t_{50} =$	10.39

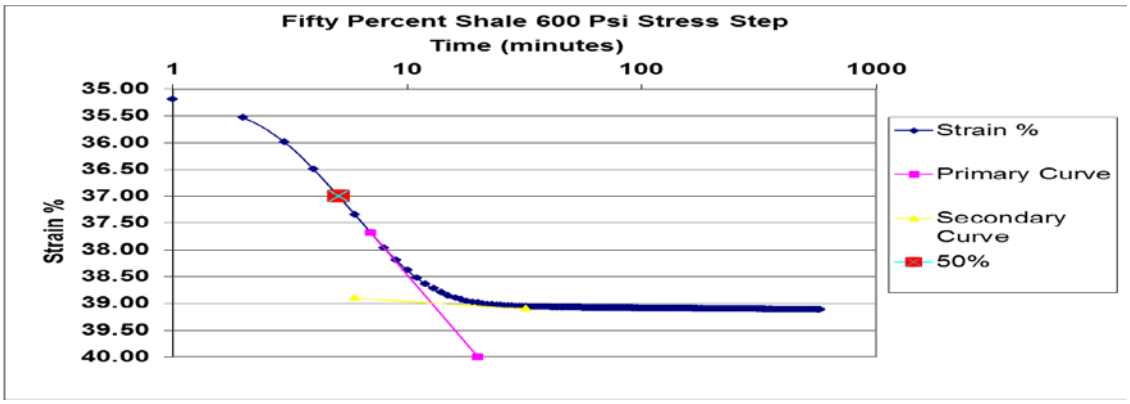

Figure 114 Strain versus the logarithm of time at a constant stress of 600 Psi.

Table 65 Time and strain at 100% and 50% consolidation at 600 Psi

$t_p =$	12.66
$\varepsilon_{100} =$	38.989
$\varepsilon_{50} =$	36.993
$t_{50} =$	5.13

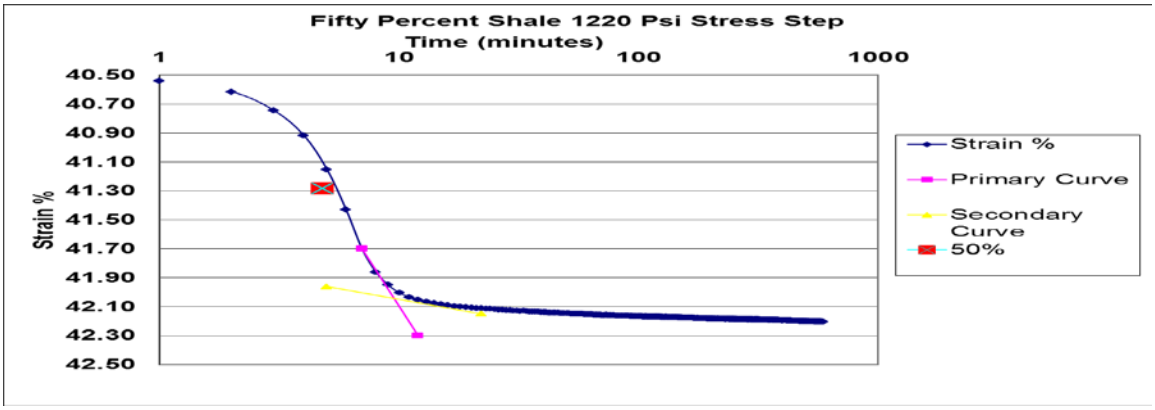

Figure 115 Strain versus the logarithm of time at a constant stress of 1220 Psi.

Table 66 Time and strain at 100% and 50% consolidation at 1220 psi

$t_p =$	9.52
$\varepsilon_{100} =$	42.043
$\varepsilon_{50} =$	41.284
$t_{50} =$	4.82

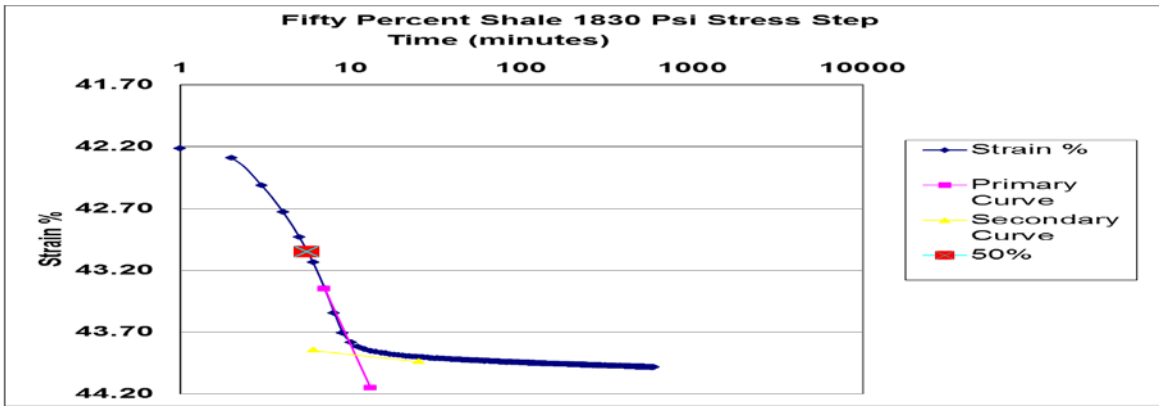

Figure 116 Strain versus the logarithm of time at a constant stress of 1830 Psi.

Table 67 Time and strain at 100% and 50% consolidation at 1830 Psi

$t_p=$	10.60
$\varepsilon_{100}=$	43.886
$\varepsilon_{50}=$	43.049
$t_{50}=$	5.55

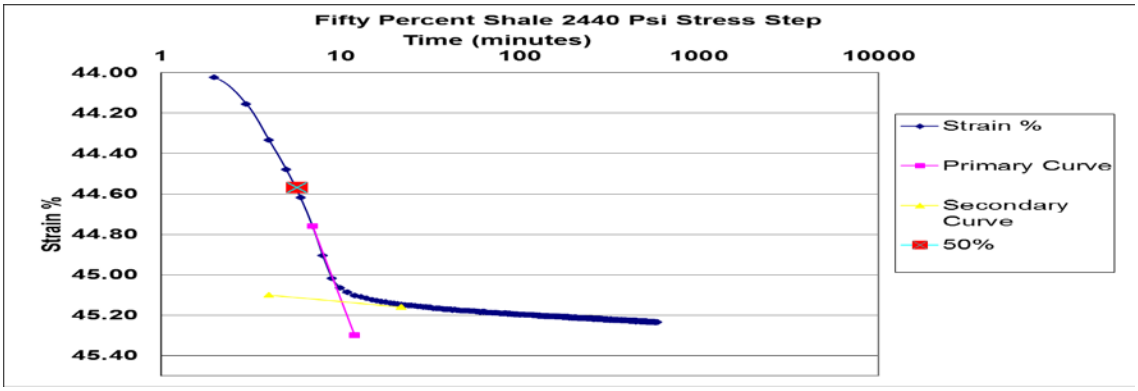

Figure 117 Strain versus the logarithm of time at a constant stress of 2440 Psi

Table 68 Time and strain at 100% and 50% consolidation at 2440 Psi

$t_p=$	10.16
$\varepsilon_{100}=$	45.133
$\varepsilon_{50}=$	44.569
$t_{50}=$	5.79

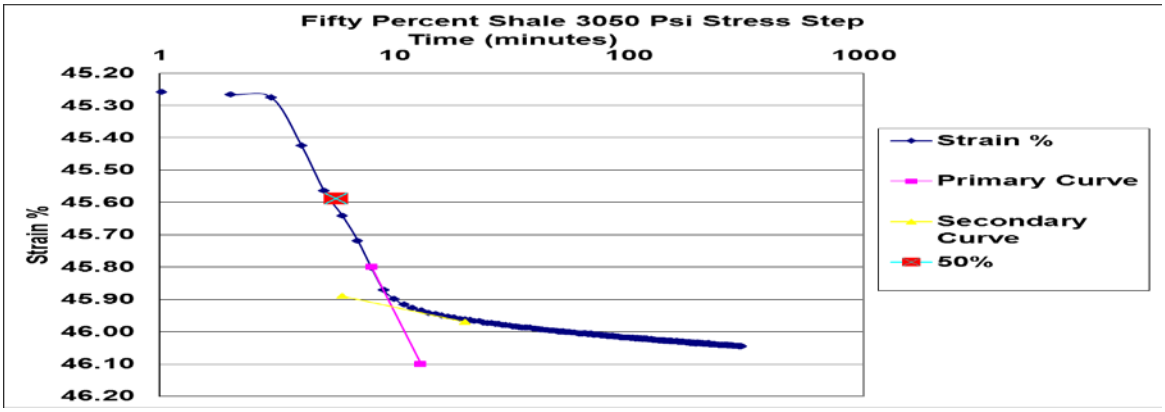

Figure 118 Strain versus the logarithm of time at a constant stress of 3050 Psi.

Table 69 Time and strain at 100% and 50% consolidation at 3050 Psi

$t_p =$	9.75
$\varepsilon_{100} =$	45.922
$\varepsilon_{50} =$	45.588
$t_{50} =$	5.68

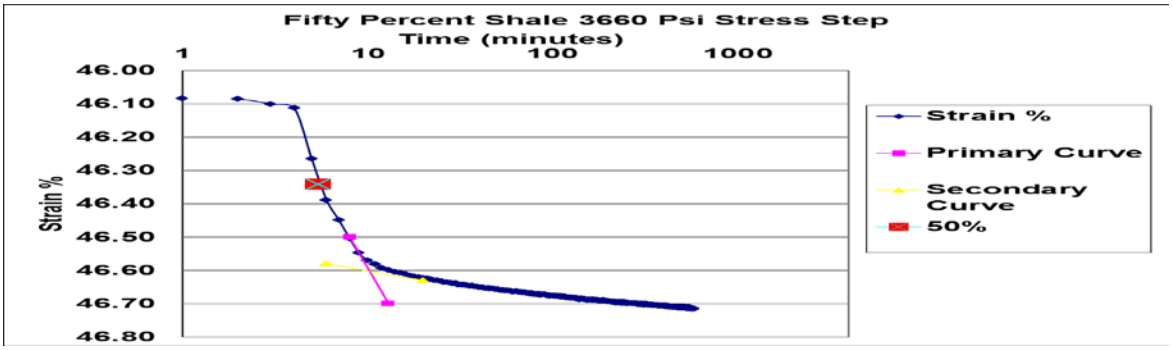

Figure 119 Strain versus the logarithm of time at a constant stress of 3660 Psi.

Table 70 Time and strain at 100% and 50% consolidation at 3660 Psi

$t_p =$	10.25
$\varepsilon_{100} =$	46.602
$\varepsilon_{50} =$	46.341
$t_{50} =$	5.44

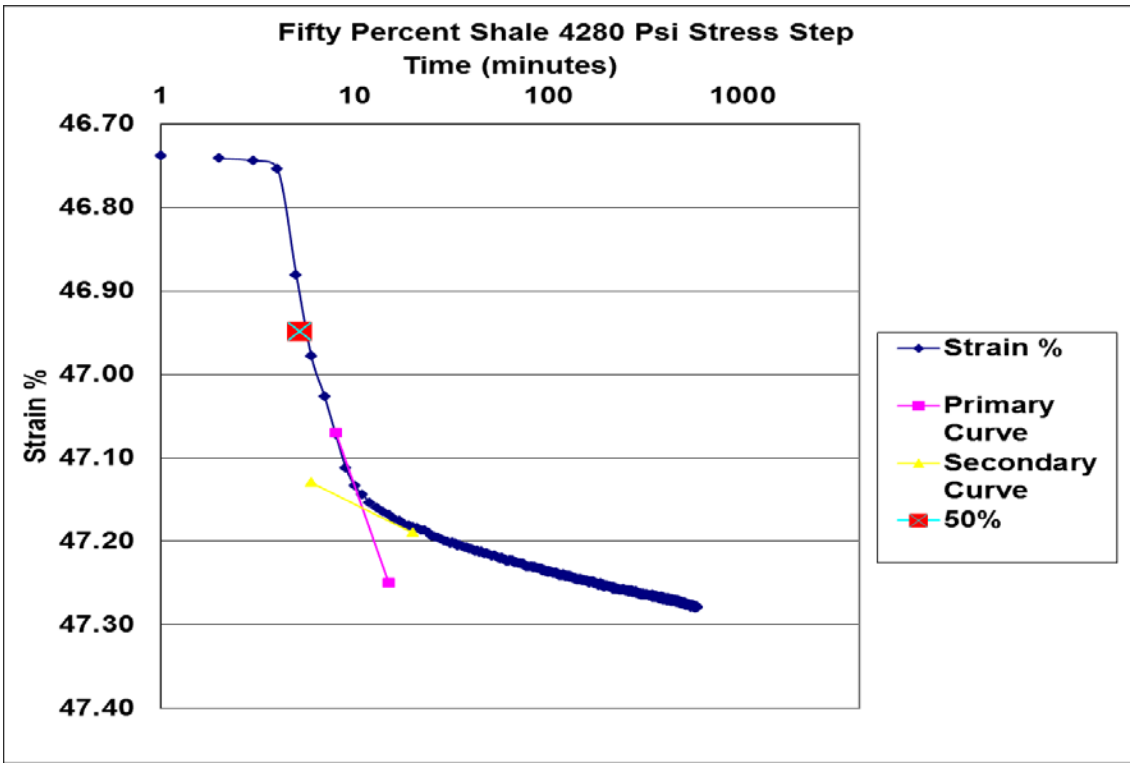

Figure 120 Strain versus the logarithm of time at a constant stress of 4280 Psi.

Table 71 Time and strain at 100% and 50% consolidation at 4280 Psi

$t_p =$	10.95
$\varepsilon_{100} =$	47.160
$\varepsilon_{50} =$	46.949
$t_{50} =$	5.24

5.6 Sample-A Multistage Test

In this section, multistage strength data is presented for Sample-A reconsolidated at salinities of 35 KPPM, and 100 KPPM). Fountain plots consist of axial, radial, and volume strain as a function of axial stress ramp at a constant confining stress. The positive point of dilatancy is determined at the point where the volume strain starts to become constant at poisson ration equals half. The correction for maximum compressive strength is corrected by a factor of 2.

5.6.1 Sample A-35

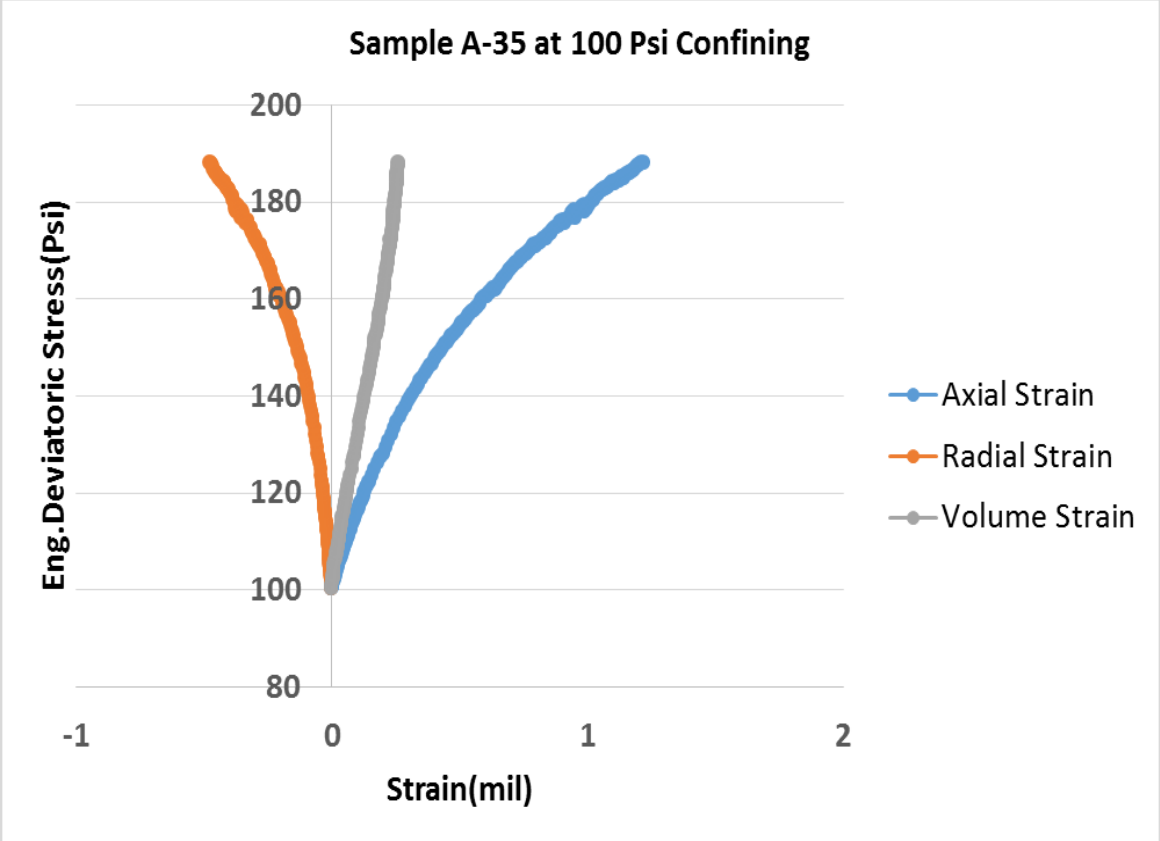

Figure 121 Deviatoric stress is increased at 100 Psi confining pressure. The deviatoric stress starts at 100 Psi. Axial Strain, Radial, and Volume strain are measured. The point of positive dilatancy is chosen to be at 186 Psi.

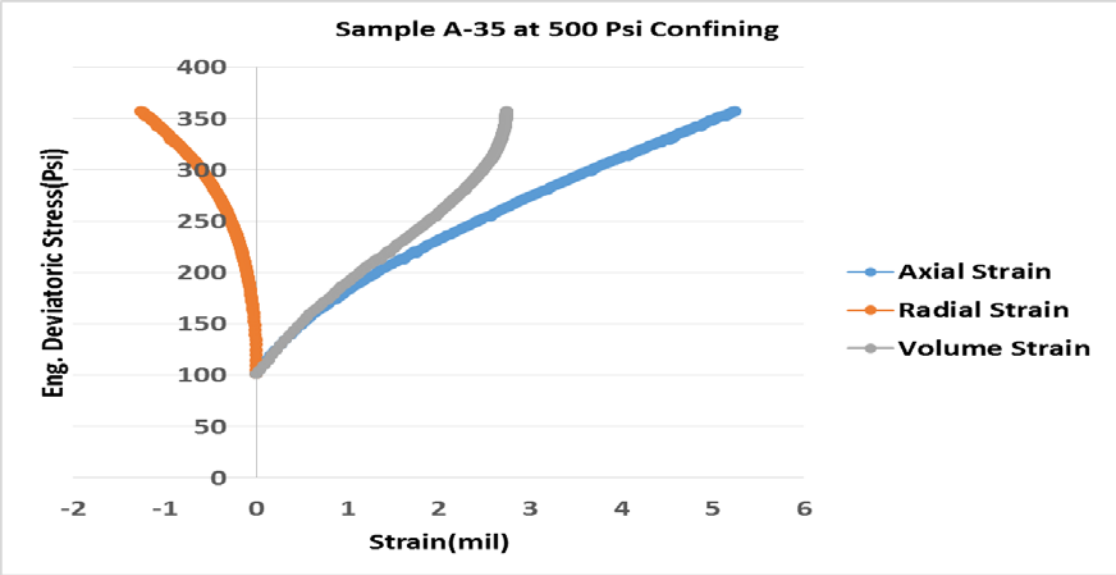

Figure 122 Deviatoric stress is increased at 500 Psi confining pressure. The deviatoric stress starts at 100 Psi. Axial Strain, Radial, and Volume strain are measured. The point of positive dilatancy is chosen to be at 321 Psi.

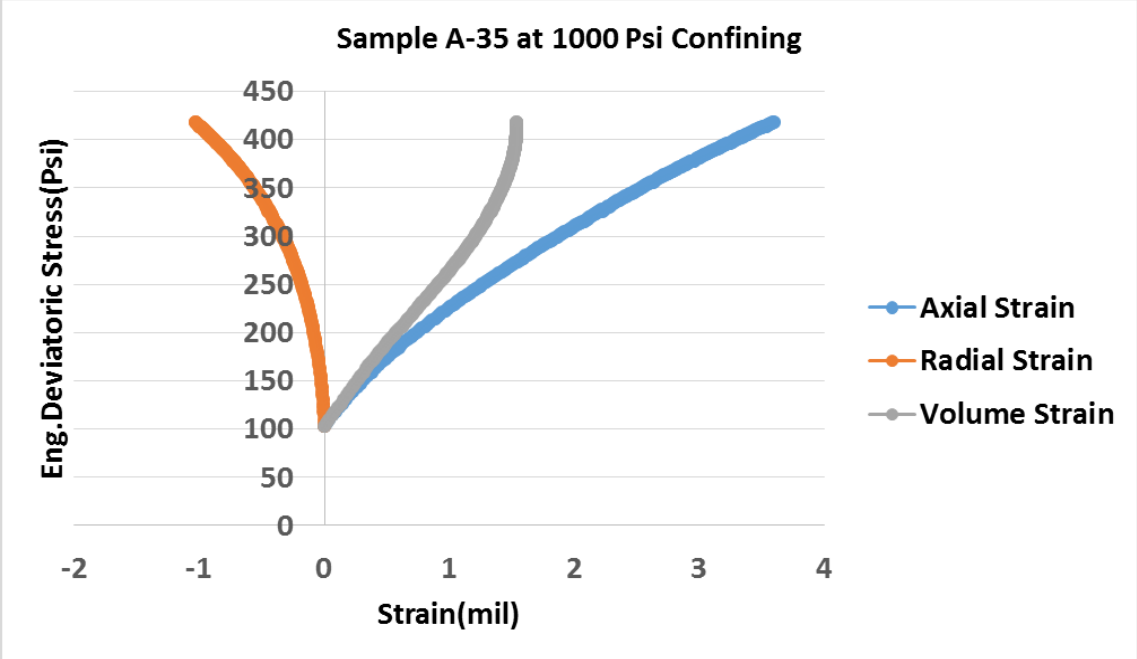

Figure 123 Deviatoric stress is increased at 1000 Psi confining pressure. The deviatoric stress starts at 100 Psi. Axial Strain, Radial, and Volume strain are measured. The point of positive dilatancy is chosen to be at 390 Psi.

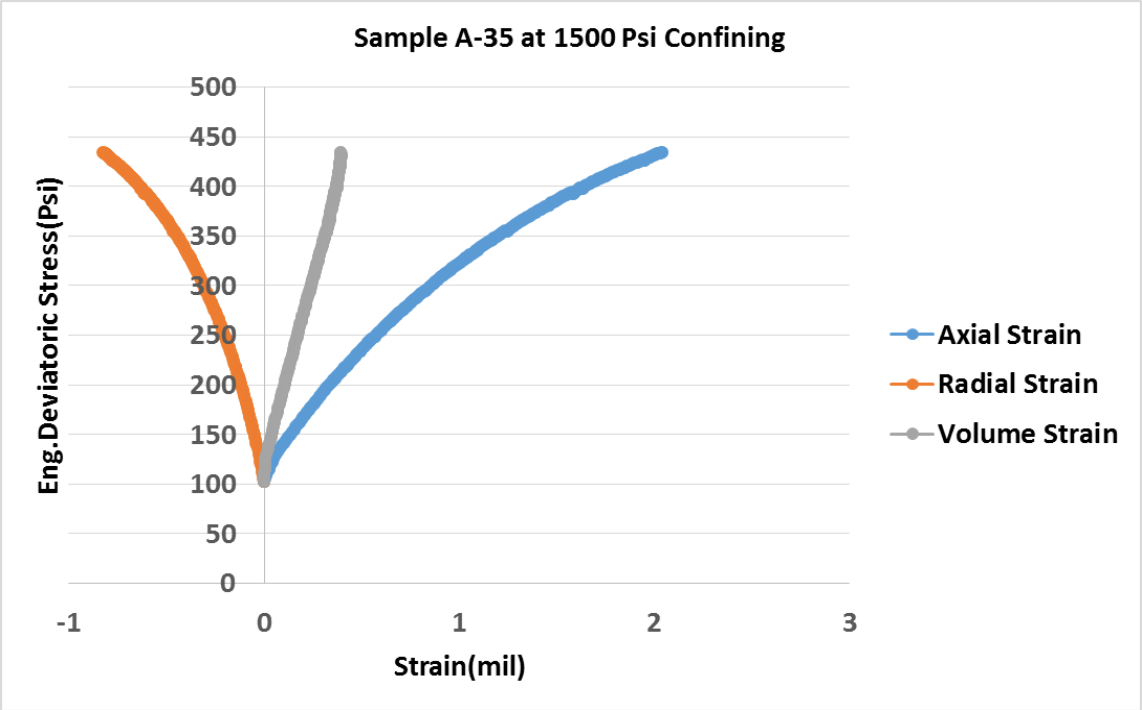

Figure 124 Deviatoric stress is increased at 1500 Psi confining pressure. The deviatoric stress starts at 100 Psi. Axial Strain, Radial, and Volume strain are measured. The point of positive dilatancy is chosen to be at 433 Psi.

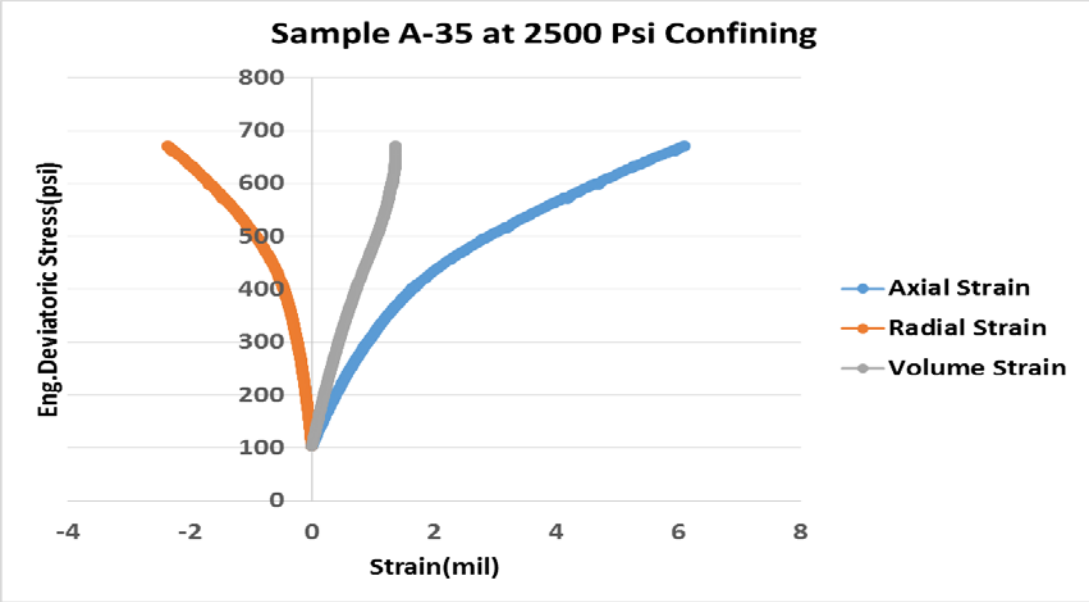

Figure 125 Deviatoric stress is increased at 2500 Psi confining pressure. The deviatoric stress starts at 100 Psi. Axial Strain, Radial, and Volume strain are measured. The point of positive dilatancy is chosen to be at 670 Psi.

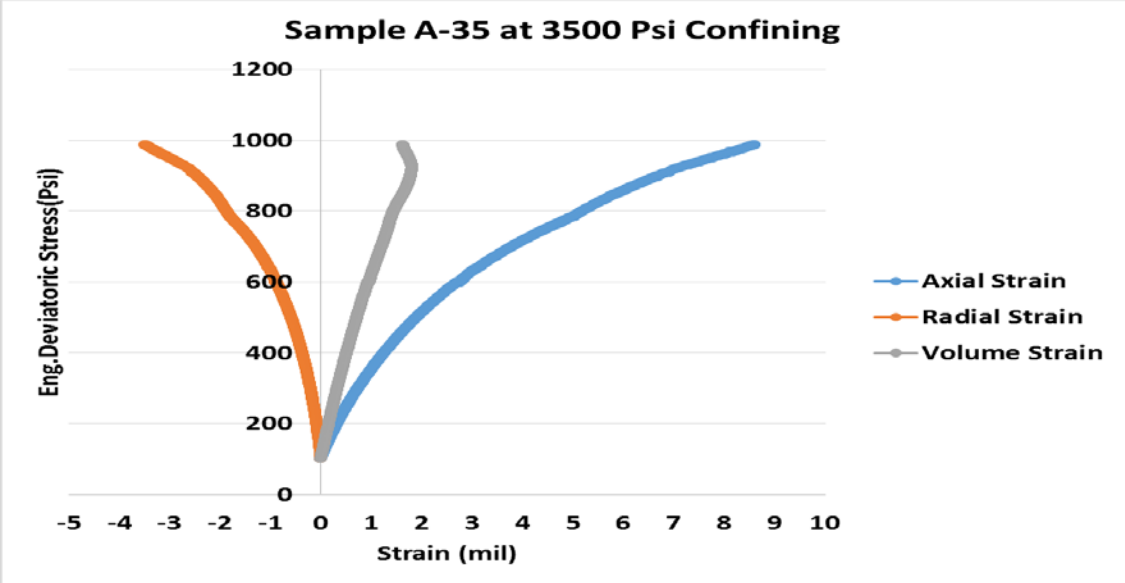

Figure 126 Deviatoric stress is increased at 3500 Psi confining pressure. The deviatoric stress starts at 100 Psi. Axial Strain, Radial, and Volume strain are measured. The point of positive dilatancy is chosen to be at 922 Psi.

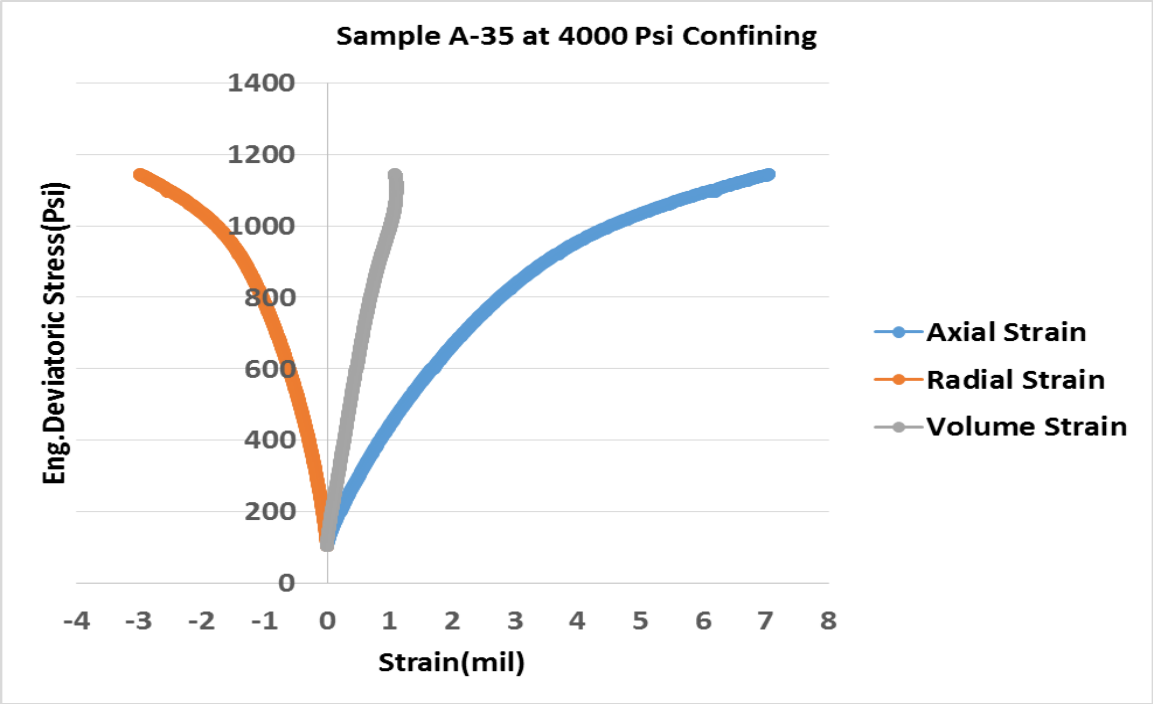

Figure 127 Deviatoric stress is increased at 4000 Psi confining pressure. The deviatoric stress starts at 100 Psi. Axial Strain, Radial, and Volume strain are measured. The point of positive dilatancy is chosen to be at 1076 Psi.

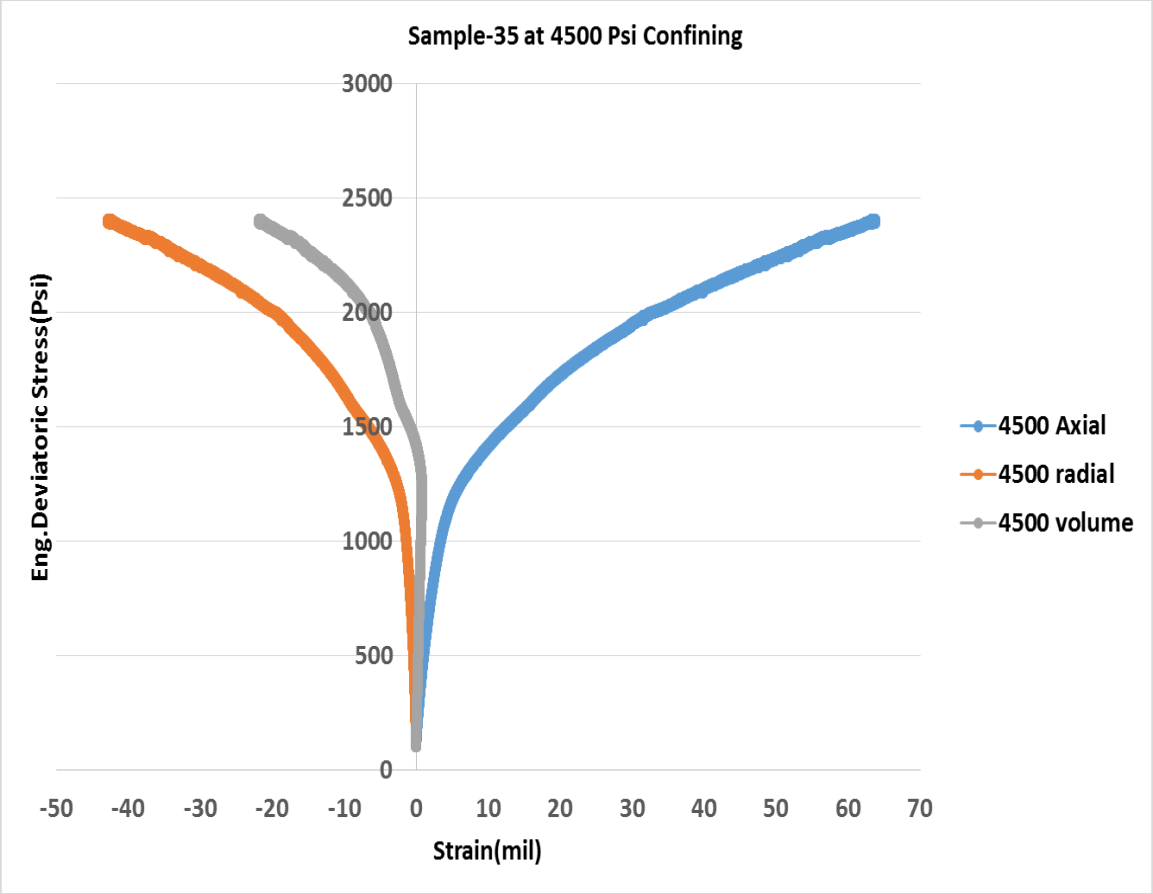

Figure 128 Deviatoric stress is increased at 4000 Psi confining pressure. The deviatoric stress starts at 100 Psi. Axial Strain, Radial, and Volume strain are measured. The point of positive dilatancy is chosen to be at 1185 Psi.

Summary Table

Table 72 Strength data for Sample A-35, sample salinity is 35 KPPM, sample length is 2033 mill-inch, correction factor=2 is used to calculate the maximum compressive strength from the positive point of dilatancy.

Confining(Sigma-3)	100	500	1000	1500	2500	3500	4000	4500
Point of Dilatancy (Psi)	186	321	390	433	670	922	1076	1185
Maximum compressive Strength(Psi)	372	642	780	866	1340	1844	2152	2370
Sigma-1	472	1142	1780	2366	3840	5344	6152	6870

5.6.2 Sample A-100

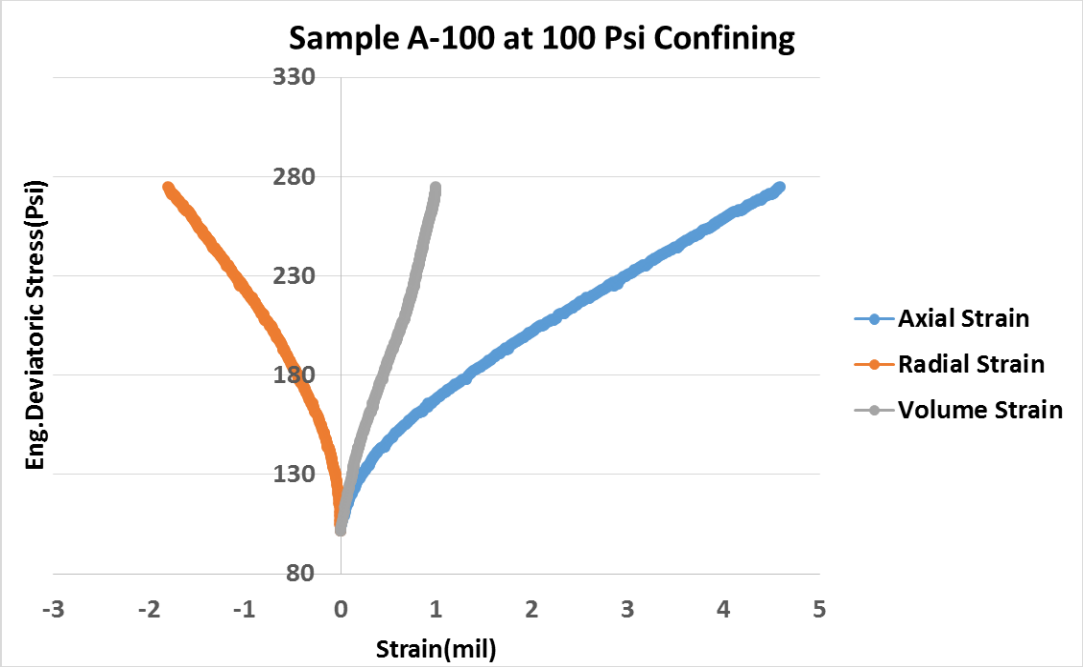

Figure 129 Deviatoric stress is increased at 100 Psi confining pressure. The deviatoric stress starts at 100 Psi. Axial Strain, Radial, and Volume strain are measured. The point of positive dilatancy is chosen to be at 274 Psi.

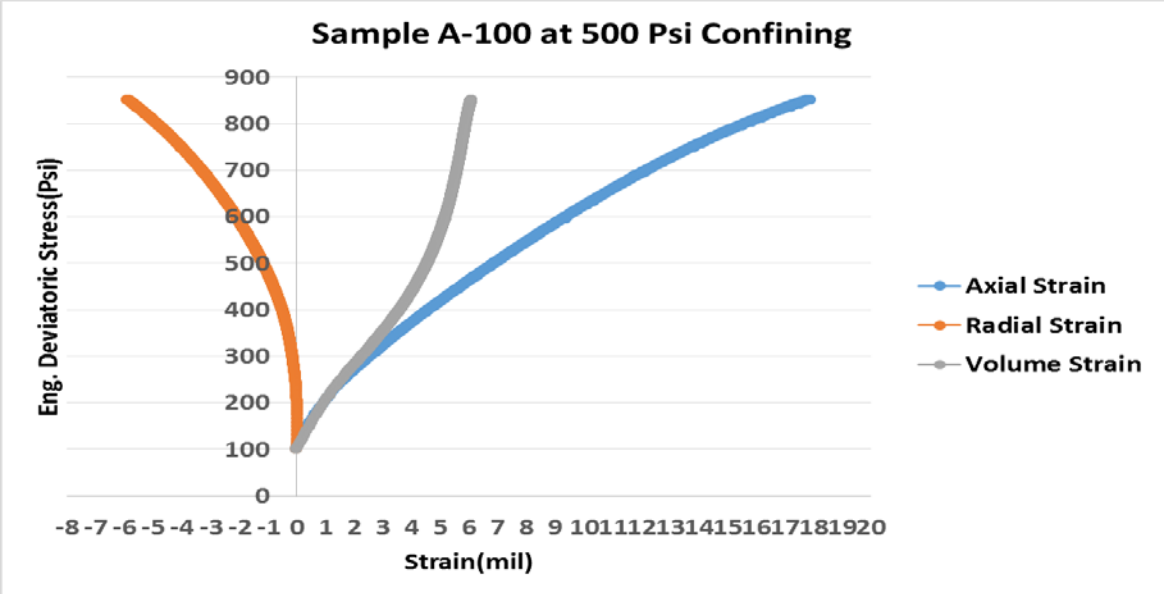

Figure 130 Deviatoric stress is increased at 500 Psi confining pressure. The deviatoric stress starts at 100 Psi. Axial Strain, Radial, and Volume strain are measured. The point of positive dilatancy is chosen to be at 851 Psi.

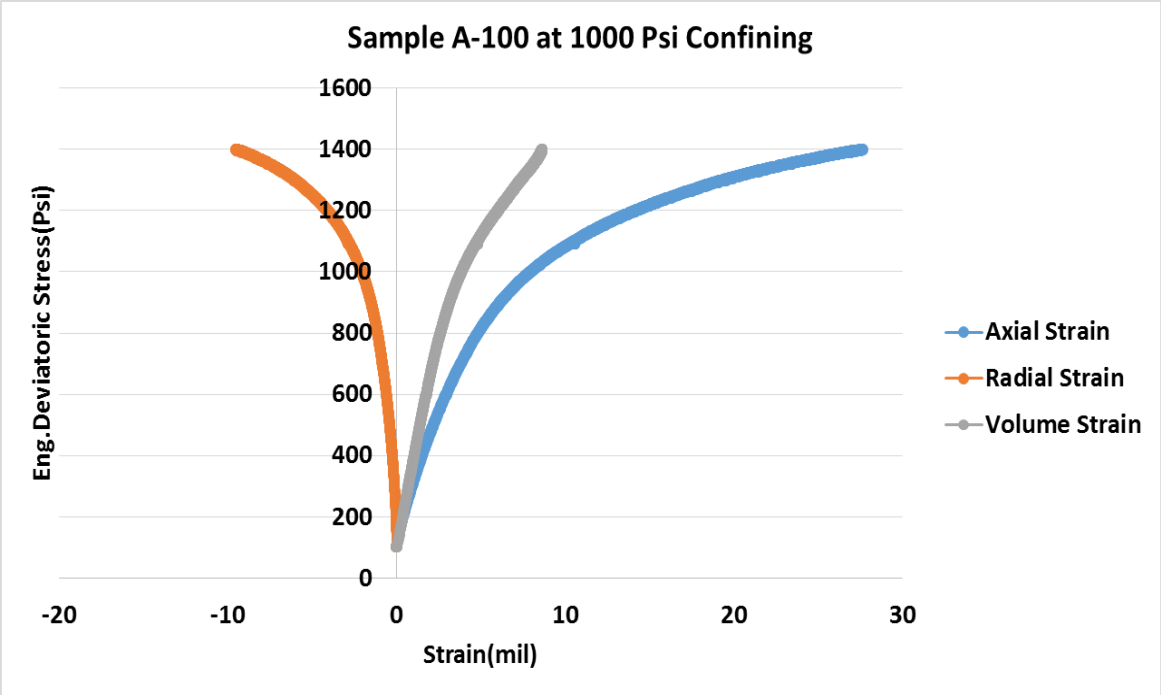

Figure 131 Deviatoric stress is increased at 1000 Psi confining pressure. The deviatoric stress starts at 100 Psi. Axial Strain, Radial, and Volume strain are measured. The point of positive dilatancy is chosen to be at 1398 Psi.

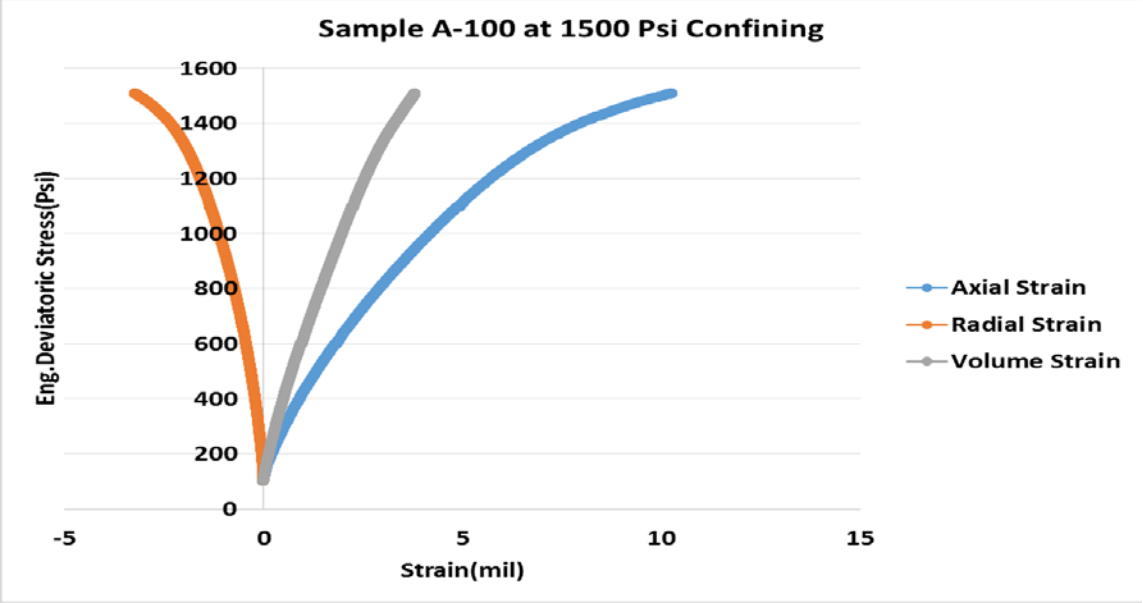

Figure 132 Deviatoric stress is increased at 1500 Psi confining pressure. The deviatoric stress starts at 100 Psi. Axial Strain, Radial, and Volume strain are measured. The point of positive dilatancy is chosen to be at 1569 Psi.

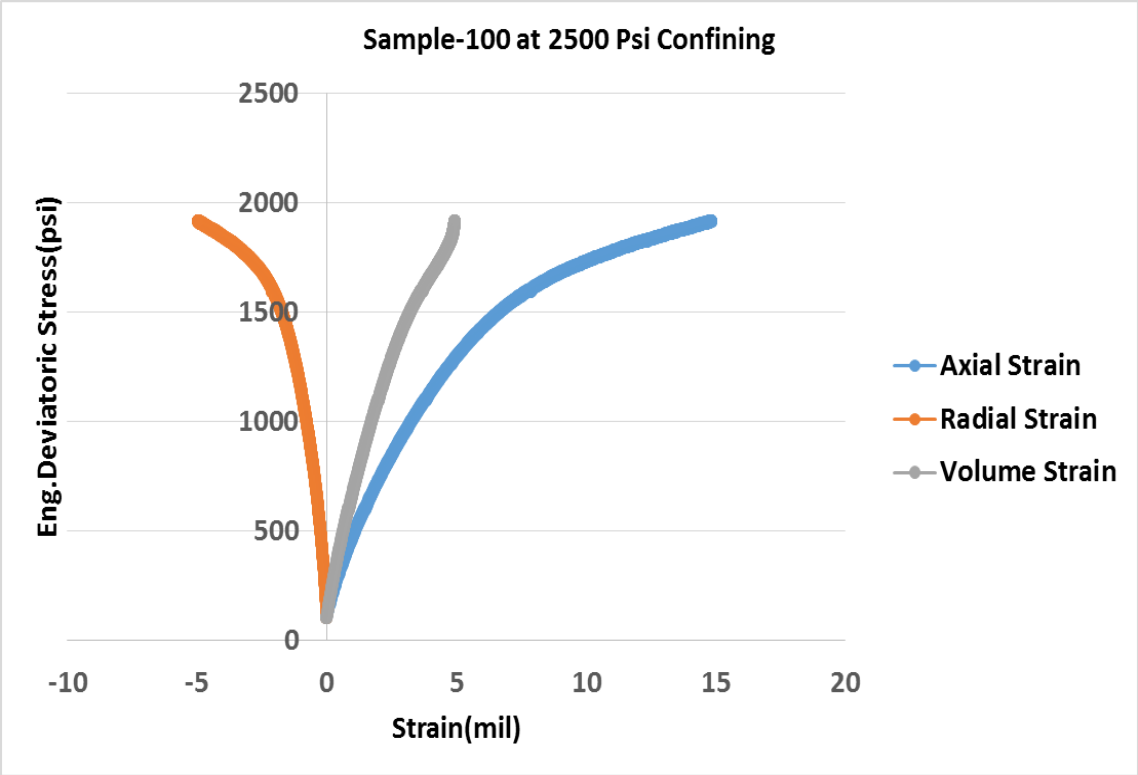

Figure 133 Deviatoric stress is increased at 2500 Psi confining pressure. The deviatoric stress starts at 100 Psi. Axial Strain, Radial, and Volume strain are measured. The point of positive dilatancy is chosen to be at 1906 Psi.

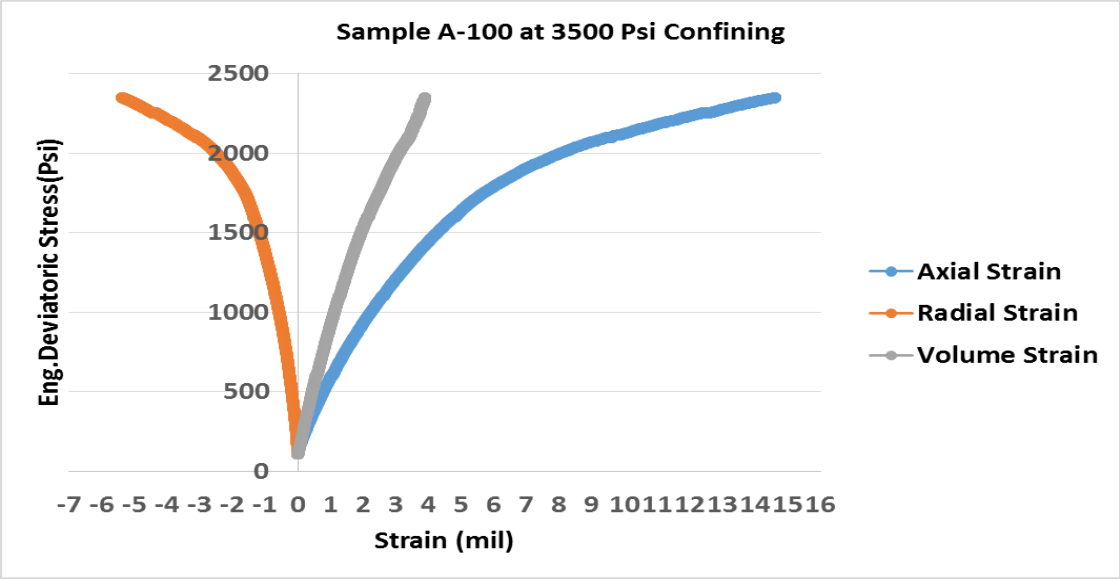

Figure 134 Deviatoric stress is increased at 3500 Psi confining pressure. The deviatoric stress starts at 100 Psi. Axial Strain, Radial, and Volume strain are measured. The point of positive dilatancy is chosen to be at 2340 Psi.

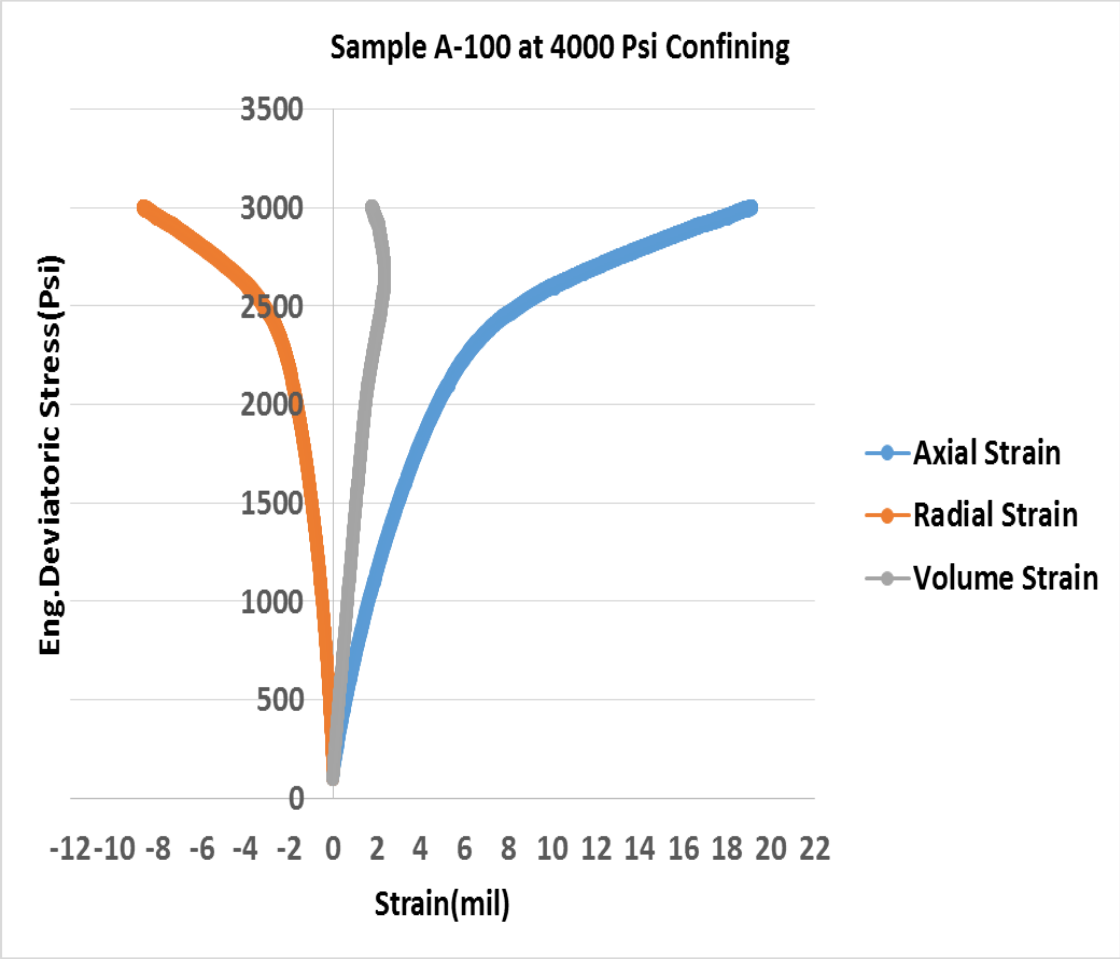

Figure 135 Deviatoric stress is increased at 4000 Psi confining pressure. The deviatoric stress starts at 100 Psi. Axial Strain, Radial, and Volume strain are measured. The point of positive dilatancy is chosen to be at 2649 Psi.

Summary Table:

Table 73 Strength data for Sample A-100, sample salinity is 100 KPPM, sample length is 2037 mill-inch, correction factor=2 is used to calculate the maximum compressive strength from the positive point of dilatancy.

Confining(Sigma-3)	500	1000	1500	2500	3500	4000
Point of Positive Dilatancy	851	1398	1569	1906	2340	2649
Maximum Compressive Strength	1702	2796	3138	3812	4680	5298
Sigma-1	2202	3796	4638	6312	8180	9298

5.7 Sample-B Multistage Test

In this section, multistage strength data is presented for Sample-B reconsolidated at salinities of 35 KPPM and 100 KPPM). Fountain plots consist of axial, radial, and volume strain as a function of axial stress ramp at a constant confining stress. The positive point of dilatancy is determined at the point where the volume strain starts to become constant at poisson ration equals half. The correction for maximum compressive strength is corrected by a factor of 2.

5.7.1 Sample B-35

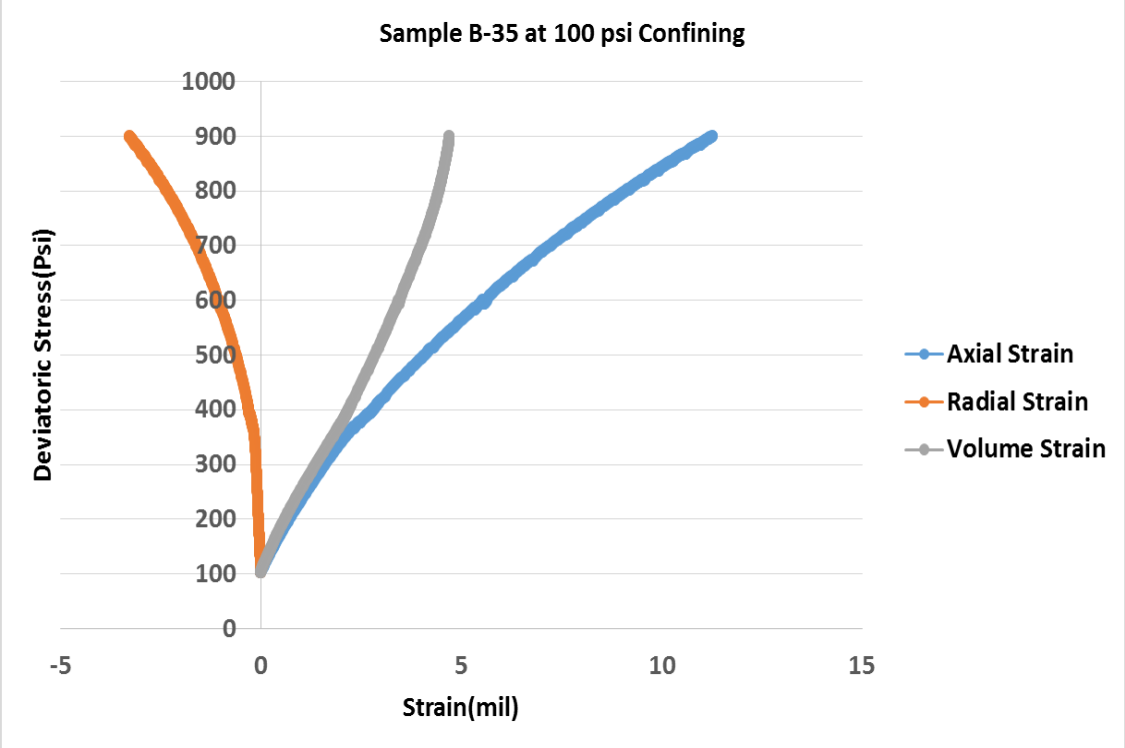

Figure 136 Deviatoric stress is increased at 100 Psi confining pressure. The deviatoric stress starts at 100 Psi. Axial Strain, Radial, and Volume strain are measured. The point of positive dilatancy is chosen to be at 896 Psi.

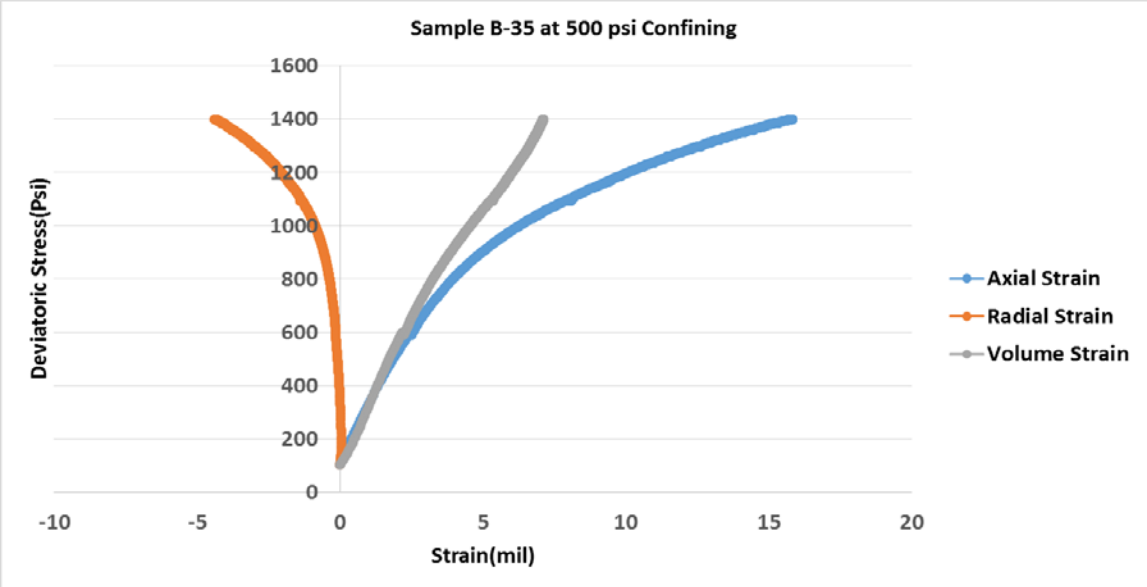

Figure 137 Deviatoric stress is increased at 500 Psi confining pressure. The deviatoric stress starts at 100 Psi. Axial Strain, Radial, and Volume strain are measured. The point of positive dilatancy is chosen to be at 1397 Psi.

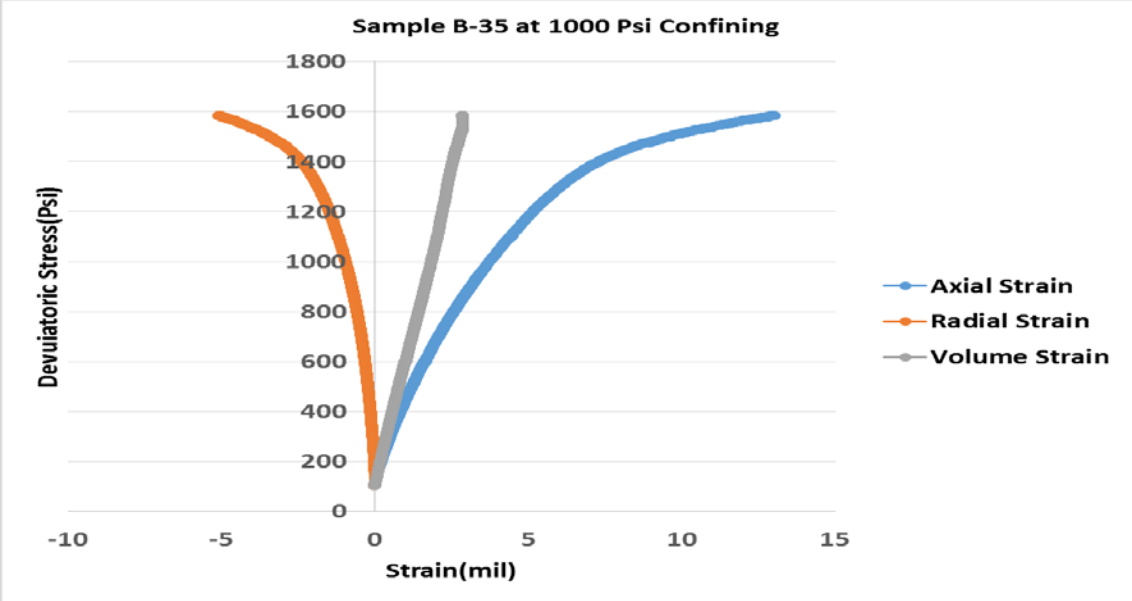

Figure 138 Deviatoric stress is increased at 1000 Psi confining pressure. The deviatoric stress starts at 100 Psi. Axial Strain, Radial, and Volume strain are measured. The point of positive dilatancy is chosen to be at 1508 Psi.

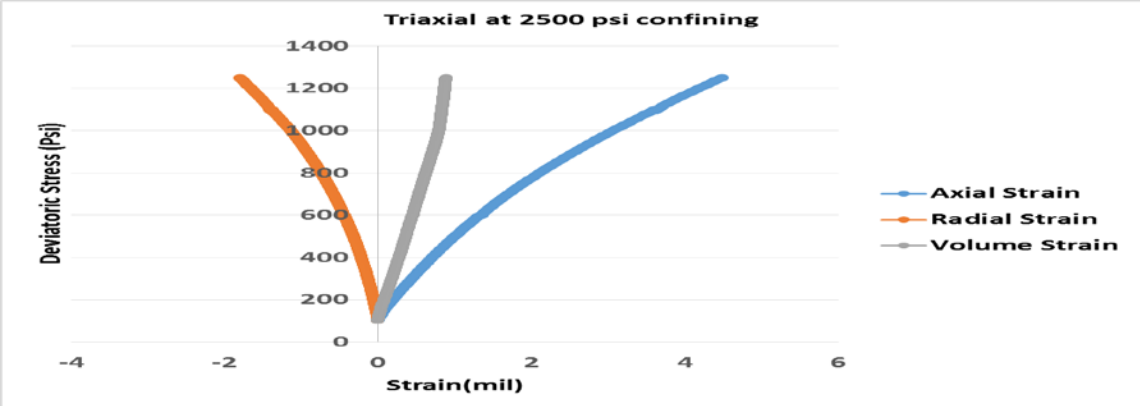

Figure 139 Deviatoric stress is increased at 2500 Psi confining pressure. The deviatoric stress starts at 100 Psi. Axial Strain, Radial, and Volume strain are measured. The point of positive dilatancy is chosen to be at 1249 Psi.

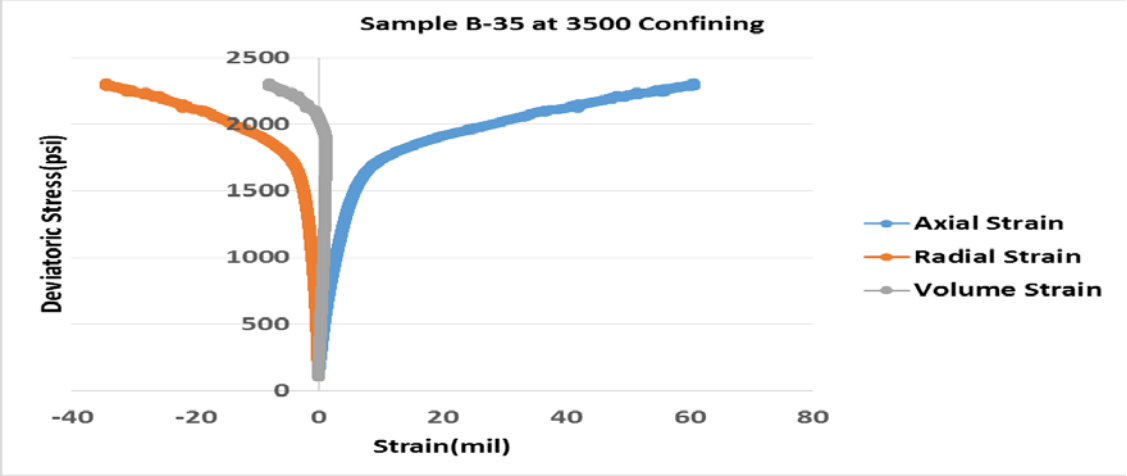

Figure 140 Deviatoric stress is increased at 3500 Psi confining pressure. The deviatoric stress starts at 100 Psi. Axial Strain, Radial, and Volume strain are measured. The point of positive dilatancy is chosen to be at 1959 Psi.

Summary Table:

Table 74 Strength data for Sample B-35, sample salinity is 35 KPPM, sample length is 2040 mill-inch, correction factor=2 is used to calculate the maximum compressive strength from the positive point of dilatancy.

Confining(Sigma-3)	500	1000	3500
Point of Positive Dilatancy	1397	1508	1959
Maximum Compressive Strength	2794	3016	3918
Sigma-1	3294	4016	7418

5.7.2 Sample B-100

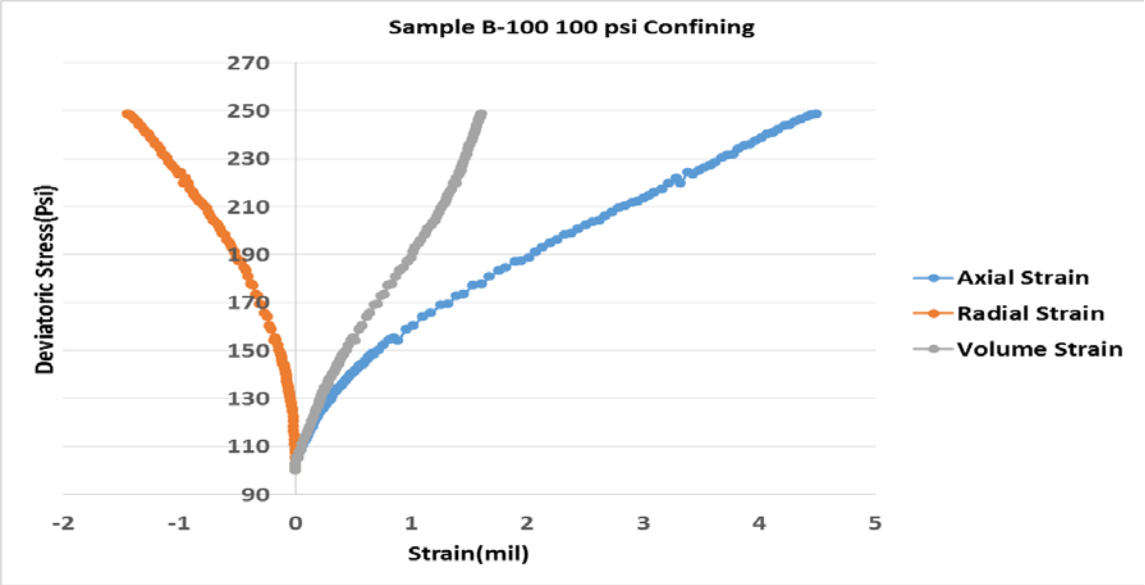

Figure 141 Deviatoric stress is increased at 100 Psi confining pressure. The deviatoric stress starts at 100 Psi. Axial Strain, Radial, and Volume strain are measured. The point of positive dilatancy is chosen to be at 246 Psi.

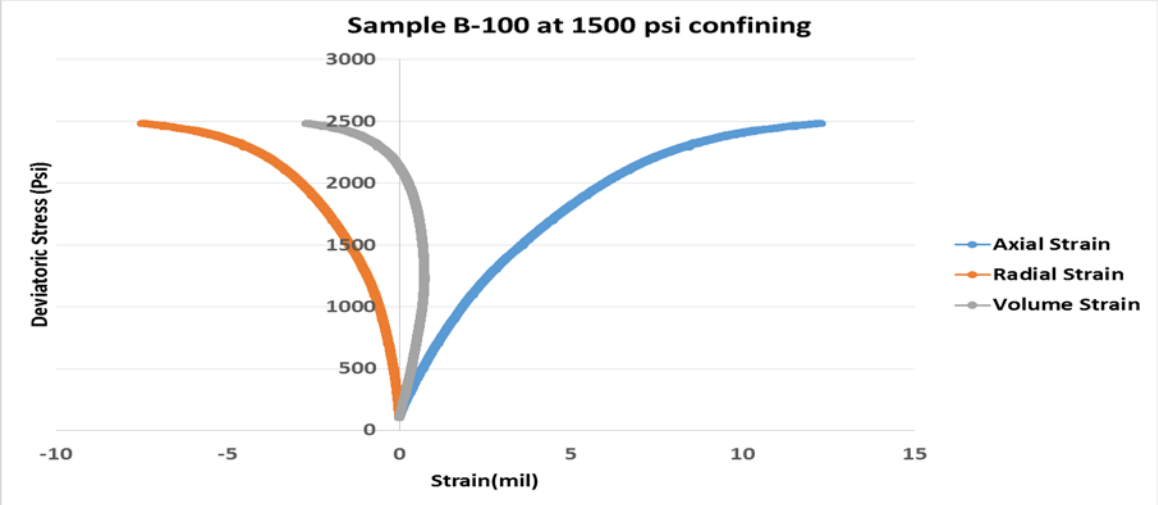

Figure 142 Deviatoric stress is increased at 1500 Psi confining pressure. The deviatoric stress starts at 100 Psi. Axial Strain, Radial, and Volume strain are measured. The point of positive dilatancy is chosen to be at 1181 Psi.

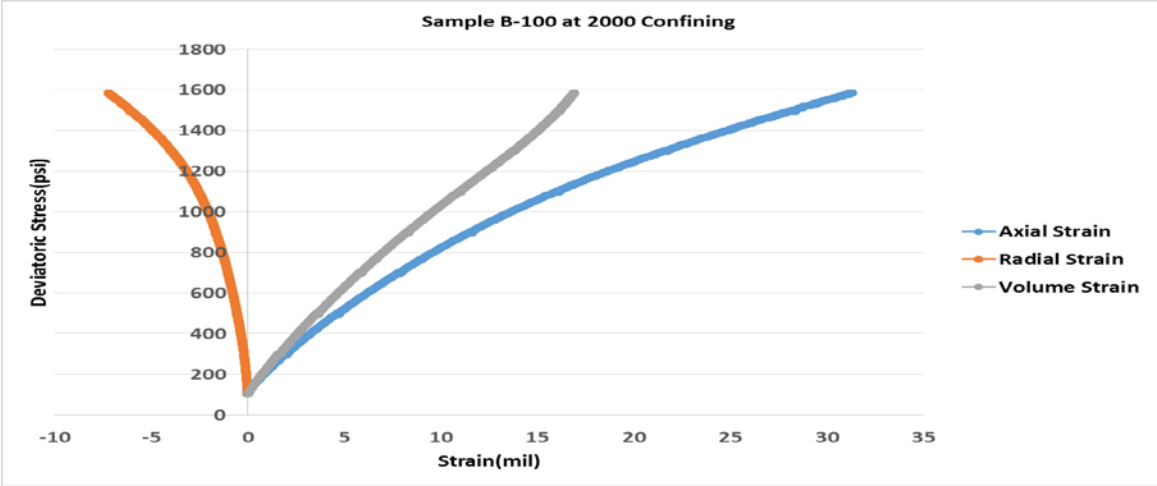

Figure 143 Deviatoric stress is increased at 2000 Psi confining pressure. The deviatoric stress starts at 100 Psi. Axial Strain, Radial, and Volume strain are measured. The point of positive dilatancy is chosen to be at 1570 Psi.

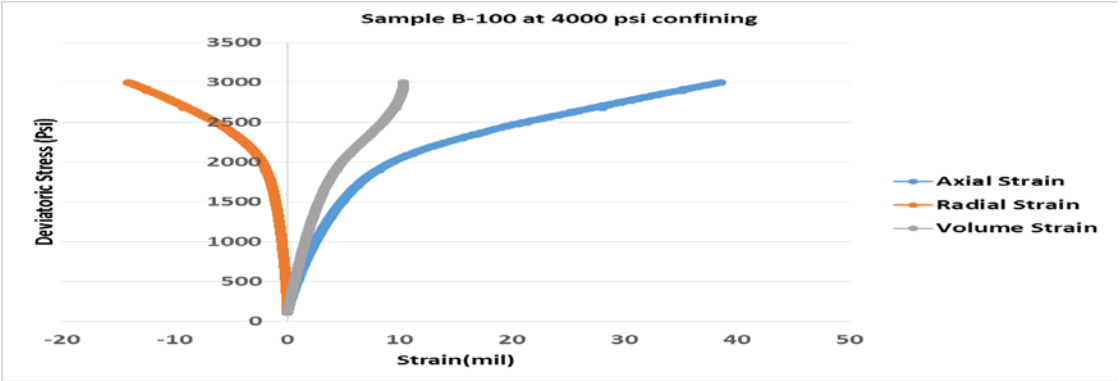

Figure 144 Deviatoric stress is increased at 4000 Psi confining pressure. The deviatoric stress starts at 100 Psi. Axial Strain, Radial, and Volume strain are measured. The point of positive dilatancy is chosen to be at 2861 Psi.

Summary Table:

Table 75 Strength data for Sample B-100, sample salinity is 100 KPPM, sample length is 1931 mill-inch, correction factor=2 is used to calculate the maximum compressive strength from the positive point of dilatancy.

Confining (Sigma-3)	100	1500	2000	4000
Point of Positive Dilatancy(Psi)	246	1181	1570	2861
Maximum Compressive Strength (Psi)	492	2362	3140	5722
Sigma-1	592	3862	5140	9722

5.8 Pierre Shale Multistage Test

In this section, multistage strength data is presented for Pierre shale reconsolidated at salinities of 35 KPPM, 100 KPPM, and 200 KPPM). The correction for maximum compressive strength is corrected by a factor of 2.

5.8.1 Pierre Shale-35

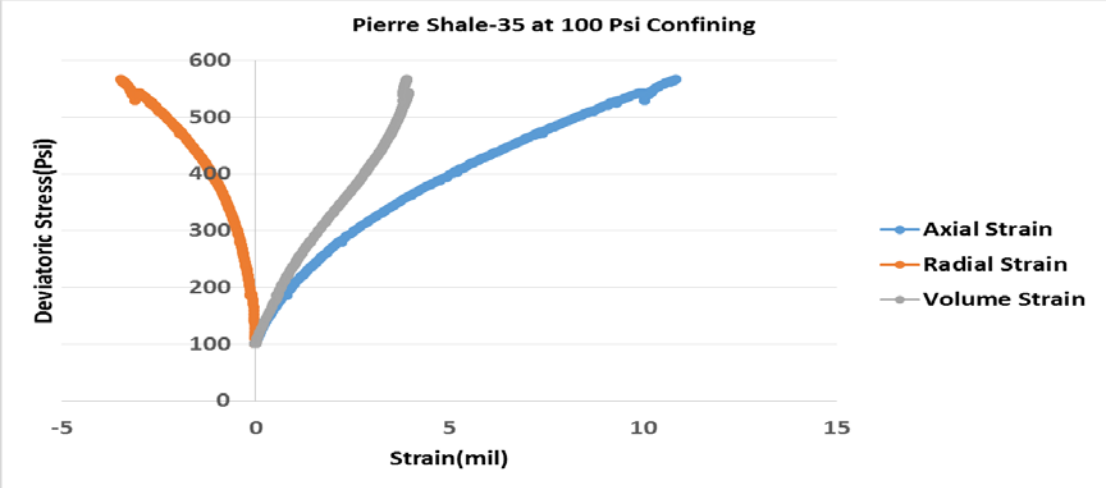

Figure 145 Deviatoric stress is increased at 100 Psi confining pressure. The deviatoric stress starts at 100 Psi. Axial Strain, Radial, and Volume strain are measured. The point of positive dilatancy is chosen to be at 536 Psi.

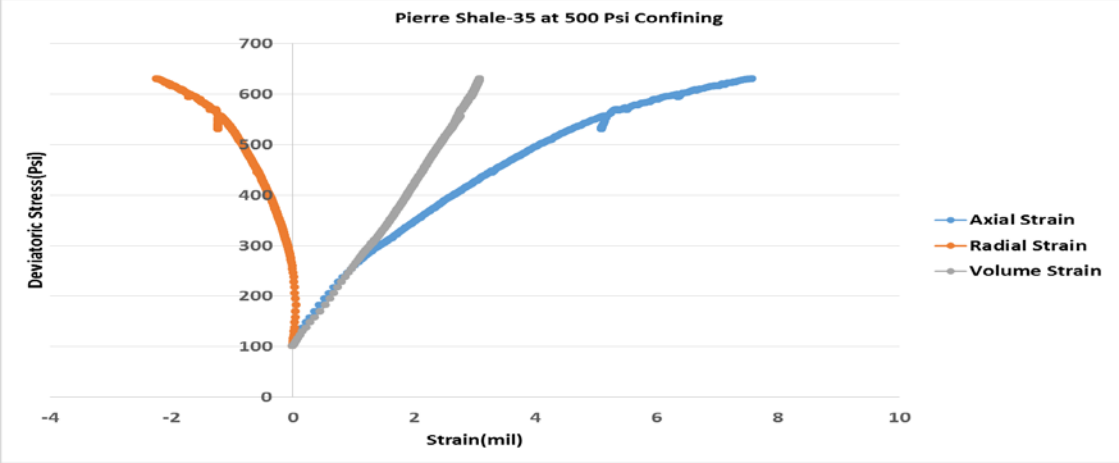

Figure 146 Deviatoric stress is increased at 500 Psi confining pressure. The deviatoric stress starts at 100 Psi. Axial Strain, Radial, and Volume strain are measured. The point of positive dilatancy is chosen to be at 630 Psi.

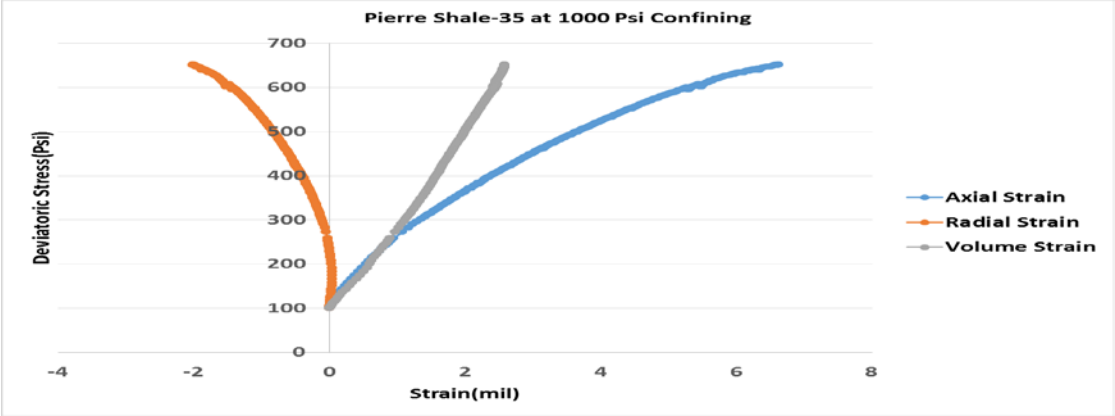

Figure 147 Deviatoric stress is increased at 1000 Psi confining pressure. The deviatoric stress starts at 100 Psi. Axial Strain, Radial, and Volume strain are measured. The point of positive dilatancy is chosen to be at 647 Psi.

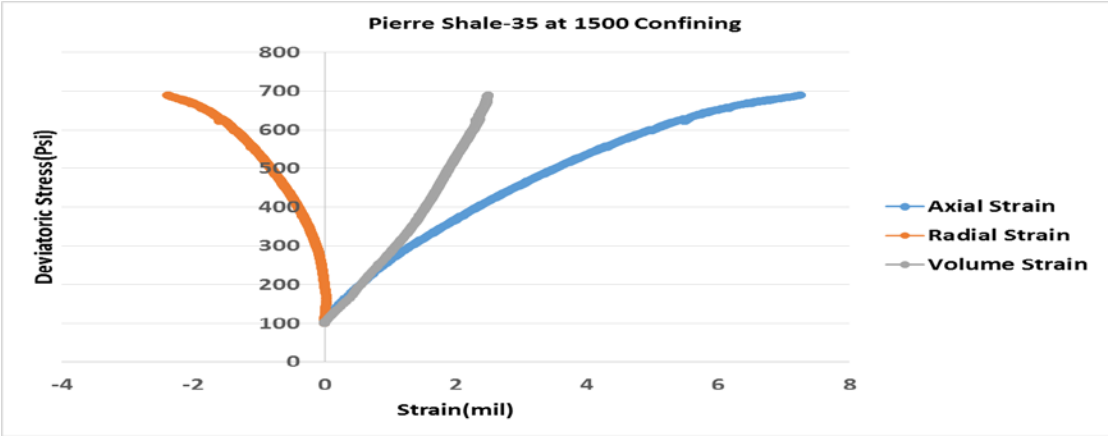

Figure 148 Deviatoric stress is increased at 1500 Psi confining pressure. The deviatoric stress starts at 100 Psi. Axial Strain, Radial, and Volume strain are measured. The point of positive dilatancy is chosen to be at 679 Psi.

Summary Table:

Table 76 Strength data for Pierre Shale-35, sample salinity is 35 KPPM, sample length is 1931 mill-inch, correction factor=2 is used to calculate the maximum compressive strength from the positive point of dilatancy.

Confining	100	500	1000	1500
Point of Positive Dilatancy(Psi)	566	624	647	679
Maximum Compressive Strength(Psi)	1132	1248	1294	1358
Sigma-1	1232	1748	2294	2858

5.8.2 Pierre Shale-100

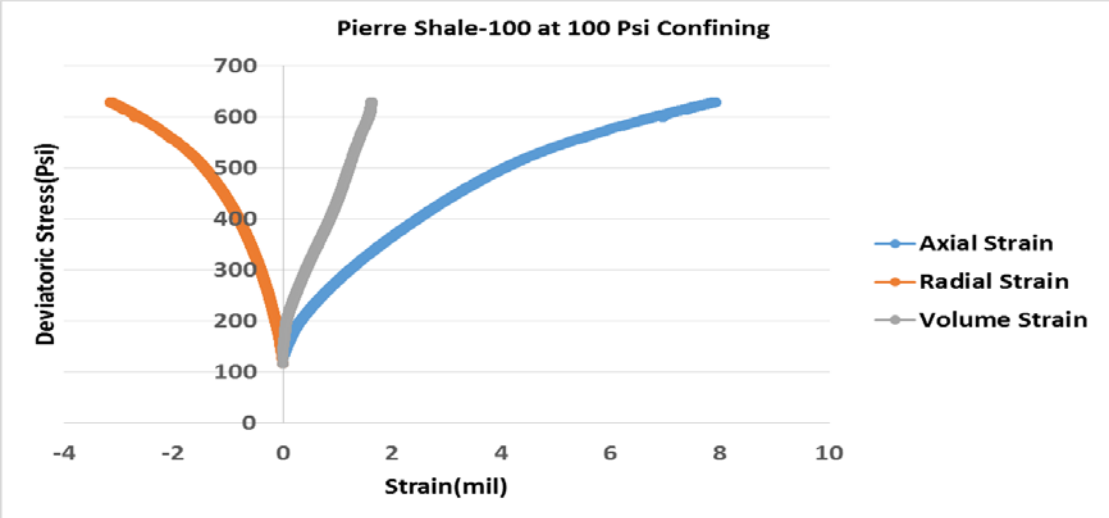

Figure 149 Deviatoric stress is increased at 100 Psi confining pressure. The deviatoric stress starts at 100 Psi. Axial Strain, Radial, and Volume strain are measured. The point of positive dilatancy is chosen to be at 614 Psi.

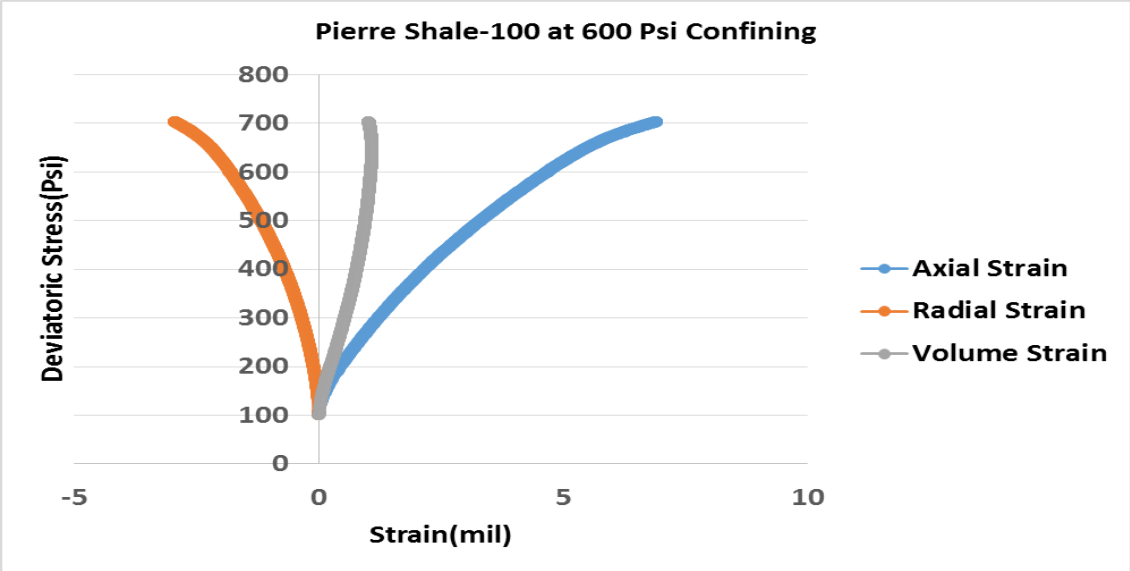

Figure 150 Deviatoric stress is increased at 600 Psi confining pressure. The deviatoric stress starts at 100 Psi. Axial Strain, Radial, and Volume strain are measured. The point of positive dilatancy is chosen to be at 642 Psi.

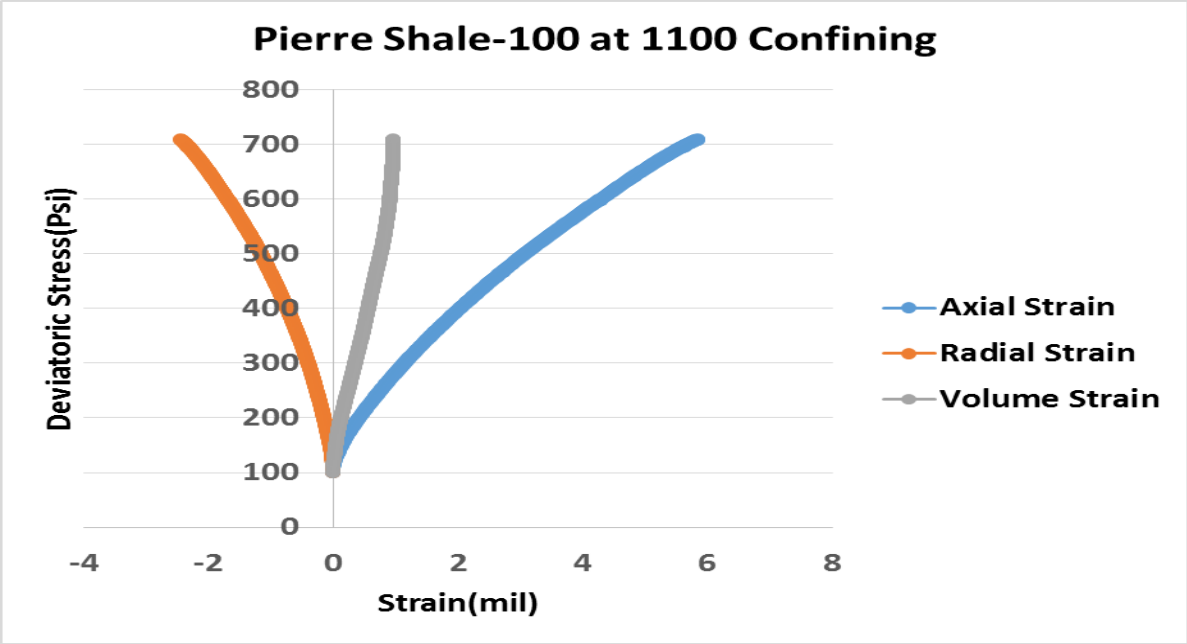

Figure 151 Deviatoric stress is increased at 1100 Psi confining pressure. The deviatoric stress starts at 100 Psi. Axial Strain, Radial, and Volume strain are measured. The point of positive dilatancy is chosen to be at 707 Psi.

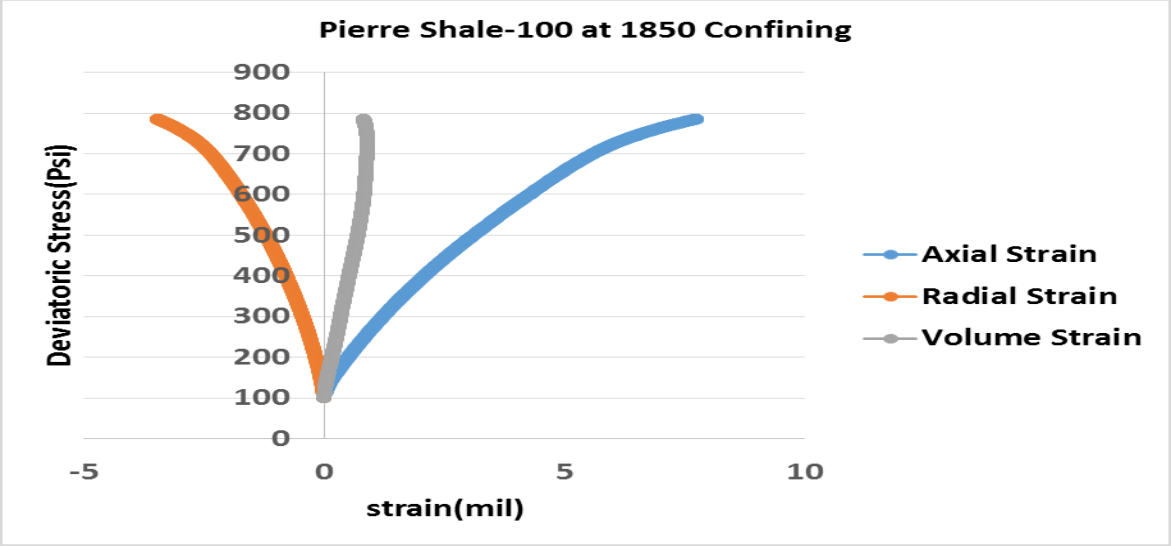

Figure 152 Deviatoric stress is increased at 1850 Psi confining pressure. The deviatoric stress starts at 100 Psi. Axial Strain, Radial, and Volume strain are measured. The point of positive dilatancy is chosen to be at 722 Psi.

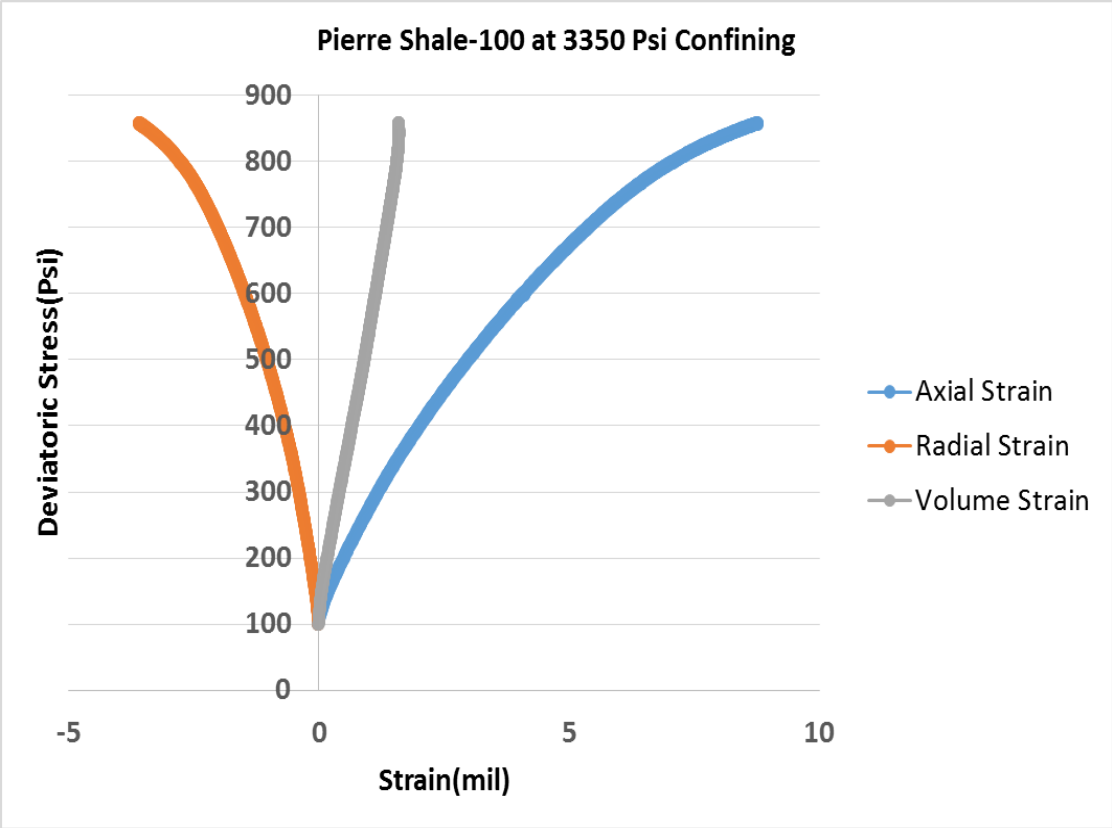

Figure 153 Deviatoric stress is increased at 3350 Psi confining pressure. The deviatoric stress starts at 100 Psi. Axial Strain, Radial, and Volume strain are measured. The point of positive dilatancy is chosen to be at 818 Psi.

Summary Table:

Table 77 Strength data for Pierre Shale-100, sample salinity is 100 KPPM, sample length is 2033 mill-inch, correction factor=2 is used to calculate the maximum compressive strength from the positive point of dilatancy.

Confining(Sigma-3)	100	600	1100	1850	3350
Point of Positive Dilatancy(Psi)	614	642	707	722	818
Maximum Compressive Strength	1228	1284	1414	1444	1636
Sigma-1	1328	1884	2514	3294	4986

5.8.3 Pierre Shale-200

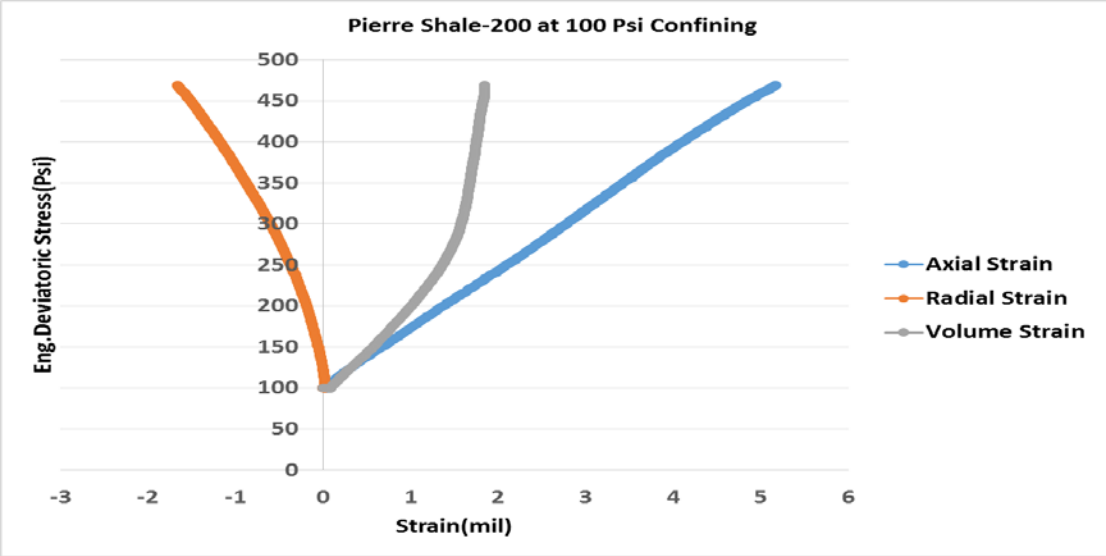

Figure 154 Deviatoric stress is increased at 100 Psi confining pressure. The deviatoric stress starts at 100 Psi. Axial Strain, Radial, and Volume strain are measured. The point of positive dilatancy is chosen to be at 468 Psi.

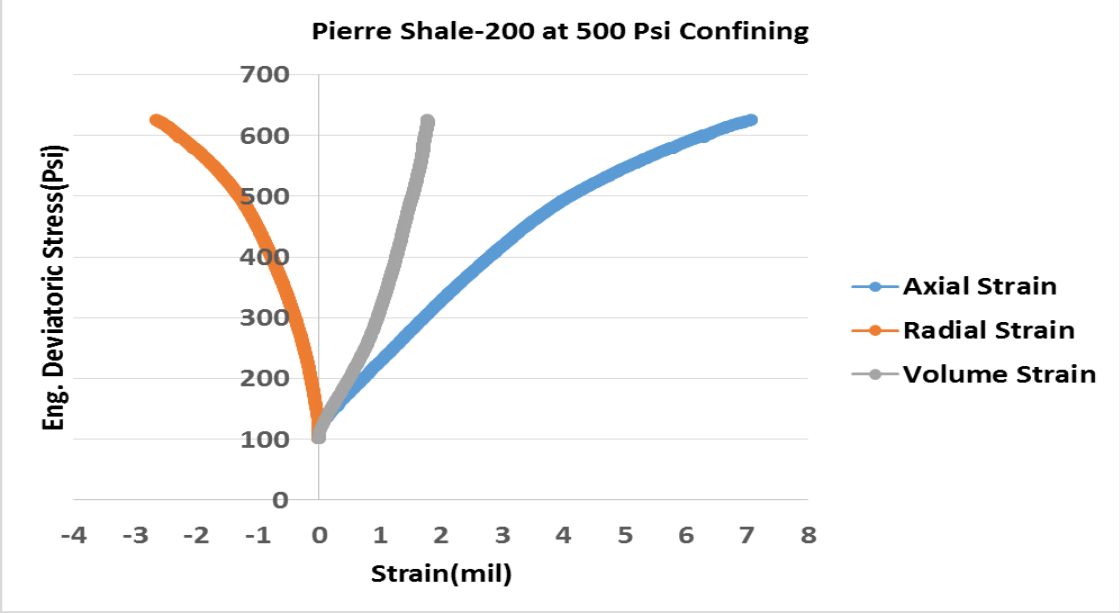

Figure 155 Deviatoric stress is increased at 500 Psi confining pressure. The deviatoric stress starts at 100 Psi. Axial Strain, Radial, and Volume strain are measured. The point of positive dilatancy is chosen to be at 598 Psi.

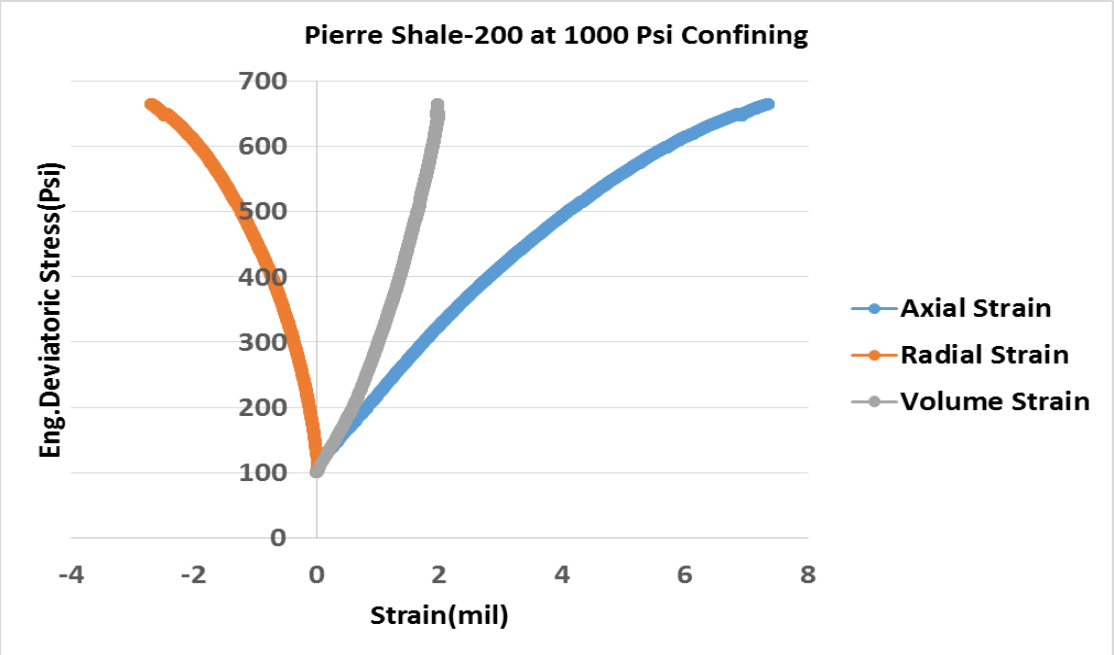

Figure 156 Deviatoric stress is increased at 1000 Psi confining pressure. The deviatoric stress starts at 100 Psi. Axial Strain, Radial, and Volume strain are measured. The point of positive dilatancy is chosen to be at 648 Psi.

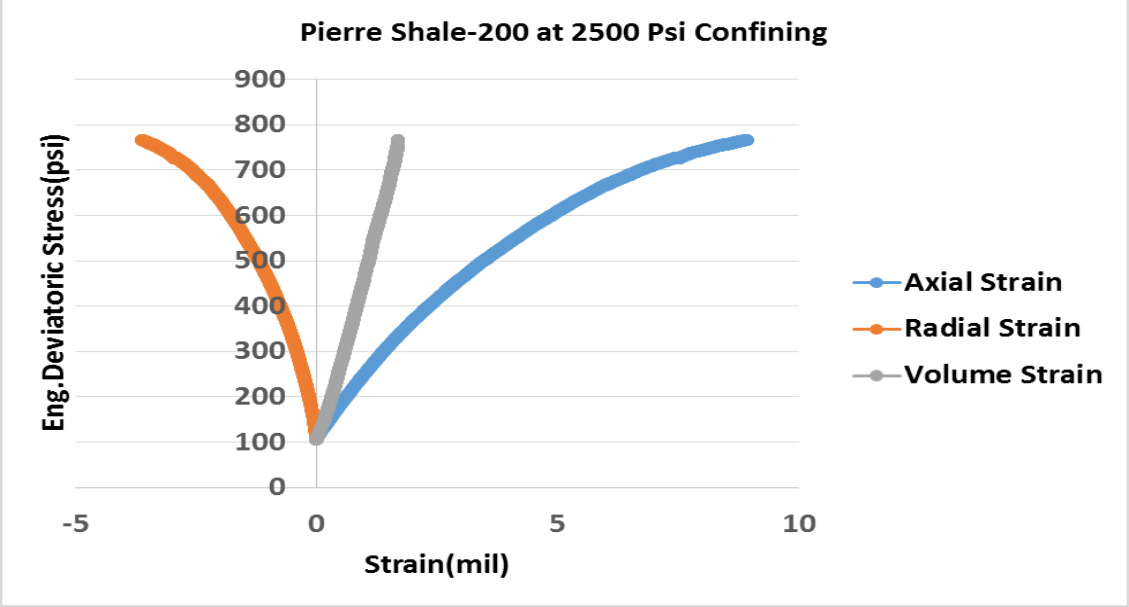

Figure 157 Deviatoric stress is increased at 2500 Psi confining pressure. The deviatoric stress starts at 100 Psi. Axial Strain, Radial, and Volume strain are measured. The point of positive dilatancy is chosen to be at 733 Psi.

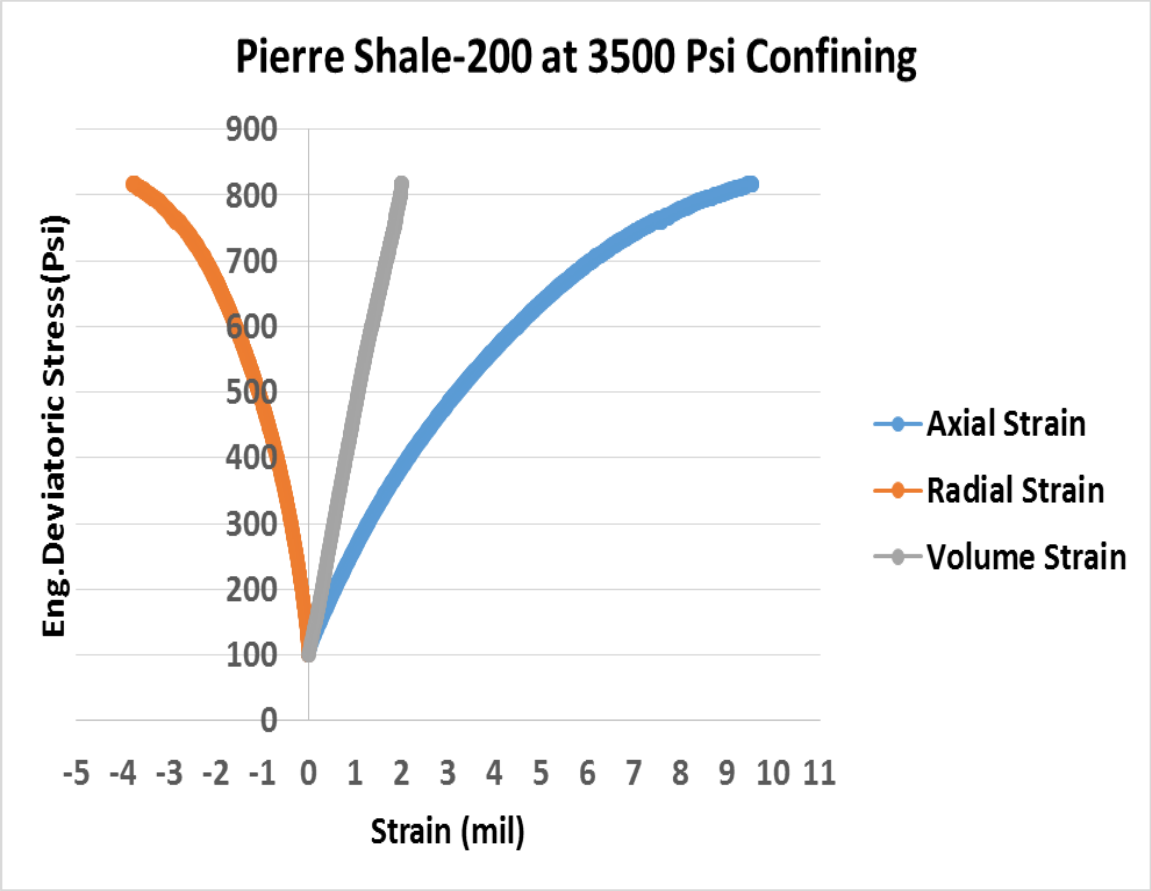

Figure 158 Deviatoric stress is increased at 3500 Psi confining pressure. The deviatoric stress starts at 100 Psi. Axial Strain, Radial, and Volume strain are measured. The point of positive dilatancy is chosen to be at 806 Psi.

Summary Table:

Table 78 Strength data for Pierre Shale-200, sample salinity is 200 KPPM, sample length is 2033 mill-inch, correction factor=2 is used to calculate the maximum compressive strength from the positive point of dilatancy.

Confining(Sigma-3)	500	1000	1500	2500	3500	4500	5500
Point of Positive Dilatancy	598	648	694	733	806	855	943
Maximum Compressive Strength	1696	2296	2888	3966	5112	6210	7386
Sigma-1	1696	2296	2888	3966	5112	6210	7386

5.9 Mixing with Sand Multistage Test

In this section, multistage strength data is presented for Sample-B mixed with 25%, 50%, and 75% of Brazos sand. The correction for maximum compressive strength is corrected by a factor of 2.

5.9.1 Seventy Five Percent

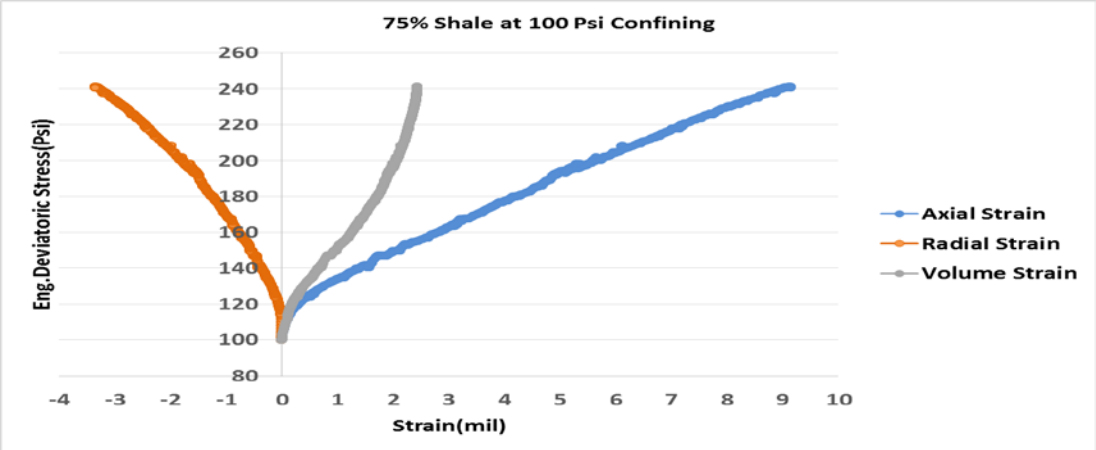

Figure 159 Deviatoric stress is increased at 100 Psi confining pressure. The deviatoric stress starts at 100 Psi. Axial Strain, Radial, and Volume strain are measured. The point of positive dilatancy is chosen to be at 240 Psi.

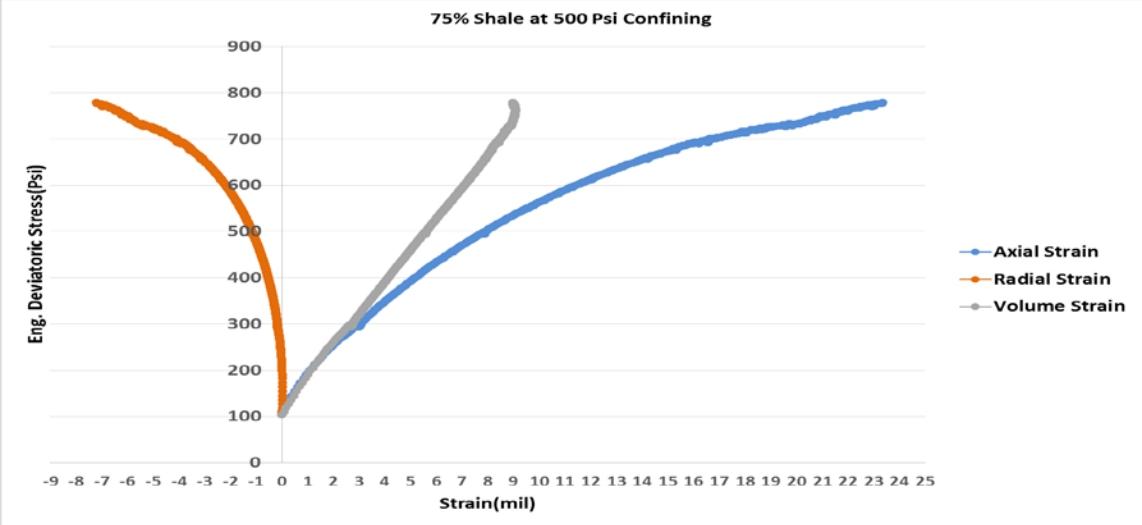

Figure 160 Deviatoric stress is increased at 500 Psi confining pressure. The deviatoric stress starts at 100 Psi. Axial Strain, Radial, and Volume strain are measured. The point of positive dilatancy is chosen to be at 763 Psi.

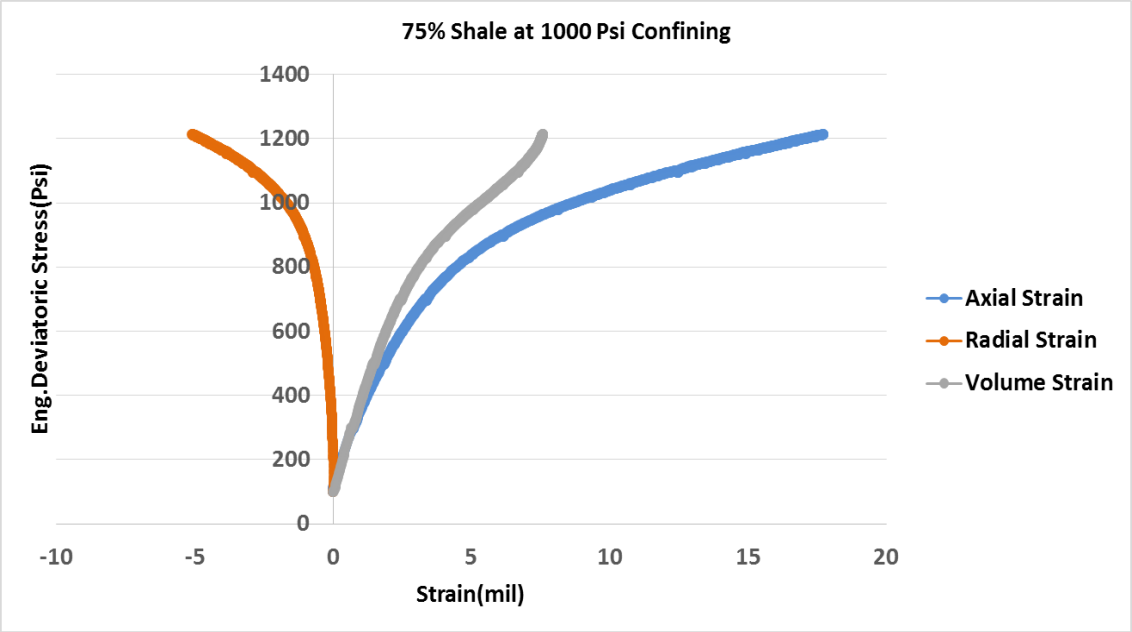

Figure 161 Deviatoric stress is increased at 1000 Psi confining pressure. The deviatoric stress starts at 100 Psi. Axial Strain, Radial, and Volume strain are measured. The point of positive dilatancy is chosen to be at 1208 Psi.

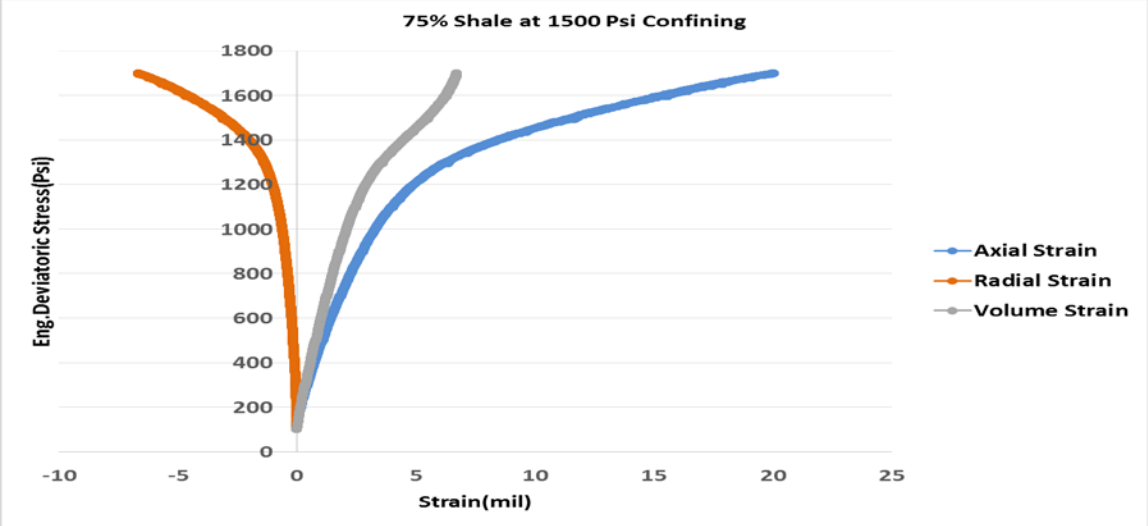

Figure 162 Deviatoric stress is increased at 1500 Psi confining pressure. The deviatoric stress starts at 100 Psi. Axial Strain, Radial, and Volume strain are measured.The point of positive dilatancy is chosen to be at 1694 Psi.

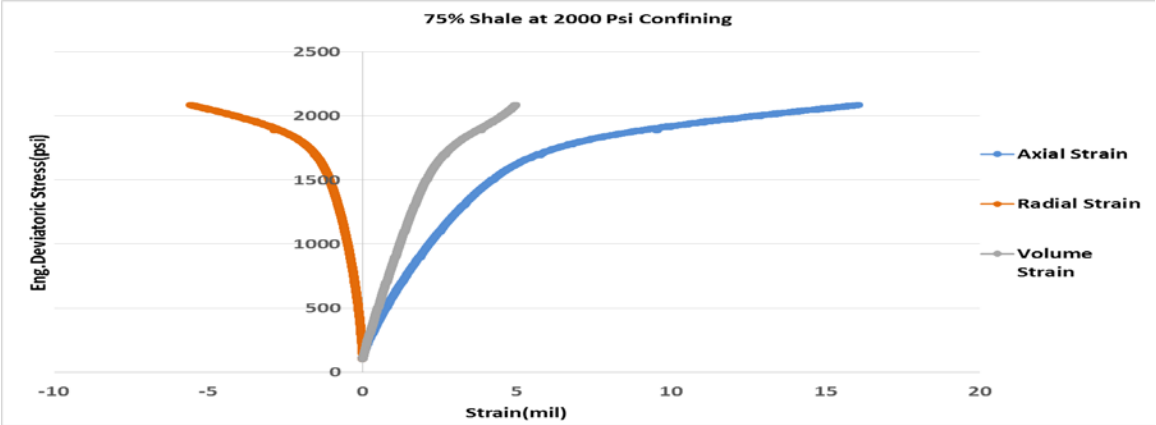

Figure 163 Deviatoric stress is increased at 2000 Psi confining pressure. The deviatoric stress starts at 100 Psi. Axial Strain, Radial, and Volume strain are measured. The point of positive dilatancy is chosen to be at 2082 Psi.

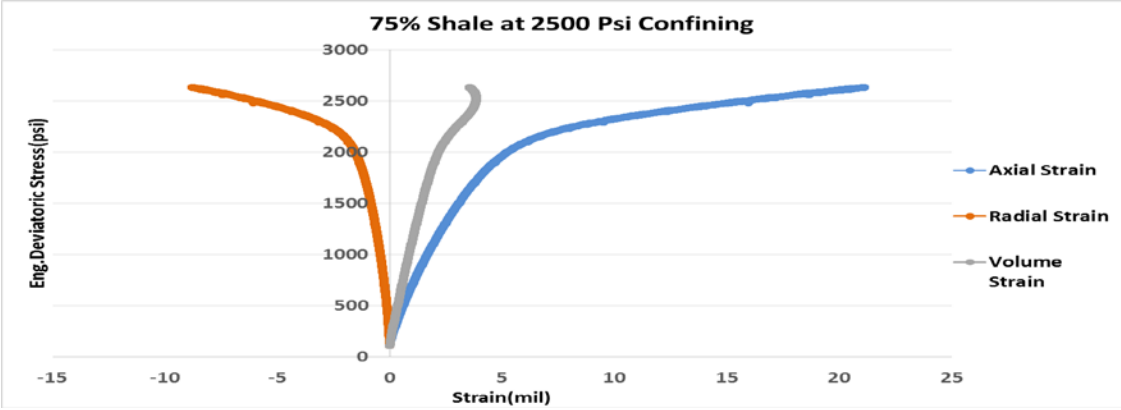

Figure 164 Deviatoric stress is increased at 2500 Psi confining pressure. The deviatoric stress starts at 100 Psi. Axial Strain, Radial, and Volume strain are measured. The point of positive dilatancy is chosen to be at 2507 Psi.

Summary Table:

Table 79 Strength data for Seventy Five Percent Shale, sample salinity is 100 KPPM, sample length is 2049 mill-inch, correction factor=2 is used to calculate the maximum compressive strength from the positive point of dilatancy.

Confining(Sigma-3)	100	500	1000	1500	2000	2500
Point of Positive Dilatancy(Psi)	240	763	1208	1694	2082	2507
Maximum Compressive Strength(Psi)	580	2026	3416	4888	6164	7514
Sigma-1	580	2026	3416	4888	6164	7514

5.9.2 Fifty Percent Shale

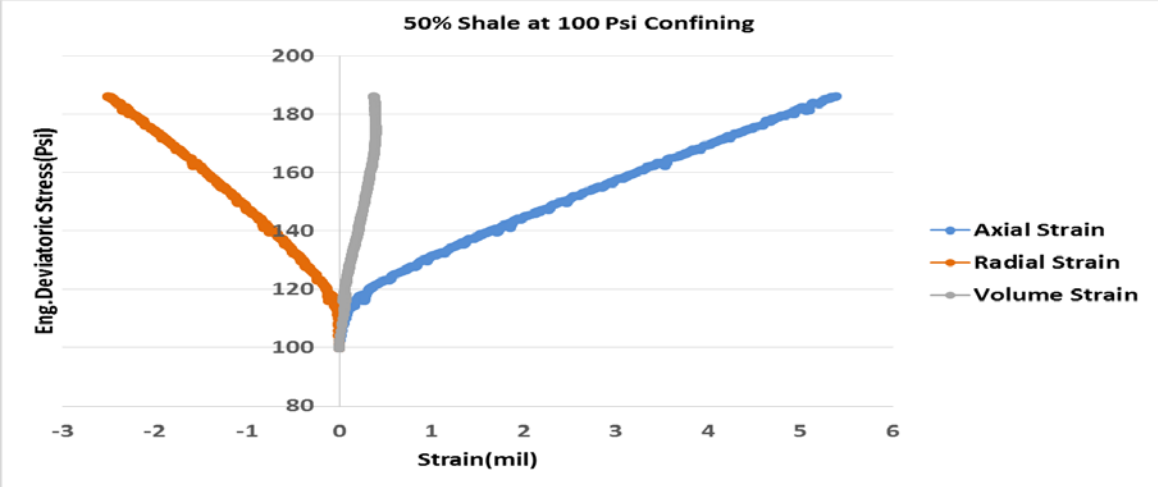

Figure 165 Deviatoric stress is increased at 100 Psi confining pressure. The deviatoric stress starts at 100 Psi. Axial Strain, Radial, and Volume strain are measured. The point of positive dilatancy is chosen to be at 180 Psi.

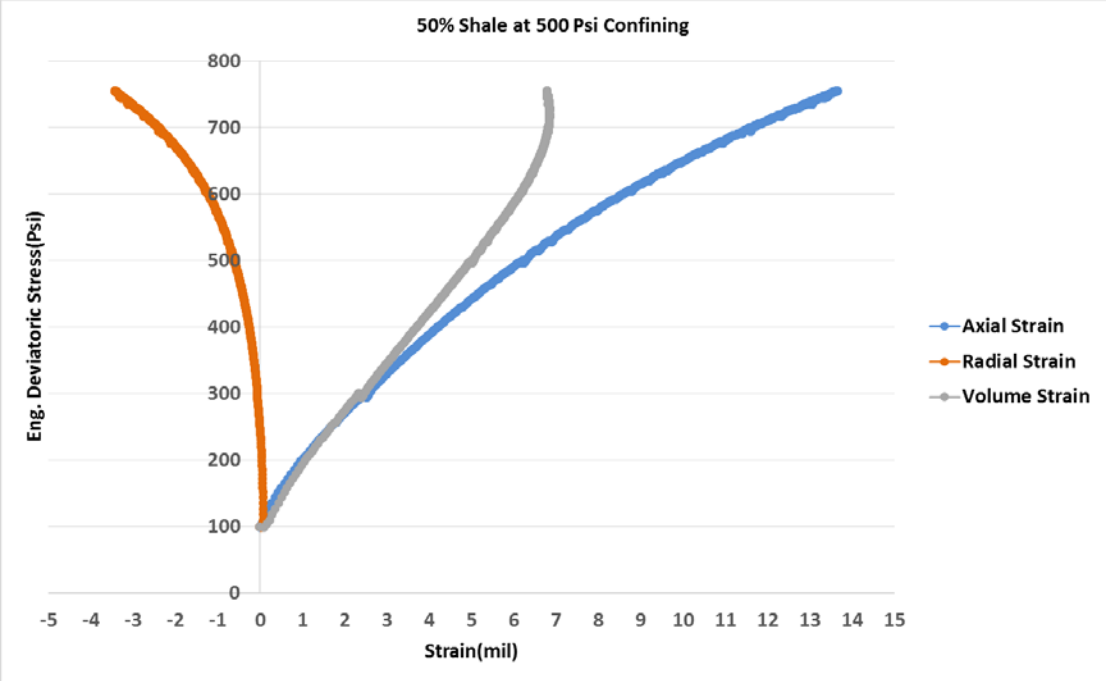

Figure 166 Deviatoric stress is increased at 500 Psi confining pressure. The deviatoric stress starts at 100 Psi. Axial Strain, Radial, and Volume strain are measured. The point of positive dilatancy is chosen to be at 727 Psi.

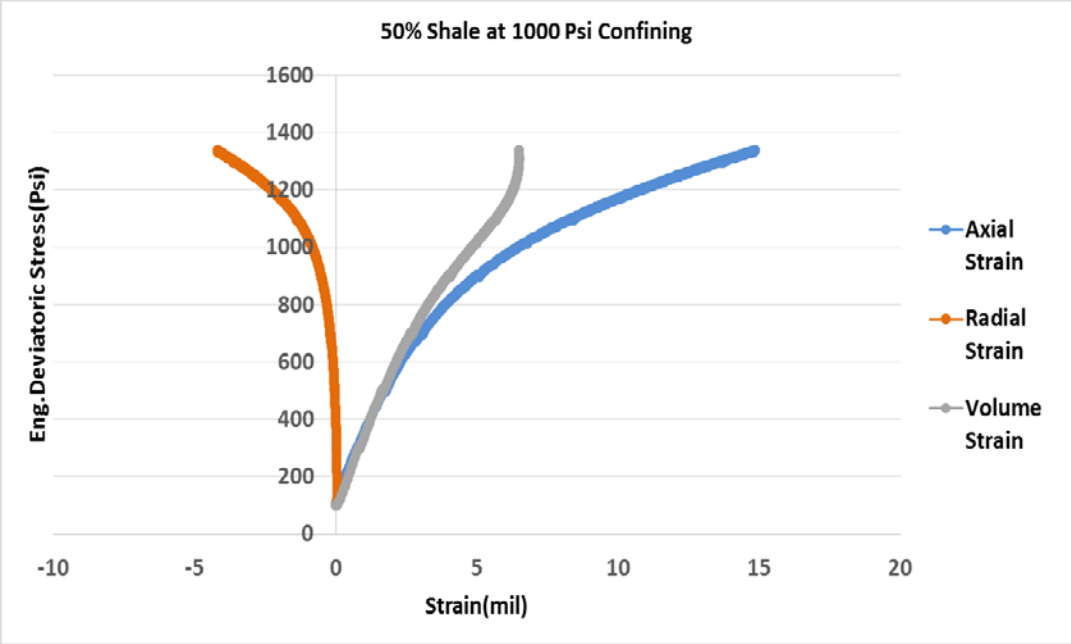

Figure 167 Deviatoric stress is increased at 1000 Psi confining pressure. The deviatoric stress starts at 100 Psi. Axial Strain, Radial, and Volume strain are measured. The point of positive dilatancy is chosen to be at 1308 Psi.

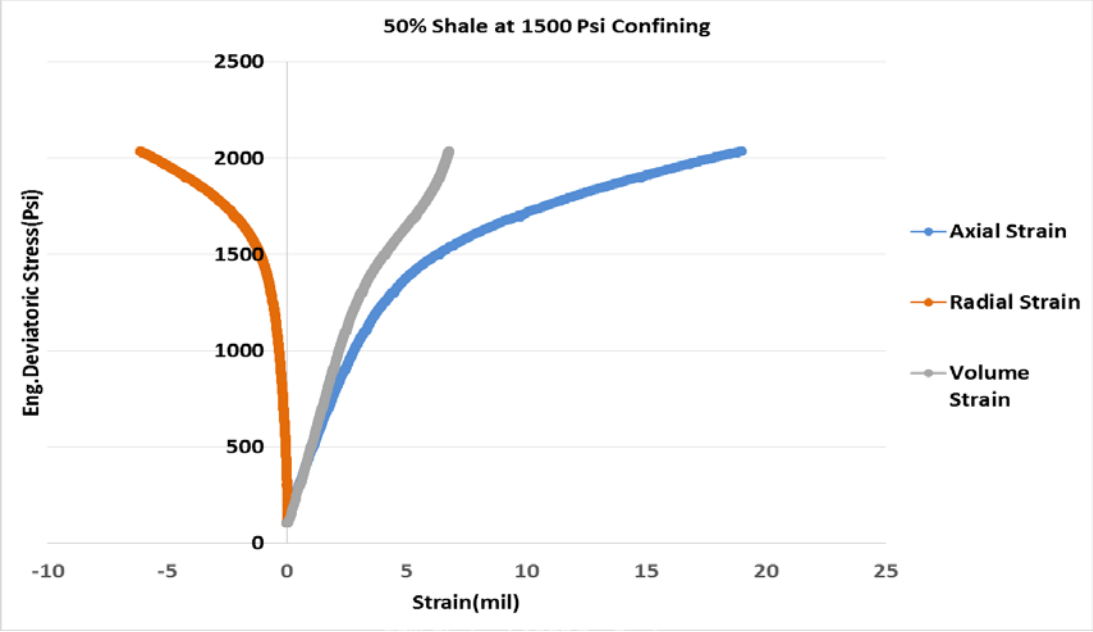

Figure 168 Deviatoric stress is increased at 1500 Psi confining pressure. The deviatoric stress starts at 100 Psi. Axial Strain, Radial, and Volume strain are measured. The point of positive dilatancy is chosen to be at 2031 Psi.

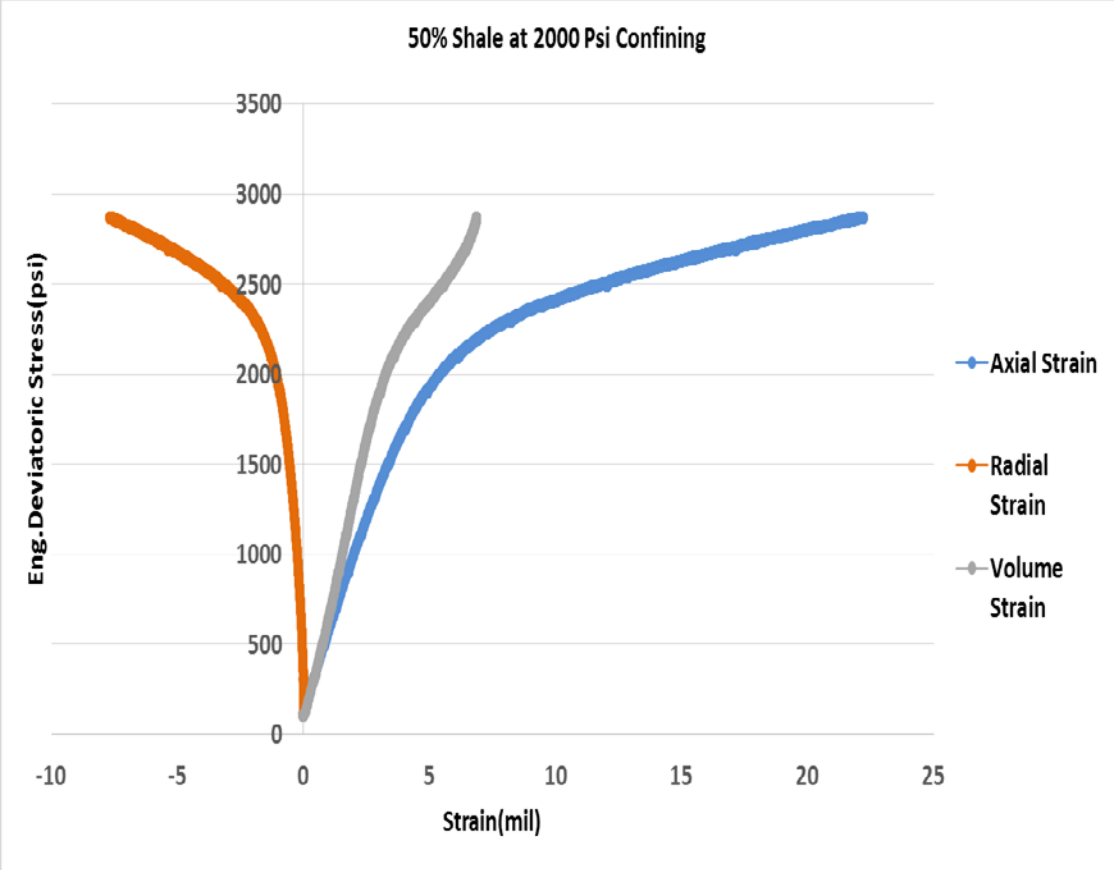

Figure 169 Deviatoric stress is increased at 2000 Psi confining pressure. The deviatoric stress starts at 100 Psi. Axial Strain, Radial, and Volume strain are measured. The point of positive dilatancy is chosen to be at 2648 Psi.

Summary Table:

Table 80 Strength data for Fifty Percent Shale, sample salinity is 100 KPPM, sample length is 2049 mill-inch, correction factor=2 is used to calculate the maximum compressive strength from the positive point of dilatancy.

Confining (Psi)	100	500	1000	1500	2000
Point of Positive Dilatancy(Psi)	180	727	1308	2031	2648
Maximum Compressive Strength(Psi)	360	1454	2616	4062	5296
Sigma-1	460	1954	3616	5562	7296

5.9.3 Twenty Five Percent Shale

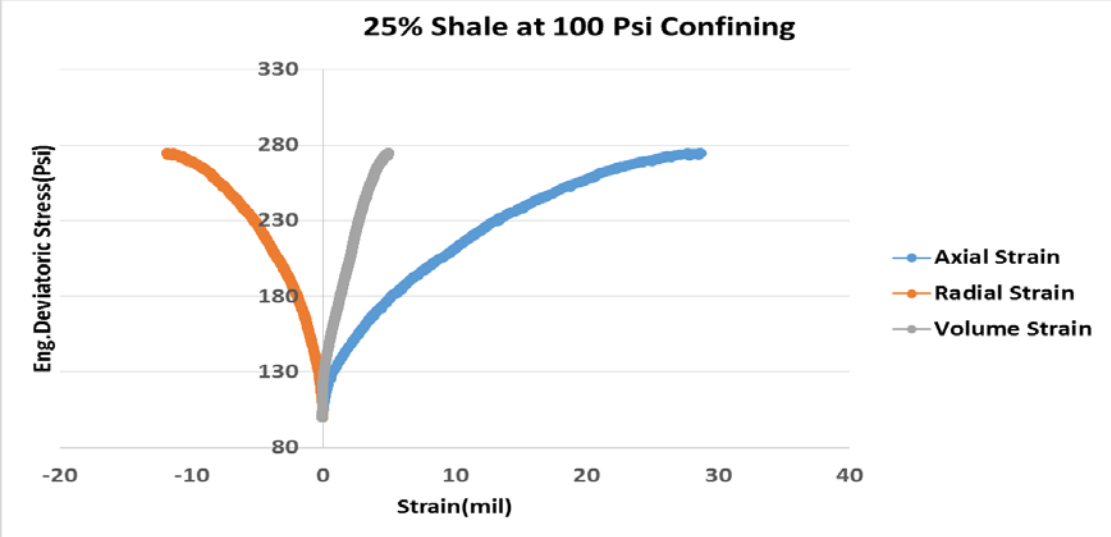

Figure 170 Deviatoric stress is increased at 100 Psi confining pressure. The deviatoric stress starts at 100 Psi. Axial Strain, Radial, and Volume strain are measured. The point of positive dilatancy is chosen to be at 272 Psi.

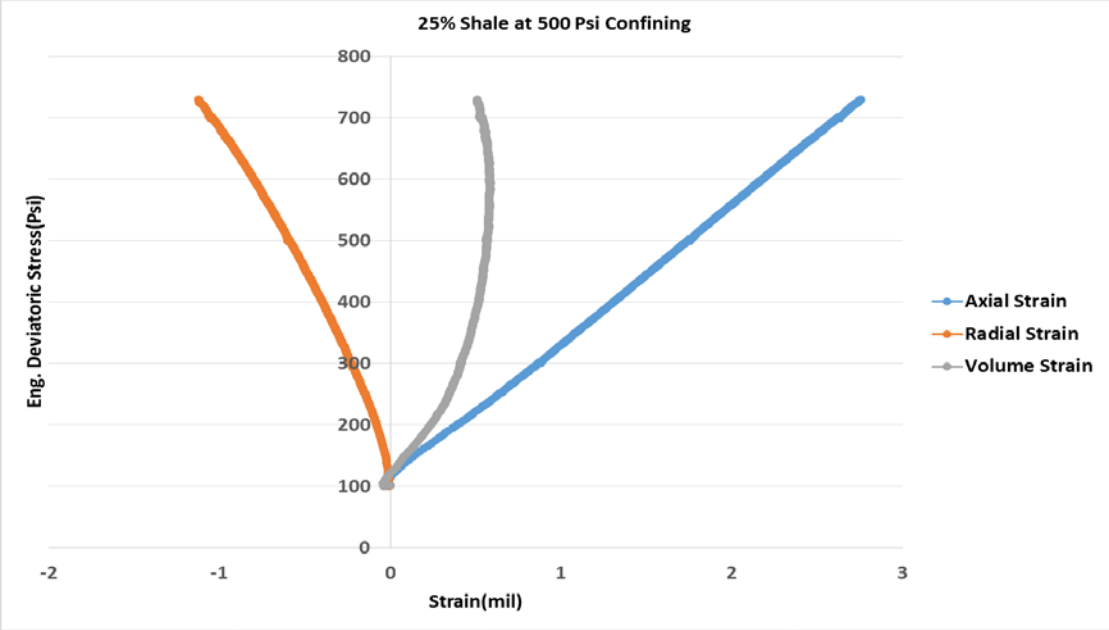

Figure 171 Deviatoric stress is increased at 500 Psi confining pressure. The deviatoric stress starts at 100 Psi. Axial Strain, Radial, and Volume strain are measured. The point of positive dilatancy is chosen to be at 600 Psi.

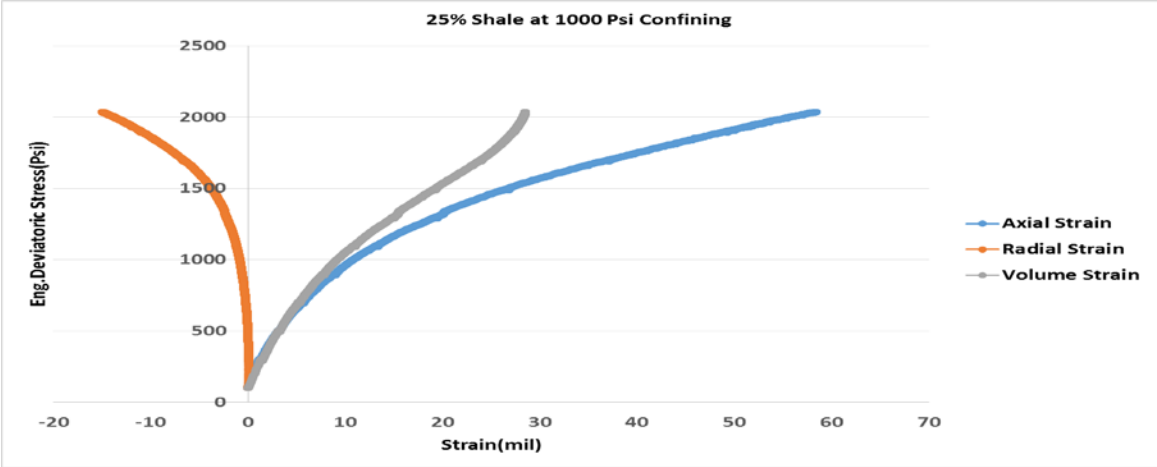

Figure 172 Deviatoric stress is increased at 1000 Psi confining pressure. The deviatoric stress starts at 100 Psi. Axial Strain, Radial, and Volume strain are measured. The point of positive dilatancy is chosen to be at 1970 Psi.

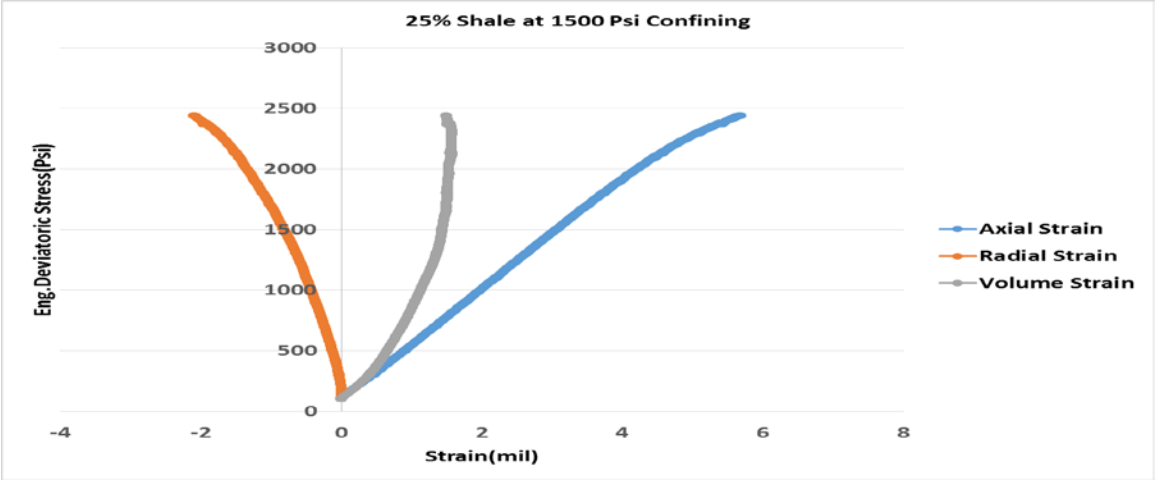

Figure 173 Deviatoric stress is increased at 1500 Psi confining pressure. The deviatoric stress starts at 100 Psi. Axial Strain, Radial, and Volume strain are measured. The point of positive dilatancy is chosen to be at 2341 Psi.

Summary Table:

Table 81 Strength data for Twenty Five Percent Shale, sample salinity is 100 KPPM, sample length is 2049 mill-inch, correction factor=2 is used to calculate the maximum compressive strength from the positive point of dilatancy.

Confining(Sigma-3)	100	500	1000	1500
Point of Positive Dilatancy(Psi)	272	600	1970	2341
Maximum Compressive Strength(Psi)	644	1700	4940	6182
Sigma-1	570	1808	4940	6182

Bibliography

Bishop, A. (1966). The Strength of Soils as Engineering Materials.

Casagrande, & Fadum. (1940). *Notes on Soil Testing for Engineering Purposes.*

Casagrande, & Fadum. (1940). *Notes on Soil Testing for Engineering Purposes.*

Coleff, D., & Myers, M. (2011). Reconsolidation Procedures. Houston, Texas, USA.

Germaine, J., & Germaine, A. (2009). *Geotechnical Laboratory Measurements For Engineers.*

Hathon, L., & Myers, M. (2011). A Survey of the Production Time-Scale Compaction Behavior of Unconsolidated Sands. *ARMA*.

Hill, H., Shirley, O. J., & Klein, G. E. (1979). Bound Water in Shaly Sands- Its Relation to Qv and Other Formation Properties. *SPWLA*.

Holtz, R. D., & Kovacs, W. D. (1981). *An Introduction to Geotechnical Engineering.*

http://flexiblelearning.auckland.ac.nz/rocks_minerals/minerals/plagioclase.html. (n.d.). Retrieved from www.auckland.ac.nz: http://flexiblelearning.auckland.ac.nz/rocks_minerals/minerals/plagioclase.html

http://geology.com/minerals/barite.shtml. (n.d.). Retrieved from www.geology.com: http://geology.com/minerals/barite.shtml

http://geology.com/minerals/dolomite.shtml. (n.d.). Retrieved from www.geology.com: http://geology.com/minerals/dolomite.shtml

http://geology.com/minerals/muscovite.shtml. (n.d.). Retrieved from www.geology.com: http://geology.com/minerals/muscovite.shtml

http://webmineral.com/data/Clinoptilolite-Ca.shtml#.Vf9k-WeFOUk. (n.d.). Retrieved from webmineral.com: http://webmineral.com/data/Clinoptilolite-Ca.shtml#.Vf9k-WeFOUk

http://webmineral.com/data/Halite.shtml#.Vf9nPGeFOUk. (n.d.). Retrieved from www.webmineral.com: http://webmineral.com/data/Halite.shtml#.Vf9nPGeFOUk

http://webmineral.com/data/Illite.shtml#.Vf9rXWeFOUk. (n.d.). Retrieved from www.webmineral.com: http://webmineral.com/data/Illite.shtml#.Vf9rXWeFOUk

http://webmineral.com/data/Kaolinite.shtml#.Vf9ygGeFOUk. (n.d.). Retrieved from www.webmineral.com: http://webmineral.com/data/Kaolinite.shtml#.Vf9ygGeFOUk

http://webmineral.com/data/Montmorillonite.shtml#.Vf9u3WeFOUk. (n.d.). Retrieved from www.webmineral.com: http://webmineral.com/data/Montmorillonite.shtml#.Vf9u3WeFOUk

http://www.minerals.net/mineral/anatase.aspx. (n.d.). Retrieved from www.minerals.net: http://www.minerals.net/mineral/anatase.aspx

http://www.minerals.net/mineral/chlorite.aspx. (n.d.). Retrieved from www.minerals.net: http://www.minerals.net/mineral/chlorite.aspx

http://www.minerals.net/mineral/pyrite.aspx. (n.d.). Retrieved from www.minerals.ne: http://www.minerals.net/mineral/pyrite.aspx

http://www.minerals.net/mineral/siderite.aspx. (n.d.). Retrieved from www.minerals.net: http://www.minerals.net/mineral/siderite.aspx

https://www.esci.umn.edu/courses/1001/minerals/potassium_feldspar.shtml. (n.d.). Retrieved from www.esci.umn.edu: https://www.esci.umn.edu/courses/1001/minerals/potassium_feldspar.shtml

https://www.esci.umn.edu/courses/1001/minerals/quartz.shtml. (n.d.). Retrieved from www.esci.umn.edu: https://www.esci.umn.edu/courses/1001/minerals/quartz.shtml

Kodama, H. (n.d.). *http://www.britannica.com/science/clay-mineral*. Retrieved from www.britannica.com: http://www.britannica.com/science/clay-mineral

Lambe, W., & Whitman, R. (1969). *Soil Mechanics.*

Mitchell, J. (1993). *Fundamentals of Soil Behavior.* John Wiley & Sons.

Murthy. (2002). *Principles and Practices of Soil Mechanics and Foundation Engineering.*

Myers, M. (1991). A Saturation Interpretation Model for Dielectric Constant of Shaly Sands. *SCA*.

Olsen, R. (1974). Shearing strength of kaolinite, illite, and montmorillonite. *Journal of Soil Mechanics and Foundations Division*.

Salman, M., Myers, M., & Sharf Aldin, M. (2015). Comparison and Correction of Multistage Triaxial Tests to Single Stage Triaxial Test for the Rock Mechanical Testing. Houston, Texas, USA: University of Houston.

Sposito, G., Skipper, N., Sutton, R., Park, S., Soper, A., & Greathouse, J. (1998).

Terzaghi, K., Peck, R., & Mesri, G. (1963). *Soil Mechanics in Engineering Practice.*

U.S Gelogical Survey. (n.d.). Retrieved from www.usgs.gov: http://pubs.usgs.gov/of/2001/of01-041/htmldocs/clays/illite.htm